STUDY OF COMPOSITES COMPRISING OF HEXAFERRITE, BISMUTH COPPER TITANATE AND CONDUCTING POLYMER FOR ELECTROMAGNETIC SHIELDING

A thesis submitted to

Lovely Professional University

In partial fulfilment of the requirements for the award of the degree of

Doctor of Philosophy (Ph.D.) in Physics

Submitted by: **Supervised by:**

Tchouank Tekou Carol Trudel   Dr. Ajeet Kumar Srivastava

Reg. No: 11614119   (Professor)

Lovely Faculty of Technology and Sciences

School of Chemical Engineering and Physical Sciences

Department of Physics

Lovely Professional University

Phagwara-144411, Punjab, India

2019

Declaration

I hereby declare that the thesis titled "**Study of Composites Comprising of Hexaferrite, Bismuth Copper Titanate and Conducting Polymer for Electromagnetic Shielding**" submitted for the award of Ph.D. degree in physics is entirely my original work and all the ideas and references have been duly acknowledged. It does not contain any work for the award of any other degree of diploma from any other university.

Author: Supervisor:

Tchouank Tekou Carol Trudel   **Dr. Ajeet Kumar Srivastava**

Reg. number: 11614119   **Professor, Department of Physics**

Lovely Professional University

Phagwara-144411

Punjab, India.

Certificate

This is to certify that **Tchouank Tekou Carol Trudel** has completed the thesis titled "**Study of Composites Comprising of Hexaferrite, Bismuth Copper Titanate and Conducting Polymer for Electromagnetic Shielding**" under my guidance and supervision. To the best of knowledge, the present work is the result of his original investigation and study. No part of the thesis has ever been submitted for any other degree or diploma at any university. The thesis is fit for submission and partial fulfilment for the award of Ph.D. degree in Physics.

Supervisor:

Dr. Ajeet Kumar Srivastava (Professor)

 Department of Physics

Lovely Professional University

Phagwara-144411

Punjab, India.

Acknowledgments

I say a big thank you to all the African i met in India who have contributed to my fulfilment especially the Ivorian community.

I will not be able to finish these thanks without saying a big thank you to Ayinkamiye Clarisse from Rwanda. Her friendship was a great importance to me.

Author: **Tchouank Tekou Carol Trudel**

Registration number: 11614119

List of symbols

Symbol	Description
ε^*	Complex permittivity
ε'	Real part of complex permittivity (Dielectric constant)
ε''	Imaginary part of complex permittivity (Dielectric loss)
$\tan \delta_e$	Dielectric loss tangent
δ_e	Dielectric loss angle
μ^*	Complex permeability
μ'	Real part of complex permeability
μ''	Imaginary part of complex permeability
$\tan \delta_m$	Magnetic loss tangent
δ_m	Magnetic loss angle
$\tan \delta_T$	Total loss tangent
Z^*	Complex impedance
Z'	Real part of complex impedance
Z''	Imaginary part of complex impedance
Z_{in}	Normalized input impedance
ε_0	Permittivity of vacuum
μ_0	Permeability of vacuum
f	Frequency of electric field
ω	Angular frequency
R_L	Reflection loss
σ_t	Total conductivity
σ_{AC}	Frequency dependent part of total conductivity (AC conductivity)
σ_{DC}	Frequency independent part of total conductivity (DC conductivity)
SE_T	Total shielding effectiveness
SE_A	Shielding effectiveness for absorption
SE_R	Shielding effectiveness for reflection
A_{eff}	Effective absorption of the EM wave absorber
T	Transmission coefficient
R	Reflection coefficient

H_c	Coercivity or coercive field
M_s	Saturation magnetization
M_r	Remnant magnetization or Remanence
T_c	Curie temperature
T_N	Neel temperature
λ	X-ray wavelength
hkl	Miller indices
β	Full width at half maximum
d_{hkl}	Spacing between the lattices
θ	Angle of diffraction (Braggs angle)
a	Lattice constant
c	Lattice constant
V_{cell} or V	Volume of unit cell
D	Crystallite size
k	Shape factor
R_p	Profile R-factor
R_{wp}	Weighted profile R-factor
R_{exp}	Expected R-factor
χ^2	Goodness of fit (chi-squared)
C	Capacitance
E_g	Band gap
α	Absorption coefficient
υ	Frequency of incident photon
R_{gb}	Grain boundary resistance
R_g	Grain resistance
C_{gb}	Grain boundary capacitance
C_g	Grain capacitance
d_m	Bulk or experimental density
d_x	X-ray or theoretical or calculated density
P	Porosity
S	Surface area

I	Transmitted intensity	
I_0	Incident intensity	
m	Mass of pellet	
M	Molecular weight	
t	Thickness of pellet	
m_e	Orbital magnetic moment	
m_s	Spin magnetic moment	
$\boldsymbol{M}$	Magnetization vector	
$\boldsymbol{H}$	Magnetic field vector	

List of figures

List of tables

ABSTRACT

Today, with the great advance in the technology especially in the fields of telecommunications, the electromagnetic waves are at the origin of several problems observed in the society. High-frequency devices are essential for humans, but they also produce electromagnetic waves that can harm human health as well as some electronic devices. Then one might ask: Should we go back to the time when all this did not exist? However, with the improvement of the living conditions due to this advance, all these devices are presented as being a necessary evil. So, it makes more sense to ask how to stop or reduce these negative effects. In order to answer this question, the researchers began to synthesize materials capable of absorbing or attenuating the intensity of these undesired waves.

Electromagnetic waves are composed of both electric and magnetic fields. So the absorber materials must be able to absorb these two fields. Hexaferrite and bismuth copper titanate materials are suitable candidates for absorbing the magnetic and electrical fields respectively. In this research work, a combination of hexaferrite, BCTO and polyaniline (PANI) materials was synthesized and characterized. In addition, properties such as structural, optical, magnetic and dielectric have been studied for various compositions. . The synthesis of hexaferrite and BCTO was carried out utilizing autocombustion sol-gel technique. An oxidative polymerization technique was employed to prepare PANI. In this research work, following samples been prepared and investigated:

- ✓ $Ba_{1-x}Al_xFe_{12-y}Mn_yO_{19}$ (x=0.6 and y=0.3)
- ✓ $BaFe_{12-2x}Al_xCr_xO_{19}$ (x=0.0, 0.2, 0.4)
- ✓ $SrFe_{12-2x}Cr_xBi_xO_{19}$ (x=0.0, 0.15, 0.2)
- ✓ $BaFe_{12-2x}Bi_xAl_xO_{19}$ (x=0.1)
- ✓ $BaFe_{12-x}Bi_xO_{19}$ (x=0.2)
- ✓ $Ba_{1-x}Dy_xFe_{12-y}Cr_yO_{19}$ (x=0.3 and y=0.6)
- ✓ $Ba_{2-2x}Cr_xNi_xCo_2Fe_{12}O_{22}$ (x=0.0, 0.1, 0.15, 0.2)
- ✓ $Bi_{2/3}Cu_{3-2x}Ni_xCo_xTi_4O_{12}$ (x=0.0, 0.1, 0.2)
- ✓ $[Bi_{(1-x)}La_x]_{2/3}Cu_3Ti_4O_{12}$ (x=0.1, 0.2)

The structural, magnetic, dielectric, EMI shielding and optical properties of these synthesized samples were examined by the use of X-ray diffraction (XRD), Raman spectroscopy, Fourier Transform Infrared (FTIR) spectroscopy, Field emission scanning electron microscope

(FESEM), Impedance analyzer, UV-Vis-NIR spectroscopy, Vector network analyzer (VNA), and Vibrating sample magnetometer (VSM).

The effect of heat-treatment temperature on the structural, dielectric, magnetic and optical properties of M-type barium hexagonal ferrites $Ba_{1-x}Al_xFe_{12-y}Mn_yO_{19}$ (x=0.6 and y=0.3) sintered at 750℃, 850℃, 950℃ and 1050℃ was investigated. From XRD patterns, all diffraction planes defining magnetoplumbite hexaferrite were observed with presence of secondary phases (α-Fe_2O_3). FTIR spectra revealed characteristic absorption bands of hexaferrite between 400 and 600 cm^{-1}. Saturation magnetization and remanence were observed to increase with the temperature from 6.78 to 33.97emu/g and 4.14 to 20.55emu/g; however the highest value of coercivity was found to be 7779.94 Oe at 850℃. The dielectric constant was increased with the temperature at lower frequencies and the highest value was found to be 575. Band gap energy of prepared samples was observed to fluctuate in the range 3.31-3.62 eV which makes them suitable for UV-blue light emitting diodes (LEDs).

XRD analysis of $BaFe_{12-2x}Al_xCr_xO_{19}$ (x=0.0, 0.2, 0.4) samples reveals the formation of hexaferrites with single phase and no impurity phase was detected. FTIR spectra show bands at 437 cm^{-1} and 590 cm^{-1} which indicate the possible of hexaferrites. The micrographs of FESEM shows agglomerated grains with hexagonal plate-like shape while the EDX spectra confirm the composition of the synthesized samples. Dielectric constant decreases abruptly at lower frequencies and an increment in dielectric constant at much higher frequency region was observed Grain boundaries dominate the AC conductivity at lower frequencies while the grains could be responsible for the observed dispersion at higher frequencies. The values of coercivity for all the samples were found to be greater than 1200 Oe. This makes the prepared samples useful for high-density perpendicular magnetic recording media.

The influence of Cr-Bi substitution on the structural, optical, electrical and magnetic properties of strontium hexaferrites with general formula $SrFe_{12-2x}Cr_xBi_xO_{19}$ (with x=0.0-0.2) was studied. XRD analysis reveals the single M-type hexaferrite formation with crystallite size ranging from 33 nm to 42 nm. The observed peaks at 441, 552 and 598 cm^{-1} wavenumber were observed using the FTIR spectra spectroscopy technique confirms the formation of hexaferrite nanoparticles of $SrFe_{12-2x}Cr_xBi_xO_{19}$, the hexagonal shape of hexaferrite was observed in the FESEM images. The band gap of the material lies between 2.11 to 2.37 eV. The saturation magnetization (Ms) and remanence (Mr) enhances with

increasing Cr^{3+}-Bi^{3+} concentration. AC conductivity increases at higher frequencies while dielectric constant and dielectric loss tangent decrease with frequency.

The single crystal structure of Co_2Y barium hexaferrite ($Ba_{2-2x}Cr_xNi_xCo_2Fe_{12}O_{22}$ (x=0.0-0.15)) has been revealed by XRD analysis and confirmed by Rietveld refinement. The crystallite size was found to be in the range 31.73-34 nm and lattice parameters (a and c) were found to vary between 5.8611-5.8648Å and 43.398-43.5088 Å respectively. FESEM micrographs show a flat hexagonal shape and non-uniform particles with 0.167 µm and 0.165 µm as the average particle size for x=0.0 and x=0.15 respectively. Highest values of saturation magnetization and remanence were obtained for x=0.1 whereas the coercivity (Hc) enhances with Cr^{3+}-Ni^{2+} concentration. Typical behaviour of ferrite materials was been observed with decrease in dielectric constant with the frequency. The optical band gap of prepared samples lies between 0.74 to 2.16 eV which makes them adequate for many electronics applications.

The XRD patterns revealed that the prepared BCTO electroceramic with chemical composition $Bi_{2/3}Cu_{3-2x}Ni_xCo_xTi_4O_{12}$ (x=0.0, 0.1, 0.2) are of single phase without the presence of any other phases such as CuO and TiO_2. FESEM micrographs showed particles with well-defined cubic shape of bismuth copper titanate ceramics. EDX spectra showed all the chemical elements of the prepared composition, this confirm the stoichiometry and the purity of the synthesized electroceramic. UV-Vis-NIR spectrophotometer was used to study the optical band gap in the region of 225-1000 nm wavelength and the highest value of 3.69 eV was observed in the sample having x=0.1. The dielectric response and impedance spectroscopy of the electroceramic are discussed based on Debye-type relaxation process and Maxwell-Wagner model. The sample having x=0.0 shows the highest dielectric constant (3800) at room-temperature and a frequency of 42 Hz as compared to x=0.1 and x=0.2. The Cole-Cole plots of complex impedance and complex electric modulus indicate that grain-boundary resistance is the major contributor to the dielectric response of the prepared BCTO electroceramic.

The effect of polyaniline (PANI) on optical properties of Bi-Al doped M-type barium hexaferrite was investigated using UV-Vis-NIR spectrometer (Varian, Cary 5000). XRD analysis of the prepared sample reveals the magnetoplumbite phase of M-type hexagonal ferrites without the presence of any secondary phase. From XRD pattern, the presence of polyaniline was also observed at around 25°. Lattice constants were found to increase with

the increase in PANI. Rietveld refinement confirmed the purity of prepared M-type hexaferrite with GoF (Good of fit) in the range 1.6-1.8. FTIR spectra show the presence of two significant absorption bands between 400 cm^{-1} and 600 cm^{-1}, indicating the formation of ferrite phase. The peaks observed at 800 cm^{-1} and 1600 cm^{-1} wavenumber confirm the presence of polyaniline. Band gap energies of prepared samples were found to be 2.24, 2.36 and 2.21 eV for HP1, HP2 and HP3 respectively.

Structural and optical properties of $Ba_{0.7}Dy_{0.3}Fe_{11.4}Cr_{0.6}O_{19}$ nano-sized particles embedded in PANI were carried out. XRD spectra of the prepared sample show magnetoplumbite phase of M-type hexaferrite along with the presence of hematite (α-Fe_2O_3). The presence of polyaniline was also observed at around 25°. Two specific bands in the range 400-600 cm^{-1} were observed from FTIR spectra confirm the hexaferrites structure formation. Increasing the amount of PANI caused the band gap to decrease from 1.96 to 1.59 eV.

Structural and magnetic properties of $BaFe_{12-x}Bi_xO_{19}$ (x=0.2) (BaM) and $[Bi_{(1-x)}La_x]_{2/3}Cu_3Ti_4O_{12}$ (x=0.2) (BCTO) particles coated in poly pyrrole (PPY) were investigated. XRD patterns show that prepared samples are of single phase without the presence of any other phases. FTIR spectra show the characteristic functional groups of PPY in the range 800-1700 cm^{-1}. The lattice parameters of prepared BaM were found to be a=5.8976 Å and c=23.2051 Å whereas the lattice constant of prepared BCTO was a=7.433 Å. Saturation magnetization of BaM was found to decrease after adding BCTO and PPY.

Co_2Y/BCTO/PANI composite was synthesized using mechanical blending method. The XRD analysis shows that the composite exhibit pure phase of Co_2Y barium hexaferrite and bismuth copper titanate (BCTO) which is also supported by Raman analysis. Resonance occurs over the whole frequency region in the spectra of Co_2Y/BCTO/ PANI composite with dielectric losses dominating the lower frequency region due to interfacial polarization and magnetic losses dominating the higher frequency region as a result of eddy current losses, natural and exchange resonance. The observed values of shielding effectiveness for reflection are higher than those of shielding effectiveness for absorption, this indicates that most of the incident EM wave is reflected rather than absorbed. The Co_2Y/BCTO/PANI composite shows total shielding effectiveness value above 20 dB with maximum total shielding effectiveness value of 31.97 dB at 10.30 GHz and matching thickness of 2 mm. The high value of total shielding effectiveness is attributed to good impedance matching between the components of the

Co$_2$Y/BCTO/ PANI composite as well as higher dielectric losses as compared to magnetic loses.

Six chapters were used in this thesis, with chapter one as a brief introduction to the research including notions on magnetic materials, dielectric materials, conducting polymers and theory on microwave absorption. Chapter two presents a review of the literature on the materials used. Chapter Three gives methods of synthesis. Here, the method of synthesis of each material is well detailed. Chapter four presents the principles of characterizations techniques. The presentation and explanation of experimental data for each sample is given in chapter five and the summary and conclusion are given in chapter six.

TABLE OF CONTENTS

Dedicated to my family

I love you so much

"…by the grace of God I am what I am…"

(1 Corinthians 15:10)

Chapter 1: General Introduction

1.1 Preamble

Today, the world is experiencing state-of-the-art technology due to the discovery of certain materials with interesting physical and chemical properties. Areas such as telecommunications and high-frequency industries are the sources of electromagnetic waves, which in some cases are a problem for electronic devices and for human health [1]. In fact, such as cell phones, wireless local area networks, automatic control systems, sensors and radio antennas are exactly the sources of unwanted electromagnetic (EM) waves. To solve this problem, researchers have embarked on the synthesis of materials capable of absorbing these unwanted electromagnetic waves at different frequencies.

Hexaferrite materials discovered in 1950 [2] have received great attention because of their magnetic and dielectric properties, which is interesting compared to spinel ferrites and garnets and has been used to absorb EM waves. However, these have shown limits for certain frequencies. To improve the absorption properties, several hexaferrite-based materials have been synthesized such as: M-type doped M-type hexaferrite / polyaniline [3], BZF / ATO[4], PANI / BF [5], Polypyrrole / Strontium hexaferrite [6], Reduced Graphene Oxide/Strontium Ferrite/Polyaniline [7], PANI/Sr(MnTi)Fe$_{10}$O$_{19}$ [8], Sr(ZnZr)$_x$Fe$_{12-2x}$O$_{19}$/PANI [9], SrFe$_{11}$Zn$_{0.5}$Ni$_{0.5}$O$_{19}$/NiFe$_2$O$_4$/ZnFe$_2$O$_4$ [10] but the synthesis of absorber nanomaterial with a light mass and great absorption remains a challenge [5].

A variety of techniques were developed to produce nanoparticles including crystallization method, melting method, citrate precursor method, ceramic method, micro emulsion technique, solid state method [11-16]. These methods show several disadvantages such as high temperature for sintering, non-homogeneity of particles, Long reaction and calcination time, others techniques such as co-precipitation and sol-gel techniques have been employed [17-21]. The sol-gel technique presents several advantages such as low temperature formation, good homogeneity of particles and good control of microstructure [22].

In this work, the nanoparticles of hexaferrites and bismuth copper titanate will be synthesized by the sol-gel method. The conductive polymer (polyaniline) used will be synthesized by oxidative polymerization. The magnetic, structural and absorption properties for the hexaferrites and the dielectric properties of the BCTO will be studied. Finally, the

nanocomposite consisting of hexaferrite, bismuth copper titanate (BCTO) and conducting polymer (PANI) will be synthesized and the absorption properties studied in details.

1.2 Origin of magnetism

Magnetism is a phenomenon present in everyday life through magnetic materials. This phenomenon is due to the magnetic moments of atoms that constitute matter. It is well known that an atom consists of a nucleus and an electronic cloud that gravitates around the nucleus. Consider the case of an electron that revolves around the nucleus as shown in the **Fig. 1.1**:
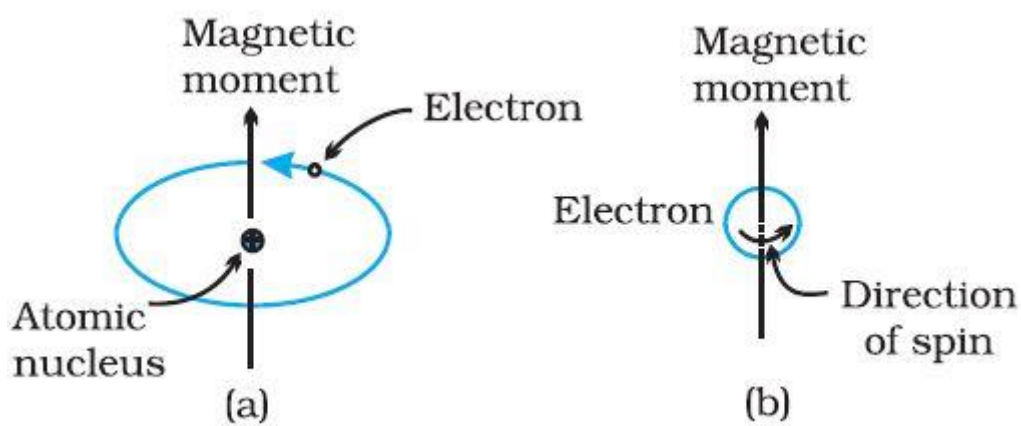
Fig. 1.1 Movements of the electron

From this figure, two behaviours of the electron can be observed:

The electron gravitates around the nucleus, describing an almost circular orbit. The movement of the electron around the nucleus will create a current i which will be at the origin of a magnetic moment called the orbital magnetic moment and defined by:

$$\boldsymbol{m_e} = i.S.\boldsymbol{n} \tag{1.1}$$

Where $S=\pi r^2$ is the surface of the orbit of radius r and $\boldsymbol{n}$ the normal to the surface of the orbit passing through the centre of the nucleus.

- The electron also performs a spinning motion on itself and creates a magnetic moment called the magnetic moment of spin and defined by:

$$m_s = \frac{e}{2m}\hbar \tag{1.2}$$

With $\hbar = \frac{h}{2\pi}$ where h is the constant of Planck, e and m are respectively the charge and the mass of electron.

Then the magnetic moment given by an atom will be the sum of the orbital magnetic moments and the spin moments of the electrons.

1.3 Magnetic materials

To classify magnetic materials, it is important to introduce the notion of magnetic susceptibility (χ), which represents the ease with which the material reacts when it is subjected to external magnetic excitation. Consider a magnetic material to which an external magnetic field **H** is applied. The material will acquire a magnetization **M** which will be proportional to the applied field (eq. 1.3).

$$M = \chi \cdot H \tag{1.3}$$

Magnetic susceptibility has an electronic origin and depends on the temperature and nature of the material. In the material, the electronic spins present a certain orientation. When the material is subjected to a thermal agitation (elevation of the temperature), a disorder is observed in the alignment of the spins; which reduces the susceptibility of the material. Depending on the value of χ the materials can be categorized as being diamagnetic, paramagnetic, ferromagnetic, ferrimagnetic or antiferromagnetic.

1.3.1 Diamagnetism

The total magnetic moment of a diamagnetic material is zero, since all the electrons are paired. The magnetic field applied to the material induces magnetization which is opposite to its direction (**Fig. 1.2**), for this reason the diamagnetic materials are repelled by the magnetic field, as soon as the external magnetic field is cut, the electrons go back to their initial positions.

The diamagnetic materials are characterized by a negative magnetic susceptibility ($\chi<0$), very weak ($|\chi|\sim 10^{-5}$) and independent of the temperature.

Diamagnetic property is present in every atom, molecule and magnetic material. However, any other magnetic behaviour will mask it because χ is very small.
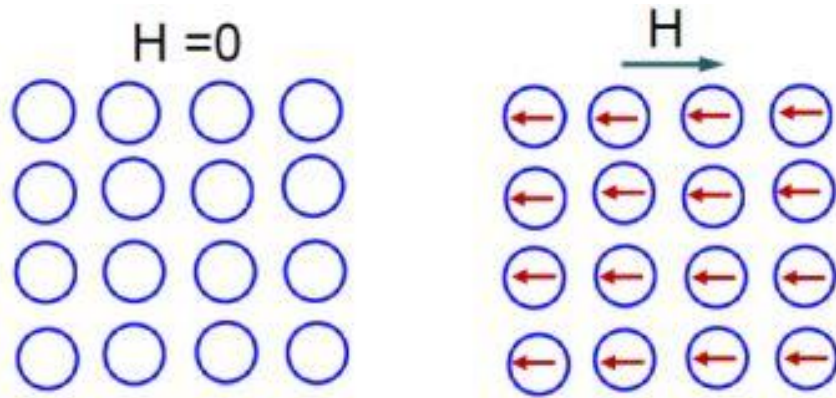
Fig. 1.2 Diamagnetic material

1.3.2 Paramagnetism

Unlike diamagnetic materials, the atoms contained in paramagnetic materials have unpaired electrons. These electrons of paramagnetic material are randomly oriented such that their net magnetic moment is zero in the absence of an external magnetic field. Once the magnetic field is applied, magnetic moments align automatically parallel to the applied field (**Fig. 1.3**), thus the material acquire a magnetization which disappears directly when the external field is suppressed.
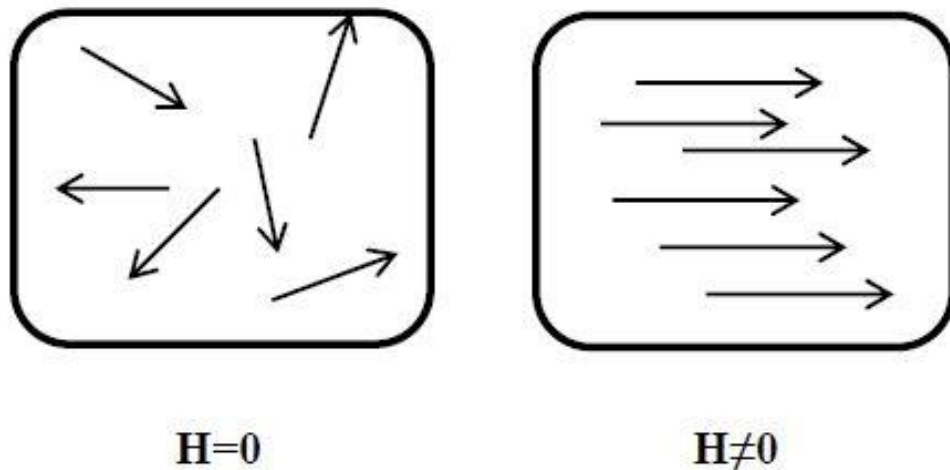
Fig. 1.3 Paramagnetic material

Paramagnetic materials have small, positive and temperature dependent value of susceptibility. This susceptibility is inversely proportional to the temperature and is defined by:

$$\chi = \frac{c}{T} \tag{1.4}$$

Where, *C* represents the constant of Curie.

1.3.3 Ferromagnetism

As in paramagnetic materials, ferromagnetic materials also have atoms that have unpaired electrons. These electrons are responsible for the magnetization of the material. Unlike paramagnetic materials which do not exhibit spontaneous magnetization, ferromagnetic materials exhibit a spontaneous magnetization in the absence of magnetic excitation. This spontaneous magnetization is observed in regions called Weiss domains. Indeed, in ferromagnetic materials, there are domains each containing spins. These domains are separated from each other by a wall called Bloch wall. The spins contained in a domain are all oriented in the same direction. This orientation varies randomly from one domain to another so that the total magnetization of the material is zero (**Fig. 1.4**).

$H=0$ $H\neq0$
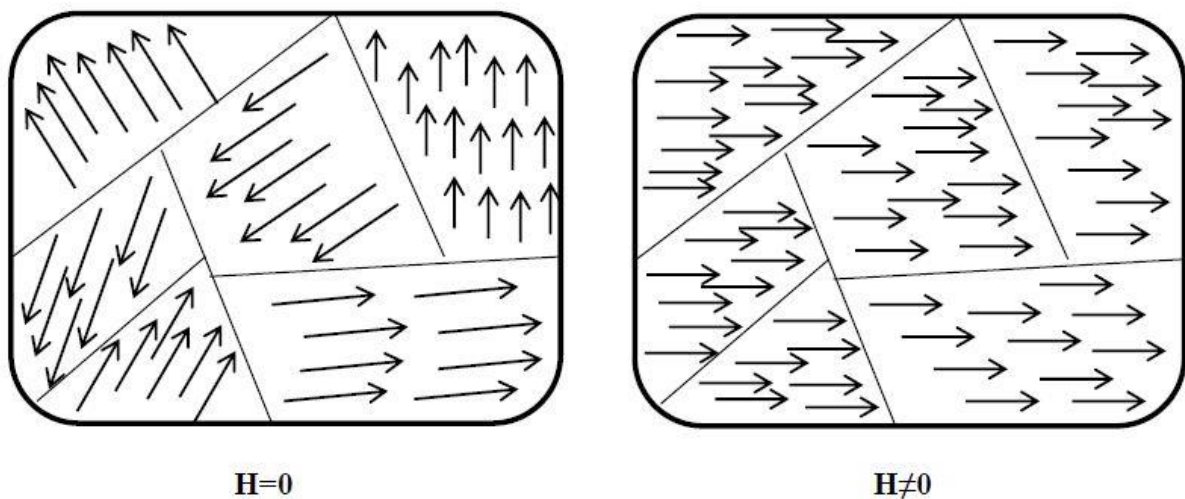
Fig. 1.4 Ferromagnetic material

Diamagnetic and paramagnetic materials exhibit linear magnetization under the effect of an applied magnetic field. However, the magnetization depends on the intensity of the applied field for the ferromagnetic materials. Indeed, when the ferromagnetic material is under an external magnetic field, a progressive orientation of spins from one domain to another in the direction of field will be observed (**Fig. 1.4**). However, when a weak field is applied, the material can present a magnetization with Weiss domains still existing. But for a sufficiently strong external field, all the spins of the material will be aligned in the direction of the applied field. In this case, the material changes from a multi domain state to a single magnetic

domain state and is strongly attracted by the field. Removing the magnetic field describes the magnetization type as seen in the hysteresis loop.

The positive and large value of susceptibility conforms to ferromagnetism in materials. It decreases with increasing temperature. The material exhibits a ferromagnetic behaviour when the temperature is below the Curie temperature (T_C). At a temperature above T_C, the susceptibility decreases according to the eq. 1.5 thus making the material a paramagnetic material.

$$\chi = \frac{C}{T - T_C}$$ (1.5)

1.3.4 Antiferromagnetism

As in paramagnetic and ferromagnetic materials, antiferromagnetic materials also possess atoms that have unpaired electrons. But between two adjacent atoms, spins are oriented in opposite direction (**Fig. 1.5**). The material then behaves like it consists of two regions A and B possessing each a spontaneous magnetization which are oriented in opposite direction. In the absence of applied magnetic field, there is no magnetization is observed in the material.
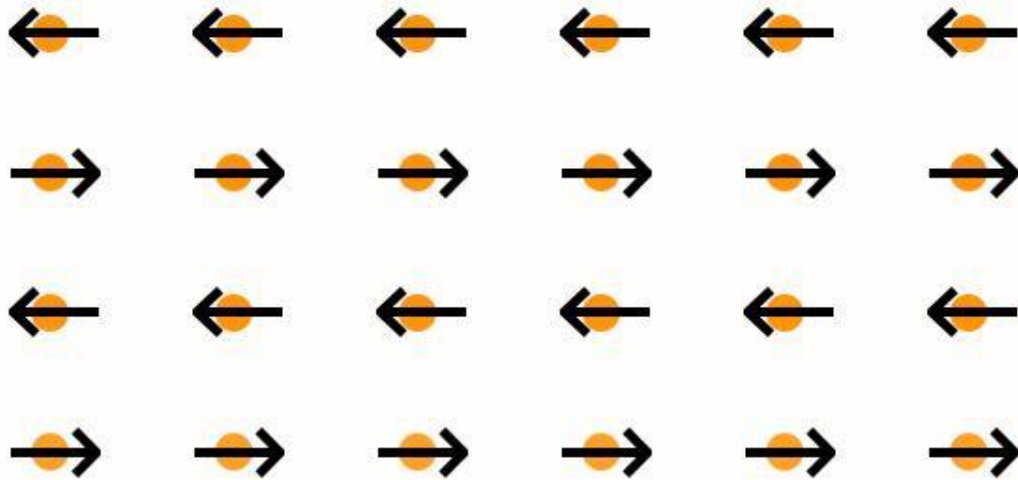
Fig. 1.5 Antiferromagnetic material

When an external field is applied, a weak magnetization (χ is small) appears in the material. This magnetization increase with the temperature up to a critical temperature called Neel

temperature (T_N). Above T_N, the susceptibility of the material decreases according to eq. 1.6 and the material displays a paramagnetic behaviour.

$$\chi = \frac{C}{T + T_N} \tag{1.6}$$

1.3.5 Ferrimagnetism

A particular case of antiferromagnetic material is ferrimagnetic material. In this type of material, atoms possess spontaneous magnetization. This magnetization has a different intensity and is oriented in the opposite direction between two neighbouring atoms (**Fig. 1.6**). The material behaves as if it consists of two regions A and B. The total magnetization in the ferrimagnetic material is therefore non-zero. Ferrimagnetic materials generally exhibit behaviour very close to ferromagnetism. Below the Curie (Tc) temperature, magnetization is dominant in a region. Above Tc, the behaviour of the material is rife with paramagnetism.
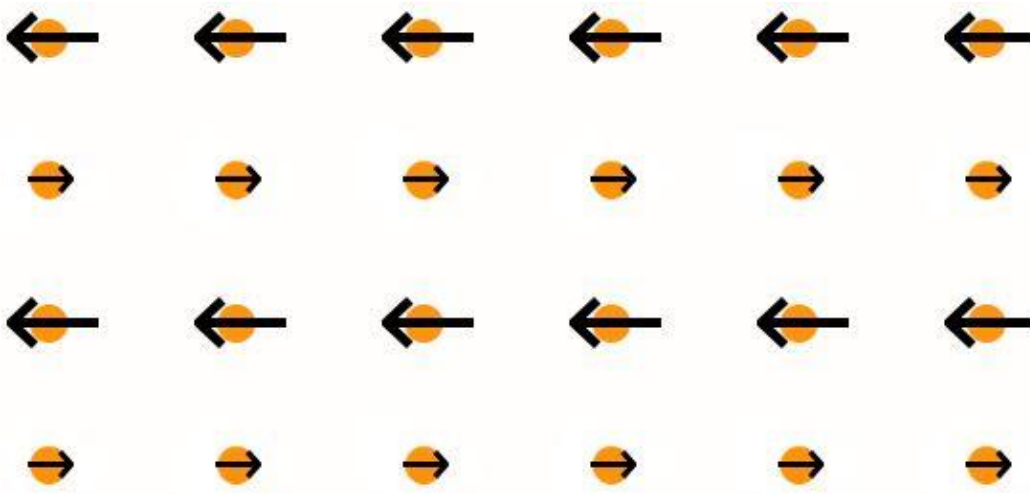
Fig. 1.6 Ferrimagnetic materials

1.4 Hexaferrites

Magnetic materials are very useful in industries and have technological applications. Since their discovery in 1950 by Philips [23], ferrites with hexagonal structure (hexaferrite) have retained a great attention due to their good magnetic properties. However, classic magnetic materials (metals) show some limitations in the process of miniaturization which is

fundamental in the advancement of the technology. This is due to their high density and high weight. Considering their excellent magnetic properties and their relatively low density, hexaferrite materials present themselves as adequate substitute of metals. Due to their magnetic properties, these hexaferrites are used in applications such as permanent magnet, magnetic record media, chip soft-magnetic components, motor components, telecommunication, absorber material, sensors, microwave devices, military, radiation shielding, EMI devices and biomedical [24-27]. Up to now, only six types hexaferrites are recognized namely M-type ($AFe_{12}O_{19}$), Y- type ($A_2Me_2Fe_{12}O_{22}$), U-type ($A_4Me_2Fe_{36}O_{60}$), W-type ($A_2Me_2Fe_{16}O_{27}$), X-type ($A_2Me_2Fe_{28}O_{46}$) and Z-type ($A_3Me_2Fe_{24}O_{41}$) where A can be barium and strontium and Me represents a divalent cations such as nickel, magnesium, copper, cobalt and zinc [28]. Based on these two types and spinel ferrite, it is possible to form others such as W=M+S, Z=M+Y, X=2M+S and U=2M+Y.

1.4.1 M-type hexaferrite

Hexaferrites of M-type have a general chemical formula of $MeO.6Fe_2O_3$ (with Me= Ba or Sr) has the same structure as magnetoplumbite (space group $P6_3/mmc$) [2] with typical lattice constants of a=5.88 Å and c=23.2 Å [29]. M-type hexaferrite structure is built from the S^*RSR^* sequence, where R is the block containing the barium or strontium atom (R = $MeFe_{12}O_{11}$) and S (S = Fe_6O_8) is the spinel block containing two layers of oxygen. Rotating S and R blocks $180^°$ on the c-axis, S*and R* blocks are obtained (**Fig. 1.7**) [30, 31]. M-type hexaferrite contains 38 O^{2-}, 24 Fe^{3+} and 2 Me^{2+} ions per unit cell. The main source of magnetic properties in M-type hexaferrite structure is Fe^{3+} ions which occupy octahedral site ($12k$, $2a$ and $4f_2$), trigonal, bipyramidal site ($2b$) and tetrahedral site ($4f_1$). The tetrahedral ($4f_1$) with octahedral ($4f_2$) crystallographic sites possess spin down that is responsible of magnetic moment reduction of the structure [32]. High value of coercivity, saturation magnetization and Curie temperature of Barium M-type hexaferrite ($BaFe_{12}O_{19}$) was observed to be 6700 Oe, 72 emu / g and 502 °C respectively [19, 33, 34] whereas M-type strontium hexaferrite ($SrFe_{12}O_{19}$) showed high coercivity of 7500 Oe, saturation magnetization of 67.7 emu/g [21] and curie temperature Tc=475 °C [35]. For the enhancement properties, the replacement of Fe^{3+} ions by a cation from transition metals and/or rare earth can be done. Different researchers modified the M-type hexagonal ferrite magnetic properties by substituting Me^{2+} or/and Fe^{3+} ions sites with single or combination of cations such as Mg^{2+}-Ti^{4+} [16, 36], Cr^{3+}-Ga^{2+} [37], Ni^{2+} [38], Al^{3+}-Mn^{2+} [39], Gd^{3+}-Co^{2+} [40], Mn^{2+}-Ti^{4+} [41], Co^{2+}-Ti^{4+} [42], Gd^{3+}-Na^+ [43], Sc^{3+}-Mg^{2+} [44], La^{3+}-Zn^{2+} [45].
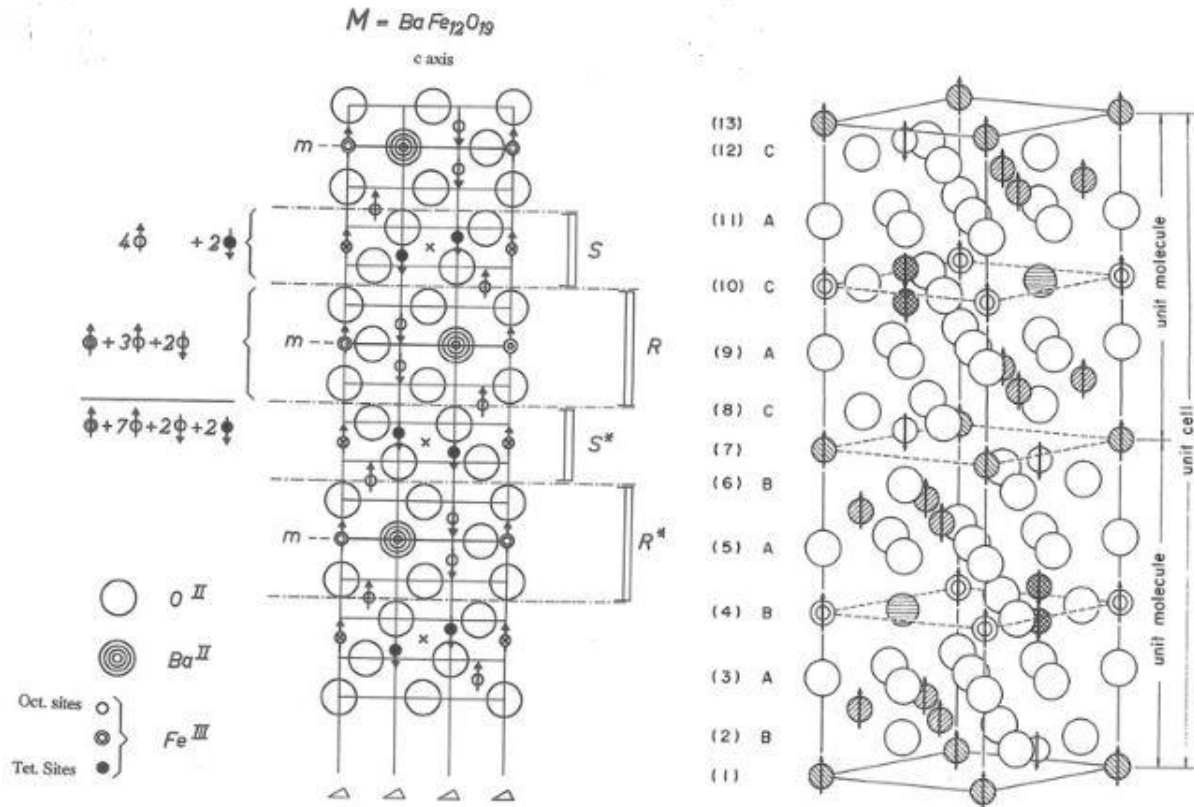
Fig. 1.7 Left: cross section view of the M-type hexaferrite ($BaFe_{12}O_{19}$) structure. Right: Perspective view of the M-type hexaferrite structure

1.4.2 Y-type hexaferrite

Y-type hexaferrite shows a hexagonal structure with space group R-3m and lattice constants a~5.9 Å and c~43.5 Å [46]. Whereas M-type hexaferrite are generally hard material because of their high coercivity value, compared to their counterpart Y-type hexaferrite with general formula $A_2Me_2Fe_{12}O_{22}$ (A can be Ba or Sr and Me can be Co, Ni, Mg, Cu and Zn) that are known to be soft magnetic material with planar magnetic anisotropic [2, 47, 48]. Y-type hexaferrite is formed by sequence (RS) (RS)* and (TS) (TS)' (TS)" respectively where S ($MeFe_4O_8$) represent the spinel block, R (AFe_6O_{11}) and T ($A_2Fe_8O_{14}$) blocks consisted of three and four oxygen layers (**Fig. 1.8**)[49]. Asterisk and prime blocks are obtained by a rotation of 180 and 120 respectively along c-axis [30, 46]. The magnetic properties of this type are dominated by Me^{2+} and Fe^{3+} ions which are represented in six crystallographic sites especially $3a_{VI}$, $3b_{VI}$, $18h_{VI}$, $6c_{VI}$, $6c_{IV}$ and $6c^*_{IV}$ (**Fig. 1.8**)[50]. Among these sites there are four octahedral sites ($3a_{VI}$, $3b_{VI}$, $18h_{VI}$ and $6c_{VI}$) and two tetrahedral sites ($6c_{IV}$ and $6c^*_{IV}$) which have spin up and down as reported in **Table 1.1**.
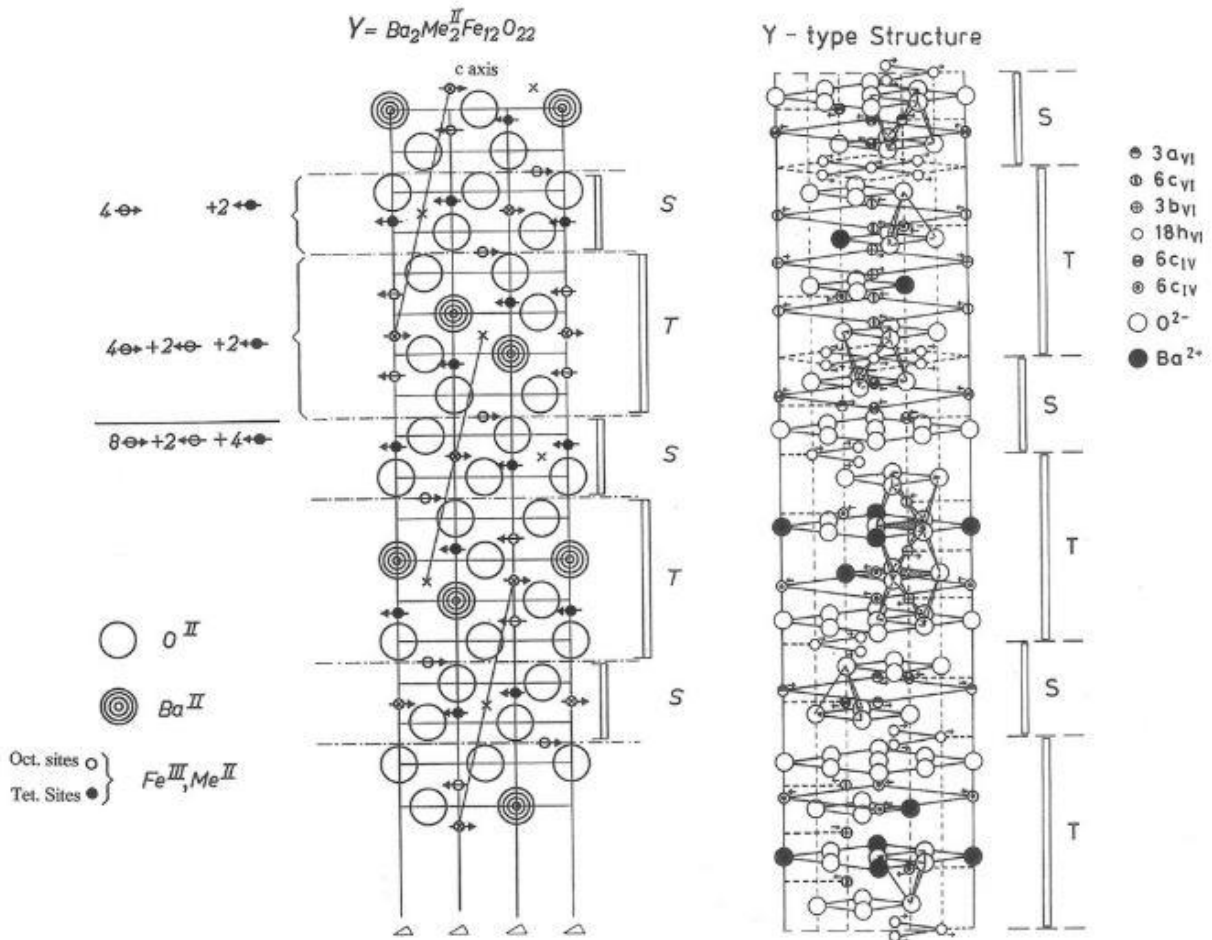
Fig. 1.8 Left: cross section view of the Y-type hexaferrite (BaMe$_2$Fe$_{12}$O$_{19}$) structure. Right: Perspective view of the Y-type hexaferrite structure

To improve the magnetic and dielectric properties of this material, many authors modified the orientation of spins in those sites by doping with rare earth and/or transition metals. Lee and Kwon studied magnetic properties of Co$_{1-x}$Zn$_x$ Y-type barium hexaferrite [51]. They reported that Curie temperature decreased from 600K (for x=0.0) to 378K (for x=1) whereas saturation magnetization showed linear increase with Zn^{2+} content. Highest value of Ms was found to be 68 emu/g for x=1 at 0K while at room temperature (298K) it was found to be 34.9 emu/g for x=0.75.

Table 1.1 Distribution in crystallographic sites of Y-type hexaferrite, spin orientation and number of ions of magnetic ions (Fe^{3+}, Me^{2+})

Sublattice	Spin orientation	Crystallographic sites	Block	Number of ions
$3a_{VI}$	↑	Octahedral	S	1
$3b_{VI}$	↑	Octahedral	T	1
$18h_{VI}$	↑	Octahedral	S-T	6
$6c_{VI}$	↓	Octahedral	T	2
$6c_{IV}$	↓	Tetrahedral	S	2
$6c^{*}_{IV}$	↓	Tetrahedral	T	2

1.5 Bismuth copper titanate (BCTO)

Dielectric materials are materials known for their insulating properties. They are characterized by a very high resistivity of the order of 10^8 to $10^{16}\Omega$.m. From the macroscopic point of view, these materials contain no charges because they do not conduct the electric current. At the atomic scale, these materials contain so-called localized charges. Under the action of an applied field, these charges move slightly from their equilibrium position creating a dielectric polarization of the material. The positive charges are displaced in the direction of the electric field and the negative charges in the opposite direction creating an electric dipole and causing an electrical polarization.

The discovery of the perovskite material calcium copper titanate (CCTO) having chemical composition $CaCu_3Ti_4O_{12}$ and giant dielectric constant by Subramanian et al. in 2000 has prompted renewed interest in materials with giant dielectric constant [52]. This is as a result of the fact that advancement in miniaturization of electronics devices, supercapacitors, actuators, catalysis and memory devices requires nanomaterials with giant dielectric constant greater than 1000 [28, 53-56]. Unlike ferroelectric materials such as barium titanate ($BaTiO_3$), CCTO do not show ferroelectric properties even though they exhibit giant dielectric constant ($\varepsilon \approx 10^4$ for polycrystalline and $\varepsilon \approx 10^5$ for single crystals) from 100 to 600 K in the kilohertz region [57-59]. Although the internal barrier layer capacitance (IBLC) model is commonly accepted as the origin of the high dielectric observed in CCTO ceramic, the origin of the giant dielectric constant of this perovskite material has remained a subject of

debate among the scientific community [60]. This is further supported by impedance spectroscopy where the perovskite material was observed to exhibit a single-step internal barrier layer capacitor where insulating grain boundaries separates the semiconducting grains [61].

Bismuth copper titanate (BCTO) ($Bi_{2/3}Cu_3Ti_4O_{12}$) as a member of titanate family with general formula $ACu_3Ti_4O_{12}$ (where A=Ba, Ca, Sr, $Gd_{2/3}$, $Pr_{2/3}$, $Y_{2/3}$, $Bi_{2/3}$ or $La_{2/3}$) shows a dielectric constant above 1000 and has been rarely explored. It possess cubic structure with *Im-3* as space group and lattice parameter close to that of CCTO (7.391 Å [62, 63]). **Fig. 1.9** shows the unit cell structure of BCTO in 3D.
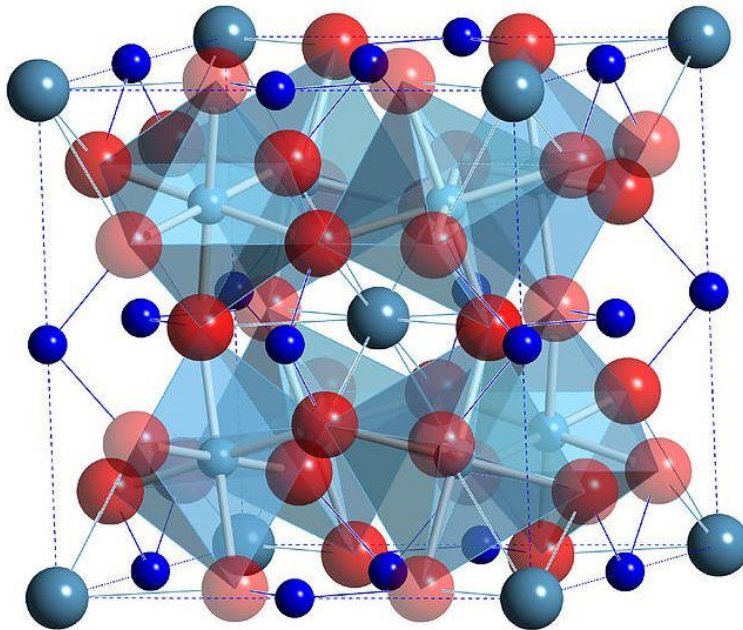
Fig. 1.9 BCTO structure in 3D

In this figure, big light blue balls placed at the extreme corners represent bismuth atoms (1/3 of bismuth sites are vacant) and centre of the unit cell, copper atoms (small blue balls) are located at the centre of the edges and faces of the face of cube edge and titanium atoms are located at the centre of TiO_6 octahedra.

Although some researchers have attempted to synthesized BCTO [64-66], the challenge of obtaining giant dielectric constant while maintaining reasonable low dielectric loss still remains an issue [67].

1.6 Conducting polymers: polyaniline (PANI) and polypyrrole (PPY)

Plastics also called chemically polymer are a repeated chain of identical molecules called monomers linked together by covalent bonds. These organic compounds are generally known for their insulating properties and are used extensively as electrical insulators. At the end of the 1970s, a new category of polymers was discovered by A. J. Heeger, A. G. Mac Diarmid and H. Shirakawa: Intrinsic Conductive Polymers (ICP). Indeed, the ICPs are obtained by doping a conjugated polymer (an unsaturated polymer containing an alternation of double and simple bonds on the main chain) by oxidation or reduction. The alternation of the double and simple bonds in the ICP allows having a delocalization of the charges which ensures the conjugated bonds. For this reason, ICPs have properties similar to the properties of semiconductors. The conductivity of the ICP is therefore done by doping which consists of removing electrons (by oxidation) or adding (by reduction). These electrons can move along the polymer chain which makes the polymer conductive.

Unlike saturated polymers such as polyethylene, ICPs have a different organic structure: each carbon atom is bonded to only three atoms and there remains one free electron per carbon atom that is responsible for the conductivity in the polymer. This conductivity depends on the length of conjugation, the type of doping and the doping rate.

From the microscopic point of view, materials are classified into three categories: insulation, semiconductors and conductors. This classification can be used for conductive polymers except that charge carriers are not electrons as in metals but polarons and bipolarons. Because of their π-conjugated bond, conducting polymers exhibit interesting electrical properties which make them useful for many applications such as electro-chromic smart windows, rechargeable batteries, sensors, antistatic coating, corrosion inhibitors, electronic, EMI shielding, supercapacitors and electrodes [68-73]. The first conductive polymer is polyacetylen (PAC) discovered by A. J. Heeger, A. G. Mac. Diarmid and H. Shirakawa. The latter showed a conductivity of 10^7 S.m^{-1} comparable to that of copper ($5.7*10^7$ S.m^{-1}). Subsequently, several other conductive polymers have been synthesized such as polypyrrole (PPY), polythiophene (PTH), polyparaphenylene (PPP), polyaniline PANI). The figure compares the conductivity of ICP with that of classical materials (**Fig. 1.10**). Among these polymers, PANI and PPY present excellent properties and advantages such as low cost and easy synthesis, good solubility, high conductivity, good redox properties, good environmental

and chemical stability, tuneable properties and availability of raw materials which make it convenient for many technological applications [73-75].
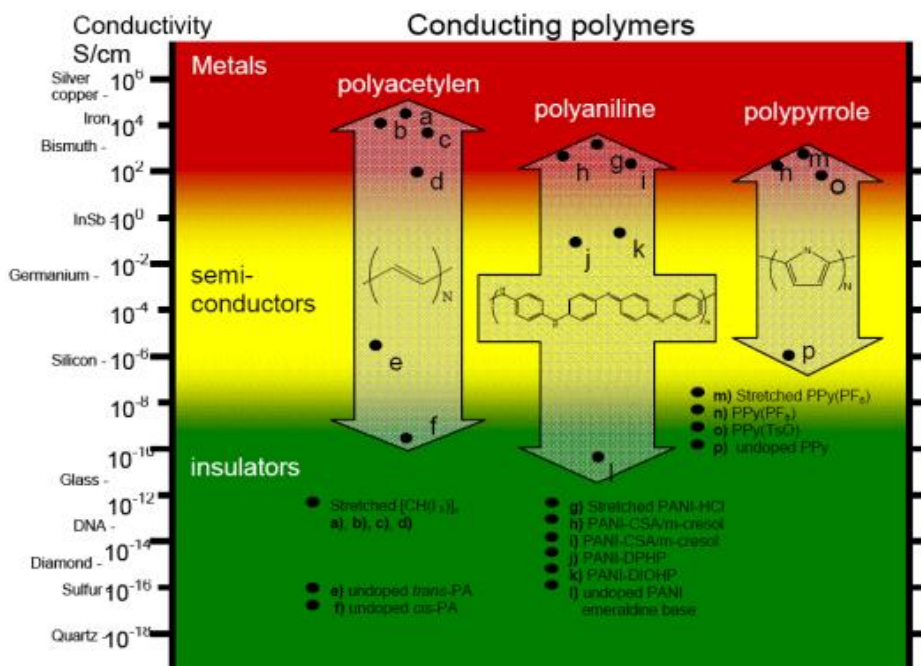
Fig. 1.10 Electrical conductivity of various polymers (depending on doping) and conventional materials [76]

Conducting polymers can be good conductors. They also possess interesting mechanical properties which gives them a wide range of applications. As compared to other ICPs, polyaniline has remarkable properties such as stability to air.

PANI is obtained after polymerization of the aniline. This polymer results from the repetition of the aniline of formula (**Fig. 1.11**)
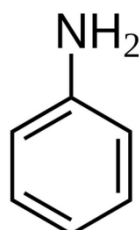
Fig. 1.11 Structure of aniline

The aniline can polymerize by forming C-NH-C amine bonds or C = N-C imine bonds, the respective proportion of which defines the degree of oxidation of the final polymer. The amine bonds indicate the reduced state and the imine bonds indicate the oxide state. Then the general structure of the PANI can be obtained by the following reaction (**Fig. 1.12**):
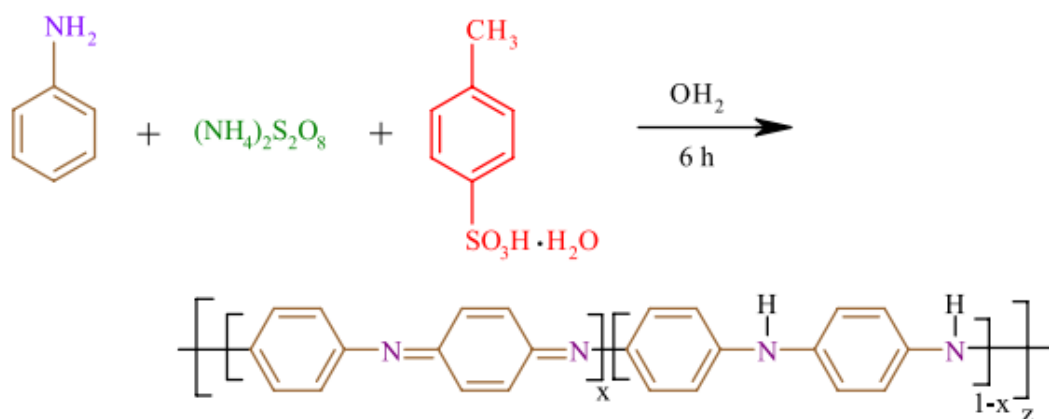
Fig. 1.12 General formula of Polyaniline (PANI) [77]

where z is the degree of polymerization and (1-x) expresses the oxidation state. Three cases are considered as a function of the value of x:

- $(1-x) = 0$, the molecular chain is completely reduced and **Leucoemeraldine** is obtained. (**Fig. 1.13**)

- $(1-x) = 0.5$. The molecular chain is reduced to half and the **Emeraldine** base is obtained. (**Fig. 1.14**)

- $(1-x) = 1$, a complete oxidation of the molecular chain is obtained and **pernigraniline** is obtained. (**Fig. 15**)
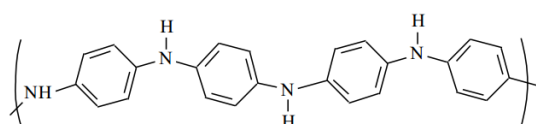
Fig. 1.13 Leucoemeraldine
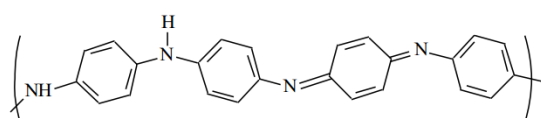
Fig. 1.14 Emeraldine base
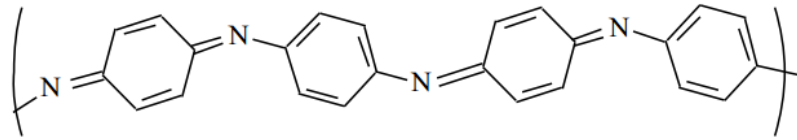
Fig. 1.15 Pernigraniline

Of all three forms of PAni, only Emeraldine is stable at room temperature and has interesting properties.

1.7 Shielding phenomenon

The absorption of electromagnetic waves is characterized by the attenuation of its intensity through the passage of a material which plays the role of absorber. This electromagnetic shield must be endowed with interesting absorption properties (permeability and permittivity). Permittivity is a physical property that describes the response of a given medium to an applied electric field, whereas magnetic permeability defines the ability of a material to allow a magnetic field to pass through it. The electromagnetic shield is therefore characterized by its permittivity, permeability, thickness and the propagation frequency of the EM waves. In fact, electronic systems consist of electronic components operating at low or high frequency and also emitting electromagnetic waves. These waves are capable of creating malfunctions in the circuit. In this case the impact is of internal origin. On the other hand, these waves can come from external sources such as radars and wireless communications. Ideally, the purpose of shielding is to prevent any impact of these waves on a sensitive device. However, the reality is not the case. We always observe some of these waves that cross the circuit and endanger some electronic components. The goal is to reduce the intensity of these waves as much as possible. **Fig. 1.16** shows the representation of the electromagnetic shield. In this figure, we note that the shielding is based on the principle of reflection, absorption and multiple reflections. In order to minimize the intensity of the wave, it would be important to return a large part by the phenomenon of reflection on the first surface of the shield. For this, the material must have good conductivity. Another part of this wave will cross the first surface of the shield and will reach the second surface (exit surface) on which one part of the wave will be reflected and another will be transmitted. The intensity of this transmitted wave must be sufficiently reduced so that the impact on an electronic

component is less. It is important to note that during the passage of the wave through the shielding material, it loses its intensity due to the fact that the material absorbs a part; it is the phenomenon of absorption. The phenomenon of multiple reflections can be observed inside the shield as shown in **Fig. 1.16**. The shielding effectiveness of the electromagnetic radiation defined as being the ability of the material to block or attenuate the wave intensity can be expressed as:

$$SE_T = SE_R + SE_A + SE_M \tag{1.7}$$

Where, SE_R, SE_A, SE_M respectively represent shielding effectiveness due to the reflection, absorption, multiple reflections and SE_T represent the total shielding effectiveness. The total shielding efficiency represents the logarithmic quantity of the transmitted and incident power ratio and is defined as follows:

$$SE_T \ (dB) = -10 \log_{10}\left(\frac{P_T}{P_I}\right) = -20 \log_{10}\left(\frac{E_T}{E_I}\right) = -20 \log_{10}\left(\frac{H_T}{H_I}\right) \tag{1.8}$$

Where, P, E and H represent power, electric field and magnetic field respectively.

In the practical, one of the objectives sought is to neglect the phenomenon of multiple reflection that one could observe if certain conditions are not respected. For this, SE_M can be neglected ($\sim$ -10dB) if $SE_A \geq 10$dB [78]. In this case the total shielding effectiveness can be written as:

$$SE_T = SE_R + SE_A \tag{1.9}$$

With

$$SE_R = -10 \log_{10}(1 - R) \tag{1.10}$$

$$SE_A = -10 \log_{10}(1 - A_{eff}) = -10 \log_{10}\left(\frac{T}{1-R}\right) \tag{1.11}$$

Where, $A_{eff} = \frac{1-R-T}{1-R}$ is effective absorption, T and R are transmission and reflection coefficients respectively.

When the phenomenon of multiple reflection exists, SE_M is defined as [79]:

$$SE_M = -20 \log_{10}(1 - e^{-2t/\delta}) \tag{1.12}$$

17

Where δ and t are skin depth and shield thickness in inches. The skin depth is the distance required for the wave to be attenuated to 1/e or 37% as observed in **Fig. 1.16**.
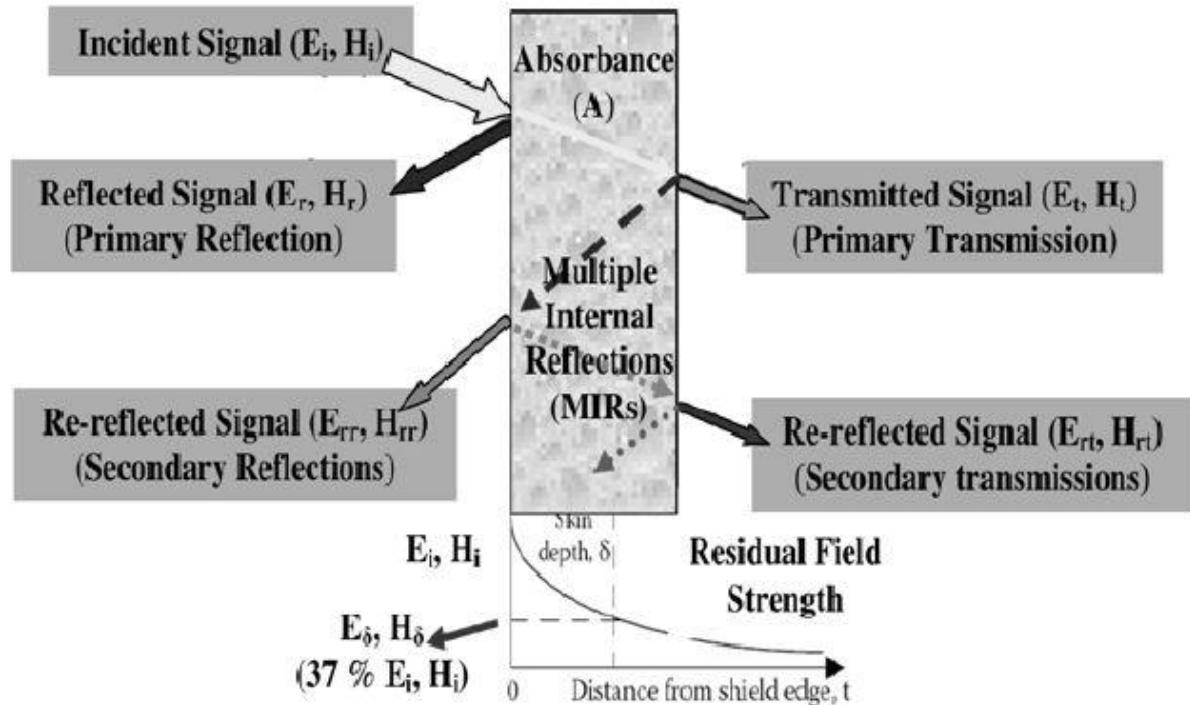
Fig. 1.16 Graphical EMI shielding representation

When the phenomenon of multiple reflections exists, we notice that SE_M depends on both δ and t. When the shield is thin ($t<\delta$), the multiple reflections will generally be observed. However, if the shield thickness is considerable ($t\geq\delta$), then the shield could show $SE_A \geq 10$dB. Therefore SEM can be safely neglected. In this case SE_A can be written as:

$$SE_A = 20\left(\frac{t}{\delta}\right)\log e = 8.68t(\sigma f\mu)^{1/2} \tag{1.13}$$

Where, σ, f and μ represent conductivity, frequency and permeability.

From this equation, we notice that SE_A depends on physical characteristics of shield (t, δ and μ) unlike SE_R that depends on impedance of incident wave and therefore of the type of source.

As mentioned above, the shield should have good dielectric, electrical and magnetic properties. The quality of shield is then characterized by its magnetic and electric storage and

losses defined by the complex (ε^*) permittivity and complex permeability (μ^*) given by equations (1.14) and (1.18).

$$\varepsilon^*(\omega) = \varepsilon'(\omega) - j\varepsilon''(\omega) \qquad (1.14)$$

Where the real part ε' is the dielectric constant that represents the storage ability of the electrical energy and the imaginary part ε'' represents the dielectric loss [5]. ε' and ε'' are defined by the following expressions:

$$\varepsilon'(\omega) = \varepsilon_r.\cos(\delta_e) \qquad (1.15)$$

$$\varepsilon''(\omega) = \varepsilon_r.\sin(\delta_e) \qquad (1.16)$$

$$tan\delta_e = \frac{\varepsilon''}{\varepsilon'} \qquad (1.17)$$

Where δ_e represents dielectric loss angle which is formed by the electric field and electric displacement vectors and $tan\delta_e$ is dielectric loss tangent. High value of dielectric loss tangent implies high attenuation of the wave as it moves through the material.

$$\mu^*(\omega) = \mu'(\omega) - j\mu''(\omega) \qquad (1.18)$$

Where the real part (μ') represents the storage ability of the magnetic energy and the imaginary part (μ'') represents magnetic loss [5].

The magnetic loss tangent of shield is given by

$$tan\delta_m = \frac{\mu''}{\mu'} \qquad (1.19)$$

Where δ_m represents magnetic loss angle, high value of magnetic loss tangent implies high attenuation of the wave as it moves through the material.

The attenuation ability of shield is also determined by the nature of total loss tangent ($tan\delta_T$) defined by the following relation:

$$tan\delta_T = tan\delta_m + tan\delta_e \qquad (1.20)$$

$$tan\delta_T = \frac{\mu''}{\mu'} + \frac{\varepsilon''}{\varepsilon'} \qquad (1.14)$$

The reflection loss (*RL*) of a EM shielding having certain thickness can be evaluated from the using the equation below [80-82]:

$$RL \ (dB) = 20log \left| \frac{Z_{in}-1}{Z_{in}+1} \right| \qquad (1.15)$$

With

$$Z_{in} = \sqrt{\frac{\mu^*}{\varepsilon^*}} \tanh \left(j \frac{2\pi t}{\lambda} \right) \sqrt{\mu^* \varepsilon^*} \qquad (1.16)$$

Where Z_{in} is the normalized input impedance relating to the impedance in free space, ε^* and μ^* are respectively complex permittivity and complex permeability, λ is the wavelength of electromagnetic wave and t is the shield thickness.

Chapter 2: Literature review

2.1 M-type hexaferrite

Kaur et al. (2017) have discussed M-type barium Gd-Co substituted $Ba_{1-x}Gd_xCo_xFe_{12-x}O_{19}$ (0.0, 0.1, 0.2, 0.3, 0.4, 0.5, and 0.6) hexaferrite. Typical modified Pechini sol gel method was utilized for the synthesis. XRD was used to verify the crystalline magneto-plumbite structure development. FT-Raman spectra of vibrational mode depicted the P63/mmc formation. UV-Vis-NIR spectra illustrated the substitution of material the gap band of optical energy augmented from 3.99eV to 4.28eV. TEM and XRD have confirmed hexaferrite phase development through non-homogeneous phase. The saturation magnetization and coercivity have been analyzed using VSM. The material formulated can be utilized as recording media as it possess high surface area, magnetization saturation (>2500 Oe) and high coercivity. The nun-consistent ferroelectric feature was observed in comparison to the ferroelectric hysteresis loops standards.

Baykal et al. (2017) have studied the Cu-Mn substituted M-type $Ba_{1-2x}Mn_xCu_xFe_{12}O_{19}$ ($0.0 \leq x \leq 0.1$) hexaferrites. The sol-gel auto combustion method was utilized. Electron microscopy was used for confirmation of nano size of formulated products. Fe Mossbauer along with VSM was opted for coercive field of $BaFe_{12}O_{19}$ hexaferrites and saturation magnetization (M_s) and revealed that there were reducing as the Mn and Cu concentration increased. FT-IR and XRD confirmed the pure M-type hexagonal phase formation. SEM analysis depicted crystalline of high purity with flaked nano-size. The product compositional purity was illustrated by EDX as well as elemental mapping.

Alange et al. (2016) have discussed the barium hexaferrites Al-Cr Co-substituted M-type $BaCr_xAl_xFe_{12-2x}O_{19}$ (x=0.0, 0.2, 0.4, 0.6, 0.8 and 1.0) nanoparticles. The method opted for synthesis was sol-gel auto combustion. For the characterization of prepared product SEM, XRD and FT-IR were utilized. SEM image revealed grain sizes found in nanometer range. XRD patterns indicated the hexagonal features of the formulated material. The Mr, Hc and M_s Values were intensely affected by Cr^{3+} as well as Al^{2+} co-substitution. The loss of tangent (tan δ), dielectric constant (ε') and dielectric loss (ε") showed compositional dependence and frequency.

Ghzaiel et al. (2016) have studied the barium hexaferrites ($BaMeFe_{11}O_{19}$) polyaniline/substituted. The composites had electromagnetic wave absorbing properties lying

between 1 to 18 GHz range of frequency. For the preparation of 10%volume hexaferrite fraction solid-based polymerization was opted. There was shift of polyaniline/ substituted in reflexion loss to low frequencies from the KU band to X band. Magnetic studies revealed the ferromagnetic characteristics to all the composites. There was slight increase in coercivity values because of PANI matrix. Vector network analyser was sued to measure the EM parameters. Dielectric constant was found to increase in addition of hexaferrites. There was reduction in maximum of magnetic losses and high frequencies shift caused by Fe^{3+} doping.

Pattanayak et al. (2016) discussed the electrical features, fabrication as well as the magnetic properties of composite system in view of ferroelectric material ($Na_{0.5}Bi_{0.5}TiO_3$) and strong ferromagnetic ($BaFe_{12}O_{19}$). Solid state reaction technique was used in preparation of polycrystalline composite system. XRD patterns illustrated the pure NBT and BaM phases. Analysis of conductivity properties and electric relaxation was performed in the range of frequency from 100 HZ to 1MHz with 30-200°C temperature range. Detection of grain boundary revealed three existing grain boundaries that are: a) BaM-BaM interface, b) NBT-NBT interface and c) BaM-NBT interface. The saturation magnetization and coercive field showed decrease for composite system based on magnetization study. SEM analysis revealed polygonal and hexagonal grains packed individually.

Alam et al. (2015) studied the microwave absorption, structural as well as magnetic behaviours of Zn-Co-Zr substituted barium M-type hexaferrite nanoparticles, and they employed co-precipitation technique for the synthesis using polyvinyl alcohol. For characterization of prepared material, SEM, XRD FT-IR, VSM and thermal analysis (TGA-TDA) were used. XRD depicted the formation of magnetoplumbite structure in all samples with 44±3nm average nanoparticle crystallite size range. The thermal curves illustrated the production of barium hexaferrite at 709°C as low temperature. VSM revealed a decrease in H_c and M_s when the dopants percentage increased. The reflection loss outcome shown that the ferrite barium composition possessed suitable reflection loss (RL ≤ -10dB) with the bandwidth which was used as single layer absorber in 8 to 12 GHz frequency range.

Pattanayak et al. (2015) have studied the polycrystalline M-type hexagonal Barium ferrite ($BaFe_{12}O_{19}$). The solid state technique was opted for product preparation. XRD and SEM analysis confirmed the grain growth and single phase of micrometer range. XPS study illustrated the Fe^{2+} and Fe^{3+} presence. The investigation of electric transport properties was done in 100HZ to 1MHz frequency range with 30°C to 200°C. The polarization of the

interfacial (electrode surface and grain boundary) at room temperature was found to be active. The appearance of the intrinsic grain boundary as well as extrinsic grain boundary conduction was the single relaxation mechanism.

Chawla et al. (2014) Synthesized Co-Zr doped barium M-type hexaferrites nanocrystalline via sol-gel route at low temperature. For the characterization of the Co-Zr powder, XRD, FTIR, EDS TEM and TGA-DTA were utilized. XRD confirmed the single M type phase of barium hexagonal ferrites. x=1.0 was the maximum substitution. The observed hexagonal platelets average size was 41.62nm. M vs H studies demonstrated that for Ms slightly varied from 63.63 to 56.94emu/g whereas for Hc the observation shown a drastic decrease from 5428 to 630 Oe. The preparation of pure Co-Zr doped nano scale ferrites comprised of $BaCo_xZr_xFe_{(12-2x)}O_{19}$ was successfully done using sol-gel technique at 850°C.

Singh et al. (2014) investigated the $BaFe_{12}O_{19}$ hexaferrite. The sol-gel technique was used for the synthesis. TEM and XRD used to characterize the obtained product. XRD patterns depicted the hexagonal structure of the obtained product without the secondary phase in which the particle size was 49nm. The high value of DC resistivity was resulted at room temperature it was found to be 5.5×10^6 Ω cm. Both of dielectric constant and loss tangent decreased with the rise in frequency whereas the electrical conductivity increased with rise in frequency. The μ_i and RLF investigation was performed investigation was performed in the frequency range of 75 KHz to 30 KHz. The coercivity value was found to be high (2151.3 Oe) as well as high saturation magnetization (32.5 emu/gm). The obtained nano hexaferrite possessed high T_c (764 K) as described by M-T study.

Cernea et al. (2013) discussed the preparation of hexagonal ferrites $Ba_xSr_{1-x}Fe_{12}O_{19}$ (x=0.05, 0.15, 0.25, 0.35) using sol-gel technique with conventional solid state reaction method. For the investigation of their magnetic behaviours, Mössbauer spectroscopy and magnetometry were used. The hexaferrites obtained using the conventional solid state reaction method exhibit low quantity of $BaFe_2O_4$ as secondary phase while the hexaferrites prepared using sol-gel method present nearly a single phase. Using the Mössbauer spectra, the specific elemental five Fe^{3+} sites cells have been discovered and their relative occupancy has been shown. The analyzed samples magnetic features depict magnetic properties sensitivity (anisotropy and magnetic moment) in respect to various Fe^{3+} sites occupancy.

Ali et al. (2013) Reported for the Cr-Ga doped barium M-type hexaferrites) using rare earth new substitution. Sol-gel method was opted for the preparation. XRD, FT-IR, Thermogravimetric, DSC, EDS, VSM and SEM were utilized for the characterization. XRD patterns depicted the M-Type hexaferrite phase formation. The crystallite size range was observed between 17nm and 45nm. The retentivity and also the saturation magnetization reduced from 36.8-18.1 emu/g and 48.9-26.9 respectively. The 'c/a' value ratio of M-Type hexaferrites were ranging between 0.67 and 0.76. SEM analysis illustrated the grain size of the formed M-Type hexagonal platelets.

Sharbati et al. (2012) have discussed M-Type hexaferrites Mn-Ti-Sn substituted strontium $(SrMn_{x/2}(TiSn)_{x/4}Fe_{12-x}O_{19})$. The method opted was citrate sol-gel. TEM, XRD, VSM and VNA were used for the product analysis. The resulted products exhibited the high purity hexagonal structures. XRD patterns depicted the hexagonal crystalline features. The absorbers thicknesses were found to be 1.6mm. The minimum reflection loss of -39dB was shown by the composite of x=3 at 9.7 GHz possessing -20dB bandwidth above the prolonged range of frequency between 9.3 GHz and 12 GHz.

Xie et al. (2012) have synthesized the magnetic composites $SrCo_xFe_{12-x}O_{19}$ (x=0.0-0.3) product using co-precipitation high temperature sintering technique utilizing low reagents of low cost. For characterization of the products, SEM, XRD, FTIR and VSM were used. The saturation magnetization was shown to be the largest based on the magnetic analysis which was 42.5emu/g. FTIR, XRD, SEM analysis depicted the soft and hard magnetic phases as composition of the resulted composites.

Dhage et al. (2011) discussed the synthesis of Al-doped M-type hexaferrite $BaFe_{12-x}Al_xO_{19}$ nanocrystalline. For sample solution synthesis, combustion method was used. The sintered samples were characterized using SEM, EDX, VSM, XRD and TEM techniques. For the pure barium hexaferrite a unique single hexagonal phase structure was observed and as for the samples, the barium hexaferrite M-phase α-Fe_2O_3 peaks are observed at $0.25 \leq x \geq 1.00$ in XRD pattern. The saturation magnetization (M_s) as well as magnetic moment (n_B) reduces from 38.567 to 21.732emu/g; also from 7.6752 to 4.2126μ_B correspondingly, with rise in substituted Al^{3+} x whereby x= 0.0 to 1.0.

Liu et al. (2002) studied the magnetic characteristics of $Sr_{1-x}La_xFe_{12}O_{19}$ along with the effects of La^{3+}-substitution on structure. They opted sol-gel method for preparation and XRD, VSM and TEM for the investigation. The end product was composed of $Sr_{0.85}La_{0.15}Fe_{11.85}O_{19}$

calcined at 850 $^{\circ}$C. Magnetic properties of σ_s = 74.1 Am^2/kg with H$_{cJ}$= 498.4 kA/m were obtained. Results showed that suitable quantity of La^{3+} augments the σ_s and H$_{cJ.}$ With Sr$_{1-x}$La$_x$Fe$_{12}$O$_{19}$ (x= 0.15) fine grains, magnetic parameters of H$_{cJ}$ = 498.4 kA/m and σ_s = 74.1 Am^2/kg were resulted.

Dimri et al. (2009) discussed the dielectric and magnetic parameters of barium hexaferrite nanoparticles. The chemical method was used for the synthesis. The observation indicated that the permeability and permittivity values of nanoparticles are lower in comparison to the bulk material values. The calculated bulk values using Looyenga's formulae utilizing the measured values were shown to be less when compared to bulk samples values. The CoZr increase concentration is directly proportional to lattice parameters values.

 Maswadeh et al. (2015) have synthesized and characterized barium hexaferrites BaFe$_{12}$O$_{19}$ (BaM) using 11.5-16.16 ratio for Fe:Ba by ball milling. They reported that the preparation of BaM can be accompanied by the secondary nonmagnetic phases which may affect the magnetic properties by decreasing the yield of the desired BaM magnetic phase. XRD diffraction revealed the presence of both pure hexaferrite and α-Fe$_2$O$_3$ phases with no other secondary nonmagnetic phases. Rietveld refinement was used for quantitative analysis which revealed that the optimum Fe:Ba required to fabricate a pure M-type barium hexagonal ferrite is between 11.7-12.

Iqbal et al. (2008) have investigated on the magnetic and electrical properties of nanoparticles of Sr-M type hexaferrite with formula Sr$_x$Zr$_x$Cu$_x$Fe$_{12-2x}$O$_{19}$ (with x= 0.0- 0.8) fabricated using chemical co-precipitation route. Structural characterization of synthesized samples was carried out by XRD, FTIR, SEM, TEM and EDX analyses. For M-type hexaferrite the single phase pattern was revealed by XRD characterization and FTIR spectra. Scherrer formula was used to estimate particle size between 26 and 37 nm, which is comparable to that obtained from SEM (40-80 nm) and TEM (30-60 nm). They also reported that in the temperature range 300-675 K, SrFe$_{12}$O$_{19}$ was a semiconductor. However, the resistivity reached a maximum value at a temperature called metal-semiconductor temperature (T$_{M-S}$) by adding Zr$_x$Cu$_x$ with x=0.2-0.8. T$_{M-S}$ increased with substitution for $x \leq 0.4$. Curie temperature was decreased with the addition of Zr-Cu substitution. Moreover, dielectric constant, dielectric loss factor and drift mobility showed a decrease for $x \leq 0.4$ when activation energy and DC electrical resistivity increased.

Kaur et al. (2015) prepared $Ba_{0.7}La_{0.3}Fe_{11.7}Co_{0.3}O_{19}$ by the use of sol gel autocombustion route at 700, 900, 1100 and 1200°C. Influence of heating temperature on structural, magnetic, dielectric and optical properties was investigated. XRD analysis revealed that at 700 °C the pure M-type hexaferrite phase formation was observed. Weight loss of the samples was found to remain unchangeable from 680°C. The metal-oxygen bond vibration was observed at 432 cm^{-1} and 586 cm^{-1} in FTIR spectra. The sample heated at a temperature of 900°C was found to have the highest value of coercivity of 5602 Oe and optical band gap of 4.1 eV.

2.2 Y-type hexaferrite

Mahmood et al. (2016) have employed the conventional ball milling technique to synthesize at 1200°C and characterize T- doped Me_2Y hexaferrites with Me = Co^{2+}, Mg^{2+} and Cr^{2+}, and T = Fe^{3+} and Ga^{3+}. The single phase pattern of Co_2Y ferrite was revealed by the XRD analysis, magnetic parameters and Mossbauer spectra. Moreover, the presence of second phases of M-type hexaferrite and $BaCrO_4$ were also observed in XRD patterns of CoCr-Y sample. Saturation magnetization was observed to slightly increase from 34emu/g to 37.5emu/g as a result of growth of M-type hexaferrite in the sample. Concerning the Cr_2Y sample, XRD patterns reveals M-type phase as the majority in the sample which caused the high value of coercive field (1445 Oe). However, the $Ba_2CoMgFe_{11}GaO_{22}$ sample exhibited the smallest value of saturation magnetization (26.6 emu/g) as a result of reduction of super-exchange interactions caused by the Mg^{2+} substitution.

Adeela et al. (2016) have synthetized nanoparticles of $Ba_2Co_{2-x}Mn_xFe_{12}O_{22}$ (*x*= 0.0, 0.1, 0.3, 0.5, 0.7, and 0.9) utilizing hydrothermal technique. XRD and FTIR analysis established the Y-type hexaferrite structure formation. From SEM and EDX analysis, they observed that the grain size increased with the increase in Mn concentration. Additionally, the increase in Mn concentration contributed to the increase in the coercivity and squareness ratio form 4550e to 2550e and 0.26 to 0.56 respectively.

Irfan et al. (2016) used XRD, SEM and the dielectric spectroscopy to carried out the magnetic, grain morphology and dielectric properties of synthetized $Sr_2MnNiFe_{12}O_{22}$ + xY_2O_3 (x=0-5 wt.%) ferrite. Capacitive and resistive properties of samples were characterized by the single semicircle in Cole-Cole plot as a result of grain boundary contribution.

Odeh et al. (2016) defined the synthesis of $Ba_2Co_{2-x}Zn_xFe_{12}O_{22}$ hexaferrites by sol-gel technique. XRD outcome depicted the stable sample of Zn-substituted structure possessing

standard Y type hexaferrites patterns. The sample coercive field value was the least value at x=2.0. On basis of the dielectric measurements results, the samples were observed as insulators. As zinc content increased, it leads to decrease in AC conductivity. The dielectric constant of obtained barium hexaferrites was high in low-frequency range while there was increase in relative dielectric permittivity with rise in frequency.

Ahmad et al. (2015) have synthesized Y-type hexaferrite $Sr_2Ni_2Fe_{12}O_{22}$ using sol gel autocombustion with various temperatures (800-1200°C). SEM, VSM, XRD and FT-IR techniques were used for sample analysis. The pure hexaferrites Y type appeared at 1000°C and the complete formation was observed at 1200°C using XRD analysis. Using IR spectrum, the heated sample at 1200°C depicted the hexagonal Y type ferrite single phase of the sample. The saturation magnetizations along with the coercivity highest values were obtained at the 1000°C because of M-type hexaferrite presence.

Awawdeh et al. (2014) have studied Mossbauer and physical properties of Zn doped Co_2Y hexaferrite ($Ba_2Zn_xCo_{2-x}Fe_{12}O_{22}$) samples. The sample synthesis was done through citrate sol-gel auto combustion technique for 4 hours at 1100 °C. The sample was analyzed using XRD, SEM and Mossbauer spectroscopy. The single Y-type hexaferrite presence among the sintered materials was depicted by XRD analysis. SEM images revealed the change in particle shape along with the size reduction by factor 10. There was a decrease in hyperfine field (B_{hf}) that was related to both components in regard with milling time increase.

Ahmad et al. (2013) discussed the Sr-substitution effect on Sr-doped Ni_2Y ferrites Y type. The synthesis was done at 1150°C for 3 hours using sol-gel combustion technique. SEM, XRD, VSM and EDX spectroscopy were used for the sample analysis. XRD patterns illustrated that the samples single phase can be resulted by the substitution of Sr^{2+} ions with Ba^{3+} sites. The bulk density along with the X-ray density showed a decrease as well as increased porosity in respect to rise of Sr-concentration. SEM spectrum depicted the grain size ranging from 2.68µm and 2.06µm. There was increase in coercivity with respect to Sr concentration increase. The saturation magnetization obtained was ranging between (51.5-57.8 emu/g).

Ali et al (2013) investigated the synthesis of Y-type strontium hexaferrite $Co_2Sr_2Fe_{12}O_{22}$ utilizing the micro emulsion route as well as the polypyrrole doped with dodecylbenzenesulphonic acid (PPY·DBSA) synthesis. FTIR, XRD, VSM and SEM were used for the sample analysis. The observation revealed that the ferrite polymer mixture enhanced the coercivity, whereas reduction in remanence and saturation magnetization was observed. They illustrated that the coercivity value improvement assured the synthesized products benefit that was 1896 Oe in the prepared samples. The signal-to-noise ratio achievement was as a result of small sized particles obtained in the synthesized composite of expected composite ferrite-polymer sample used in high density recording media.

Elahi et al. (2013) reported the synthesis of $Sr_2Ni_{2-x}Mg_xFe_{12}O_{22}$ (x=0.0, 0.1, 0.2, 0.3, 0.4, 0.5) hexagonal Y type ferrites employing sol-gel autocombustion route. Investigation of electrical, magnetic and structural behaviours was done with Mg^{2+} substitution at Ni^{2+} sites. FTIR spectra depicted the ferrites peaks absorption features of sintered sample. XRD patterns illustrated the single Y type hexaferrite phase and different parameters including; bulky density, cell volume, lattice constants and X-ray density. The ferrites revealed hexagonal platelet shape like which is appropriate for microwave absorption. Retentivity (Mr), saturation magnetization (Ms), magnetic moment (n_B) and coercivity (Hc) shown decrease with rise in Mg content.

Ali et al. (2014) discussed the Tb-Mn substitution role of Y type hexaferrite magnetic behaviours. Micro emulsion method was utilized for the synthesis. The study of the manganese doping effect at octahedral terbium site and tetrahedral site was conducted. The sample SEM analysis depicted the plate like shape grains. The Sr-Y great approximation formula was obtained at the highest substitution. The coercivity high values confirm the present samples use in the perpendicular recording media.

Song et al. (2016) illustrated the Al-substitution impact on microwave absorption characteristics along with magnetic characteristics of $Ba_{1.5}Sr_{0.5}CoZnAl_xFe_{12-x}O_{22}$ (x=0-1) hexaferrites single phase. SEM, VSM and XRD analysis were used. The results depicted that there was no Al-substitution effect on Y type hexaferrites structure. The observed samples morphologies revealed a plate-like structure. The $Ba_{1.5}Sr_{0.5}CoZnAl_xFe_{12-x}O_{22}$ permeability as well as the complex permittivity was analyzed employing VNA. Reflection loss was determined between 1-18 GHz frequency range. The maximum sample absorption was found to be -19dB at 11.5GHz.

Bierlich et al. (2012) used mixed-oxide technique for the preparation of Y-type polycrystalline hexaferrites with general formula $Ba_2Co_{2-x-y}Zn_xCu_yFe_{12}O_{22}$ ($0 \leq x \leq 2$ and $0 \leq y \leq 0.8$). They reported the formation of single Y-type hexaferrite phase after sintering at $1000°C$. Large grains and dense samples were obtained after sintering at $1200°C$ which showed an increase in permeability with increase in Zn concentration. The maximum of permeability was found to be μ'=35 at 1MHz when x=1.6 and y=0.4. They also reported that a resonance frequency of 500MHz was observed for Zn-rich samples (y=0 and y=0.4).Saturation magnetization showed an increase with increase in concentration of Zn. It was observed that the temperature of maximum shrinkage was decreased up to $950°C$ by the addition of Bi_2O_3. In addition, an increase in Cu-concentration also decreases the temperature of sintering up to $900°C$ which permits the amalgamation of the ferrites with Ag metallization for multilayer technologies. Nevertheless, a sintering at low temperature of Co_2Y exhibits good properties at high frequency such as permeability of μ'= 10 and a resonance frequency of 1 GHz.

Haijun et al. (2002) investigated on the preparation and microwave properties of Zn doped Co_2Y hexaferrite ($Ba_2Zn_zCo_{2-z}Fe_{12}O_{22}$) using citrate sol-gel route and sintered at a temperature of 1100°C for 5h. The method of transmission/reflection coaxial line was utilized for measuring of complex dielectric constant and permeability of prepared specimen in the frequency range 100 MHz- 6GHz. In 0.1-6 GHz, complex permittivity showed a decrease with rise in frequency. Moreover, it was observed that the frequency of resonance of samples was strongly dependent on the concentration of Zn.

Xu et al. (2012) presented the high absorbance of absorbing materials of Cu-doped Co_2Y hexaferrite rod ($Ba_2Co_{1.8}Cu_{0.2}Fe_{12}O_{22}$). The synthesis was done employing conventional solid-state technique. The anisotropy magnetocrystalline fields along with the shape self-bias field excitement results into FMR. In the range frequency of 10GHz -12.2 GHz, the ferrite rod absorbance *(A(ω))* was found higher than 98%. The light weight with high absorbance of the ferrite rod made it ideal for microwave –absorbing material.

2.3 Bismuth copper titanate (BCTO)

Deng et al. (2017) studied the $Y_{2/3}Cu_3Ti_4O_{12}$ (YCTO) ceramic dielectric and mechanism characteristics. The sintering of YCTO was done in pure O_2 atmosphere and air. There was a drastic decrease in YCTO-O_2 dielectric loss and permittivity in low frequency. The modulus (M") as well as frequency dependent impedance (Z") YCTO-O_2 with YCTO air spectra

revealed the thermal activated procedure. The relaxation times distribution was observed to be temperature independent based on Z" and M" spectra scaling features. The Nyquist plot of impedance adherence depicted that the sample electrical response origin was from grains boundaries and grains. The electrical local response time distribution was shown to be temperature independent.

Gautam et al. (2016) discussed the $0.5Bi_{2/3}Cu_3Ti_4O_{12}$-$0.5Bi_3LaTi_3O_{12}$ nano composite magnetic and dielectric properties. Semi wet route was used for the sample synthesis utilizing metal nitrate of high purity along with solid TiO_2 in a stoichiometric ratio. XRD analysis depicted $Bi_{2/3}Cu_3Ti_4O_{12}$ (BCTO) and $Bi_3LaTi_3O_{12}$ (BLTO) presence in the compounds sintered for 8 hours at 900°C. The composite TEM analysis revealed the nanoparticles presence between the range of 55±3 nm. SEM images depicted the spherical grains as well as plate-like structure. The weak nature of ferromagnetic in M-H and M-T curve was shown by the composite magnetic feature. The space charge polarization presence led to high dielectric constant value (ε'=13.94×103).

Gautam et al. (2016) studied $Bi_{2/3}Cu_3Ti_4O_{12}$ (BCTO) ceramic characterization with semi-wet route synthesis. For characterization of the sample EDX, XRD and SEM were used. XRD spectra revealed the ceramic BCTO single phase development at 1073K. The calculated grains average dimensions analyzed by AFM and SEM were ranging from 0.73 ±0.2 μm exhibiting perfect grain boundaries. The investigation of magnetic properties was done at temperature range of 2 to 300k with 7tesla magnetic field. The field cooled (M^{FC}) along with the zero field cooled (MZ^{FC}) were used for the calculation of Curie temperature with applied magnetization at 100 Oe, the obtained Curie temperature was 125K. The BCTO sintered ceramic highest dielectric constant was (ε'=2.9×104).

Yang et al. (2016) investigated $Bi_{2/3}Cu_3Ti_4O_{12}$ (BCTO) ceramic mechanism and colossal dielectric permittivity. Solid state reaction route was utilized for the sample fabrication. SEM depicted uniform dense grains of size ranging between 2 to 3μm. The dielectric permittivity obtained was $3.3×10^5$ with low frequency. The detected $Bi_{2/3}Cu_3Ti_4O_{12}$ ceramic dielectric response comprised of three types which situated in high frequency range, middle frequency range and low frequency range. The activation energy of 0.30 eV was obtained for dielectric response middle frequency whereas 0.70eV activation energy was found for dielectric response in high frequency.

Yang et al. (2016) studied the $Bi_{2/3}Cu_3Ti_4O_{12}$ ceramics dielectric constant vs non-Ohmic and voltage properties. Sol- gel technique (BCTO-SG) as well as traditional solid state technique (BCTO-SS) was used for the sample preparation. A high dielectric constant value of BCTO-SG ceramics was revealed as 1.1×10^4 whereas that of BCTO-SS ceramics showed low value of dielectric constant (3200). With increased voltage application at 100 KHz, BCTO-SS ceramics dielectric constant reduced whereas that of BCTO-SG ceramics augmented. Non-linear coefficients of BCTO-SG ceramic as well as BCTO-SS were 1.01 and 1.65 respectively. The BCTO-SG and BCTO-SS ceramics electric fields breakdown were 0.48 and 1.21 kV/cm correspondingly.

Kumonsa et al. (2015) reported a novel approach for perovskite $ACu_3Ti_4O_{12}$ ceramic product. The $ACu_3Ti_4O_{12}$ A-sites were occupied by Bi^{3+}, Ca^{2+} and Na^+ at 33% at each level allowing $Na_{1/3}Ca_{1/3}Bi_{1/3}Cu_3Ti_4O_{12}$ formation. The ceramic showed high $\varepsilon^{'}$ value equals to 2.5×10^4 and low loss tangent of 0.038 at 1 KHz stable temperature. The dielectric relaxation feature of high frequency exhibited the activation energies between 0.110-0.121 eV. X-ray photoelectron spectroscopy was used to analyze the Cu cations valence states (*i.e.*, Cu^+, Cu^{2+}, and Cu^{3+}) in the ceramic product. The impedance spectroscopy analysis depicted that the formed product consisted of insulating grain boundaries and semiconducting grains.

Singh et al. (2015) discussed $Bi_{2/3}Cu_3Ti_{2.90}Fe_{0.10}O_{12}$ combustion synthesis with the help of raw material of TiO_2. Gycine-nitrate solution combustion method was opted for the sample synthesis. The powder of solid TiO_2 was applied as the main source for titanium at lowest temperature. XRD patterns depicted the ceramic single phase sintered for 12 hours at 900°C. The particle size was analyzed by Bright-field TEM and was observed to be 16±07 nm. SEM images illustrated the presence of distributed bimodal grains of sizes ranging between 500nm- 1.5μm. The electrode effects along with the grain boundaries activation energies were obtained as 0.54 and 0.47 eV respectively.

Yang et al. (2015) reported $Bi_{2/3}Cu_3Ti_4O_{12}$ ceramics dielectric features and the synthesis using sol-gel technique. The dielectric properties of the resultant measured at 1 KHz was found to be 1.2×10^4. The Maxwell-Wagner relaxation led to the occurrence of dielectric relaxation I at 200°C. On the other hand the dielectric relaxation II was obtained at 300°C, for the sample that was obtained using the sol-gel technique.

Liang et al. (2014) investigated $Na_{0.5}Bi_{0.5}Cu_3Ti_4O_{12}$ (NBCTO) ceramics behavior phase formation and the electric features. Solid-state and sol-gel techniques were used for the sample synthesis. TG-DSC and XRD outcome depicted that there was temperature reduction by 100°C in the NBCTO phase formation while using sol-gel technique. The NBCTO ceramics obtained using sol-gel method exhibited stable temperature and low dielectric loss in the temperature ranging from RT to 150°C.

Piir et al. (2014) studied bismuth copper titanate pyrochlores characteristics and chemistry. The ceramic process was used to obtain the copper that comprised pyrochlores bismuth titanates ($Bi_yCu_xTi_2O_7 - \delta$) with the range of concentration from $0.08 \leq x \leq 0.6$ and $1.4 \leq y \leq 2$. A copper part atom reversibly undergo reduction to Cu^{2+} at 930-960°C due to the substitution of copper ions to A-sites. The total dependence of samples conductivity in temperature range T>450°C followed the Arrhenius law.

2.4 Objectives of the study

The aim and objectives of this research project is to synthesize a new nanocomposite material based on hexaferrite material (with a high anisotropy and high coercivity), dielectric material bismuth copper titanate (BCTO) (with a dielectric constant above 1000) and conducting polymer (polyaniline) which will be able to absorb electromagnetic wave in the frequency range 0-40 GHz. Polyaniline is used as matrix and conducting material. The main objectives are:

- Investigation of magnetic properties of rare-earth/transition metals doped hexaferrite
- Investigation of dielectric properties rare-earth/transition metals doped bismuth copper titanate (BCTO).
- Investigation of microwave absorption properties the composites comprise of hexaferrite /BCTO/conducting polymer.

2.5 Scope of the study

Recently, radiation or electromagnetic waves remain a great danger not only to humans but also to certain electronic devices. To solve this problem, one solution is to design the materials capable of absorbing these radiations. EM waves are constituted of the magnetic and electric fields and therefore excellent magnetic and dielectric properties of absorber

material are sought. Ferrites such as hexaferrites are known for their good magnetic properties which makes them good candidate for absorbing magnetic field. Generally, these magnetic materials don't have good dielectric properties. So, it is necessary to associate to them materials with excellent dielectric properties. Dielectric materials such as bismuth copper titanate (BCTO) have a very high electrical permittivity (greater than 1000). This makes it an excellent electrical field absorber.

In the electromagnetic shielding mechanism, the material in addition to being a good absorber of magnetic and electric fields must also have good electrical conductivity in order to reduce the intensity of the electromagnetic wave by reflection when it falls on the shielding material. Indeed, the theory of shielding suggests that the absorber material must be highly conductive with low permittivity and permeability [83]. For this reason, the metals have been very good candidates. Due to the evolution of technology in miniaturization, metals have several limitations such as high density (e.g. 8.9 g/cm^3 for copper). However, conjugated polymers also known as conductive polymers contain π-bonds which are responsible of their conduction. The conductive polymers therefore have conductivity comparable to that of metals and unique properties such as flexibility, corrosion resistance, low density ($\tilde{}$ 1.1-1.3 g/cm^3) etc.

Chapter 3: Method of synthesis

3.1 Introduction

Synthesis methods are one of the most important things that have to be mastered for preparing of nanomaterials. Due to the used method, structural properties such as particle size, purity and even magnetic properties as coercivity can be affected. In order to obtain inorganic nanoparticles, several techniques are used for the synthesis which include hydrothermal reaction, salt-melt technique, glass crystallization technique, co-precipitation process, solid-state reaction technique, reverse micro-emulsion method, melting method, citrate precursor method, conventional mechanical grinding, stearic acid gel, ceramic method, sol-gel auto-combustion method and so on. Among these multiple techniques some present limits and disadvantages. Glass crystallization and conventional mechanical grinding techniques exhibit some disadvantages in the synthesis for example introducing impurities into material compositions and time consuming [22]. However, synthesis routes like sol-gel and co-precipitation techniques show more advantages than others such as low cost, simplicity, low temperature of formation, low time of formation, good homogeneity and good microstructure.

In this chapter, autocombustion sol-gel technique was employed to synthesize doped hexaferrite and bismuth copper titanate nanoparticles. However, oxidative polymerization method was used to synthesize organic compounds as polyaniline and polypyrrole. Mechanical grinding technique which consists to mix a certain amount of different compounds was employed to synthesize composite materials.

3.2 Principle of synthesis methods

3.2.1 Sol gel autocombustion method

Because of its different advantages, the sol gel method is one of the most used methods in recent decades. It uses as raw materials the nitrates of metals. The procedure can be summarized in four steps.

Step 1: Obtain the sol-solution by dissolving the raw materials in a solvent that can be distilled water or ethylene glycol.

Step 2: Obtain the gel solution by homogenizing the liquid solution (sol-solution) on the magnetic stirrer till the viscous solution is obtained.

Step 3: Obtain the precursor material by evaporating the solvent.

Step 4: Carry out the calcination or the sintering on basis of temperature formation of the expected material.

3.2.2 Oxidative polymerization

This method consists of polymerizing the aniline using Ammonia persulphate $[(NH_4)_2S_2O_8]$ as oxidant. The reagents are poured in the strong acid which can be hydrochloric acid (HCl) or sulphuric acid (H_2SO_4) with concentration of 1M. The synthesis is done at a low temperature $(0-2^{\circ}C)$ due to the fact that the reaction is highly exothermic.

3.3 Synthesis of materials
3.3.1 Synthesis method of Al^{3+} -Mn^{2+} substituted M-type barium hexaferrite

M-type hexaferrite with chemical composition $Ba_{1-x}Al_xFe_{12-y}Mn_yO_{19}$($x$= 0.6 and y= 0.3) was prepared using sol-gel method auto-combustion. The starting materials were, Fe $(NO_3)_3\cdot 9H_2O$ (Loba Chemie; 98% purity), $Ba(NO_3)_2$ (Loba Chemie; 99% purity), $Al(NO_3)_3.9H_2O$(Loba Chemie; 98% purity),and $Mn(NO_3)_2.xH_2O$(Sigma Aldrich; 98% purity were dissolved in 50mL distilled water in a beaker in proper stoichiometric. Citric acid (Loba Chemie; 99.5% purity), was added to the solution with 1:1.5 as ratio. Then ammonia solution was added drop by drop to adjust the pH of solution to 7.0. This solution is stirred using stirring magnetic at $80^{\circ}C$ to homogenize the solution and was obtained the gel solution. The gel solution was heated at around$300^{\circ}C$using hot plate for ignition of the gel. Water was evaporated and gel was burnt to obtain a dendritic powder. Subsequently calcined at 750, 850 950 and $1050^{\circ}C$ for around 5 hours, hexaferrites powders were obtained.

3.3.2 Synthesis method of Al^{3+}-Cr^{3+} substituted M-type barium hexaferrite

Al-Cr substituted barium hexagonal ferrites with chemical composition $BaFe_{12-2x}Al_xCr_xO_{19}$ (x=0.0, 0.2, 0.4) were synthesized by the sol-gel autocombustion method. AR grade chemicals such as $Ba(NO_3)_2$ (Loba chemistry, purity 99%), $Fe(NO_3)_3.9H_2O$ (Loba chemistry, purity 98%), $Al(NO_3)_3.9H_2O$ (Loba chemistry, purity 98%) $Cr(NO_3)_3.9H_2O$ (Loba chemistry, 98% purity), ethylene glycol $(C_2H_6O_2)$ (Loba chemistry, 99.5% purity) and citric acid $(C_6H_8O_7.H_2O)$ (Loba chemistry, 99% purity) were used as starting materials. Initially, the appropriate measurements in stoichiometric ratios were made for each of the metal nitrates and dissolved in 50 ml of ethylene glycol. Citric acid was added with 1:1.5 molar ratio of cations to citric acid. Thereafter, ammonia solution was added drop by drop so as to neutralize the solution (pH=7.0). The resultant mixture was placed on a magnetic stirrer and

heated to a temperature of about 85-100 °C. After 3 hours, a brown viscous gel was obtained which upon further heating to 300℃ results in autocombustion and formation of a fluffy precursor material which was heated at 1000 °C for 7 hours.

3.3.3 Synthesis method of Cr^{3+}-Bi^{3+} substituted M-type strontium hexaferrite

Chemical formula of $SrFe_{12-2x}Cr_xBi_xO_{19}$ (x=0.0, 0.15, 0.2) of Cr-Bi substituted M-type strontium hexaferrite was synthesized via autocombustion sol gel route. All reagents are of AR grade with purity between 98-99.5% such as $[Sr(NO_3)_2]$, $[Fe(NO_3).9H_2O]$, $[Cr(NO_3)_3.9H_2O]$, $[Bi(NO_3)_3.5H_2O]$, $[C_2H_6O_2]$ and citric acid $[C_6H_8O_7.H_2O]$ were used as starting materials. Metal nitrates were dissolved in 50 mL of ethylene glycol in a beaker of 500 mL at the appropriate stoichiometric ratios followed by addition of citric acid (cation to citric acid ratio of 1: 1.5). Then, the pH value of the solution obtained is adjusted to 7.0 by adding ammonia hydroxide solution. Magnetic stirrer at 80-100°C was used to stir the mixture homogenously until it evaporates and form a brown gel after 4 hours. The precursor material was obtained after heating the gel at 280-300 °C, and sintered for 6 hours at 1000 °C to obtain the final $SrFe_{12-2x}Cr_xBi_xO_{19}$ (x=0.0, 0.15, 0.2) powder.

3.3.4 Synthesis method of Cr^{3+}-Ni^{2+} substituted Y-type barium hexaferrite

To synthesize Cr-Ni substituted Co_2Y hexaferrite $[Ba_{2-2x}Cr_xNi_xCo_2Fe_{12}O_{22}$ (x=0.0, 0.1, 0.15)] nanoparticles, high purity (99-99.5%) AR grade raw materials such as barium nitrate $[Ba(NO_3)_2]$, ferric nitrate $[Fe(NO_3)_3.9H_2O]$, chromium nitrate $[Cr(NO_3)_3.9H_2O]$, nickel nitrate $[Ni(NO_3)_2\cdot6H_2O]$, cobalt nitrate $[Co(NO_3)_2.6H_2O]$ and citric acid $[C_6H_8O_7.H_2O]$ were used. Metal nitrates were dissolved in 100 mL of deionised water, and then citric acid with 1:1 ratio to cations was added as fuel. Adding ammonia hydroxide drop by drop make the pH of the mixture 7.0. The mixture was stirred and heated at 80-100°C temperature until a brown gel was obtained after evaporation of most of the solvent. The brown gel was transferred and heated at 280-300°C temperature to get a dried precursor material which was sintered at 1100°C for 6h to obtain $Ba_{2-2x}Cr_xNi_xCo_2Fe_{12}O_{22}$ (x=0.0, 0.1, 0.15) powder.

3.3.5 Synthesis method of Ni^{2+}-Co^{2+} substituted bismuth copper titanate

Sol-gel autocombustion method was used to prepare $Bi_{2/3}Cu_{3-2x}Ni_xCo_xTi_4O_{12}$ (x=0.0, 0.1, 0.2). High purity AR grade materials (99%-99.5%) such as $Bi(NO_3)_3\cdot5H_2O$, $Ni(NO_3)_2\cdot6H_2O$,

$Cu(NO_3)_2 \cdot 3H_2O$, $Co(NO_3)_2 \cdot 6H_2O$, TiO_2 and $C_6H_8O_7$ were obtained from LOBA Chemie and CDH. Stoichiometric ratio of the materials is dissolved in a deionised water to form an aqueous solution; with citric acid as a fuel, with cations to citric acid molar ratio of 1:1.5. The solution prepared was heated at 80-100 °C temperature for 3 hours, a light blue gel was gotten which is further heated at 300 °C to give a black bismuth copper titanate ceramic precursor. The precursor was heated at 900 °C for 7 hours and then grinded with mortar and pestle to get the final product.

3.3.6 Synthesis method of Bi^{3+}-Al^{3+} substituted barium hexaferrite and polyaniline

Sol- gel autocombustion method was used to synthesize $BaFe_{11.8}Bi_{0.1}Al_{0.1}O_{19}$ powder. Initially, AR grade chemical with high purity (98-99.5%) such as $Ba(NO_3)_2$, $Fe(NO_3)_3.9H_2O$, $Al(NO_3)_3.9H_2O$, $Bi(NO_3)_3.5H_2O$, ethylene glycol ($C_2H_6O_2$) and citric acid ($C_6H_8O_7.H_2O$) obtained from LOBA Chemie and CDH were used as raw materials. Appropriate stoichiometric measurement of each metal nitrate was done and 50 mL of ethylene glycol solvent was used to dissolve the metal nitrates. Addition of citric acid in the molar ratio 1:1.5so as to serve as agent of autocombustion. Then, the neutral mixture was obtained by adding ammonia hydroxide. The obtained solution is homogenized with a magnetic stirrer at a temperature of 80-100°C for 3 hours, a brown gel was formed which was placed under 280-300°C to evaporate the remaining solvent and the precursor material was formed. A high temperature furnace has been used to get $BaFe_{11.8}Bi_{0.1}Al_{0.1}O_{19}$ powder at 1000 °C after 6 hours.

The synthesis of PANI has been done via oxidative polymerization method. In this process, hydrochloric acid has been placed under rotation at 0°C in an ice bath, and then a certain amount of aniline monomer was added gradually. After 30 min, Ammonia persulphate (APS) dissolved in water has been added. The set has been allowed for 6 hours to permit the reaction to take place. Then the filtration and washing were done using deionised water and methanol then dried in an oven at 60°C temperature. After 2 days, PANI was obtained with green colour.

Mechanical grinding process has been using to blend the previous prepared samples using a mortar and pestle. The mixture has been done according to the ratios (hexaferrite: PANI) 1:1, 1:1.5 and 1:2 (**Table 3.1**).

Table 3.1 Sample code and composition of $BaFe_{11.8}Bi_{0.1}Al_{0.1}O_{19}$-PANI

Sample code	Ratio
HP1	1:1
HP2	1:1.5
HP3	1:2

3.3.7 Synthesis method of Dy^{3+}-Cr^{3+} substituted barium hexaferrite and polyaniline

Dy-Cr doped barium hexaferrite ($Ba_{0.7}Dy_{0.3}Fe_{11.4}Cr_{0.3}O_{19}$) was prepared using autocombustion sol-gel technique. Chemicals with AR grade such as $Ba(NO_3)_2$ (99% purity), $Fe(NO_3)_3.9H_2O$(98% purity), $Dy(NO_3)_3.9H_2O$ (98% purity) and $Cr(NO_3)_3.9H_2O$ (98% purity) from LOBA Chemie were used. 50 mL of ethylene glycol was used to dissolve the material in the ratio 1:1.5 of cations to citric acid ,then ammonia hydroxide was added dropwise to make the pH of the solution 7.00. The resulting mixture was heated at 80-100℃ temperature for 3 hours, a gel solution was obtained which was brought to around 350℃ to evaporate the remaining water in the sample and precursor material was formed. The precursor material was put inside the furnace for a temperature of 1000℃ for 6 hours to obtain the hexaferrite powder.

The synthesis of PANI has been done via oxidative polymerization method. In this process, hydrochloric acid has been placed under rotation at 0°C in an ice bath, and then a certain amount of aniline monomer was added gradually. After 30 min, Ammonia persulphate (APS) dissolved in water has been added. The set has been allowed for 6 hours to permit the reaction to take place, then deionised water was added, and the mixture was filtered and washed with methanol and deionised water then dried in an oven at 60°C temperature. After 2 days, PANI was obtained with green colour.

The powders obtained from these two previous methods were blended in a mortar with a pestle using a mechanical grinding method. Indeed, the amount of polyaniline was varied from one sample to another according to the ratios 1: 1, 1: 2 and 1: 3 (hexaferrite: PANI) (**Table 3.2**).

Table 3.2 Sample code and composition of $Ba_{0.7}Dy_{0.3}Fe_{11.4}Cr_{0.3}O_{19}$/PANI

Sample code	Ratio
HP11	1:1
HP22	1:2
HP33	1:3

3.3.8 Synthesis method of Bi^{3+} substituted barium hexaferrite, La^{3+} substituted bismuth copper titanate and polypyrrole

$BaFe_{11.8}Bi_{0.2}O_{19}$ sample was prepared via sol-gel autocombustion method. The chemicals of AR grade having high purity of 98-99.5% include $Ba(NO_3)_2$, $Fe(NO_3)_3.9H_2O$, $Bi(NO_3)_3.5H_2O$ and ethylene glycol ($C_2H_6O_2$) from LOBA Chemie were used as raw materials. Initially, 50 ml of ethylene glycol was poured in beaker then metal nitrates in stoichiometric measurement were added. The cations to citric acid molar ratio of 1:1.5 were added. The mixture was neutralized (pH=7.00) by adding ammonia hydroxide dropwise. The mixture was homogenized at 85-100 °C temperature and the rest of the solvent was evaporated. After 3 hours, a viscous gel was obtained and dried at 300℃ on a hot plate to get the precursor material which was heated in the furnace at 1100 °C temperatures for 6 hours and $BaFe_{11.8}Bi_{0.2}O_{19}$ powder was obtained.

Also bismuth copper titanate $[Bi_{(1-x)}La_x]_{2/3}Cu_3Ti_4O_{12}$ (x=0.2) was prepared using autocombustion sol-gel technique with high purity analytic reagents grade (99%-99.5%). The starting material included bismuth nitrate $[Bi(NO_3)_3 \cdot 5H_2O]$, copper nitrate $[Cu(NO_3)_2 \cdot 3H_2O,]$, lanthanum nitrate $[La(NO_3)_3.6H2O,]$ and titanium dioxide (TiO_2,) . Materials in stoichiometric quantities were dissolved in deionised water forming aqueous solution; addition of citric acid in the ratio of 1:1.5 so as to serve as agent of autocombustion. The mixture was stirred and heated at 85-100 °C temperature. After 4 hours, a blue gel was formed and dried at 280-300 °C temperature, the precursor obtained was heated at 900 °C temperature for 7 hours and then grinded with mortar and pestle to obtain $[Bi_{(1-x)}La_x]_{2/3}Cu_3Ti_4O_{12}$ (x=0.2) powder.

Polypyrrole (PPy) was synthesized via oxidative polymerization of pyrrole monomer. 2 ml pyrrole was gradually poured in 70 ml concentrated hydrochloric acid solution (HCl) at 0 °C

in an ice bath for 30 min (A). Aside, 4.98 g of ammonia persulfate (APS) was dissolved in 30 ml HCl (B). Then (B) solution was added drop by drop inside (A) solution with vigorous stirring. After 6h around, the precipitation took place. The obtained mixture was filtered and washed with distilled water and dried in air for 5 days.

The previous prepared samples in ratio 1:1:1 were blended in a mortar with a pestle using a mechanical grinding. The obtained powder was our composite (**Table 3.3**).

Table 3.3 Sample codes and composition of prepared samples

Sample code	Sample composition
BBPY1	$BaFe_{11.8}Bi_{0.2}O_{19}$
BBPY2	$[Bi_{(1-x)}La_x]_{2/3}Cu_3Ti_4O_{12}$ (x=0.2)
BBPY3	$BaFe_{11.8}Bi_{0.2}O_{19}$ / $Bi_{(1-x)}La_x]_{2/3}Cu_3Ti_4O_{12}$ (x=0.2) /PPy

3.3.9 Synthesis of Ni^{+2}-Cr^{+3} substituted barium Co_2Y hexaferrite, La^{3+} substituted BCTO and PANI

Co_2Y hexaferrite with chemical composition $Ba_{2-2x}Cr_xNi_xFe_{12}O_{22}$ (x=0.2) was prepared via autocombustion sol gel route. AR grade reagents in stoichiometric ratios were measured and poured in 500mL beaker containing double deionised water. Citric acid was added into the beaker in the molar ratio of 1:1.5 with cations having molar ratio of 1. Drop wise ammonia addition was carried out until the pH of the mixture becomes 7.00. Constant and continuous stirring of the mixture at 80-100 °C temperature, the solvent evaporate and turns to gel, the temperature was elevated up to 280-300 °C and the gel underwent autocombustion to give the precursor material which was sintered for 6 hours at 1100 °C to give Ni^{+2}-Cr^{+3} substituted barium Co_2Y hexaferrite.

BCTO electroceramic with chemical formula $[Bi_{1-x}La_x]_{2/3}Cu_3Ti_4O_{12}$ (x=0.15) was successfully prepared via sol gel auto combustion route. AR grade reagents in stoichiometric ratios were poured into a beaker containing 50 mL of double deionised water, citric acid in 1:1 molar ratio with cations was added. The mixture was stirred and heated at 80-100°C temperature ; a light blue gel was obtained after evaporation of most of the solvent. The light blue gel undergo autocombustion after it was subjected to 280-300°C temperature, a

black BCTO precursor was obtained. The precursor obtained was crushed using mortar and pestle and calcinated at 900 °C for 7 hours.

The synthesis of PANI has been done via oxidative polymerization method. In this process, 182.3 ml of hydrochloric acid was placed under magnetic stirring in an ice bath at 0°C, and then 46.56 mL of aniline monomer was added gradually to the mixture and stirred for 6 hours for complete polymerization, this was labelled as solution A. 80.94 gm of ammonium persulphate (APS) was poured into another beaker containing 100 mL of double deionised water and allowed to dissolve, this was labelled as solution B. After 6 hours, solution B was mixed with solution A and the colour of the mixture gradually changes to dark green, deionised water was added to dilute the mixture and the resulting mixture was aged for 24 hours in room temperature. The mixture was filtered and washed with methanol and deionised water followed by drying in oven at a temperature of 60°C. The resulting PANI granules were grinded with mortar and pestle, fine green PANI powder was obtained.

Ni^{+2}-Cr^{+3} substituted barium Co_2Y hexaferrite powder, La^{3+} substituted BCTO powder, and PANI were weighed in the ratio of 1:1:1 and grinded with mortar and pestle in order to get a homogeneous mixture of Co_2Y/BCTO/PANI nanocomposite.

Table 3.4 Sample composition and code for Co2Y/BCTO/PANI nanocomposite

x	Sample composition	Sample code
0.2	$Ba_{1.6}Cr_{0.2}Ni_{0.2}Co_2Fe_{12}O_{22}$	Co_2Y
0.15	$Bi_{0.51}La_{0.15}Cu_3Ti_4O_{12}$	BCTO
-	$Ba_{1.6}Cr_{0.2}Ni_{0.2}Co_2Fe_{12}O_{22}$/ $Bi_{0.5}La_{0.15}Cu_3Ti_4O_{12}$/PANI	Co_2Y/BCTO/PANI

Chapter 4: Characterization techniques

This chapter presents the different techniques employed to characterize the prepared samples. Structural, magnetic, dielectric, optical and microwave absorption properties were investigated. For that, X-Ray Diffraction (XRD), Fourier Transform Infra-red (FTIR) spectroscopy, UV-Vis-NIR spectroscopy, Vibrating Sample Magnetometer (VSM), Raman spectroscopy, Emission Scanning Electron Microscopy (FESEM), Vector Network Analyser (VNA), Impedance analyser, Field Energy-dispersive X-ray spectroscopy and Mapping were utilized.

4.1 X-Ray Diffraction

X-Ray diffraction is a widely utilized technique for sample characterizations. This technique is non-destructive and concerns the interaction between X-ray and the matter. When the monochromatic beam of X-ray interacts with the specimen, it is scattered in random directions with the same energy with the incident photons: it is elastic diffusion or Rayleigh diffusion. It is very important to know that this characterization technique only functions on crystallized or semi-crystallized matter. So, if the sample to analyse has a regular arrangement of atoms, the scattered light is oriented in specific directions which are determined by wavelength of X-ray, dimensions and orientation of crystal lattice. **Fig. 4.1** shows the illustration of X-ray diffraction. In general, scattered rays interfere either in constructive or destructive manner.
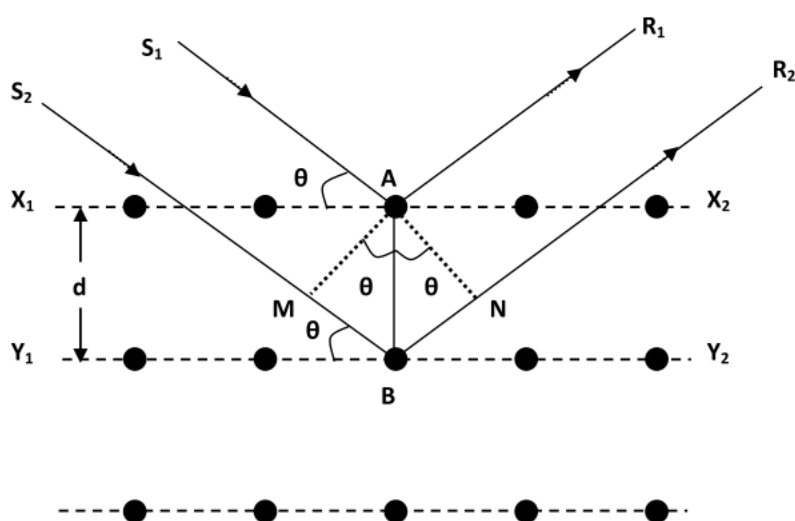
Fig. 4.1 Illustration of X-Ray Diffraction

But only constructive interferences are detected which correspond to the observed peaks in X-Ray Diffraction patterns. Those peaks represent diffraction planes of the crystal structure as shown in **Fig. 4.2**. Constructive interferences obey Bragg's Law given by:

$$2dsin\theta = n\lambda \tag{4.1}$$

Where d is d-spacing between consecutive atomic planes, λ is the wavelength of the radiation. θ is the half deflection angle, and n is the order of reflection (n is a whole number).
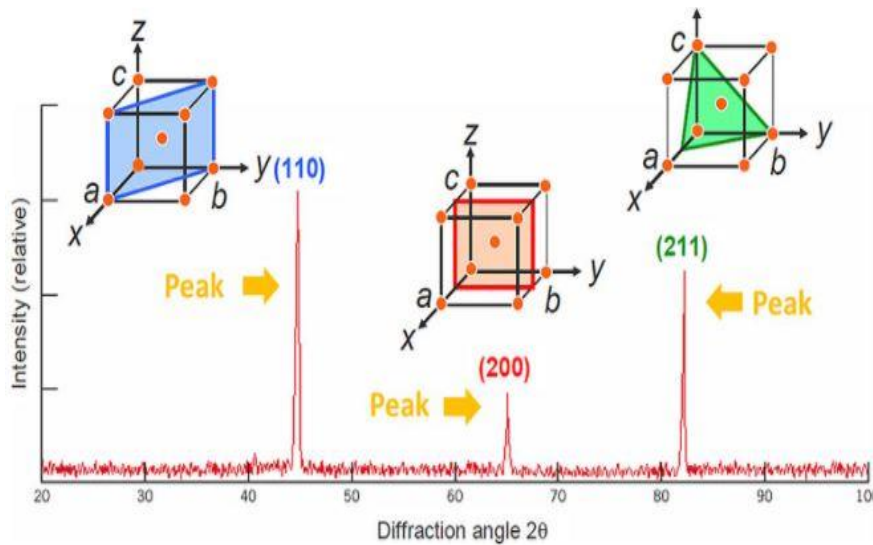
Fig. 4.2 Example of X-ray diffraction patterns of BCC crystal

The X-ray diffraction is used to:

- Identify the various compounds or phase in a sample and texture
- Measure or estimate dimension of crystal lattice (d-spacing, lattice parameters, volume)
- Define the crystal structure of a material
- Determination of crystallite size, space group, density and strain

4.2 Impedance analysis

Impedance spectroscopy is a technique which measures electrical and dielectric properties such as resistance and capacitance of a sample by applying a sinusoidal AC excitation signal and by varying the frequency in the defined range [84]. This technique is widely used to characterize various types of materials such as insulator, semiconductor and even ionic

materials using impedance analyser or LCR meter as measuring devices. Firstly, the procedure is used to make pellet of sample. Then apply or coat the sectional surface area with silver paste in order to obtain parallel plate capacitor with the sample as the dielectric medium. The measured capacitance and resistance is then used to evaluate parameters of dielectric properties (dielectric constant, dielectric loss etc.).

4.3 Electron microscopes (FESEM/EDX/Mapping)

FESEM is a helpful electron microscopic technique used to visualize images and examine structural information of micro-structured materials of specimen in high resolution. This technique is based on electrons-matter interactions. Indeed, electron generated from a X-ray tube are used to estimate the size and the morphology of specimen. The incident electrons striking the surface of the material causes electrons emission such as backscattered electrons and secondary electrons, X-ray, heat and even transmitted electrons. However, specially secondary and backscattered electrons are responsible of principal information regarding surface morphology (topological contrast) of sample. To avoid the collection of spatial charge that may destroy FESEM micrographs, the test specimen is first earthed. The electrons beam scans the surface of specimen, then exhibit the contained particles as response.

Energy-dispersive X-ray spectroscopy and mapping are used to identify each chemical element that is contained in the specimen.

Study of the morphology and composition of the prepared samples was carried out using FESEM, EDXS and mapping (FEI Nova NanoSEM 450 FESEM).

4.4 Generality on spectroscopy

In order to obtain different information with regard to the material, it is generally subjected to an excitation according to which it gives an answer. This answer exclusively depends on the excitation type which can be:

- Laser
- Polychromatic light
- Optical source
- Electrical field
- Magnetic field

Spectroscopy can therefore be defined as a characterization technique essentially based on the interaction between electromagnetic radiation and matter. This radiation depending on its wavelength can be absorbed, emitted or diffused by the material.
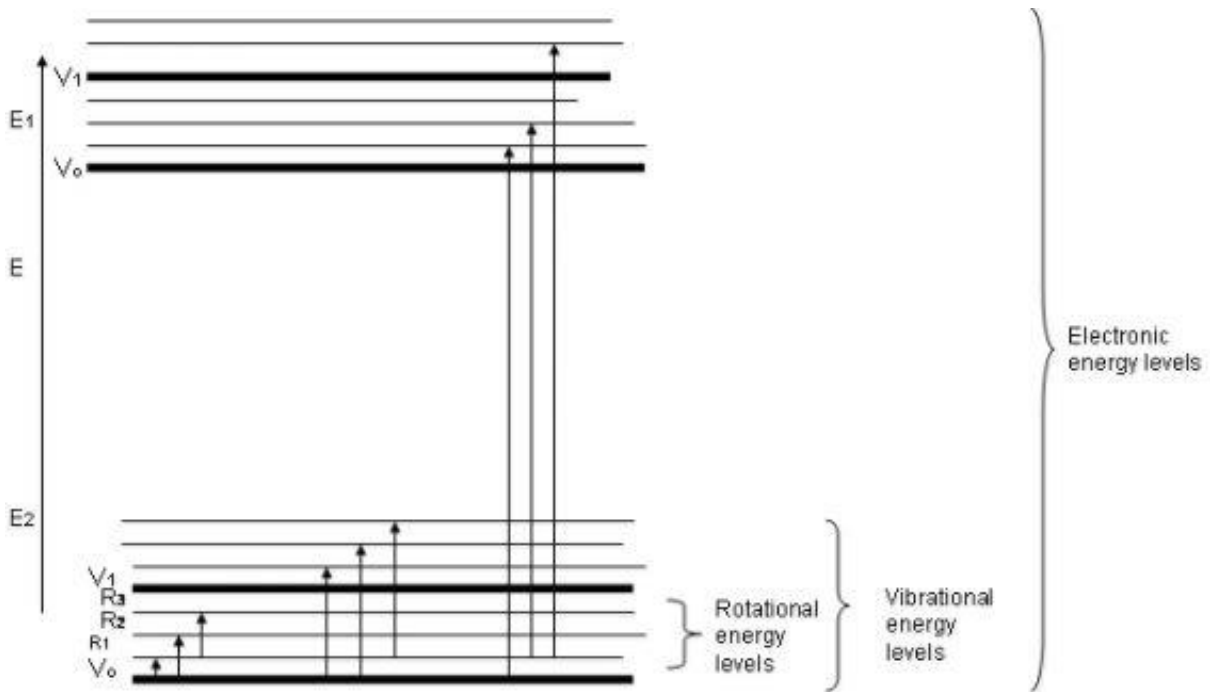
Fig. 4.3 Different types of transition

Generally, once the electromagnetic radiation in contact with the material, there will be energy transfer. Depending on the type of radiation (ultraviolet, visible or infrared) (**Fig. 4.3**), the internal structure of the material will be disturbed and there will be a transition from one energy level to another that can be:

- Rotational transition
- Vibrational transition
- Electronic transition

Since energy levels are quantified, the difference in energy between two consecutive levels must be $\Delta E = h\nu$. From **Fig. 4.3** the following relation can be written:

$E_{electronic} > E_{vibrational} > E_{rotational}$

4.4.1 Fourier Transform Infra-Red (FTIR) spectroscopy

FTIR spectroscopy being a useful technique was employed to study interactions between infrared and the matter. Its goal is the vibrational study of molecules in the matter. This technique makes it possible to determine the different functional groups and residues present in a sample. It is well known that IR region is from (0.7-1) to (200-350) μm which can be delimited into three ranges:

- Near-infrared between 13000-4000 cm^{-1}
- Mid-infrared between 4000-400 cm^{-1}
- Far-infrared between 400-10 cm^{-1}

Generally, the mid-infrared is used in FTIR spectroscopy and the wavenumber of a radiation is used instead of its wavelength or its frequency. The wavenumber (σ) refers to the number of oscillations or vibrations per unit of length and is defined by:

$$\sigma = \frac{1}{\lambda}$$
(4.2)

Where λ is the wavelength in cm and σ in cm^{-1}.

Indeed, for a covalent bond A-B modelled by two balls of masses m_A and m_B connected by a spring with constant stiffness K. The frequency of vibration can be expressed by:

$$\nu = \frac{1}{2\pi} \sqrt{\frac{K}{\mu}}$$
(4.3)

Where $\mu = \frac{m_A * m_B}{m_A + m_B}$ is the reduced mass of the system.

FTIR spectroscopy involves passing infrared radiation through the material that can be absorbed by the molecules it contains. In order for the matter to absorb energy, the vibration frequencies of the molecules must be equal to that of radiation. In general, when light falls on the sample, one part is reflected, another is absorbed and another is transmitted. The absorbed light by the specimen correspond to the specific frequencies of energy which refer to the vibrational energy of functional group in the sample. The transmitted light that carries the molecular information of the sample is collected by a detector.
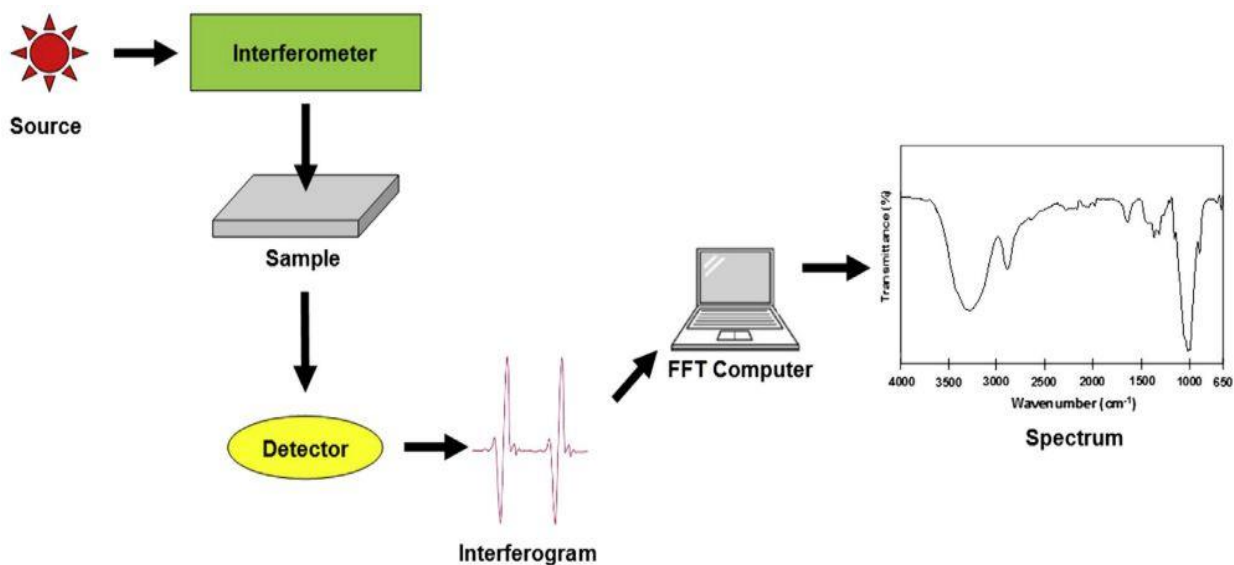
Fig. 4.4 Components in FTIR spectrometer

It is important to note that before sample analysis, a raw signal reference called interferogram is obtained which serve as a reference spectrum (background) by applying the Fourier transform. Then, when analysing the sample, there will be a superposition between the sample spectrum and the background in order to obtain the desirable spectrum, i the desirable spectrum is obtained after the interferogram automatically subtracted the spectrum from the background of the sample spectrum using Fourier transform software. **Fig. 4.4** shows the components in FTIR spectrometer [85].

The ratio of the transmitted intensity (I) and the incident intensity (I_0) defines the transmittance (T) and is given by:

$$T = \frac{I}{I_0} \tag{4.4}$$

If $I = 0$, then all incident radiation is absorbed.

If $I = 100\%$, then all incident radiation is transmitted.

The ability of the material to absorb radiation can also be defined by the absorbance (A). This is directly related to the transmittance by the following relation:

$$A = -logT \tag{4.5}$$

Today, the FTIR spectroscopy gives many advantages including

- Improved signal to noise ratio

- Faster acquisition of IR spectra

- Superior wavenumber accuracy

4.4.2 UV-Vis-NIR spectroscopy

This technique is largely for identifying chemical species in a sample. The particularity of this technique is to study the electronic transitions of atoms. This technique uses a monochromatic radiation which may be in the range of UV, visible or near infrared. When the radiation falls on the sample, it can cause an electronic transition of the molecule. From this spectroscopy, it is possible to evaluate all the electronic transitions and certain properties of the sample can also be determined such as band gap energy which makes it possible to define the nature of the sample namely insulator, semiconductor or conductor. Generally, when the light (energy) falls on the sample, it is absorbed. The absorbed energy favours the transition of the electrons from the ground state (on one of the three molecular orbitals n, σ or π) to an excited state. Depending on the amount of absorbed energy, the electron can be on σ* or π* orbital (**Fig. 4.5**). As shown in **Fig. 4.5**, only σ- σ*, π- π*, n- π* and n-σ* transitions are possible in UV-Vis spectroscopy.
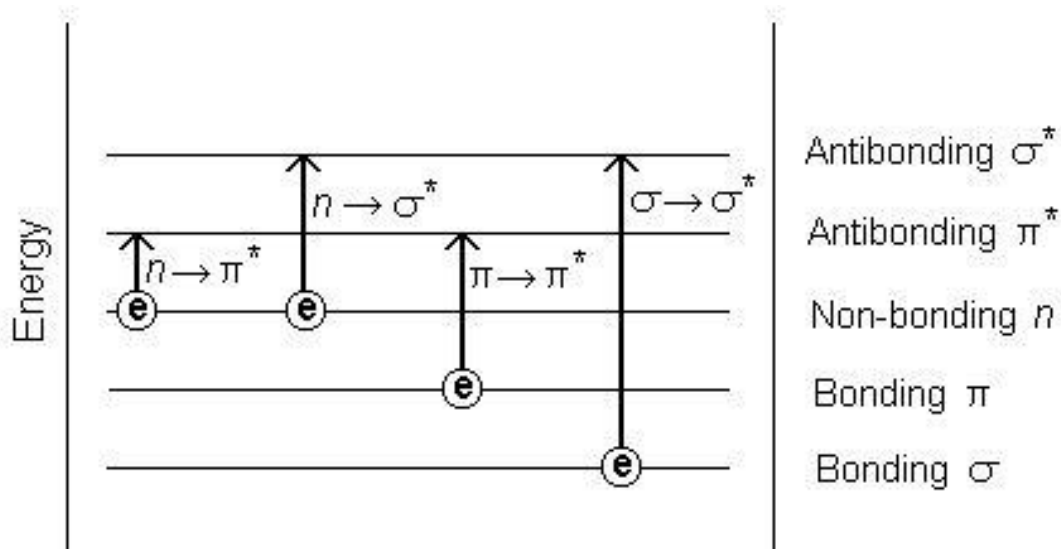
Fig. 4.5 Possible transitions in UV-Vis spectroscopy

4.4.3 Raman spectroscopy

As FTIR spectroscopy, Raman spectroscopy also concerns the vibrational transitions of atoms. It is complementary to FTIR spectroscopy because it is more interested in the diffusion of light by the material than its absorbance. After the irradiation of the material by a monochromatic radiation (Laser) taken in the region of UV, visible or infrared, the radiation is almost all transmitted (about 99%) and a thin part is diffused (1%) (change of direction propagation of photons randomly).

In the diffusion of light by matter, we distinguish two main types:

- Elastic diffusion. In this case, the frequency of scattered radiation is equal to that of incident radiation (same energy): it is Rayleigh scattering.

$$\Delta E = h\nu - h\nu' = h\Delta\nu = 0 \tag{4.6}$$

- Inelastic diffusion. The scattered radiation and incident radiation have different frequency: it is Raman scattering.

$$\Delta E = h\nu - h\nu' = h\Delta\nu \neq 0 \tag{4.7}$$

Where ν and ν' are frequencies of incident and scattered photons respectively.

Raman scattering highlights two scenarios:

- When $\nu' < \nu$ ($\nu' = \nu_0 - \nu_m$). The molecule initially in its ground state moves to a virtual vibrational state after irradiation of the sample. After a brief moment in this state, the molecule will emit a photon whose energy is lower than that of the incident photon. The molecule thus finds itself in a state of excited vibration: it is the Stokes Raman scattering (**Fig. 4.6**).
- When $\nu' > \nu$ ($\nu' = \nu_0 + \nu_m$). Here the molecule is initially in an excited state. When the electromagnetic radiation falls on it, it migrates to a virtual vibrational state and then emits a photon whose energy is higher than that of the incident photon. The molecule is then in a state inferior to the initial state: it is the anti-Stokes Raman scattering (**Fig. 4.6**). This case is very rare.
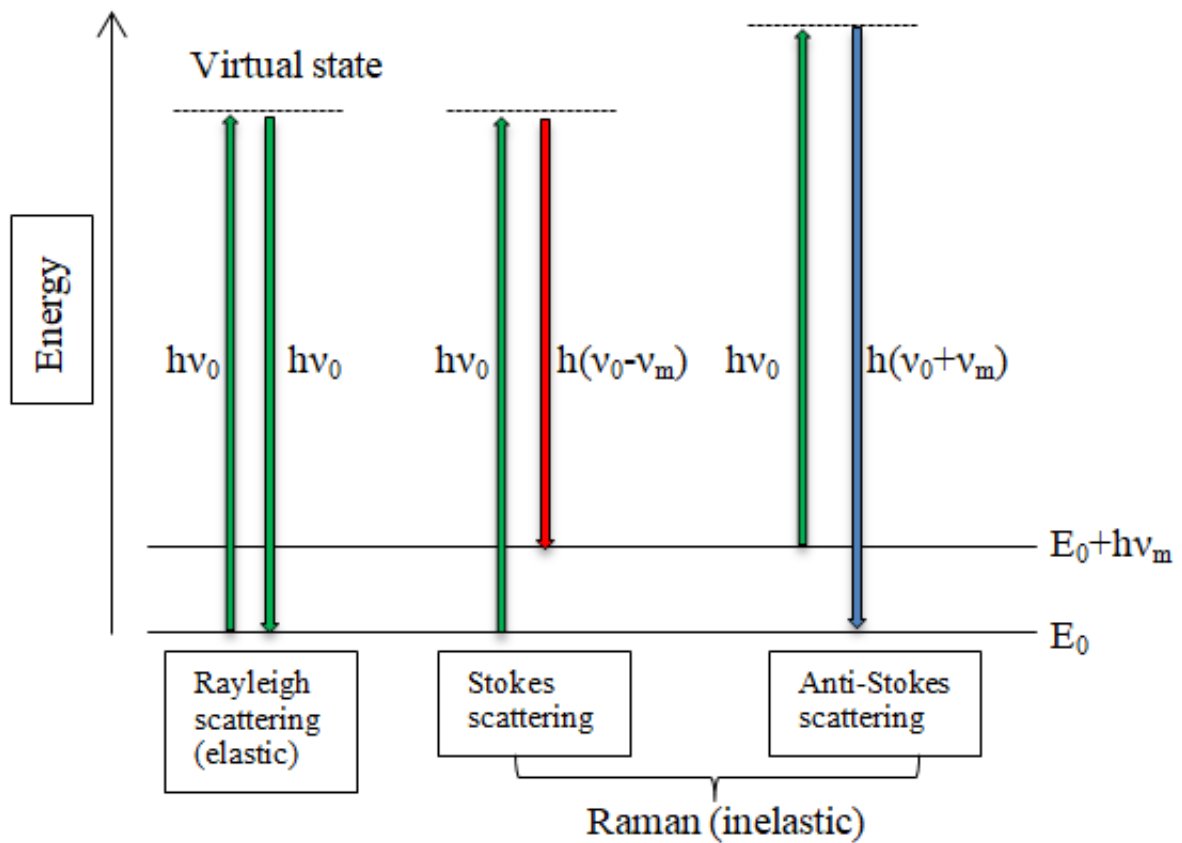
Fig. 4.6 Jablonski diagram of quantum energy transitions for Rayleigh and Raman scattering

4.5 Vibrating sample magnetometer (VSM)

The magnetic properties of the material can be determined using a VSM. This technique was discovered in 1955 by Simon Forner [86]. It is based on Maxwell's equation which explains that a change in magnetic field will produce an electric current. From this technique, magnetic parameters including coercivity (H_c), remanence (M_r), saturation magnetization (M_s) and squareness ratio (M_r/M_s) can be estimated.

To analyze the sample, it is placed in a uniform magnetic field which enables the alignment of the magnetic moments present in the sample along its direction, thereby causing a parasitic magnetic field due to magnetic dipole moments which in time varying that can be detected by a set of pick-up coils. The induced current generated is amplified using a trans-impedance and lock-in amplifier.

Vibrating sample magnetometer (Micro sense E29 VSM) was employed in this work to investigate the magnetic properties of prepared samples..

4.6 Vector network analyser (VNA)

VNA is an instrument aimed to determine the network parameters of electrical network. It uses the principle of measurement of transmitted and reflected waves when a signal passes through a device under test (DUT). From the VNA instrument it is possible to obtain the S-parameters which represent the distribution parameters of the cell (DUT), in module and in phase, in a broad band of frequencies. In fact, the S-parameters indicate the electromagnetic energy distribution and link the incoming and outgoing waves. To understand how a VNA instrument functions, let's consider the case of a device with two ports of access (**Fig. 4.7**). The second order distribution matrix [S] is defined by:

$$[S] = \begin{bmatrix} S_{11} & S_{12} \\ S_{21} & S_{22} \end{bmatrix}$$

Where S_{11} and S_{22} are the coefficients of reflection at ports 1 and 2 respectively, S_{12} and S_{21} are the coefficients of transmission from the second to the first access ports and from the first to the second access port respectively. The following relations represent the expressions of S_{11}, S_{22}, S_{12} and S_{21} coefficients.

$$S_{11} = \frac{b_1}{a_1}\bigg|_{a_2=0} \tag{4.8}$$

$$S_{12} = \frac{b_1}{a_2}\bigg|_{a_1=0} \tag{4.9}$$

$$S_{21} = \frac{b_2}{a_1}\bigg|_{a_2=0} \tag{4.10}$$

$$S_{22} = \frac{b_2}{a_2}\bigg|_{a_1=0} \tag{4.11}$$

With a_1 and a_2 are incident powers, b_1 and b_2 are transmitted powers at ports 1 and 2 respectively as shown in **Fig. 4.7**.
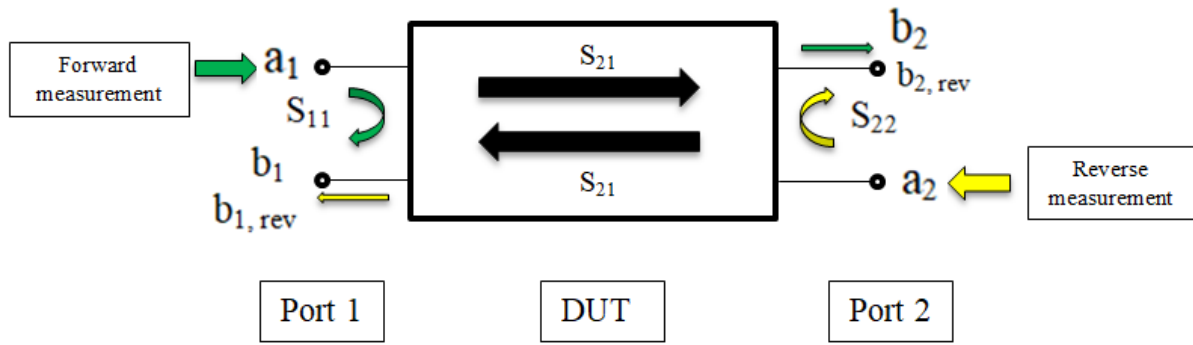
Fig. 4.7 Two-port device under test (DUT) with S-parameters

5.1 Effect of temperature on the magnetic and dielectric properties of nano-sized M-type barium hexagonal ferrites

5.1.1   XRD analysis

The powder XRD patterns of sintered $Ba_{1-x}Al_xFe_{12-y}Mn_yO_{19}$ ($x= 0.6$ and $y= 0.3$) sample at 750, 850, 950 and $1050^{\circ}C$ for 5h are shown in **Fig. 5.1**. The analysis of these patterns shows that all the calcined samples are in the crystalline phase.
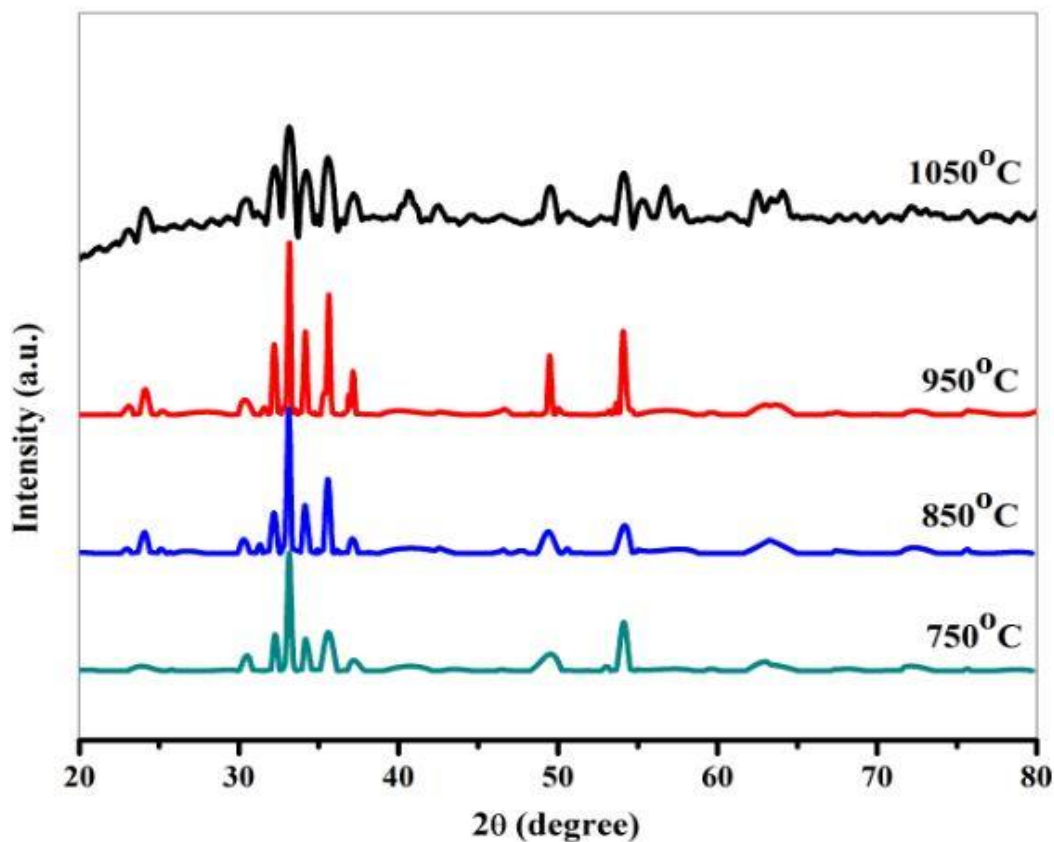
Fig. 5.1 XRD patterns for $Ba_{1-x}Al_xFe_{12-y}Mn_yO_{19}$ ($x= 0.6$ and $y= 0.3$) at different temperatures for 5h.

The presence of hkl peaks (008), (107), (114), (108), (205), (110), (217) shows the formation of M-type hexaferrite. These peaks are in agreement with literature [87, 88]. The highest peak at $1050^{\circ}C$ is (104). This peak doesn't characterize hexaferrite but the presence of hematite (α-

Fe$_2$O$_3$). This can indicate that the sample has to heat at a temperature above 1050°C to obtain monophase hexaferrite.

The variation of lattice constants (*a* and *c*) according temperature is shown in **Fig. 5.2**.
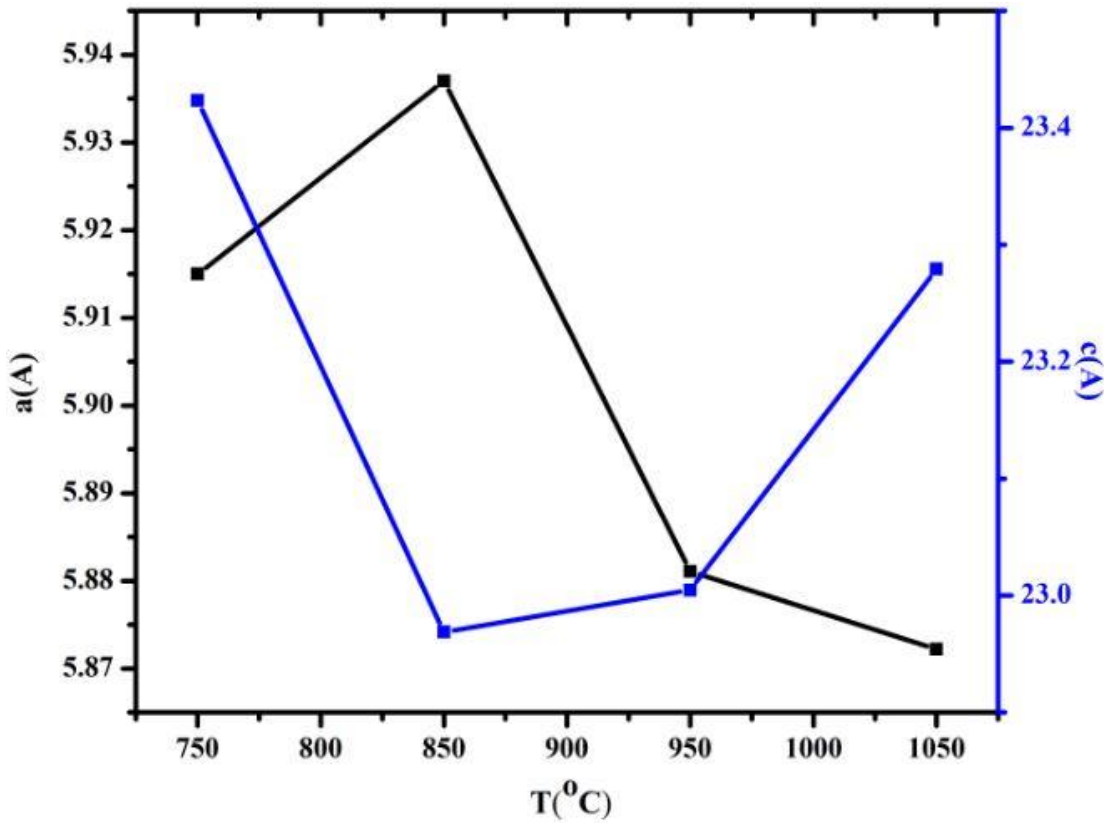
Fig. 5.2 Variation of lattice constants (a and c) with temperature

The lattice constants shown in **Table 5.1** were calculated using the following relation [89]:

$$\frac{1}{d_{hkl}^2} = \frac{4}{3}\left[\frac{h^2+hk+k^2}{a^2}\right] + \frac{l^2}{c^2}$$ (5.1)

The values of both parameters change with increase in temperature (**Fig. 5.2**).This can be due to micro structural defects and interaction between cations. The cell volume has been obtained using the following relation:

$$V_{cell=a^2c.sin120°}$$ (5.2)

Where a, and c are lattice parameters. The cell volume change with heat temperature (**Table 5.1**).

Table 5.1 Variation of diffraction angle (2theta), d spacing (d), full width at half maxima (β), lattice parameters (a and c) and volume of cell with calcination temperature for prepared samples

T(°C)	2 theta(°)	d(Å)	β(°)	a(Å)	c(Å)	D(nm)	V_{Cell} (Å³)
1050	34.22	2.6182	0.227	5.8722	23.2792	40.7	695.2
950	23.18	3.8341	0.233	5.8811	23.0046	38.7	689.1
850	32.34	2.7660	0.679	5.937	22.9688	13.5	701.1
750	35.82	2.5049	1.116	5.915	23.4234	8.3	709.7

This is due to variation of lattice parameters. The crystallite size (D) is calculated from the Sherrer's formula:

$$D = \frac{K\lambda}{\beta cos\theta}$$

(5.3)

Where K is the Sherrer's constant, λ the wavelength of the X-rays employed (1.5046 Å), β the full width at half maxima and θ is the Bragg angle. The values of crystallite size (D) increases with increase in temperature (**Table 5.1**). This can be explained by the formation of the hexaferrite agglomerations.

5.1.2 FTIR analysis

FTIR study has been done to confirm the formation of ferrites and to get information about the presence of functional groups which are remains of chemicals used in the synthesis process. **Fig. 5.3** shows different spectra of samples calcined at 750, 850, 950 and 1050°C. The peaks observed near 2361 cm⁻¹ for temperatures less than 1050°C can be attributed to the presence of CO_2 absorbed by the sample from the atmosphere.

This band disappears at 1050°C. This can indicate the contribution of CO_2^- ions in the reaction [90]. The presence of two peaks with high intensity in the range 400-600 cm⁻¹ characterizes the formation of hexaferrite. These peaks are due to stretching vibration of metal- oxygen bond [87]. The bands between 448-455 cm⁻¹ and 541-586 cm⁻¹ characterize the vibration of octahedral and tetrahedral sites [89] respectively and this indicate the occupation of sites by Al^{3+} and Mn^{2+} ions.
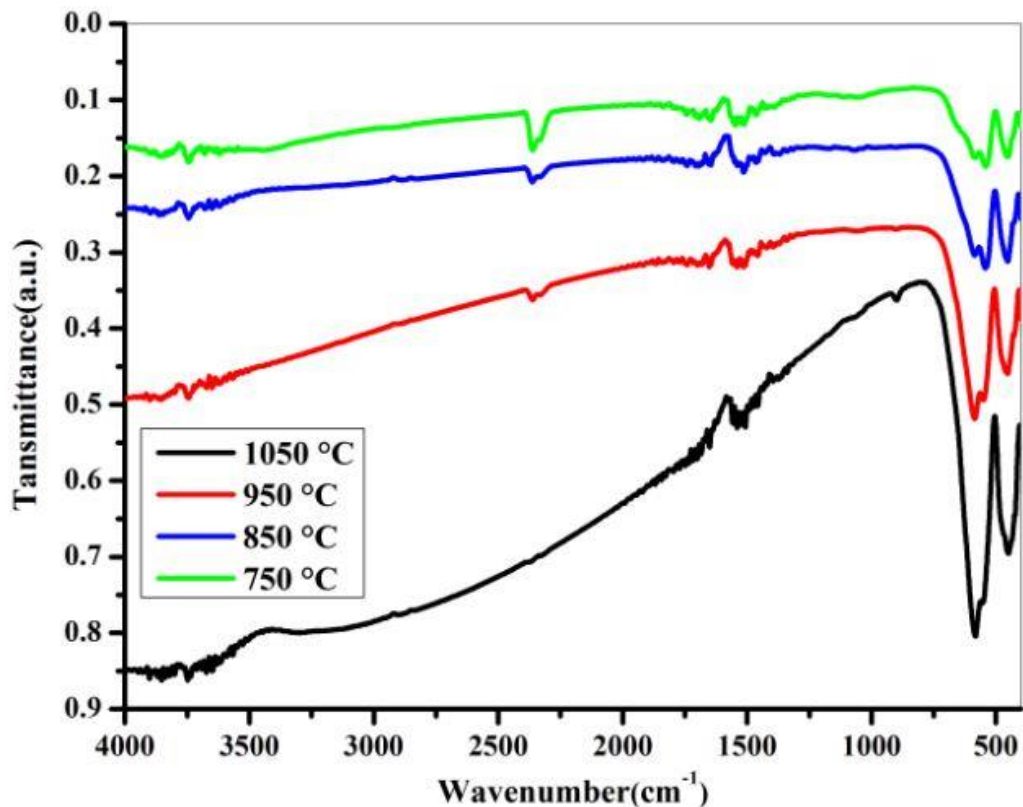
Fig. 5.3 FTIR spectra for $Ba_{1-x}Al_xFe_{12-y}Mn_yO_{19}$ (x= 0.6and y= 0.3) at different temperatures

5.1.3 FESEM analysis

Fig. 5.4 shows FESEM images of samples $Ba_{1-x}Al_xFe_{12-y}Mn_yO_{19}$ (x= 0.6and y= 0.3) calcined at 950°C and 1050°C respectively. It can be observed a homogeneous distribution of particles and non-uniformity in particle size and shape. However, some particles show a hexagonal like structure which represents the hexaferrite structure. The particle size has been determined from normal distribution of particles. The average size of particle was found to be 167 nm and 47 nm for 1050°C and 950°C respectively. It can be noticed that the particle size increases with increasing in the calcination temperature keeping the shape. Similar observation was made by A. Ataie et al [91].
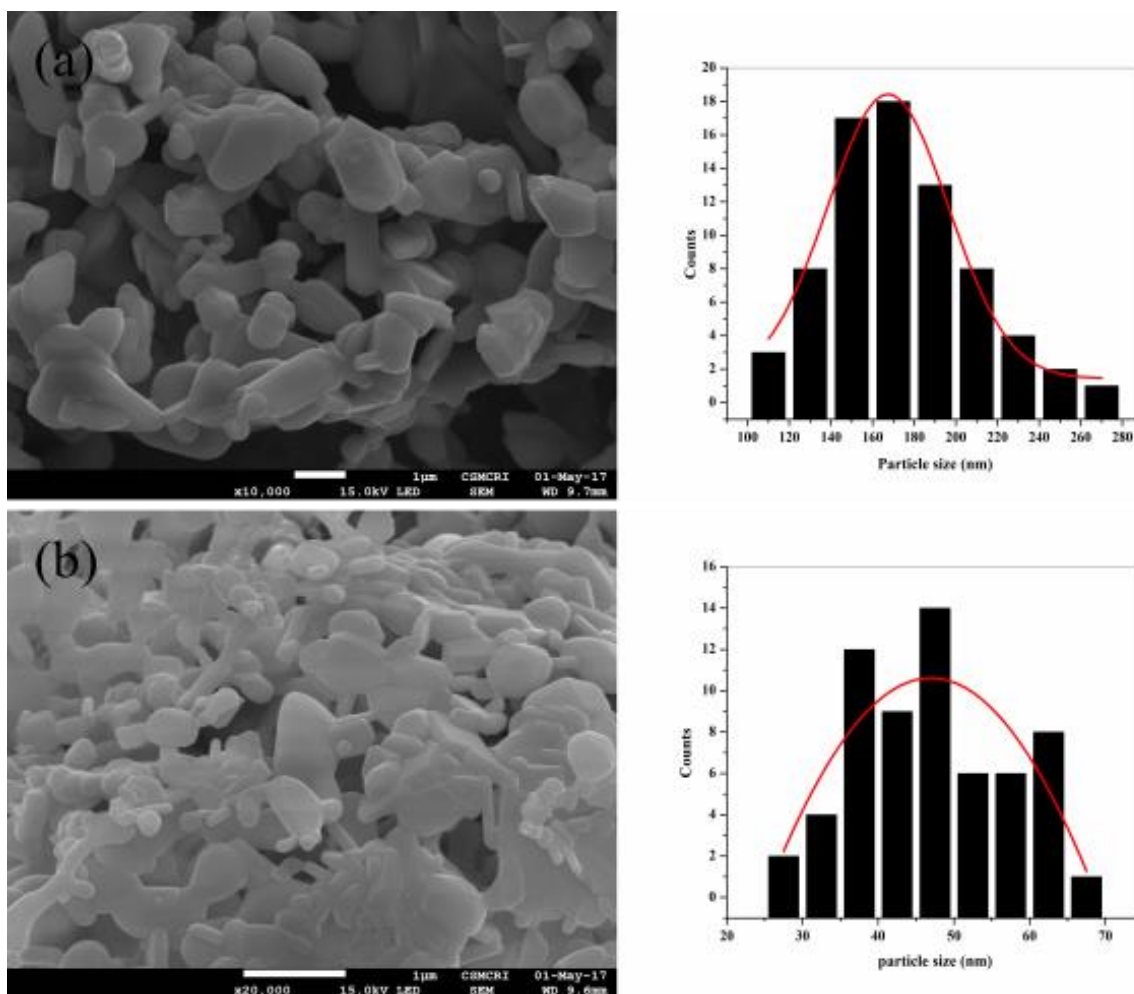
Fig. 5.4 FESEM micrograph of $Ba_{1-x}Al_xFe_{12-y}Mn_yO_{19}$ (x= 0.6and y= 0.3) samples calcined at (a) 1050°C, (b) 950°C

5.1.4 Thermogravimetric analysis

The influence of temperature on samples was studied from Thermal gravimetric analysis/differential Thermogravimetric analysis/derivative Thermogravimetric (TGA/DTA/DTG). **Fig. 5.5** shows TGA/DTA/DTG curves of M-type hexaferrite $Ba_{1-x}Al_xFe_{12-y}Mn_yO_{19}$ (x= 0.6 and y= 0.3) powder. From this figure, the weight decrease between 0 and 650°C. This is due to decomposition of remaining organic matter, decomposition of precursor and conversion of hematite into hexaferrite phase. This can be explained by the oxidation- reduction reaction between the metal nitrates and citric acid. After 650°C, weight loss becomes approximately constant which indicates the formation of M-type hexaferrite. In DTA curve, the first variation in peak is observed near about 100°C associated with endothermic peak on account of loss of water. The prominent effect shown by TGA/DTA is

at 400°C. DTG (derivative Thermogravimetric) gives slight peak at 500°C because of recrystallization of sample.
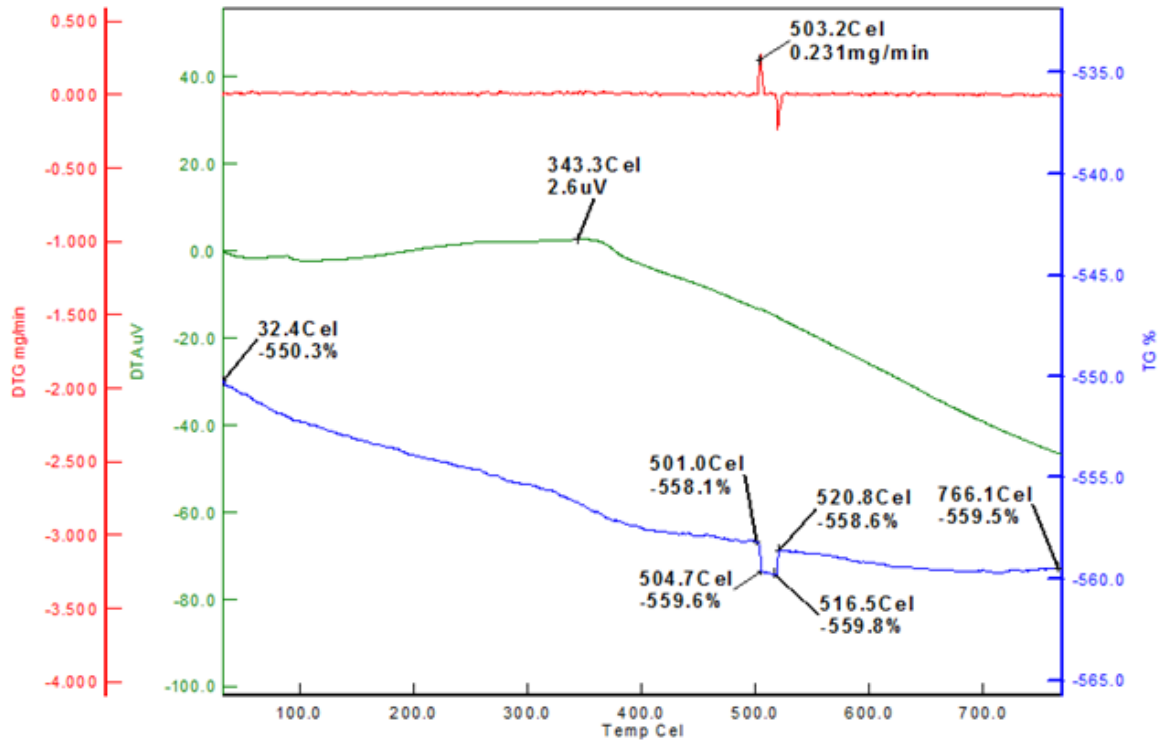
Fig. 5.5 TGA/DTA/ DTG traces for hexaferrite powders

5.1.5 Magnetic analysis

Fig. 5.6 shows hysteresis loops of Ba$_{1-x}$Al$_x$Fe$_{12-y}$Mn$_y$O$_{19}$ (*x*= 0.6and *y*= 0.3) sintered at 750, 850, 950 and 1050°C. The magnetic parameters saturation magnetization (M$_s$), coercivity (H$_c$), remnant magnetization (M$_r$), magnetic moment (η$_B$) and anisotropic constant (K) have been determined by hysteresis loop (**Table 5.2**). **Fig. 5.6** shows that saturation magnetization and remnant magnetization increase with the temperature. In the literature, the intrinsic value of coercivity of pure hexagonal ferrite is H$_c$=6700Oe calculated using the stoner and wohlfarth model of single-domain particles [19]. **Fig. 5.7** shows the highest value for coercivity (7780Oe) was found in the sample calcined at 850°C and saturation magnetization shows a continuous increase with increase in temperature. These results are in agreement with the literature [89]. The highest value for coercivity is above to the coercivity value for pure M-type barium hexaferrite (6700Oe). This is due to doping by Al^{3+} and Mn^{2+} ions. In this present investigation, coercivity range is 6341-7780Oe which is too high (above 1200Oe

or 95.6 KA.m^{-1}). So this kind of materials cannot be used as longitudinal magnetic recording media but they can be used as high density perpendicular magnetic recording media [92]. The wide width of the loop (high coercivity and high remnant magnetization) can indicate that $Ba_{1-x}Al_xFe_{12-y}Mn_yO_{19}$ (x=0.6 and y=0.3) could be suitable for applications requiring hard magnetic materials.
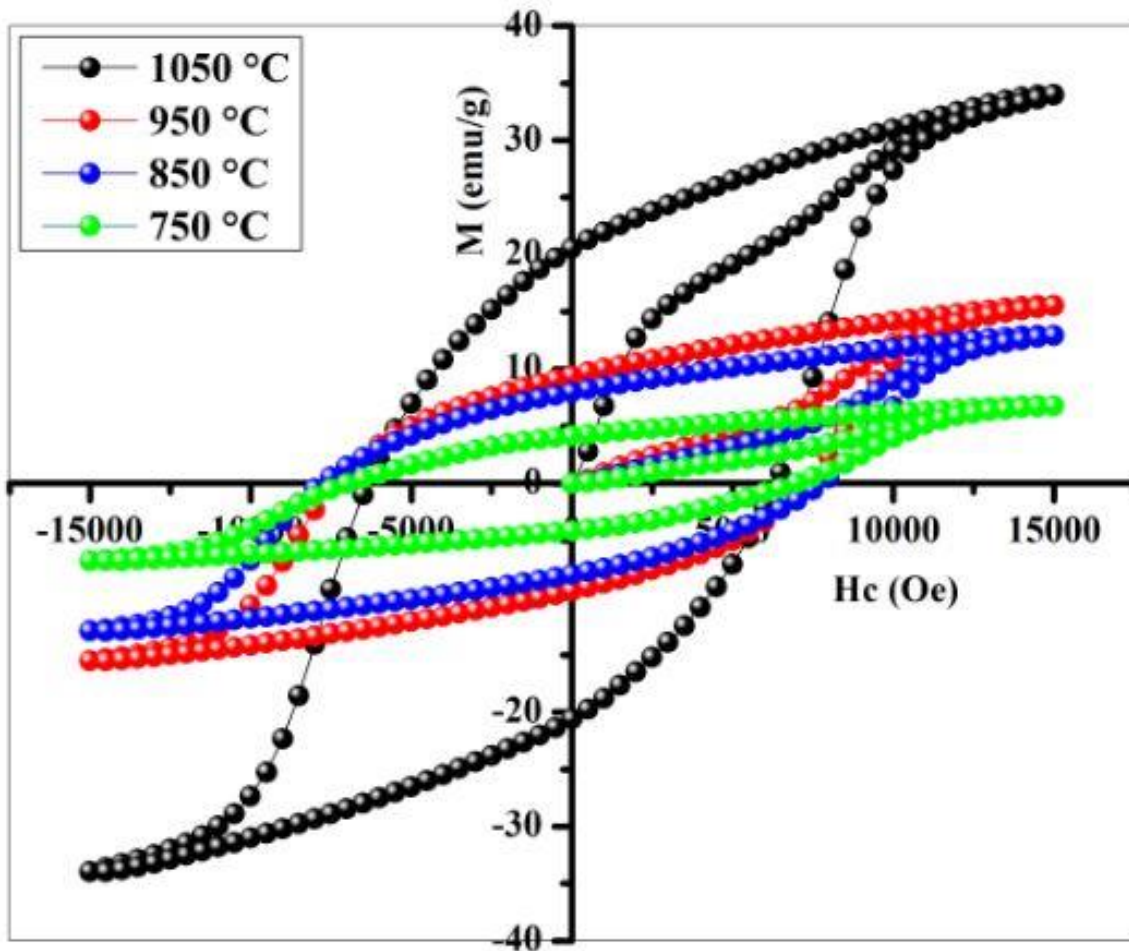
Fig. 5.6 Hysteresis loop for $Ba_{1-x}Al_xFe_{12-y}Mn_yO_{19}$ (x= 0.6 and y= 0.3) at different temperatures

The squareness ratio (Mr/Ms) has been calculated from magnetic parameters determined from hysteresis loop (**Table 5.2**). If this parameter is equal or above to 0.5, it indicates that the material is in single magnetic domain and if it is less than 0.5, it can indicate the formation of multi-domain structures [93].

Table 5.2 Effect of temperature on magnetic properties of $Ba_{1-x}Al_xFe_{12-y}Mn_yO_{19}$ ($x=0.6$, $y=0.3$)

$T(°C)$	M_s (emu/g)	M_r (emu/g)	H_c (Oe)	M_r/M_s ratio	$\eta_B(\mu_B)$	$K(HA^2/Kg)$
1050	33.97	20.55	6341.37	0.6049	6.3563	10.77 84
950	15.55	9.41	7367.81	0.6051	2.9096	5.72848
850	12.92	7.96	7779.94	0.6160	2.4175	5.02585
750	6.78	4.14	6986.78	0.6106	1.2686	2.36852
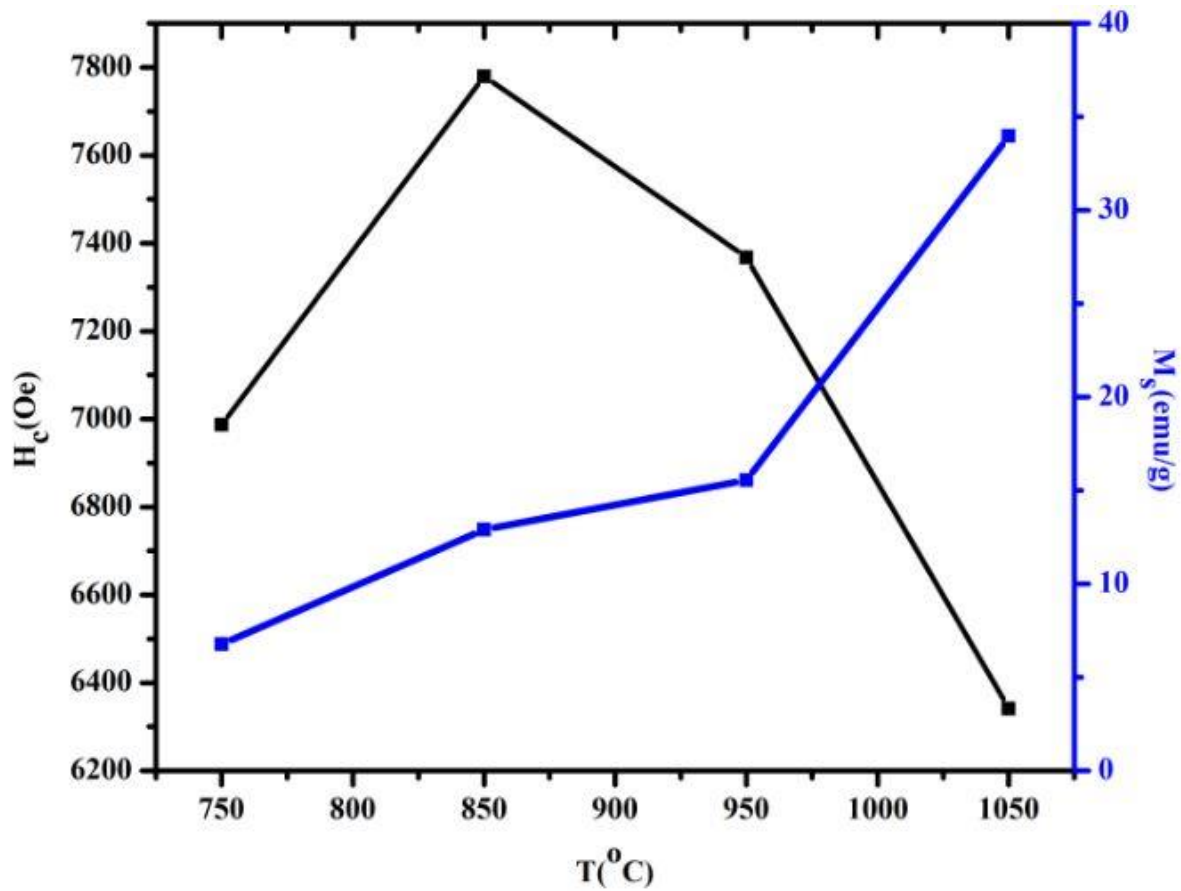
Fig. 5.7 Variation of saturation magnetization and coercivity with temperature for $Ba_{1-x}Al_xFe_{12-y}Mn_yO_{19}$ ($x=0.6$ and $y=0.3$)

In this work, the range of squareness ratio is 0.6 - 0.61(**Table 5.2**) indicating that the prepared hexaferrite is in the single magnetic domain. The following relation has been used to calculate the anisotropic constant (K) [89]:

$$H_c = \frac{2K}{\mu_0 M_s} \tag{5.4}$$

Where μ_0 is permeability in vacuum ($4\pi\times10^{-7}$H/m), Ms is saturation magnetization and Hc is coercivity.

The magnetic moment (η_B) has been calculated using the following equation[3]:

$$\eta_B = \frac{MM_S}{5585} \tag{5.5}$$

Where M represents molecular weight of sample and Ms is saturation magnetization. Magnetic moment (η_B) is proportional to Ms; then magnetic moment increases with saturation magnetization (**Table 5.2**).

5.1.6 Impedance analysis

Ambient impedance analysis was done using impedance analyzer in the range frequency of 100 Hz-120 MHz. The hexaferrite pellets were made with 1 cm of diameter and 4 mm of thickness.

Fig. 5.8 respectively shows the evolution of the real and imaginary parts of the impedance (Z' and Z" resp.) at room temperature. We note that Z' and Z" show the same evolution, i.e. say they decrease at low frequencies and become constant from 10MHz
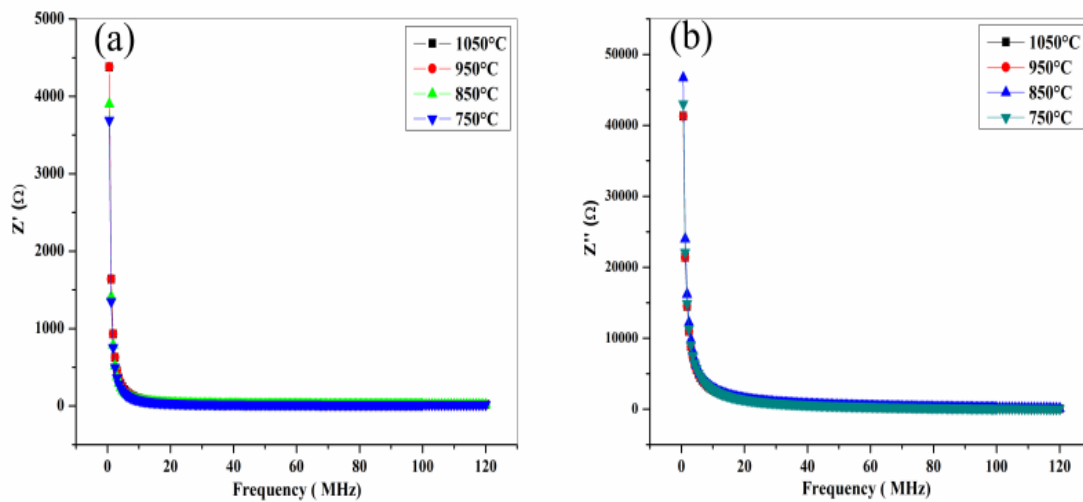
Fig. 5.8 (a) Real part of impedance; (b) Imaginary part of impedance

The evolution of Z' is confirmed by the literature [94]. Moreover, the highest values of Z' and Z" have been observed for the lowest frequencies and these values are independent of the temperature.

61
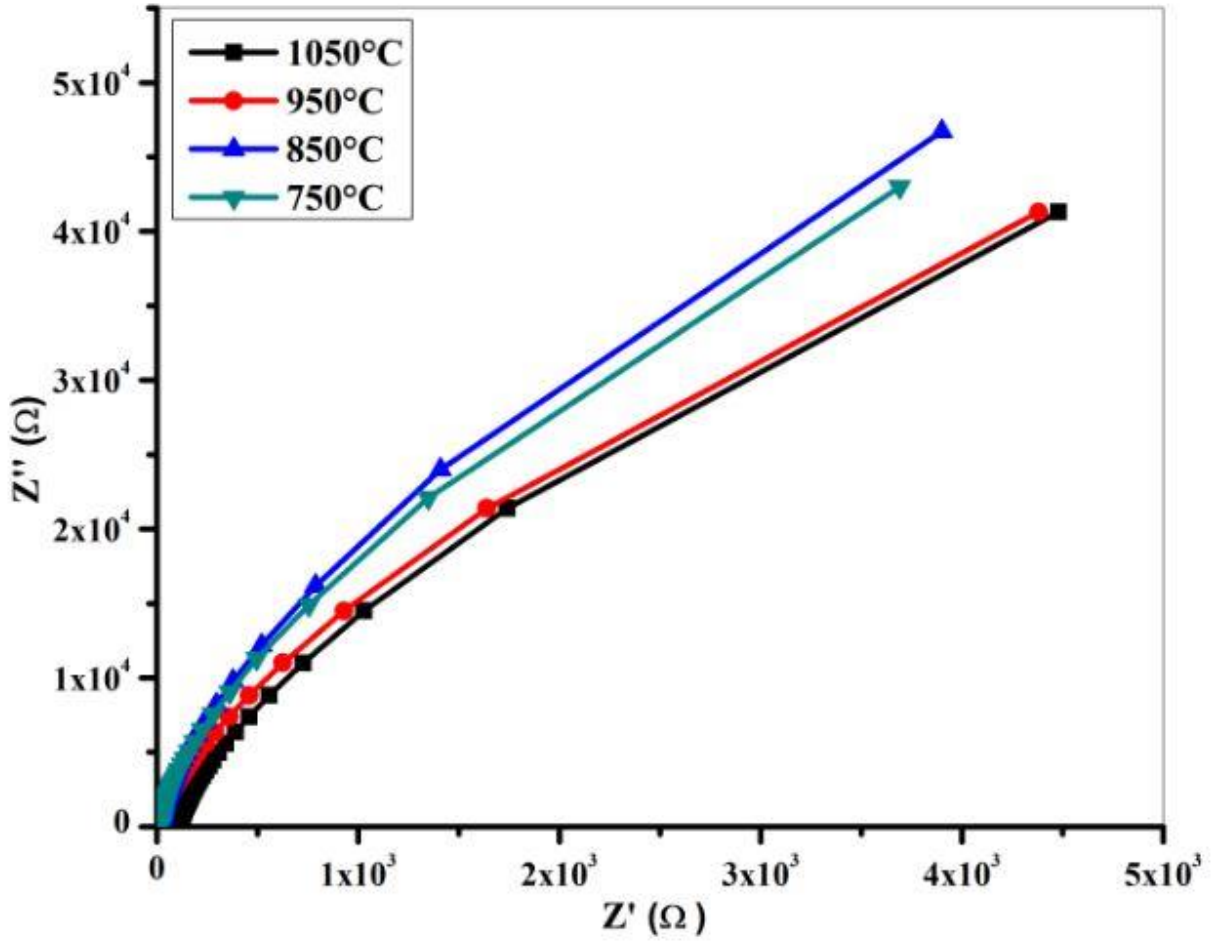
Fig. 5.9 Cole-Cole plots of $Ba_{1-x}Al_xFe_{12-y}Mn_yO_{19}$ ($x= 0.6$ and $y= 0.3$) samples

The following (5.6) and (5.7) equations can be applied to estimate the real and imaginary parts of impedance at room temperature:

$$Z^{'} = |Z|\cos\theta \tag{5.6}$$

$$Z^{''} = |Z|\sin\theta \tag{5.7}$$

Where Z represent impedance and θ is the phase angle. Complex impedance can be defined by the following relation:

$$Z^{*} = Z^{'} - jZ^{''} \tag{5.8}$$

To differentiate the grain and grain boundary contribution to conduction, we made complex impedance plane plot known as cole-cole plot. Generally, Cole-Cole plot is defined by a semi-circle of a curve or a semi-circle arc where the left side of the arc represents the contribution of grain resistance and the right side depicts the total contribution of grain boundary and grain resistance [39, 95]. This corresponds to the high and low frequencies respectively.

However, the intermediate frequencies represent the grain boundary contribution [23]. As compared to the grain contribution, the grain boundary contribution is clearly observed in **Fig. 5.9**. It can be noticed that the high value of grain boundary resistance was obtained at 850°C. The resistivity and dielectric properties depend of the high grain boundary resistance.

5.1.7 Dielectric study

The complex permittivity of ferrites can be defined by:

$$\varepsilon^* = \varepsilon' - j\varepsilon'' \tag{5.9}$$

Where ε' and ε'' are dielectric parameters of material and they represent dielectric constant and dielectric loss respectively. Equations (5.10) and (5.11) give expressions of real and imaginary parts of complex permittivity respectively[96].

$$\varepsilon' = \frac{Z''}{2\pi f C_0 Z^2} \tag{5.10}$$

$$\varepsilon'' = \frac{Z'}{2\pi f C_0 Z^2} \tag{5.11}$$

Where, C_o represents the capacitance of vacuum, Z is the impedance and f is the frequency. Dielectric loss tangent can be evaluated using the following expression:

$$\tan \delta_e = \frac{\varepsilon''}{\varepsilon'} \tag{5.12}$$

Fig. 5.10 and **Fig. 5.11 (a)** show respectively the dielectric constant, dielectric loss and dielectric loss tangent versus frequency of $Ba_{1-x}Al_xFe_{12-y}Mn_yO_{19}$ ($x = 0.6$ and $y = 0.3$) samples calcined at 750, 850, 950 and 1050°C.
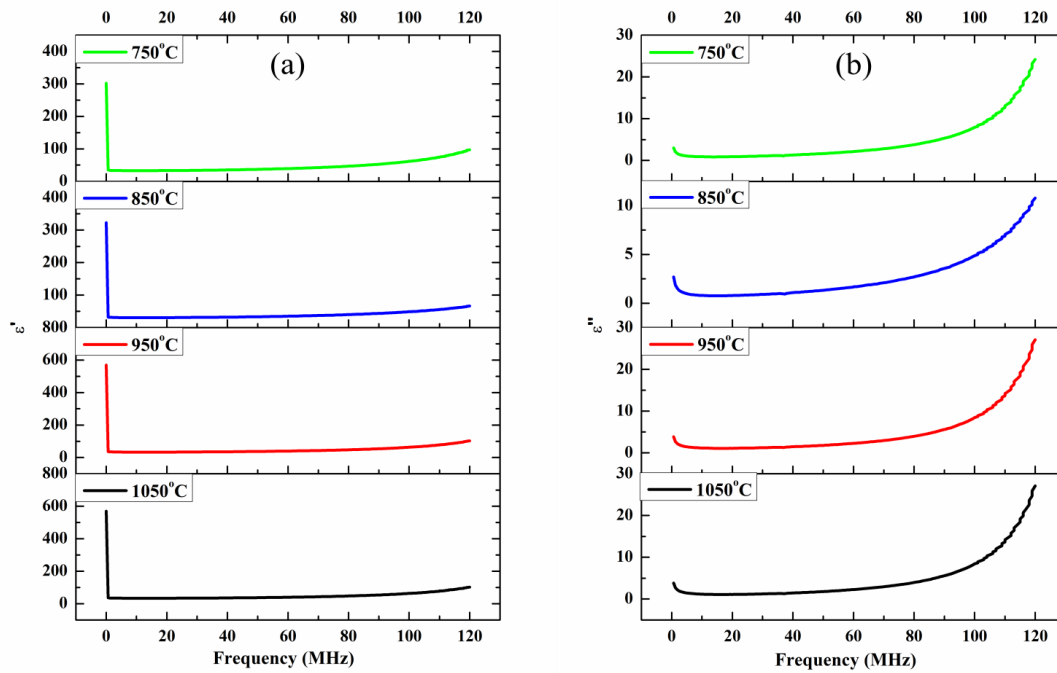
Fig. 5.10 (a) Dielectric constant of sample, (b) Dielectric loss of sample

It can be remarked that the dielectric response observed define the ferrite materials behaviour i.e. the dielectric constant is high at low temperature then decreases when the frequency of applied field increases (**Fig. 5.10(a)**). This decreasing of dielectric parameters can be explained on the basics of the space charge polarization as predicted by Maxwell- Wagner [89][97]. The presence of the space charge polarization is due to the heterogeneity of the structure of samples which can be responsible of the conduction in the sample due to the electron transfer between Fe^{2+} and Fe^{3+} ions [93][95]. In the frequency range [10MHz-120MHz], dielectric parameters of samples become almost unchangeable and there is no dielectric resonance. Highest value of dielectric constant was found to be 575 at 1050℃ at lower frequencies. At low frequency, the dielectric constant depends of the temperature i.e. it increases with the increase in the temperature (**Fig. 5.11(b)**).

5.1.8 AC conductivity analysis

AC conductivity (σ_{AC}) of samples at room temperature can be defined as a function of frequency and of the dielectric loss according the following formula:

$$\sigma_{AC} = 2\pi f \varepsilon'' \varepsilon_0 \tag{5.13}$$
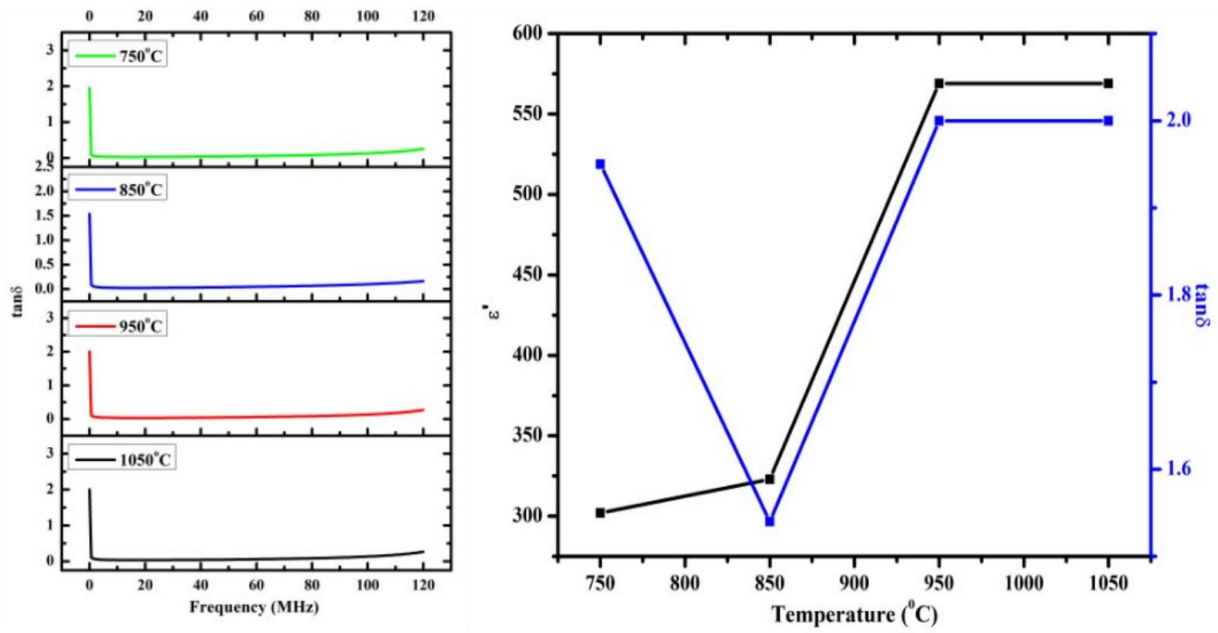
Fig. 5.11 (a) Dielectric loss tangent of sample, (b) Variation of dielectric constant and dielectric loss tangent with temperature
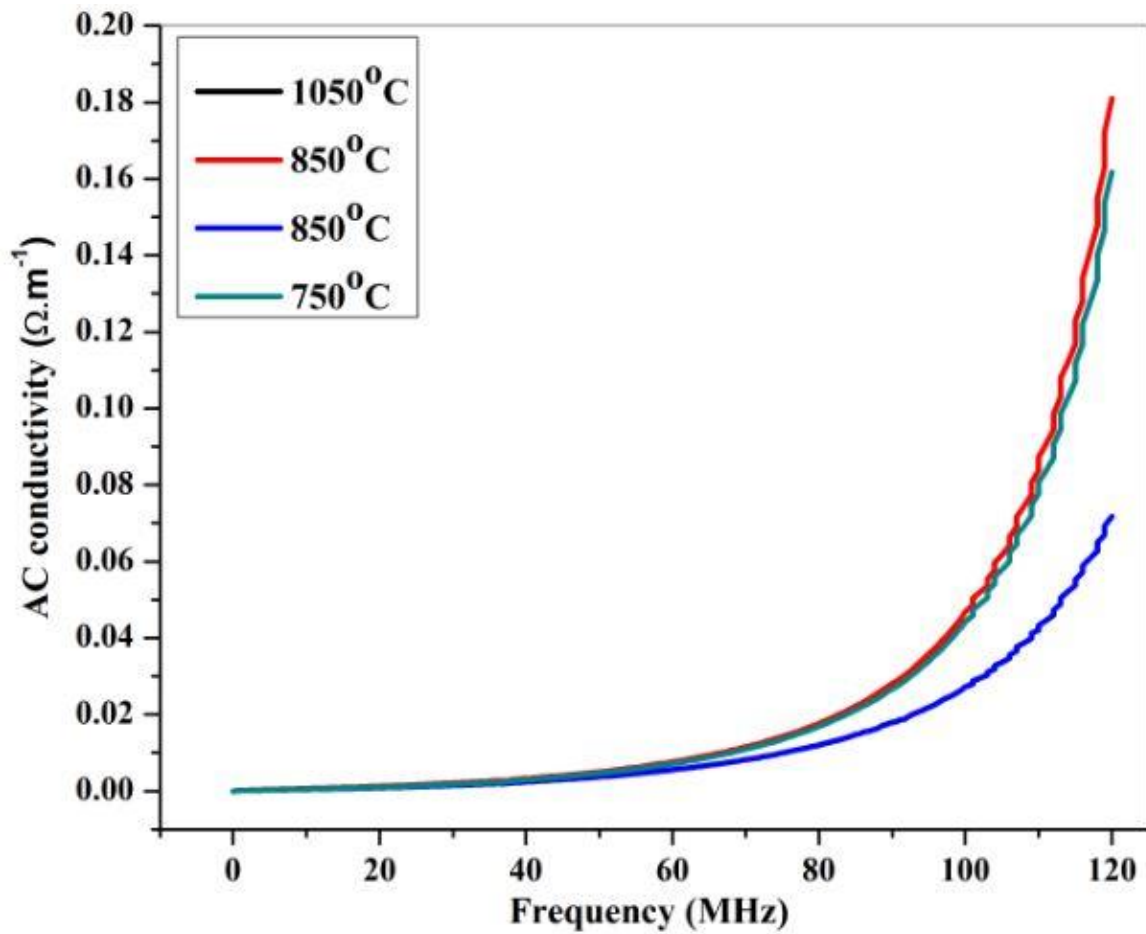
Fig. 5.12 AC conductivity (σ_{AC}) of $Ba_{1-x}Al_xFe_{12-y}Mn_yO_{19}$ ($x= 0.6$ and $y= 0.3$) samples

Where ε_0 is the permittivity of vacuum; Fig. 6 Show the evolution of AC conductivity of $Ba_{1-x}Al_xFe_{12-y}Mn_yO_{19}$ ($x= 0.6$ and $y= 0.3$) samples versus of frequency of applied field. It is observed that the conductivity increases with the increase in the frequency. This increasing is slightly in the range 100 KHz-70MHz and become significant for frequencies above 70MHz. The increase of conductivity can be a direct consequence of electron hopping between Fe^{2+} and Fe^{3+} which result in the displacement of ionic charges caused by applied field. So that makes the material polarized [89]. This increasing of conductivity can also be a consequence of the decrease in dielectric constant of material as showed on **Fig. 5.10**.

5.1.9 Optical analysis

The optical properties of $Ba_{1-x}Al_xFe_{12-y}Mn_yO_{19}$ ($x= 0.6$ and $y= 0.3$) samples were performed using UV-Vis-NIR absorption spectra. It is knew that the absorption region for ultraviolet is (200-400 nm), visible is (400-800 nm) and infrared is (800-1100 nm).
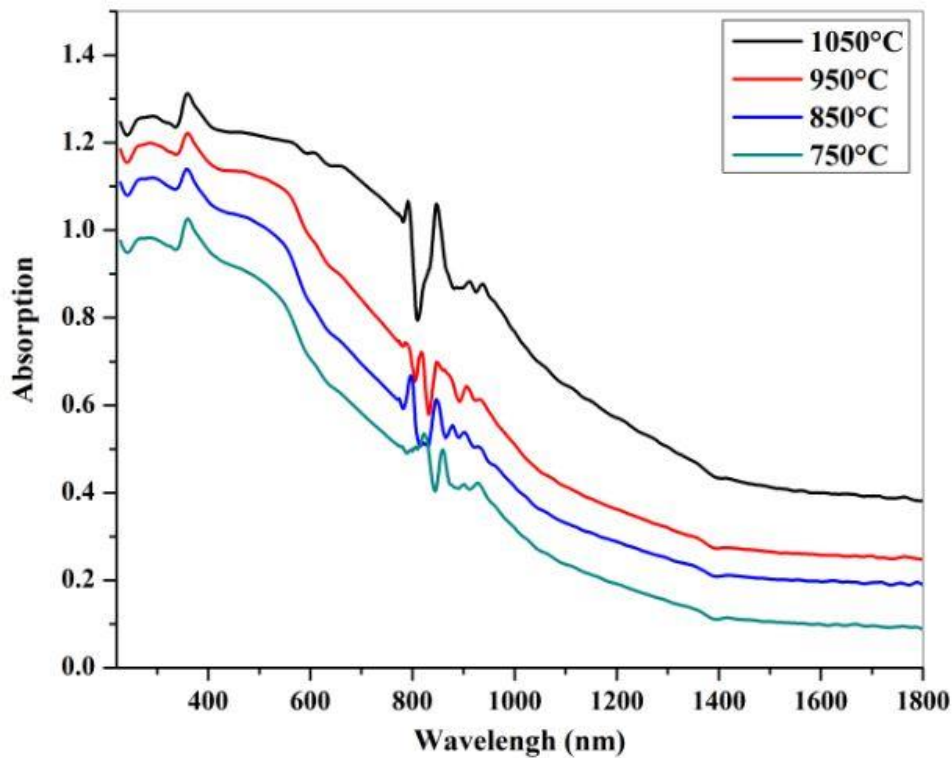
Fig. 5.13 Absorbance Spectra of $Ba_{1-x}Al_xFe_{12-y}Mn_yO_{19}$ ($x= 0.6$ and $y= 0.3$) samples
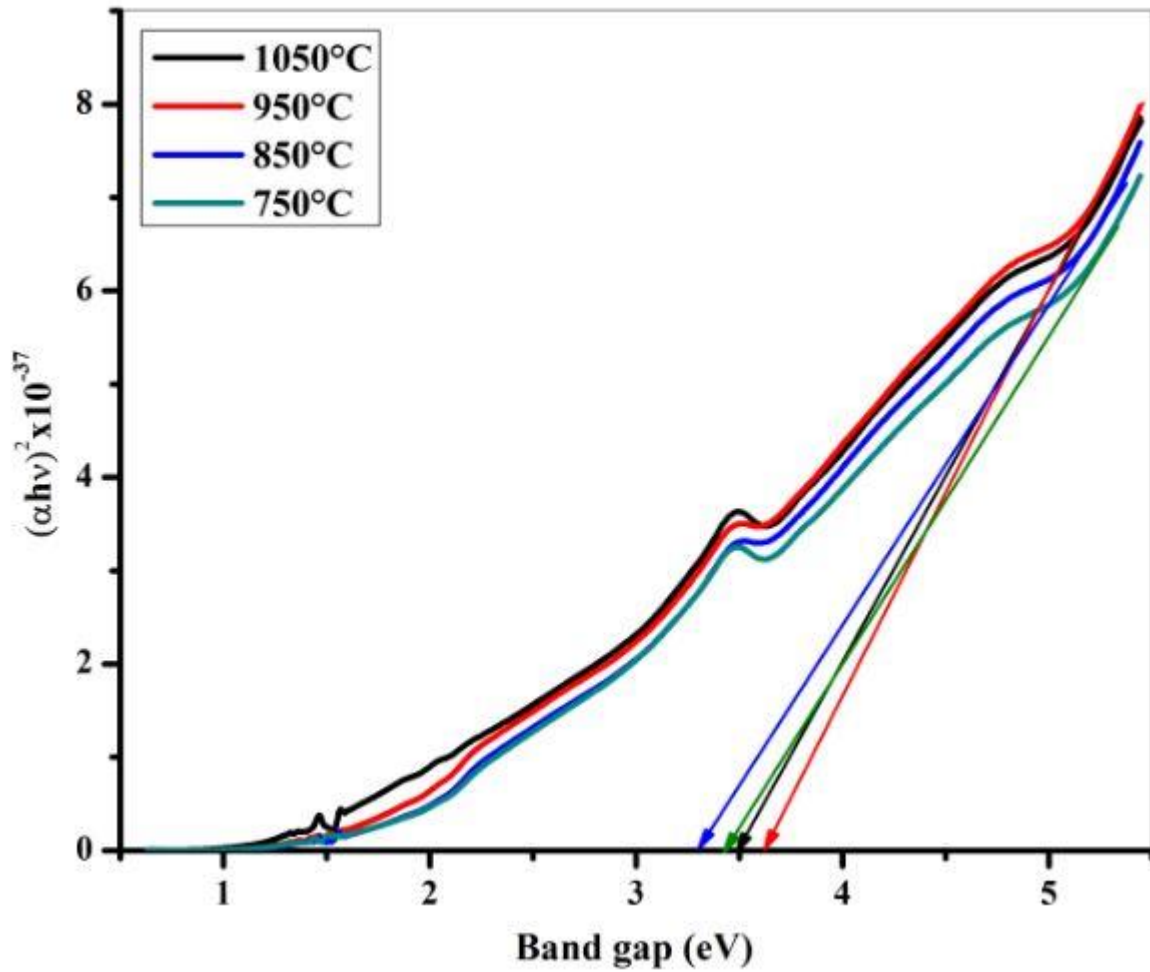
Fig. 5.14 Optical band gap for $Ba_{1-x}Al_xFe_{12-y}Mn_yO_{19}$ (x= 0.6and y= 0.3)

Fig. 5.13 shows the absorbance spectra for prepared samples. This absorption is characterized by the passage of electrons from the valence band to the conduction band. The required energy for this transition is defined by the band gap energy E_g given by [89, 98]:

$$(\alpha h v)^2 = A(h v - E_g)$$

(5.14)

Where v is frequency and A is a constant.

Table 5.3 Influence on temperature on band gap of $Ba_{1-x}Al_xFe_{12-y}Mn_yO_{19}$ ($x= 0.6$ and $y= 0.3$)

Temperature (℃)	750	850	950	1050
Band gap (eV)	3.44	3.31	3.62	3.50
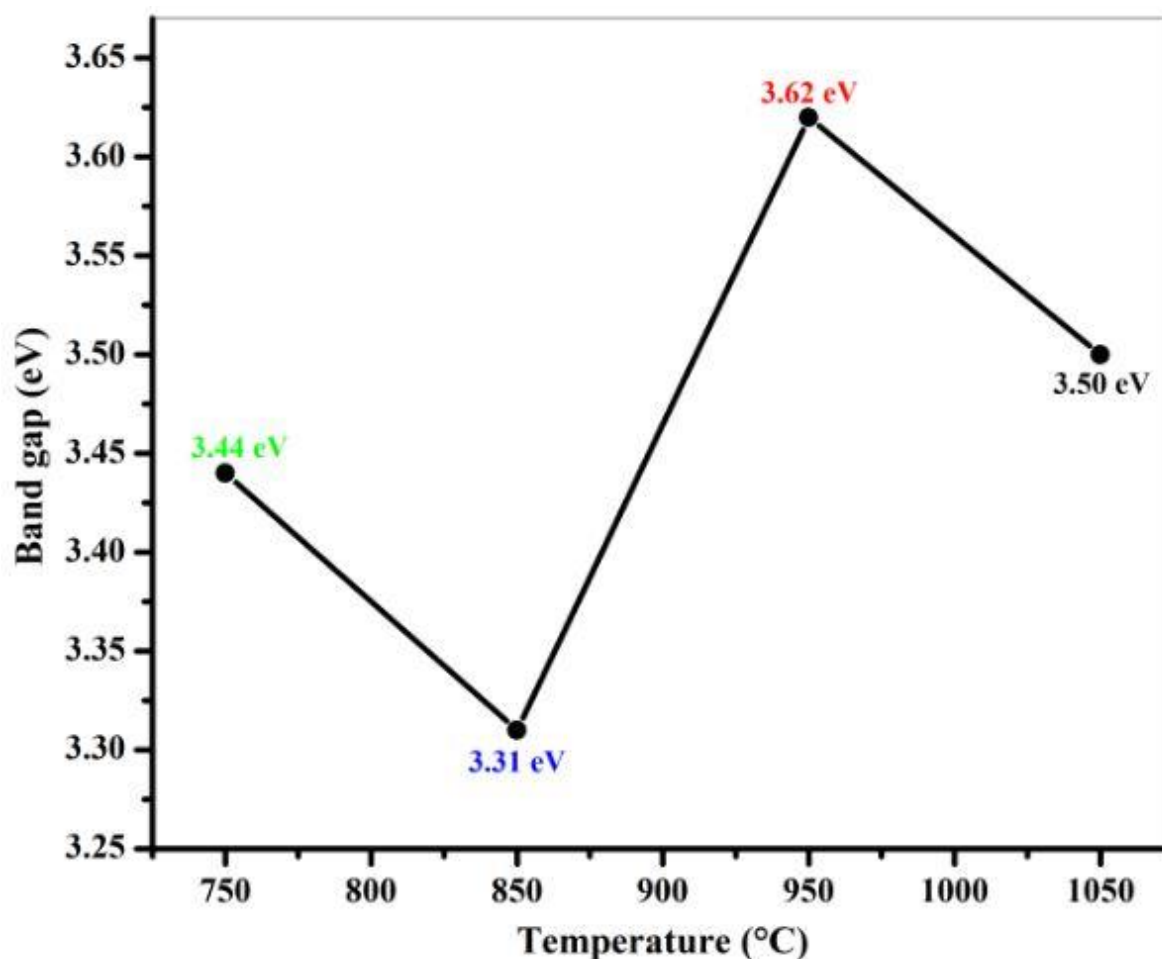
Fig. 5.15 Influence of temperature on the band gap

The band gap was obtained by plotting the graph. **Fig. 5.14** shows the spectra for band gap energy. The band gap values obtained from the graph are contained in **Table 5.3** below and its evolution according temperature is shown on the **Fig. 5.15**. It has been reported that nanomaterials with band gap values of around 3.5 eV are suitable for UV-blue light emitting diodes (LEDs) [17]. Hence the prepared material could be useful in LEDs. From UV-NIR spectra (**Fig. 5.13**), it was concluded that absorption region for the samples is ∼ 200-600 nm [18, 89].

5.2 Structural, dielectric and magneto-optical properties of Al-Cr substituted M-type barium hexaferrite

5.2.1 XRD analysis

XRD pattern of $BaFe_{12-2x}Al_xCr_xO_{19}$ (x=0.0, 0.2, 0.4) is presented in **Fig. 5.16**. The observed diffraction peaks were indexed with standard patterns (JCPDS 39-1433) and were found to conform magnetoplumbite phase of pure crystalline M-type hexagonal ferrites with space group $P6_3/mmc$ [89]. Secondary phase such as α-Fe_2O_3 has not been observed; hence, the purity of the synthesized sample can be ascertained. Additionally, the pure and crystalline phase obtained shows that the substituted ions have been successfully substituted in the crystallographic sites. The lattice parameters (a and c) and volume of unit cell (V_{cell}) of the prepared samples were determined using the following formula and tabulated in **Table 5.4** [55].

$$\frac{1}{d_{hkl}^2} = \frac{4}{3}\left(\frac{h^2+hk+k^2}{a^2}\right) + \frac{l^2}{c^2} \tag{5.15}$$

$$V_{cell} = \frac{\sqrt{3}}{2}a^2c \tag{5.16}$$

where d_{hkl} represents d-spacing, hkl are the miller indices. From **Table 5.4**, It has been observed that the values of a, c and V_{cell} decrease with increase in Al^{3+}-Cr^{3+} substitution, this could be attributed to the fact that the ionic radius of Al^{3+} (0.535 Å) and Cr^{3+} (0.520 Å) are less than that of Fe^{3+} (0.645 Å) [88, 99]. When either Al^{3+} or Cr^{3+} substitutes Fe^{3+} in the hexagonal lattice, a shrinkage or distortion of the hexagonal lattice occurs as a result of difference in ionic radius thereby leading to decrease in a, c and V_{cell}. Similar results were obtained by Dhage *et al.* [100]. The c/a ratio was found to be 3.931, 3.925, and 3.934 for the samples with x=0.0, x=0.2, and x=0.4 respectively. Hexaferrites material with c/a ratio less than 3.98 are assumed to exhibit hexagonal structure [101]. Hence, it can be concluded that the prepared material exhibit hexagonal structure. The values of crystallite size (D), X-ray density (d_x), bulk density (d_m)surface area (S), and porosity (P) were calculated from equations (5.17), (5.18), (5.19), (5.20) and (5.21) respectively, and presented in **Table 5.4** [89].

$$D = \frac{k\lambda}{\beta\cos\theta} \tag{5.17}$$

$$d_x = \frac{2M}{N_A V_{cell}} \tag{5.18}$$

$$d_m = \frac{4m}{\pi d^2 t} \qquad (5.19)$$

$$S = \frac{6000}{D d_x} \qquad (5.20)$$

$$P = \left(\frac{d_x - d_m}{d_x}\right) \times 100 \qquad (5.21)$$

Where k is the Scherer's constant whose value is 0.9 for hexaferrites, λ =1.54056 Å is X ray wavelength, β is full width at half maxima (in radian), θ is the Bragg angle, M is the molecular mass of the sample, N_A=6.022 × 10^{23} mol^{-1} is the Avogadro's number, m, d and t are respectively the mass, diameter and thickness of the pellet. According to Ashiq et al. materials with a grain size less than 50 nm are good candidates for media recording [93]. Hence, the prepared samples can be useful in magnetic recording [87].
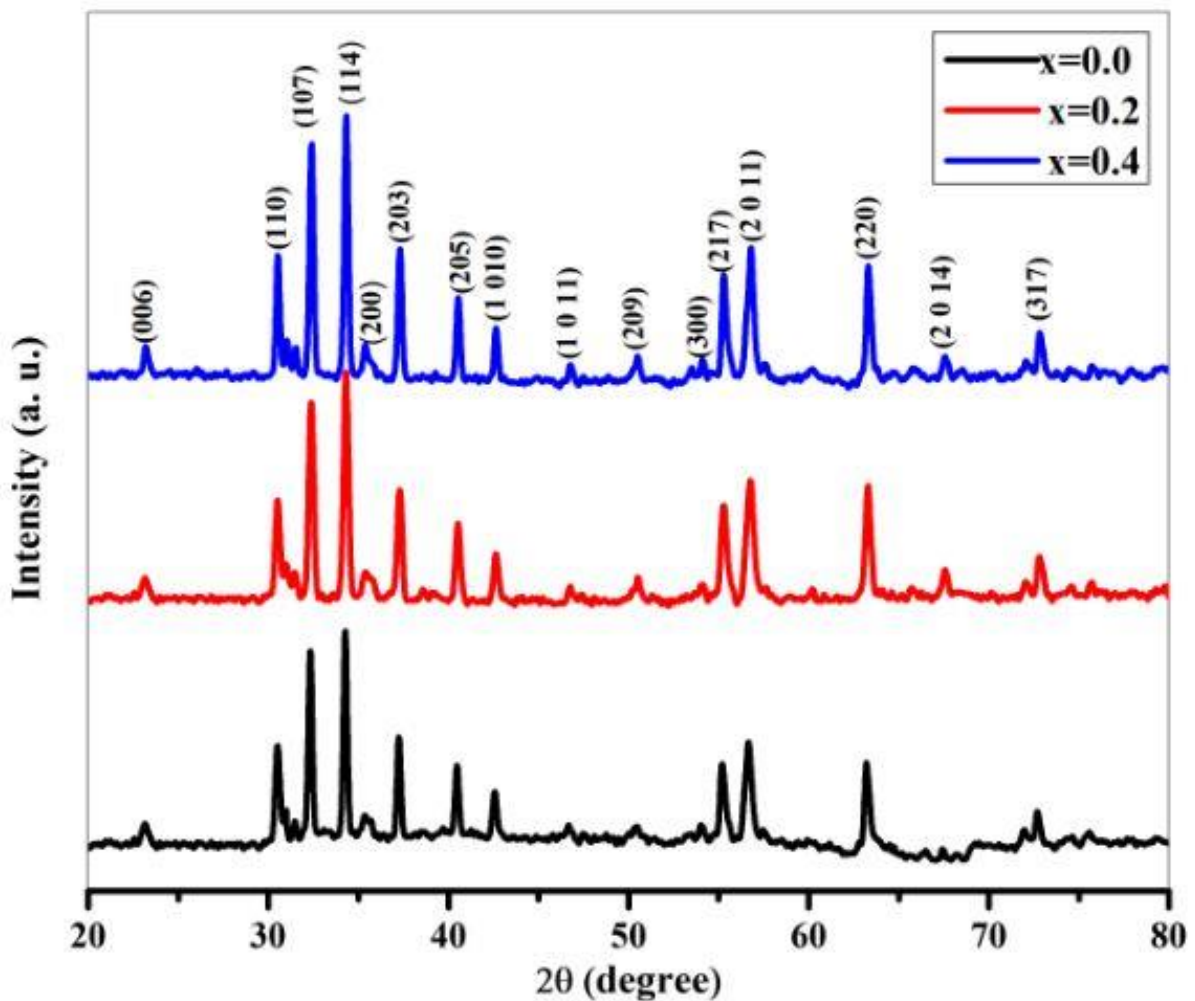
Fig. 5.16 XRD pattern of BaFe$_{12-2x}$Al$_x$Cr$_x$O$_{19}$ (x=0.0, 0.2, 0.4)

It was observed that the specific surface area of prepared sample lays in the range 28-41 cm^2/g and strongly depend of crystallite size. It can be noted that smaller the crystallites size higher the surface area and therefore the number of atoms is greater at the surface. From **Table 5.4**, it is noticed that the X-ray density decreases with increase in Al-Cr concentration; this could be due to the fact that the atomic weight of Al (26.98) and Cr (51.99) are lower than that of Fe (55.845). The bulk density is showing lower value than the theoretical one because of the presence of pores in the samples. It is observed that the bulk density decreases while the porosity of $BaFe_{12-2x}Al_xCr_xO_{19}$ (x=0.0, 0.2, 0.4) increases with the increase of Al-Cr concentration. Heat treatment or synthesis methods may be the reason for the increment of porosity. The observed values of lattice parameters are in agreement with those observed in the literature [32].

Table 5.4 Crystallite size (D), lattice constants (a and c), volume cell (V_{cell}), bulk density (d_m), X-ray density (d_x), porosity (P) and surface area (S) for $BaFe_{12-2x}Al_xCr_xO_{19}$ (x=0.0, 0.2, 0.4) samples

x	a (Å)	c (Å)	V_{cell} (Å^3)	c/a	S ($\times 10^7 cm^2/g$)	$d_m(g/cm^3)$	$d_x(g/cm^3)$	P(%)	D(nm)
0.0	5.873	23.09	689.79	3.93	28.4620	3.234	5.3504	39.56	39.40
0.2	5.869	23.04	687.04	3.93	40.5468	3.132	5.3402	41.45	27.71
0.4	5.855	23.024	685.98	3.94	31.3541	2.358	5.3168	55.62	35.38

5.2.2 FTIR analysis

The FTIR spectra of $BaFe_{12-2x}Al_xCr_xO_{19}$ (x=0.0, 0.2, 0.4) is shown in **Fig. 5.17**. Two significant peaks can be observed at 437 cm^{-1} and 590 cm^{-1}. The peaks appearing between 400 cm^{-1} and 600 cm^{-1} are the result of vibration of metal-oxygen bond which gives the idea of the formation of ferrite phase [30]. Additionally, the absorption band around 437 cm^{-1} corresponds to the assignment of the Fe-O bending by Fe-O$_4$ and Fe-O stretching by Fe-O$_6$ while the band around 590 cm^{-1} corresponds to the Fe-O stretching by Fe-O$_4$ [87]. A band around 2361cm^{-1} can be observed in the samples with x=0.2 and x=0.4, this band can be assigned to the presence of CO_2 absorbed from the atmosphere by the sample [54].
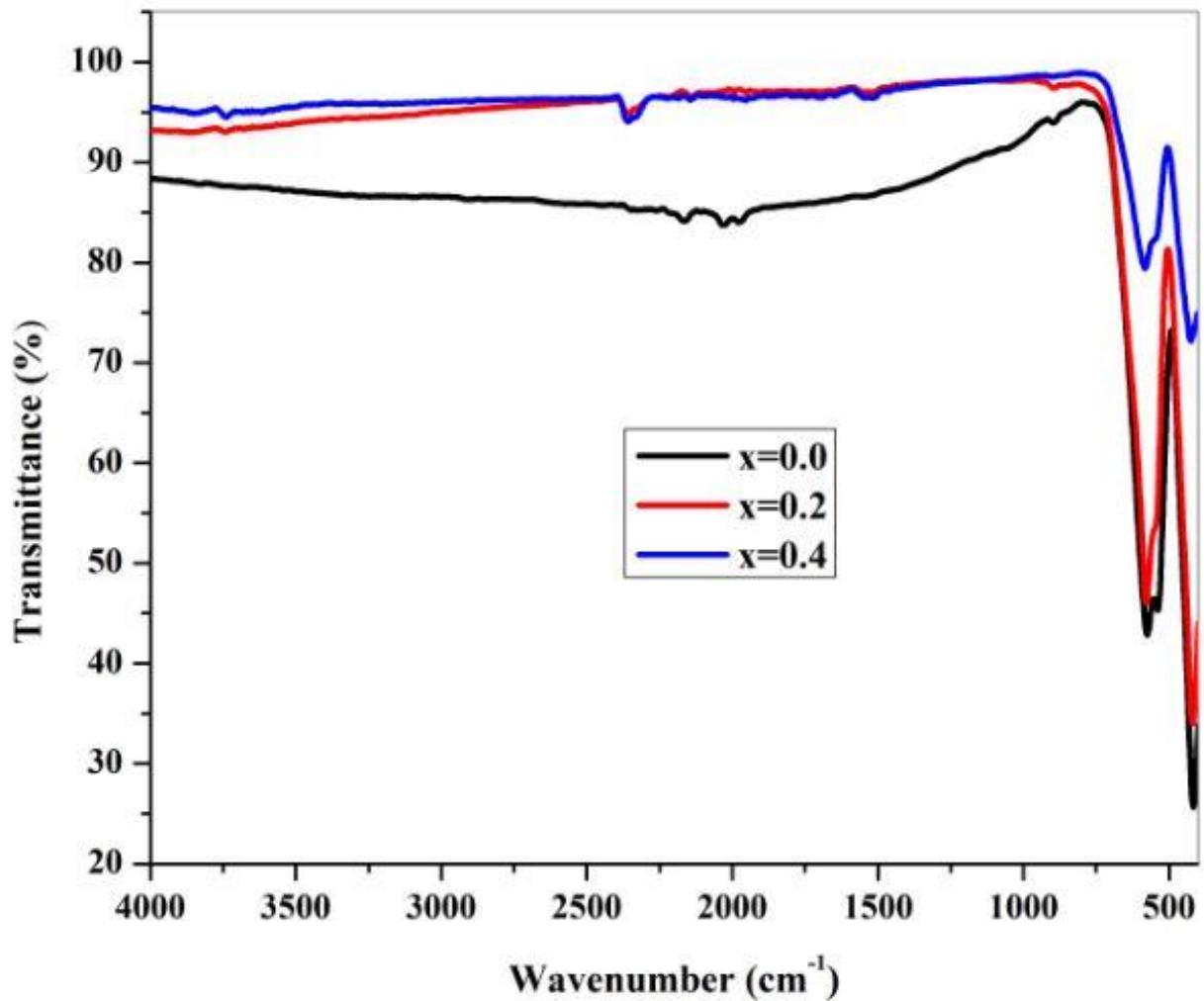
Fig. 5.17 FTIR spectra of $BaFe_{12-2x}Al_xCr_xO_{19}$ (x=0.0, 0.2, 0.4)

The lack of this peak in sample with x=0.0 can be due to the fact that CO_2 was less in the room during the FTIR spectra recording of this sample.

5.2.3 Raman spectroscopy

Fig. 5.18 shows the Raman spectra of $BaFe_{12-2x}Al_xCr_xO_{19}$ (x=0.0, 0.2, 0.4) recorded in the range 150 to 800 cm^{-1} at room temperature. It was noticed that the substitution of the Fe^{3+} ions by the ions of Al^{3+} and Cr^{3+} in the different sites causes a decrease in intensity of the peak and broadening of Raman modes.
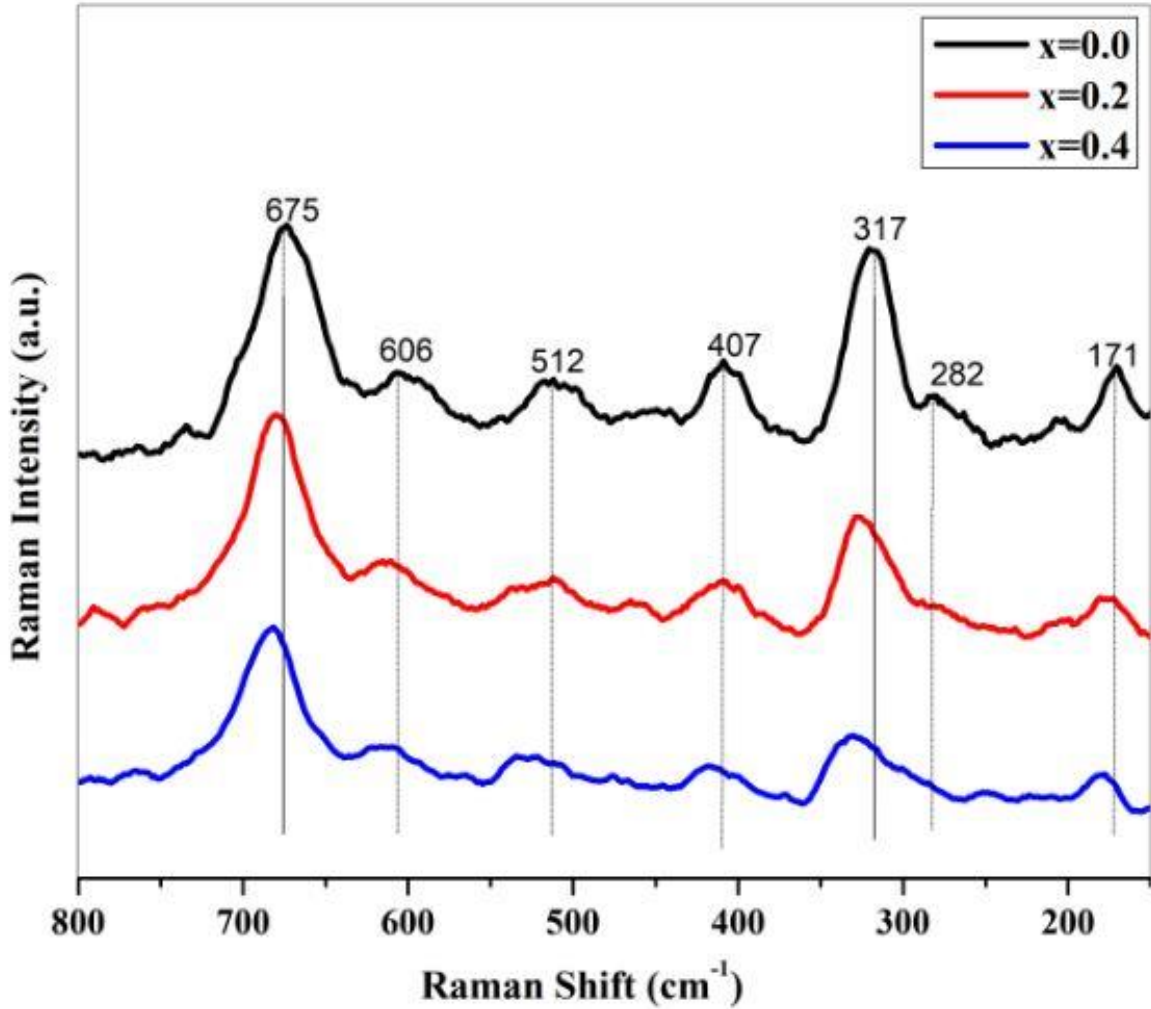
Fig. 5.18 Raman spectra of $BaFe_{12-2x}Al_xCr_xO_{19}$ (x=0.0, 0.2, 0.4)

M-type barium hexaferrite is well known for the complexity of its structure which does not allow making a direct relationship between the doping rate and the displacement of vibrational bands observed on the Raman spectra. Group theory analysis of hexaferrites on the basis of D_{6h} symmetry give rise to 42 Raman active modes which are distributed in the form of irreducible representation as $11A_{1g} + 14E_{1g} + 17E_{2g}$ [102]. Raman modes are observed at 171, 204, 281, 317, 407, 513, 606 and 674 cm^{-1}. The Raman modes at 171, 204 and 281cm^{-1} could be respectively attributed to E_{1g}, E_{1g} and E_{2g} symmetry corresponding to the vibration of S-block whereas the Raman modes at 317, 407, 513, 606 and 674 cm^{-1} corresponds to the vibrations of 12k octahedral site, 12k and 2a octahedral site, $4f_2$ octahedral site, 2b bi-pyramidal site due to of A_{1g}, E_{1g}, A_{1g}, A_{1g}, and A_{1g} symmetry respectively [40].

5.2.4 FESEM and EDX analysis

FESEM micrographs of $BaFe_{12-2x}Al_xCr_xO_{19}$ (x=0.0, 0.4) are presented in **Fig. 5.19(a) and (c)** respectively. It can be observed that the particles exhibit a homogeneous distribution with hexagonal plate-like shape. The hexagonal; shape of the prepared samples causes a decrease of grain boundary and surface energy [103]. It is also noticed that particles are agglomerated that can be due to magnetic interaction between the individual grains of the prepared samples [55]. **Fig. 5.19(b) and (d)** show particle size distribution of $BaFe_{12}O_{19}$ and $BaFe_{11.2}Al_{0.4}Cr_{0.4}O_{19}$ respectively. It has been revealed that these distributions follow normal distribution law. From these figures, average particles sizes were found to be 90.11 nm and 108.33 nm respectively. **Fig. 5.20** presents the element analysis of $BaFe_{12-2x}Al_xCr_xO_{19}$ (x=0.0, 0.4). Each element of the sample composition (Ba, Fe, Al, Cr and O) can be observed in the EDX spectra. This confirms the stoichiometry of the prepared samples
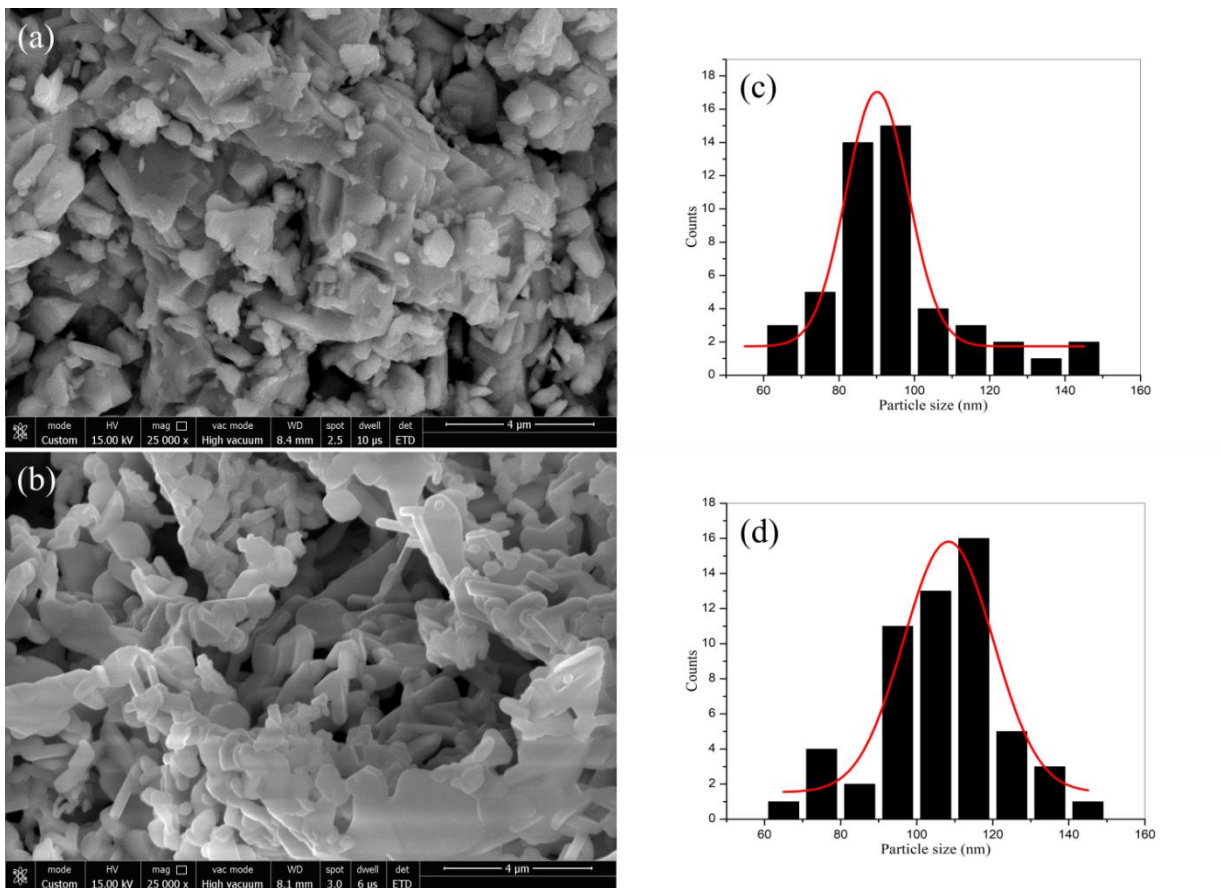
Fig. 5.19 FESEM micrograph and particles size distribution of $BaFe_{12-2x}Al_xCr_xO_{19}$ (a) x=0.0 and (b) x=0.4

5.2.5 Optical analysis

The study of the optical properties of $BaFe_{12-2x}Al_xCr_xO_{19}$ (x=0.0, 0.2, 0.4) was carried out using UV-vis spectroscopy in the range 225-800 nm. When radiation is incident on materials capable of conducting current, electrons in the valence band absorb energy from the radiation.
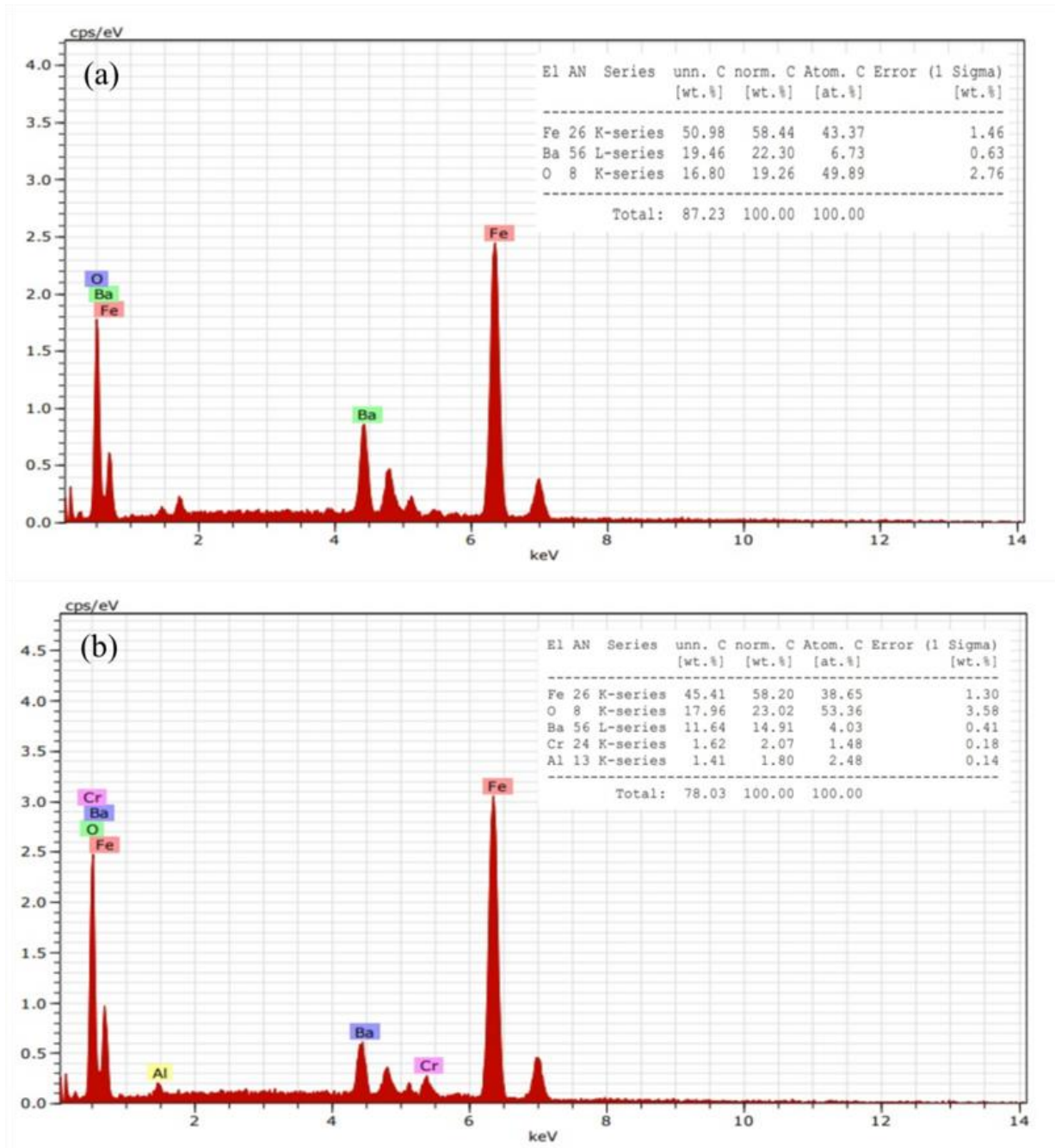
Fig. 5.20 EDX spectra of $BaFe_{12-2x}Al_xCr_xO_{19}$ (a) x=0.0 and (b) x=0.4

This absorbed energy allows them to move to higher energy levels (conduction band). This energy therefore corresponds to the energy difference between the valence band and conduction band and defines the band gap calculated by the following relation [55]:

$$(\alpha h v)^2 = A(hv - E_g) \tag{5.22}$$

Where E_g represents band gap energy, A is a constant and α is the absorption coefficient, v is the frequency of incident radiation, and $h=6.6260 \times 10^{-34} \, J.s$ is the Planck's constant.

The graph of E_g is presented in **Fig. 5.22**, the values of E_g have been evaluated by extrapolating the linear part of the graph of $(\alpha h v)^2$ against E_g.
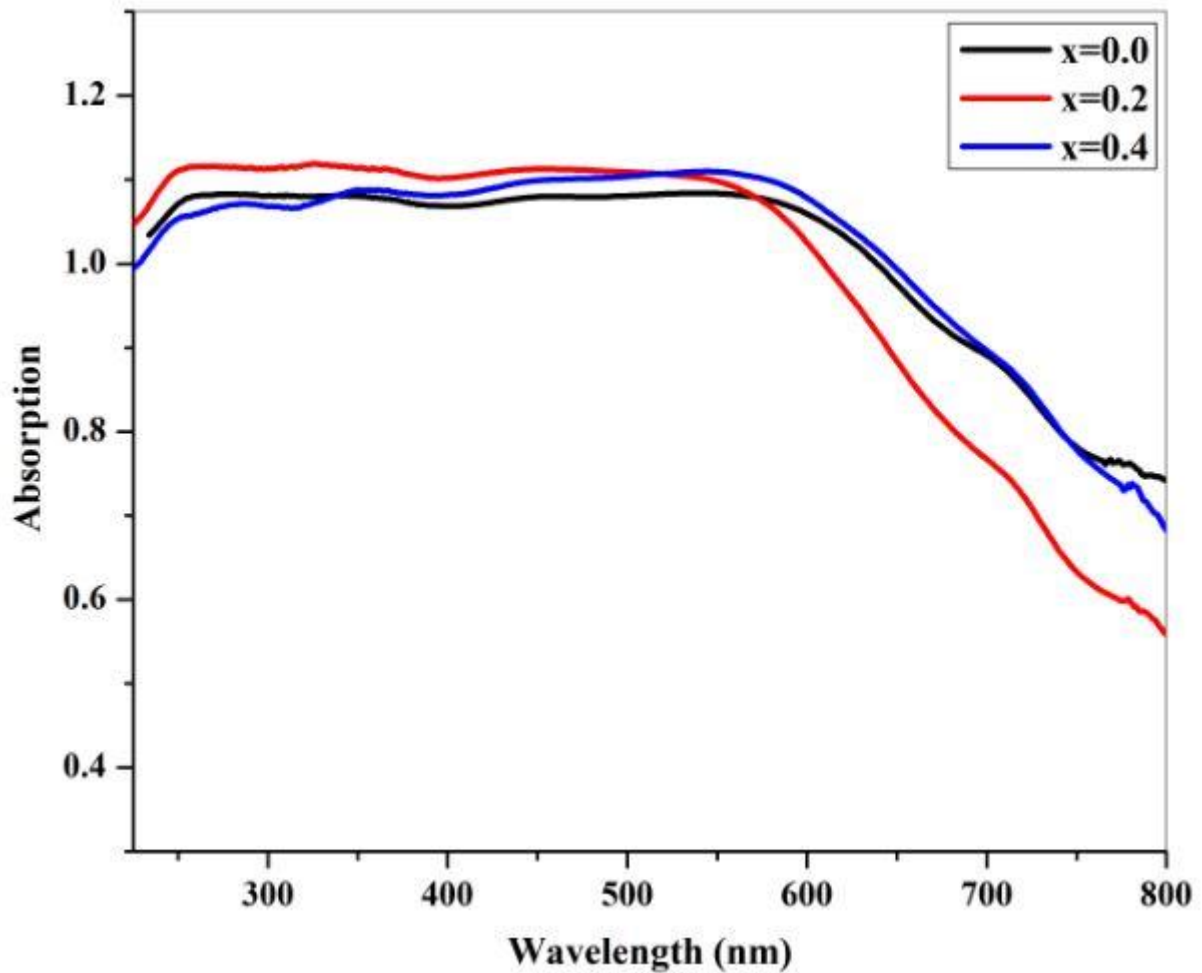
Fig. 5.21 Absorption spectra for $BaFe_{12-2x}Al_xCr_xO_{19}$ (x=0.0, 0.2, 0.4) prepared at 1000 °C
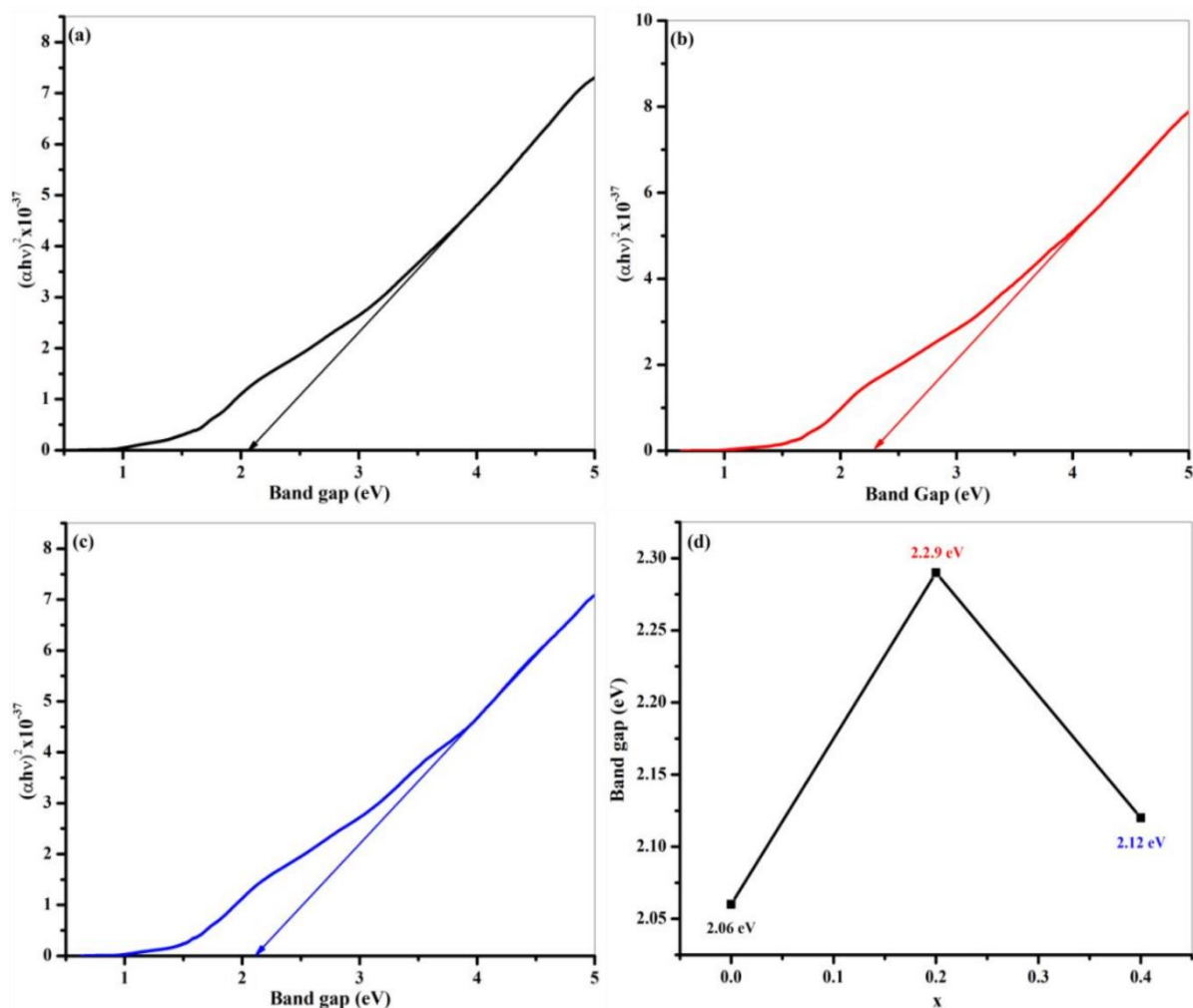
Fig. 5.22 Band gap of $BaFe_{12-2x}Al_xCr_xO_{19}$ (a) x=0.0, (b) x=0.2 and (c) x=0.4 (d) variation of band gap with composition (x)

The values of Eg for the sample with $x = 0.0$, $x = 0.2$ and $x = 0.4$ are respectively 2.06, 2.29 and 2.12 eV. It can be noted that D and E_g vary inversely i.e. the larger the crystallites size, the lower the band gap energy. This behaviour was revealed by Baykal *et al.* [104]. This can be justified by the effect of quantum confinement. From UV-Vis-NIR spectra (**Fig. 5.21**), the absorption region for hexaferrites has been found to be 200-600 nm. This result is supported by the literature[40].

5.2.6 Dielectric analysis

Fig. 5.23 and **5.24** respectively presents the variation of the dielectric constant (ε') and dielectric tangent loss ($\tan \delta_e$) with frequency for $BaFe_{12-2x}Al_xCr_xO_{19}$ (x=0.0, 0.2, 0.4). The values of ε' and $\tan \delta$ were calculated using equation (9) and (10) respectively [96] and are listed in **Table 5.5**.

$$\varepsilon' = \frac{Z''}{\omega C_0 Z^2} \tag{5.23}$$

$$tan\delta = \frac{\varepsilon''}{\varepsilon'} \tag{5.24}$$

where Z'' is the imaginary part of complex impedance, $\omega = 2\pi f$ is the angular frequency and C_0 is the geometrical capacitance. The response of the samples is matching with typical ferrite material i.e. ε' is high at lower and intermediate frequencies and decreases with increase in frequency, this could be attributed to interfacial and dipolar polarization [89]. Remarkably, a sudden and steady increase in dielectric constant is observed at higher frequencies as a result of electronic polarization. The values of dielectric constant and dielectric loss tangent at lower, intermediate, and higher frequencies are presented in **Table 5.5**. It can be observed that the values of dielectric constant decreases with increase in the concentration of Al^{3+}-Cr^{3+}. Similarly, for all frequency range, the values of $tan\,\delta_e$ decrease for the sample with $x=0.2$. At lower and intermediate frequencies, $tan\,\delta_e$ shows an increasing trend for $x=0.4$. However $tan\,\delta_e$ decreases at higher frequencies for $x=0.4$. This behaviour can be explained on the basis of Maxwell-Wagner model which assumed ferrites to be made up of conducting grains separated by insulating grain boundaries [105]. When electric field is applied, charge carriers are displaced from their mean position; the charge carriers align themselves at grain boundaries if the grain boundaries have more resistance as compared to the grains [32, 106]. This scenario causes the surface charges to gather at the interface of the grain boundaries thereby resulting in interfacial polarization and consequently large dielectric constant. Polarization in ferrites materials occur as a result of conduction by hopping of electrons between Fe^{3+} and Fe^{2+} [107]. The process of polarization decreases as the frequency of the applied electric field increases; this is because at higher frequencies, the conduction by hopping of electrons between Fe^{3+} and Fe^{2+} lag behind the applied electric field. Koop's stated that, at lower frequencies grain boundaries are more effective whereas at higher frequencies grains are more effective [108]. Hence, polarization increases as frequency increases which leads to decrease in the dielectric constant at higher frequencies. The appearance of ε' could be attributed to grain boundary defects, oxygen vacancies and space charge polarization [28]. The high values of $tan\,\delta_e$ at lower frequencies is as a result of grain boundary effects which require high energy for conduction by hopping of electrons between Fe^{3+} and Fe^{2+} to occur whereas the small values of $tan\delta_e$ are observed at higher frequencies because of the effectiveness of grains at higher frequencies [109]. **Fig. 5.25** presents the variation of AC conductivity with frequency for $BaFe_{12-2x}Al_xCr_xO_{19}$ ($x=0.0$, 0.2, 0.4).

Conductivity in ferrites is attributed to AC conductivity (σ_{AC}) as a result of band conduction and DC conductivity (σ_{DC}) as a result of hopping conduction [110]. The total conductivity (σ_t) can be evaluated using the Jonscher power law [111]

$$\sigma_t(\omega) = \sigma_{DC} + \sigma(\omega) \tag{5.25}$$

$$\sigma(\omega) = A\omega^s \tag{5.26}$$

Where $\sigma(\omega)$ is the frequency dependent conductivity also called σ_{AC}, ω is the angular frequency, s is the temperature dependent constants and A is the material intrinsic property dependent constant. σ_{AC} remains constant at lower and intermediate frequencies whereas a sudden increase in σ_{AC} at higher frequencies is vividly observed, this could be attributed to ionic conductivity [112]. Grain boundaries contribute to σ_{AC} at lower frequencies whereas the observed dispersion at higher frequencies could be due to the conductivity of grains [28]. Additionally, the activeness of the mechanism of conductivity is increased whenever the frequency of the applied field is increased thereby leading to increase in space charge polarization at higher frequencies and thus the sudden increase in conductivity at the high frequency region [113].

Table 5.5 Dielectric constant (ε') and dielectric loss tangent ($tan\ \delta_e$) of $BaFe_{12-2x}Al_xCr_xO_{19}$ (x=0.0, 0.2, 0.4) at low, intermediate and high frequency

x	Low frequency (101 Hz)		Intermediate frequency (21.667KHz)		High frequency (120 MHz)	
	ε'	$tan\delta_e$	ε'	$tan\delta_e$	ε'	$tan\delta_e$
0.0	20	0.309	12.5	0.0883	14.4	0.133
0.2	14.5	0.278	10.5	0.0494	14.2	0.0965
0.4	11.4	0.337	8.26	0.0638	9.66	0.0742

5.2.7 Magnetic analysis

Fig. 5.26 presents the M-H hysteresis loop of $BaFe_{12-2x}Al_xCr_xO_{19}$ (x=0.0, 0.2, 0.4). The values of coercivity (H_c), saturation magnetization (M_s), remnant magnetization (M_r) were determined from the hysteresis loop and tabulated in **Table 5.6**. Magnetism in ferrite results from the net magnetic moment of Fe^{3+} ions with spin up and spin down in sublattice sites [114]. The hexagonal lattice of M-type hexaferrites consists of 24 Fe^{3+} ions, these 24 Fe^{3+} ions are distributed among five crystallographic sublattice which are one tetrahedral

sublattice (4f$_1$), one bipyramidal sublattice (2b) and three octahedral sublattice (12k,2a, and 4f$_2$,) [115]. According to Gorter model, ferrites consist of a ferrimagnetic structure consisting of eight antiparallel spins (12k,2a and 2b) and four parallel spins (4f1 and 4f2) which are coupled by super exchange interactions via the O^{2-} ions [116]. The values of M_s are in the range 15.156-88.032 emu/g whereas the values of M_r are in the range 7.914-46.437 emu/g. It has been reported that Al^{3+} ion prefer to occupy 12k and 2a sites [117]. The decrease in the values of M_s and M_r (for x=0.2) are observed because Al^{3+} ion with $0\mu_B$ replaces Fe^{3+} ion with $5\mu_B$ [100]. Additionally, substitution of cation results in the weakening of the super exchange interaction of the type Fe$_A$$^{3+}$–O–Fe$_B$$^{3+}$, this causes the collapse of the magnetic colinearity of the lattice and subsequently decrease the magnetic parameters [118]. This is further supported by the fact that Al^{3+} ions substitution in the hexagonal lattice may results in the weakening of the magnetic ions interaction and collapse of long range magnetic ordering [119].
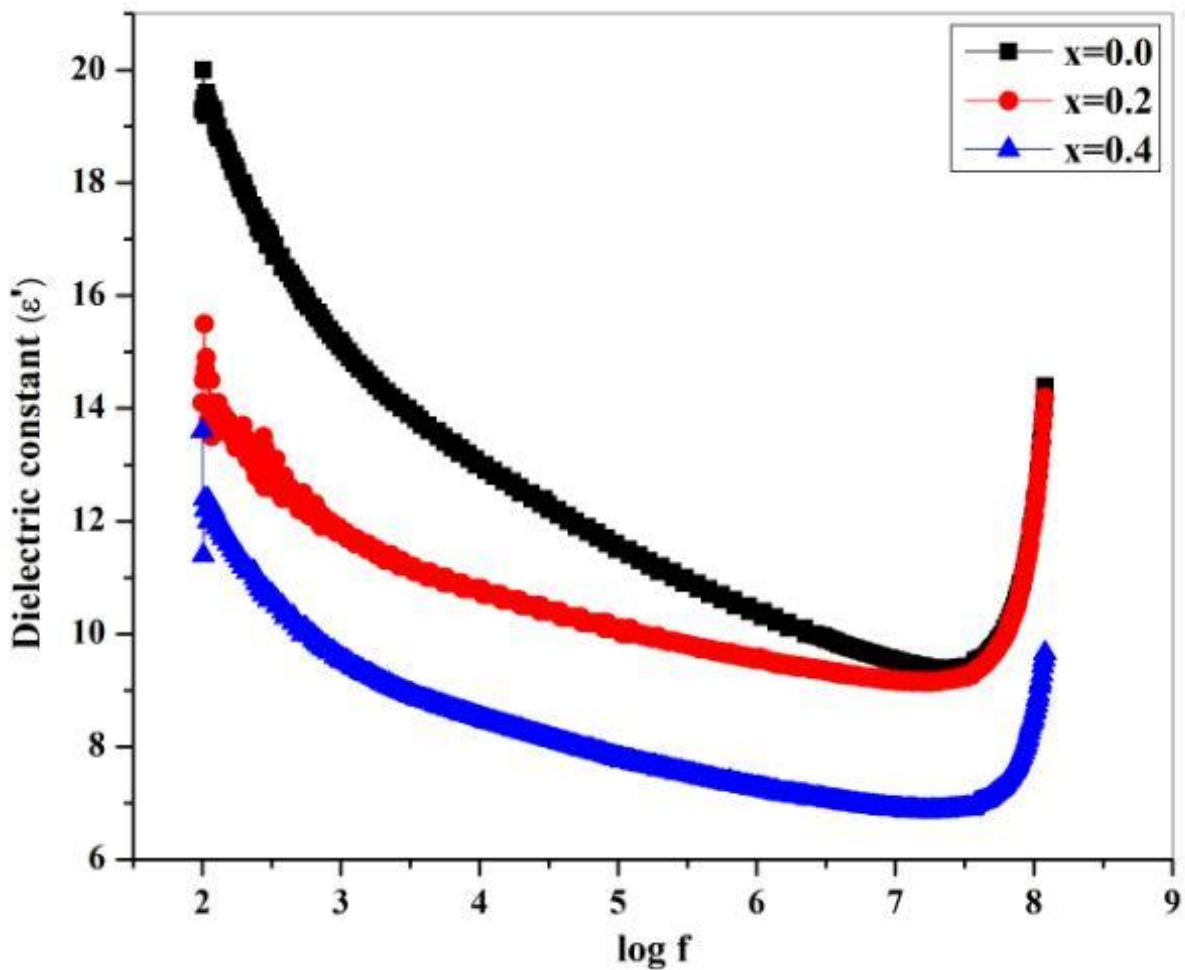
Fig. 5.23 Dielectric constant of BaFe$_{12-2x}$Al$_x$Cr$_x$O$_{19}$ (x=0.0, 0.2, 0.4)
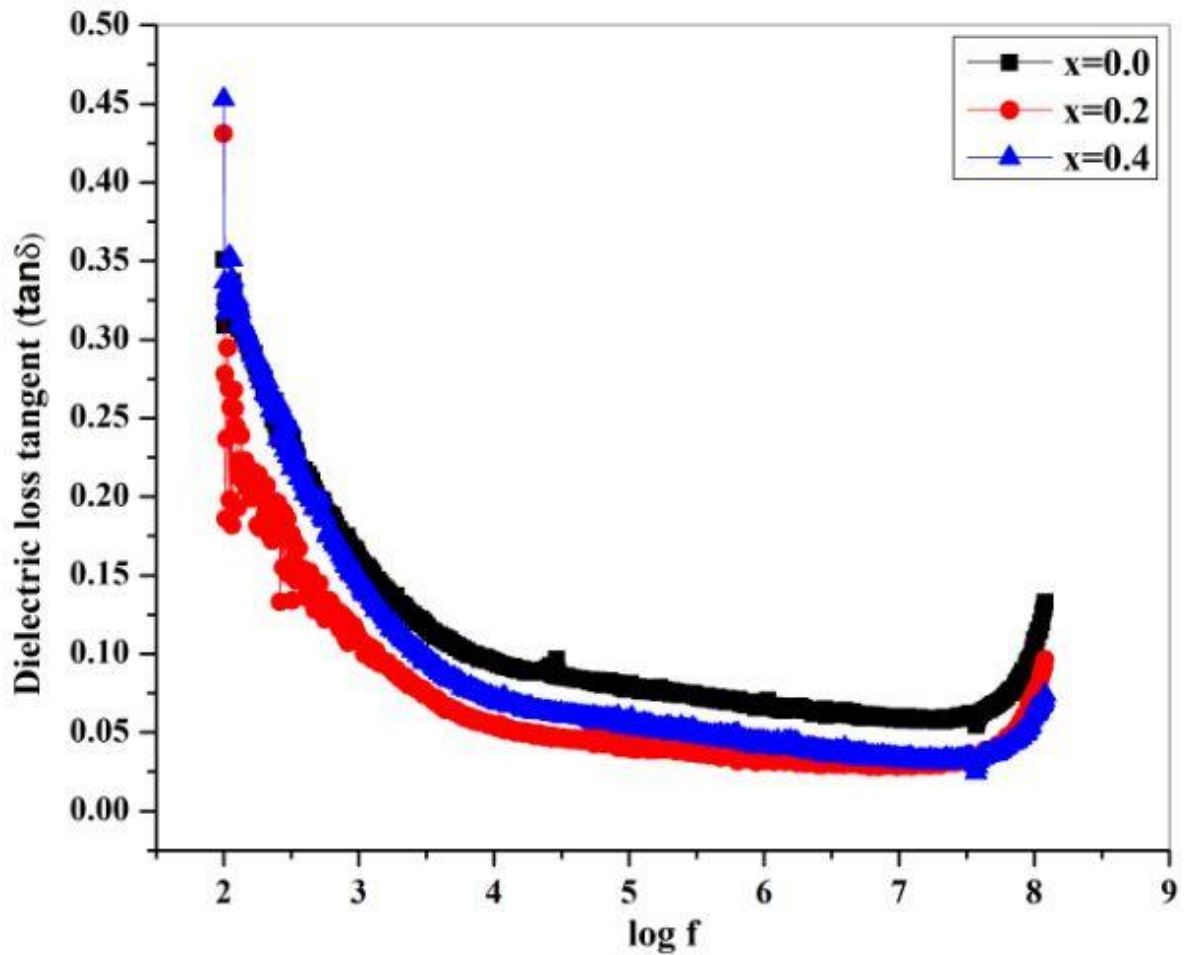
Fig. 5.24 Dielectric loss tangent of $BaFe_{12-2x}Al_xCr_xO_{19}$ (x=0.0, 0.2, 0.4)

It has been reported that Cr^{3+} ions prefer to occupy 12k, 2a and $4f_2$ sites. The observed increase in the values of M_s and M_r (for x=0.4) could be attributed to the fact that the number of Cr^{3+} ions occupying $4f_2$ site with spin up are more than those occupying 12k and 2a sites with spin down even though the magnetic moment of Cr^{3+} ion ($3\mu_B$) is less than that of Fe^{3+} ion ($5\mu_B$) [114, 120]. The values of H_c were found to be in the range 1639.35-4615.44 Oe, H_c greater than 1200 Oe are useful for high-density perpendicular magnetic recording media [92]. The values of SR was respectively found to be 0.48, 0.52 and 0.53 for the samples having x=0.0, x=0.2, and x=0.4. The prepared samples can be considered as single domain if the values of SR is greater than or equal to 0.5; on the other hand, the prepare samples can considered as multi-domain if the values of SR is less than 0.5 [121]. Hence, the sample with x=0.0 is multi-domain whereas the samples having x=0.2 and x=0.4 are single domain.
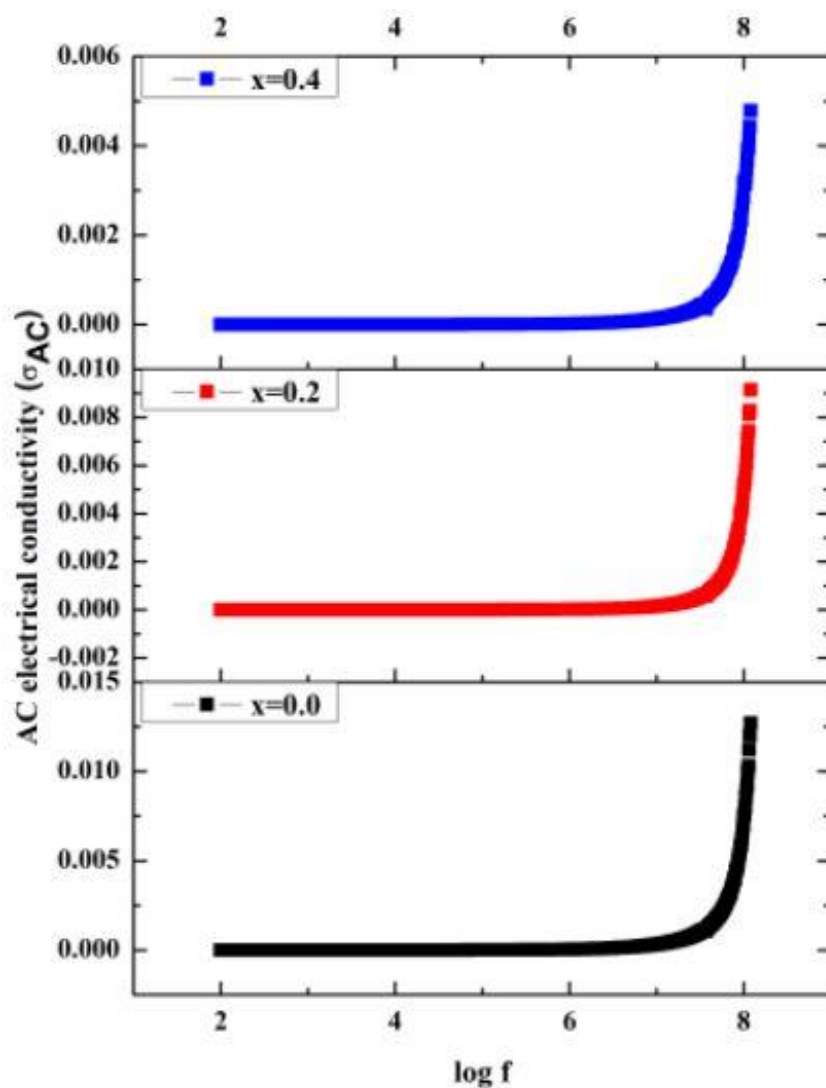
Fig. 5.25 AC conductivity of BaFe$_{12-2x}$Al$_x$Cr$_x$O$_{19}$ (x=0.0, 0.2, 0.4)

Table 5.6 Magnetic parameters of BaFe$_{12-2x}$Al$_x$Cr$_x$O$_{19}$ (x=0.0, 0.2, 0.4) samples at room temperature

x	$M_s(emu/g)$	$M_r(emu/g)$	$H_c(Oe)$	$SR(M_r/M_s)$	$K(HA^2/Kg)$	$N_B(\mu_B)$
0.0	81.25	38.78	1639.35	0.48	6.659	16.16
0.2	15.16	7.91	4615.44	0.52	3.498	2.99
0.4	88.03	46.44	4090.71	0.53	18.005	16.87
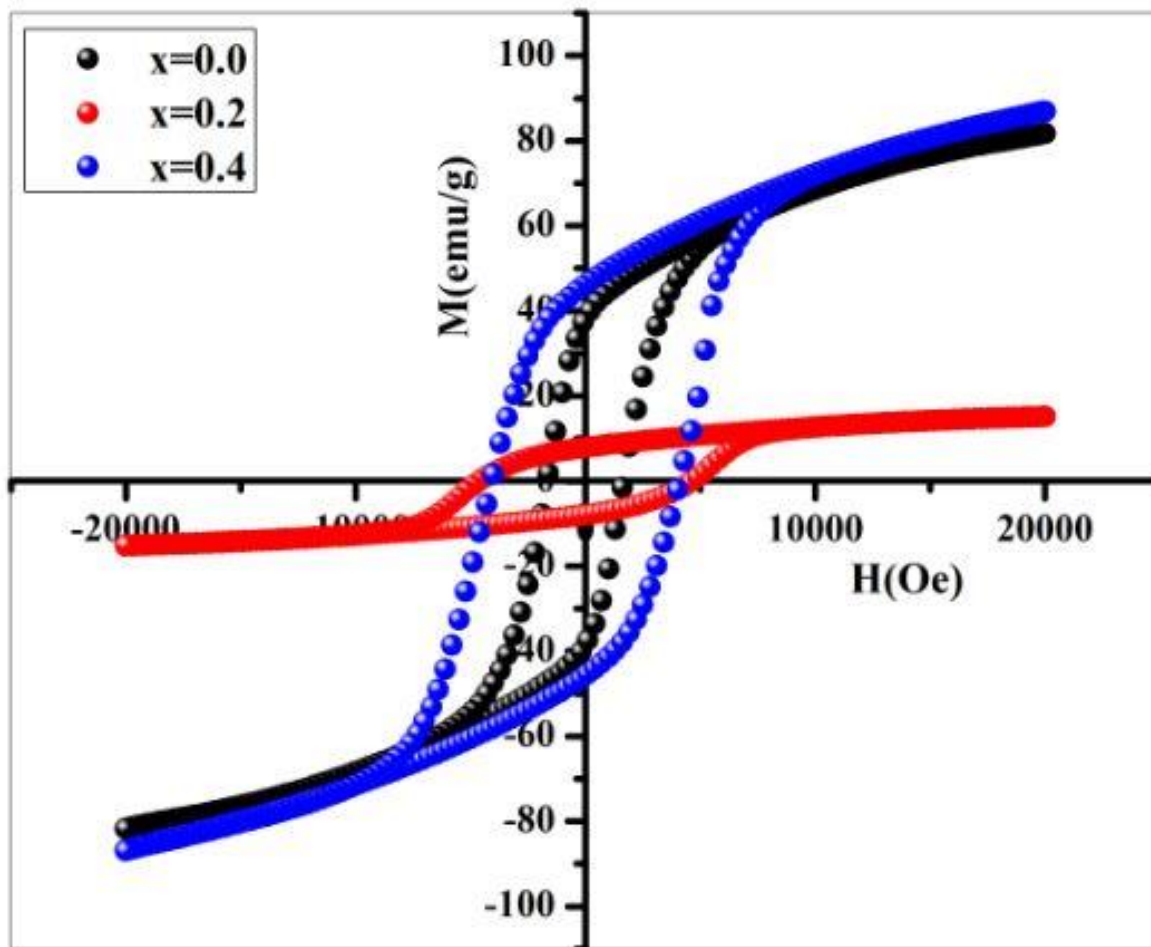
Fig. 5.26 M-H hysteresis loop of $BaFe_{12-2x}Al_xCr_xO_{19}$ (x=0.0, 0.2, 0.4)

5.3 Effect of Cr-Bi substitution on the structural, optical, electrical and magnetic properties of strontium hexaferrites

5.3.1 XRD analysis

Fig. 5.27(a) shows the XRD patterns of prepared $SrFe_{12-2x}Cr_xBi_xO_{19}$ (x=0.0-0.2) samples. The observed peaks were indexed using JCPDS card number 39-1433 [89]. These peaks correspond to the precise diffraction angles (2θ) and define the hexagonal phase of M-type hexaferrite structure with *P6₃/mmc* as space group.
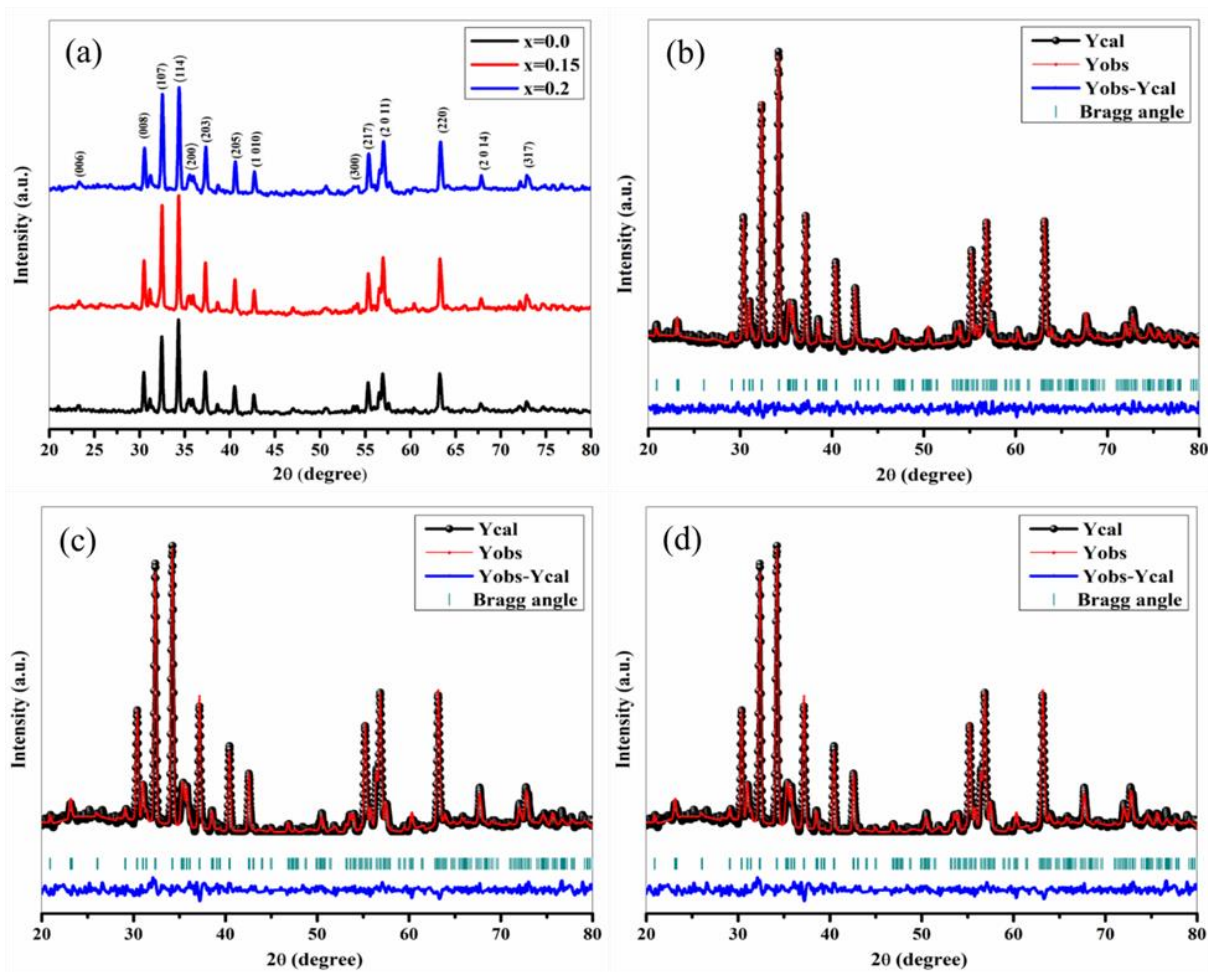
Fig. 5.27 (a) XRD patterns and Rietveld refinement (b) x=0.0, (c) x=0.15 and (d) x=0.2 of SrFe$_{12-2x}$Cr$_x$Bi$_x$O$_{19}$ (x=0.0-0.2)

The absence of impurity has been observed which indicates that the Cr^{3+} and Bi^{3+} ions have been incorporated into the hexagonal structure. This is supported by the XRD Rietveld refinement given in **Fig. 5.27 (b), (c), (d)** where it can be observed that all the reflection peaks of experiment data (Ycal) and theoretical data (Yobs) are matching. Rietveld refinement was carried out using FULLPROF package; linear interpolation method to model the background while Thompson-Cox-Hastings pseudo-Voigt (TCH p-V) with axial divergence asymmetry function was used to refine the shape of peaks. Parameters such as unit cell, atomic position, background, zero correction, half-width (U, V, W), overall B-factor and scale factor were varied in the refinement process whereas the occupancy of all the atoms remained unchangeable. It was found that goodness of fit (GoF) corresponding to space group $P6_3/mmc$ were between 1.05-1.7 which indicate the reliability of the refinement (**Table 5.8**). The unit cell parameters a, c and its volume (V_{cell}) of the prepared samples SrFe$_{12-}$

$_{2-x}Cr_xBi_xO_{19}$ (x=0.0-0.2) was calculated using formulae defining the hexagonal structure and are reported in **Table 5.7** [54, 122]

$$\frac{1}{d_{hkl}^2} = \frac{4}{3}\left(\frac{h^2+hk+k^2}{a^2}\right) + \frac{l^2}{c^2} \tag{5.27}$$

$$V_{cell} = \frac{\sqrt{3}}{2}a^2c \tag{5.28}$$

Where d_{hkl} is d-spacing, *hkl* are the miller indices for of the peaks. From **Table 5.7**, it can be observed that *a* and *c* vary between 5.85-5.87 Å and 23.2-23.7 Å respectively. Clearly, *a* and *c* does not show regular variation with change in the concentration of Cr^{3+}- Bi^{3+}, as a result of the differences in the ionic radii of the substituents with Fe^{3+} [99, 123]. The values of V_{cell} increases with increase in Cr^{3+}-Bi^{3+} substitution, this may be due to the fact the dopants ions have larger ionic radii than Fe^{3+}. Generally, substitution of Fe^{3+} ions by other cations in hexagonal lattice leads to either shrinkage or expansion of the hexagonal lattice which respectively decreases or increases the V_{cell}. M-type hexaferrite crystal structure can be ascertained when *c/a* ratio is lower than 3.98 [101]. In this research, the *c/a* ratio was found to be 3.960, 3.973 and 3.954 for x=0.0, x=0.15 and x=0.2 respectively thus confirming hexagonal structure formation of synthesized samples. Experimental density (d_m), theoretical density (d_x), crystallite size (*D*), porosity (*P*) and surface area (*S*) are respectively evaluated from eqn. (5.29), (5.30), (5.31), (5.32) and (5.33) and the values are reported in **Table 5.7** [89].

$$D = \frac{0.9\lambda}{\beta \cos \theta} \tag{5.29}$$

$$d_m = \frac{m}{\pi r^2 t} \tag{5.30}$$

$$d_x = \frac{ZM}{N_A V_{cell}} \tag{5.31}$$

$$P = \left(1 - \frac{d_m}{d_x}\right) \times 100 \tag{5.32}$$

$$S = \frac{6000}{D d_x} \tag{5.33}$$

Where λ(1.54056Å) is wavelength of the incident radiation, β is FWHM (full width at half maxima in radian), θ represents reflection angle, *M* is the sample molecular weight, N_A (6.022×10^{23} mol^{-1}) represents the number of Avogadro, *t m* and *r* are the thickness, mass,

and rayon of the pallet respectively. It was found that the average crystallite size of prepared samples is in the range of 33-42 nm.

Table 5.7 Volume of unit cell (V_{cell}), lattice parameters (a and c), Crystallite size (D), theoretical density (d_x), experimental density (d_m), porosity (P) and surface area (S) of $SrFe_{12-2x}Cr_xBi_xO_{19}$ (x=0.0-0.2)

x	0.0	0.15	0.2
D(nm)	38.67	41.993	33.258
a(Å)	5.8636	5.8572	5.8671
c(Å)	23.22	23.2722	23.2022
V_{cell} (Å^3)	691.39	691.43	691.68
c/a	3.96	3.973	3.954
d_x(g/cm^2)	5.099	5.207	5.241
d_m(g/cm^2)	3.037	3.165	2.823
P (%)	40.44	39.205	46.068
$S \times 10^7$(cm^2/g)	30.430	27.440	34.4221

It has been reported that hexaferrites with grain size less than 50 nm are convenient for low signal to noise ratio and can therefore be used for magnetic recording media [93] Furthermore, media noise resulting from the coupling between magnetic grains is a necessary factor which delimits the performance of high density recording media [124]. The theoretical density enhances with concentration of Cr^{3+}- Bi^{3+} ions, this can be attributed to the molecular mass and volume of unit cell of the sample. In comparison, the theoretical density is higher than the experimental density, the reason of this difference can be related to the appearance of certain pores that evolve during the synthesis process [125]. The values of porosity and surface area were found to be in the range 39-47% and 27-35 cm^2/g respectively. According to the equation (7), surface area is strongly linked to the crystallite size of sample and it was found that S and D vary inversely i.e. the more surface area than lesser the crystallite size and hence the number of atoms on the surface is large [126].

Table 5.8 Conditions for data recording and reliability factors of $SrFe_{12-2x}Cr_xBi_xO_{19}$ (x=0.0-0.2)

x	0.0	0.15	0.2
Wavelength (Å)	1.540590	1.540590	1.540590
Step (˚)	0.02	0.02	0.02
Profile function	TCH p-V * Axial divergence asymmetry	TCH p-V * Axial divergence asymmetry	TCH p-V* Axial divergence asymmetry
Half-width	U=0.078150 V=-0.115560 W=0.066786	U=0.239234 V=-0.253393 W=0.099911	U=0.354314 V=-0.337038 W=0.136464
Space group	P6$_3$/mmc	P6$_3$/mmc	P6$_3$/mmc
Reliability factors (%)	R_{bragg}=15.4	R_{bragg}=7.97	R_{bragg}=9.17
	R_p=29.5	R_p=19.5	R_p=19.4
	R_{wp}=26.7	R_{wp}=27.1	R_{wp}=28.0
	R_{exp}=25.4	R_{exp}=17.0	R_{exp}=16.7
	GoF=1.05	GoF=1.6	GoF=1.7
	χ^2=1.11	χ^2=2.55	χ^2=2.817

5.3.2 FTIR analysis

Fig. 5.28 shows the FTIR spectroscopy spectra of $SrFe_{12-2x}Cr_xBi_xO_{19}$ (x=0.0-0.2) samples calcinated at 1000 °C for 6h. Characteristics bands are observed on each spectrum in 400-600 cm^{-1} range specifically at 441, 552 and 598 cm^{-1}. These striking bands are usually observed as a result of a vibration of metal-oxygen (Fe-O) they give an idea of the hexaferrites structure formation [30]. The small band observed at about 1554 cm^{-1} reveals the metal-oxygen-metal (M-O-M) bond vibration which is represented by iron-oxygen-iron and cobalt-oxygen-cobalt [127].
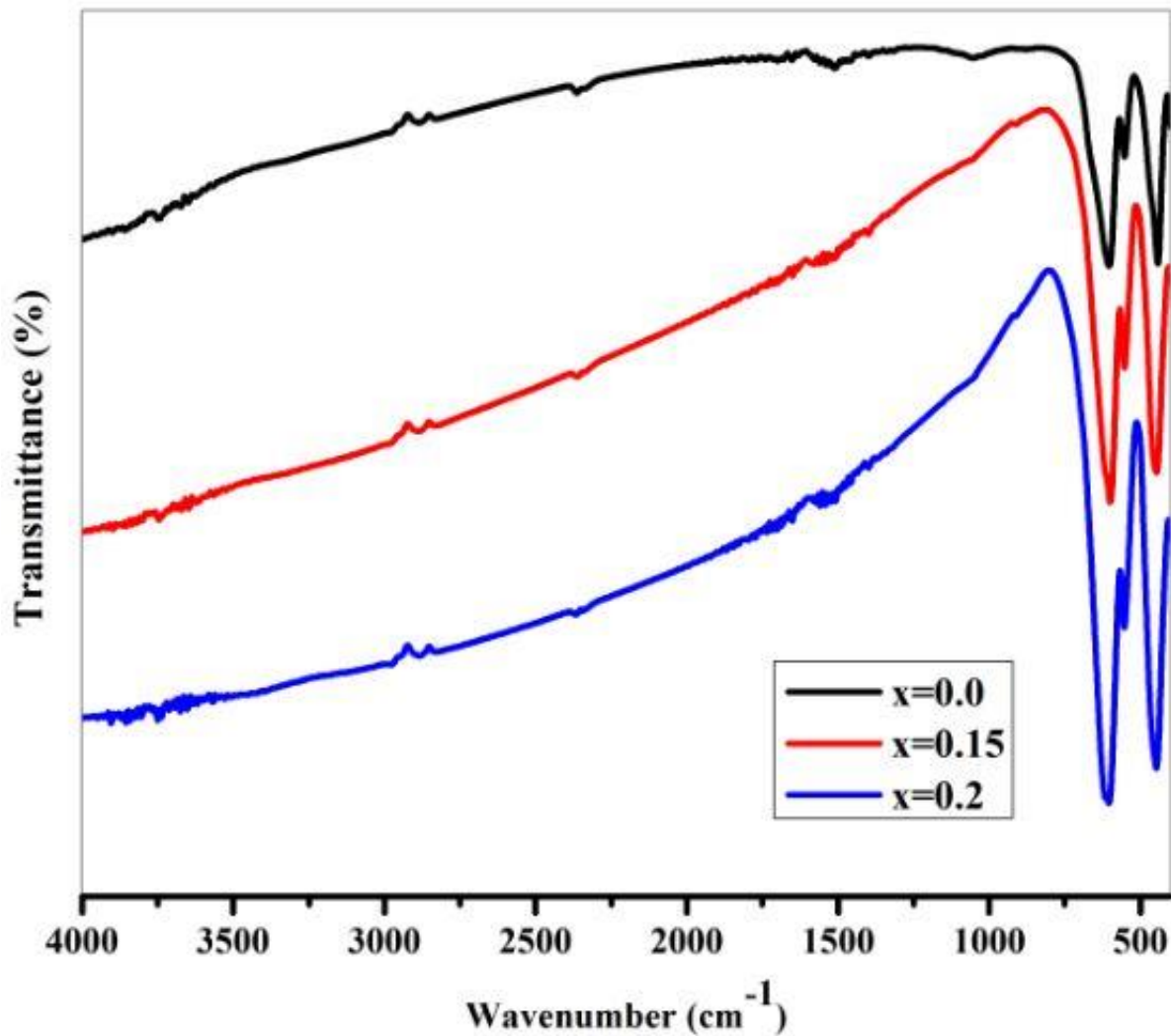
Figure 5.28 FTIR spectra of $SrFe_{12-2x}Cr_xBi_xO_{19}$ (x=0.0-0.2)

The observed band at 2354 cm^{-1} refers to the CO_2 absorption from the atmosphere [128]. The peak observed at 2900 cm^{-1} wavenumber is attributed to the moisture presence in the sample whereas the peak observed at around 3700 cm^{-1} wavenumber indicate the hydroxyl functional group in the sample [89]. From **Fig. 5.28**, It can be seen that the intensity of the peaks between 400-600 cm^{-1} increase with increase in the Bi^{3+}-Cr^{3+} substitution for the sample with x=0.2, this indicate that the sample with x=0.2 absorb more of the incident radiation used for the experiment as compared with the samples with x=0.0 and x=0.15.

5.3.3 Raman spectroscopy

The vibrational modes of the prepared samples were determined by Raman spectroscopy. **Fig. 5.29** shows the Raman spectrum of $SrFe_{12-2x}Cr_xBi_xO_{19}$ samples recorded in 150-800 cm^{-1} wavenumber range. The unit cell of BaM compound made up of 64 atoms has 42 active Raman modes including 11A1g + 14E1g + 17E2g [40, 129]. The Raman spectra shows the

different bands with varying intensities, these bands are characteristic bands of hexaferrite. Using the reference data provided by Kreisel et al. the bands observed on the Raman spectrum have been attributed to the vibrational modes (**Table 5.9**) [102]. The band at about 680 cm^{-1} may be due to bipyramidal sites (2b) vibration as a result of A_{1g} symmetry. Bands at 606, 527, 468 and 325 cm^{-1} may refer to the vibration of the Fe-O bond (metal-oxygen) corresponding to the sites 12k, 2a and 4f2. The band observed at 410 cm^{-1} is dominated by a mixed vibration of A_{1g} symmetry mainly at octahedral sites 12k and 2a whereas the band at 173 cm^{-1} corresponds to the vibration of E_{1g} symmetry of the whole spinel blocks [129, 130].

Table 5.9 Raman active modes of $SrFe_{12-2x}Cr_xBi_xO_{19}$ (x=0.0-0.2)

Raman active mode (cm^{-1})	Symmetry	Reference (cm^{-1})	Mode assignment
177	E_{1g}	173	Whole spinel block
325	E_{2g}	319	Octahedral (12k)
410	A_{1g}	409	Octahedral(12k dominated)
468	A_{1g}	467	Octahedral (12k and 2a) site
527	E_{1g}	527	Octahedral (12k and 2a) site
606	E_{2g}	606	Octahedral (4f$_2$)
680	A_{1g}	684	Bipyramidal (2b)

5.3.4 FESEM analysis

FESEM micrographs of $SrFe_{12-2x}Cr_xBi_xO_{19}$ (x=0.0 and x=0.2) are given in **Fig. 5.30**. Clearly, a homogeneous distribution of grains with shape close to hexagonal plate-like can be observed especially in the sample with x=0.2. An agglomeration of grains is also observed due to magnetic interactions between the grains [55, 104]. The average particle sizes for x=0.0 and x=0.2 were observed to be respectively 0.175 µm and 0.967 µm (**Fig. 5.30**). **Fig. 5.31** represents the EDX analysis of $SrFe_{12-2x}Cr_xBi_xO_{19}$ (x=0.0 and x=0.2). The host and substituted chemical elements along with their weight percentage are detected in the EDX spectra, this approves the stoichiometry and purity of the synthesized samples as observed from XRD analysis.
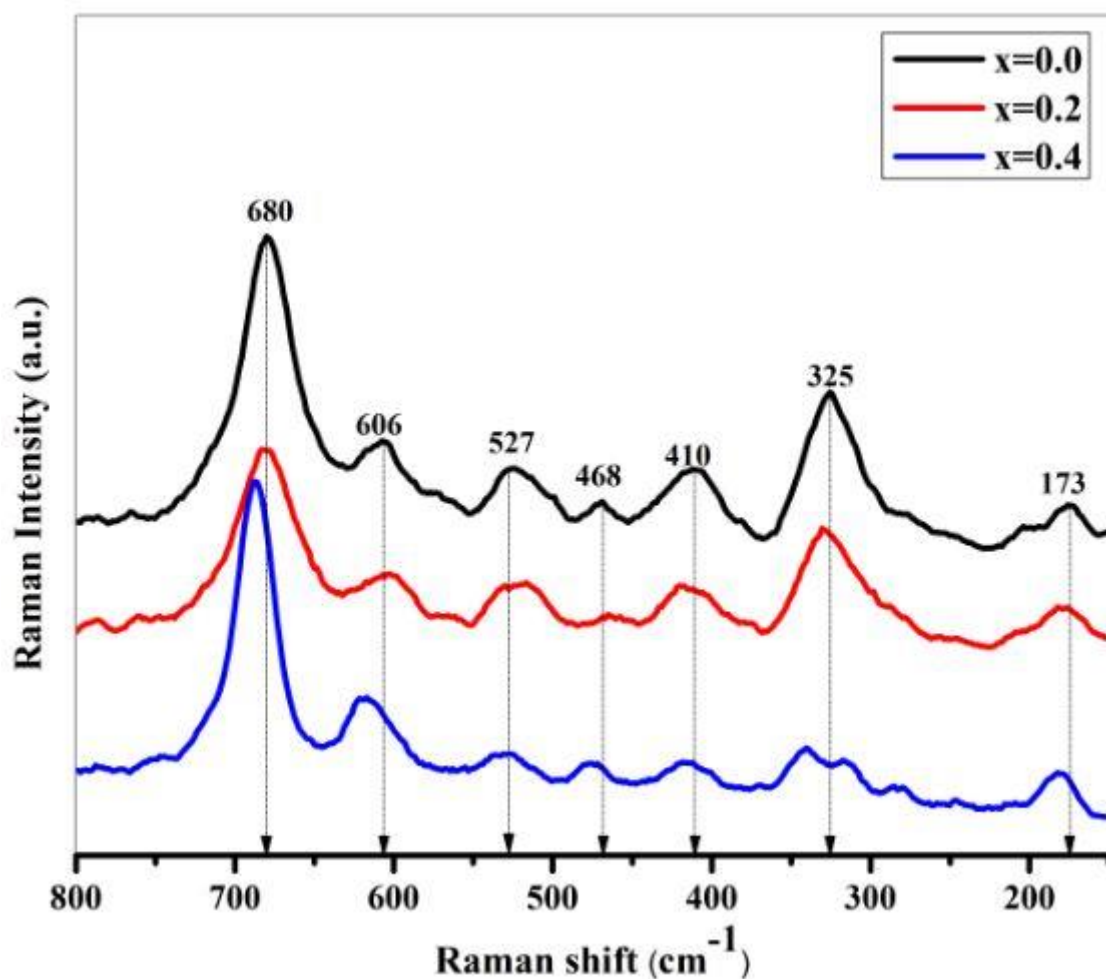
Fig. 5.29 Raman spectra of $SrFe_{12-2x}Cr_xBi_xO_{19}$ (x=0.0-0.2)

5.3.5 Optical analysis

Optical properties of $SrFe_{12-2x}Cr_xBi_xO_{19}$ (x=0.0-0.2) were studied by the UV-vis-NIR spectroscopy. **Fig. 5.32** presents the UV-Vis absorption spectrum of prepared nanoparticles recorded in the wavelength range 225-1000 nm. From this figure, it can be noticed that undoped hexaferrite (x=0.0) mainly absorbs the light with wavelength below 650 nm and samples with x>0 show a slight red-shift of spectral response up to approximately 680 nm for x=0.15 and 730 nm for x=0.2. As the Cr^{3+}-Bi^{3+} concentration increases, the absorption region shifts towards higher wavelength.
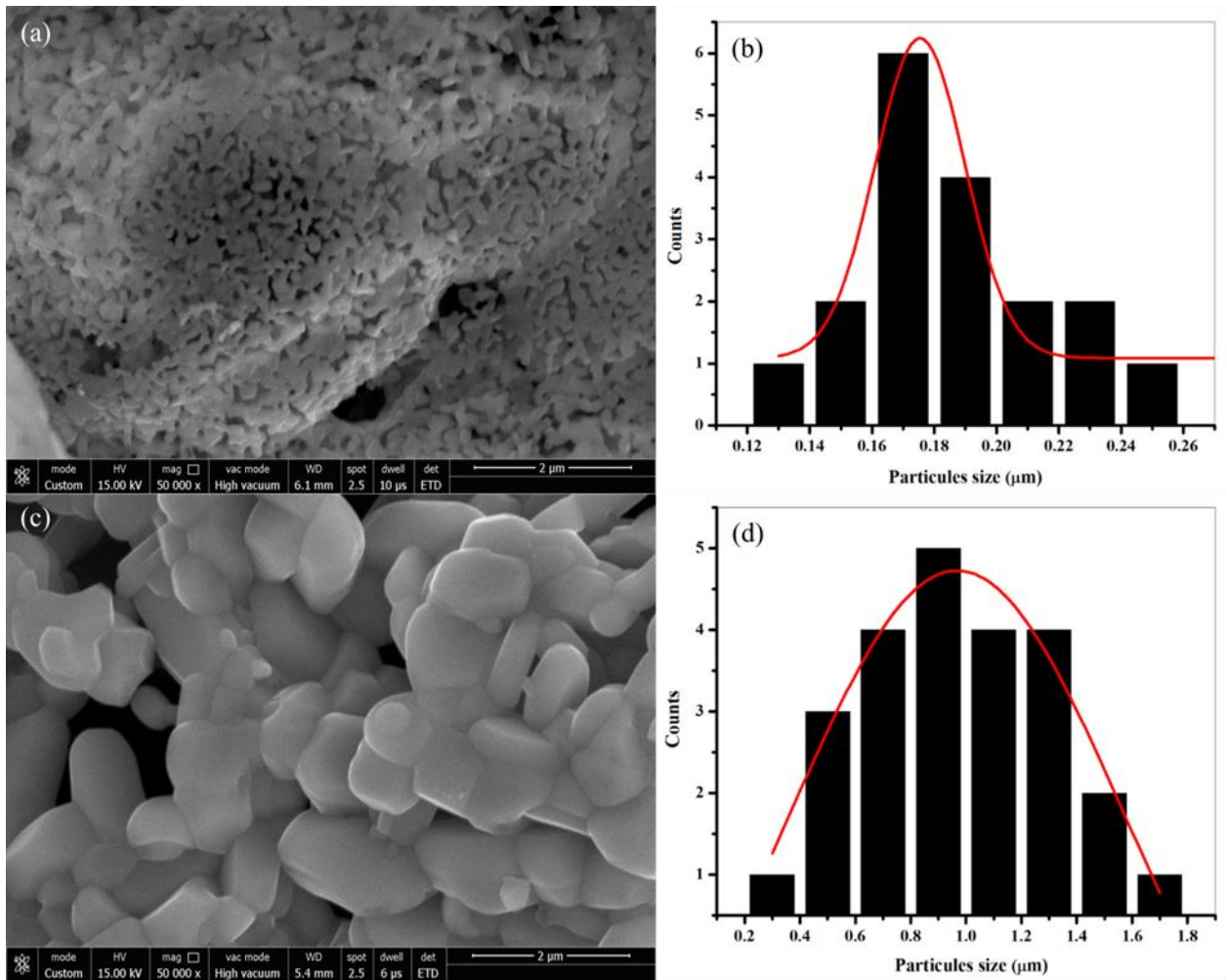
Fig. 5.30 FESEM micrographs and particle sizes distribution of $SrFe_{12-2x}Cr_xBi_xO_{19}$ (x=0.0 and x=0.2)

Due to the absorption of light, the electrons of the valence band can move to higher energy levels belonging to the conduction band. The gap between the valence band and the conduction band represents the space that must be crossed by the electron that absorbs an energy corresponding to band gap energy. The band gap energy can be evaluated from absorption coefficient (α) given by Tauc relation [131].

$$\alpha h\upsilon = A(h\upsilon - E_g)^n \tag{5.34}$$

Where $h\upsilon$ refers to the energy of photon, A represents a transition probability dependent parameter and the exponent n is an index which indicates and defines the absorption process.
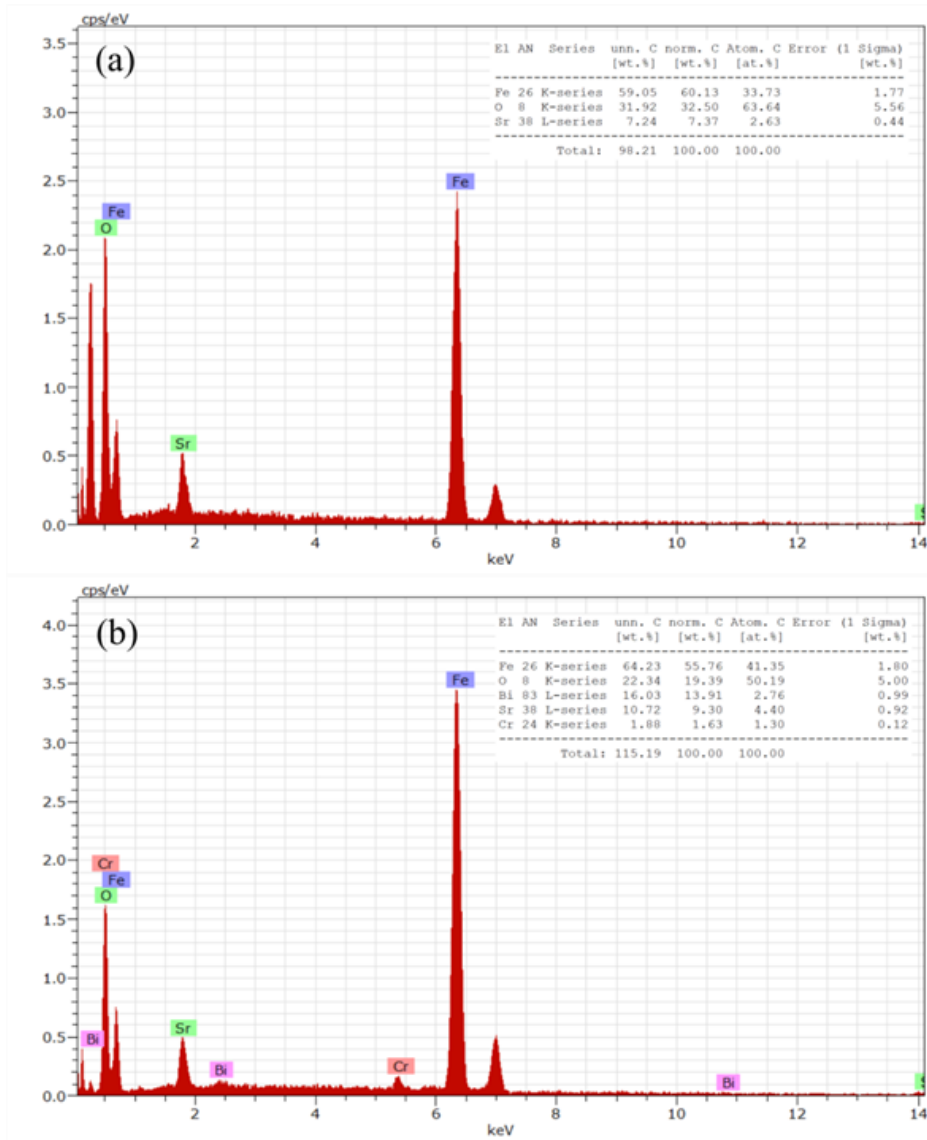
Fig. 5.31 EDX spectra of $SrFe_{12-2x}Cr_xBi_xO_{19}$ (x=0.0 and x=0.2)

The index n can take theoretical values such as 2, 1/2, 3 or 3/2 which refer to indirect allowed, direct allowed, indirect forbidden and direct forbidden transitions respectively, in this study we focus on direct allowed transition ($n = 1/2$). **Fig. 5.33** shows different plots of $(\alpha h v)^2$ as a function of the photon energy (hv), in accordance to equation (8). Band gap energy (E_g) of samples can be estimated by drawing tangents on the graph as shown in **Fig. 5.33**. Values of E_g for prepared samples were found to vary between 2.11 and 2.37 eV. The band gap energy for undoped sample (x=0.0) was found to be smaller than that found by Karmarkar et al. [132]. This is due to the fact that the band gap energy may be influenced by the crystallite size of a sample [40, 103, 133, 134]. In this work, it is noticed that D and E_g

vary inversely i.e. the more the crystallites size, the lesser the band gap energy. Baykal et al. observed similar scenario which can be attributed to quantum confinement effect [104].

The absorption spectra can be divided into weak absorption, absorption edge, and strong absorption zone. The weak absorption zones is a consequence of the presence of impurities and defects in the samples, the absorption edge occur as a result of structural or lattice disorder, and the strong absorption zone give rise to the band gap of the material [135]. The density of states will shift into the region of the band gap when excited electrons encounter these structural or lattice disorder. When these shifting of density of states into the band gap region becomes accumulated and form a sequence near the valence and conduction band, a tail like energy level called Urbach tail is created [136]. The energy associated with this so called Urbach tail is called the Urbach energy and the presence of this so called Urbach energy narrows the effective band gap [137]. The relation defining the Urbach energy (E_U) is given by

$$\alpha = \alpha_0 \exp\left(\frac{h\upsilon}{E_U}\right) \tag{5.35}$$

Where α_0 is a constant, $h\upsilon$ is the energy of the incident radiation, and E_U is the Urbach energy. Equation (5.35) can be transformed to give the equation of a straight line by applying logarithmic simplification

$$\ln \alpha = \left(\frac{1}{E_U}\right) h\upsilon + \ln \alpha_0 \tag{5.36}$$

Fig. 5.34 presents the variation of E_g and E_U with increase in Cr^{3+}-Bi^{3+} concentration. The values of E_U of the prepared samples were calculated by linear fitting of the graph of $\ln \alpha$ against $h\upsilon$ and taking the reciprocal of the slope. The values of E_U was found to be 0.78, 1.70, and 2.69 eV which respectively correspond to x=0.0, x=0.15 and x=0.2 (**Table 5.10**). The values of E_U enhances with rise in Cr^{3+}-Bi^{3+} substitution, this shows that increase in Cr^{3+}-Bi^{3+} concentration causes more structural defects in the samples. This was expected as the ionic radii difference of the substituted cations with Fe3+ results in lattice distortion thereby leading to structural defects.
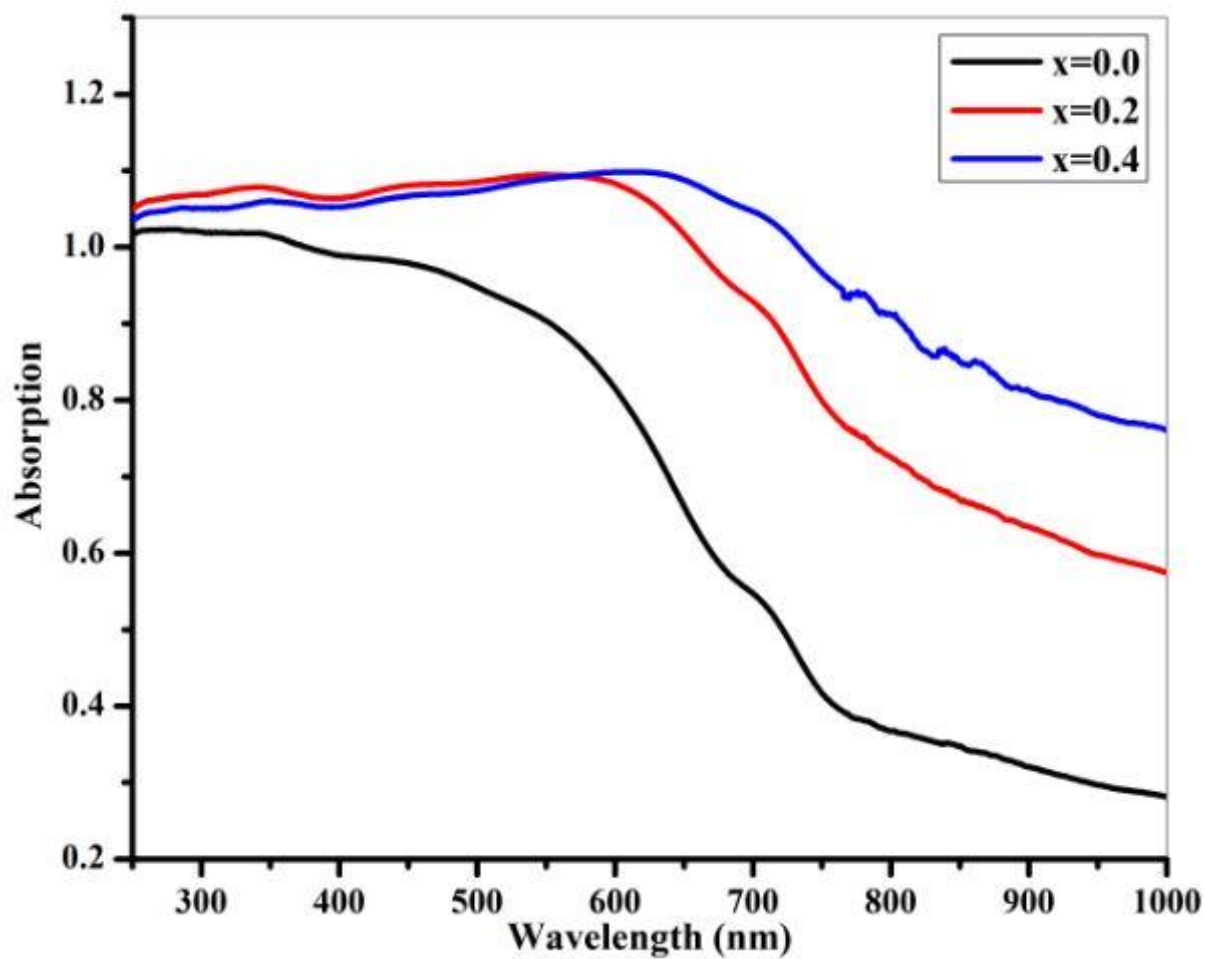
Fig. 5.32 UV spectra of $SrFe_{12-2x}Cr_xBi_xO_{19}$ (x=0.0-0.2)

Table 5.10 Urbach energy and band gap of $SrFe_{12-2x}Cr_xBi_xO_{19}$ (x=0.0-0.2)

x	Urbach energy (eV)	Band gap (eV)
0.0	0.78	2.37
0.15	1.70	2.11
0.2	2.69	2.18
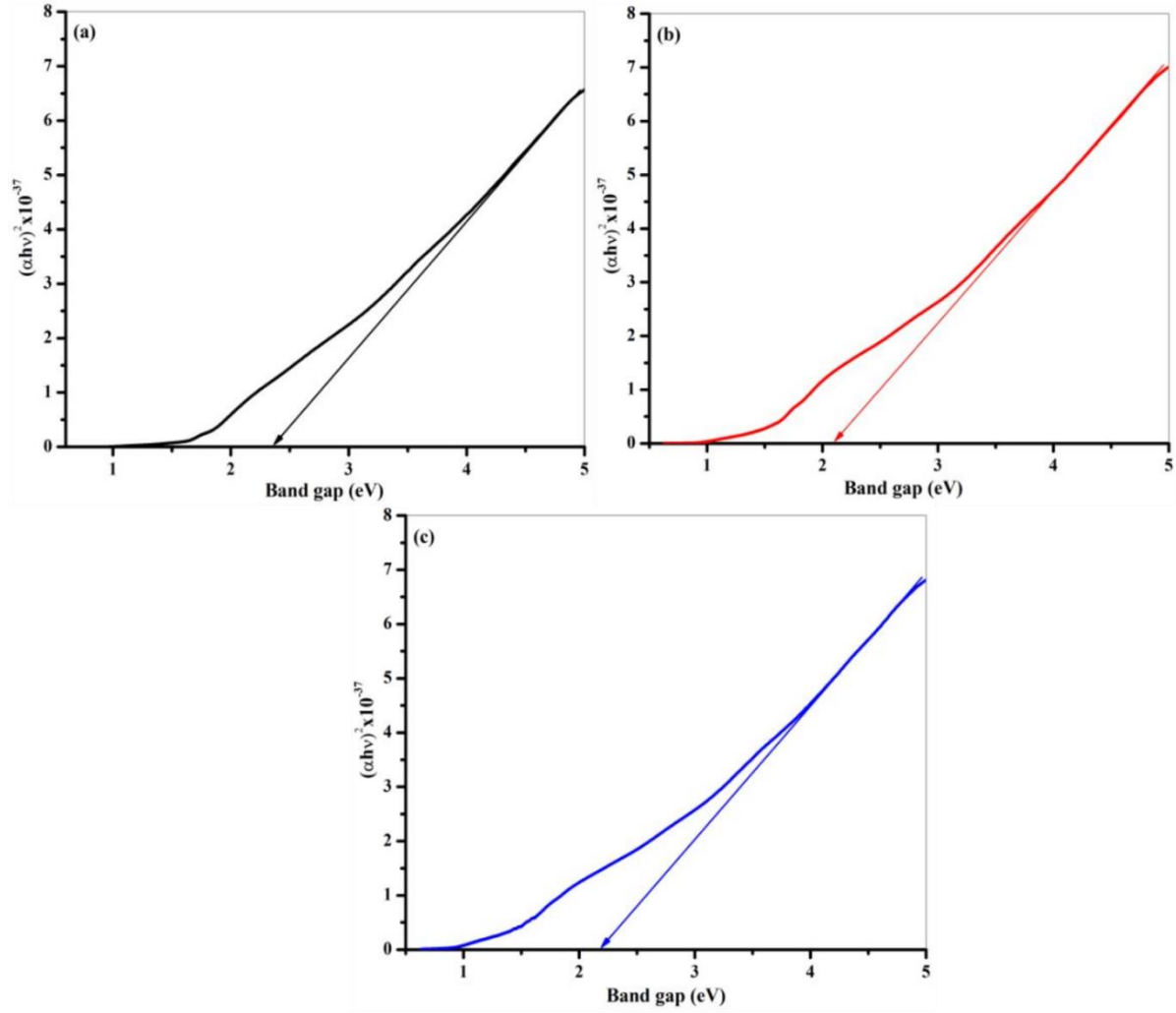
Fig. 5.33 Band gap of $SrFe_{12-2x}Cr_xBi_xO_{19}$ (x=0.0-0.2)

5.3.6 Magnetic analysis

Fig. 5.35 shows the hysteresis loop of $SrFe_{12-2x}Cr_xBi_xO_{19}$ (x=0.0-0.2) samples. These curves reveal the ferromagnetic behaviour of synthesized samples. Magnetic parameters including saturation magnetization (M_s), coercivity (H_c), and remanence (M_r) were determined from these curves. Different external factors can impact the magnetic properties of a material such as the synthesis process, heating temperature, heating time, doping and concentration of dopants [97].The highest value of Hc was found to be 6339.31 Oe for x=0.0. This obtained value of Hc is smaller than the theoretical limit value of $SrFe_{12}O_{19}$ (Hc=7500Oe) reported in the literature [91, 138-140]. The H_c varies from 2759.04 Oe to 6339.31 Oe as shown in **Table 5.11**. It was found that H_c and D vary inversely i.e. the higher the values of D, the lesser the values of H_c as reported by M. Jean et al. [141, 142].
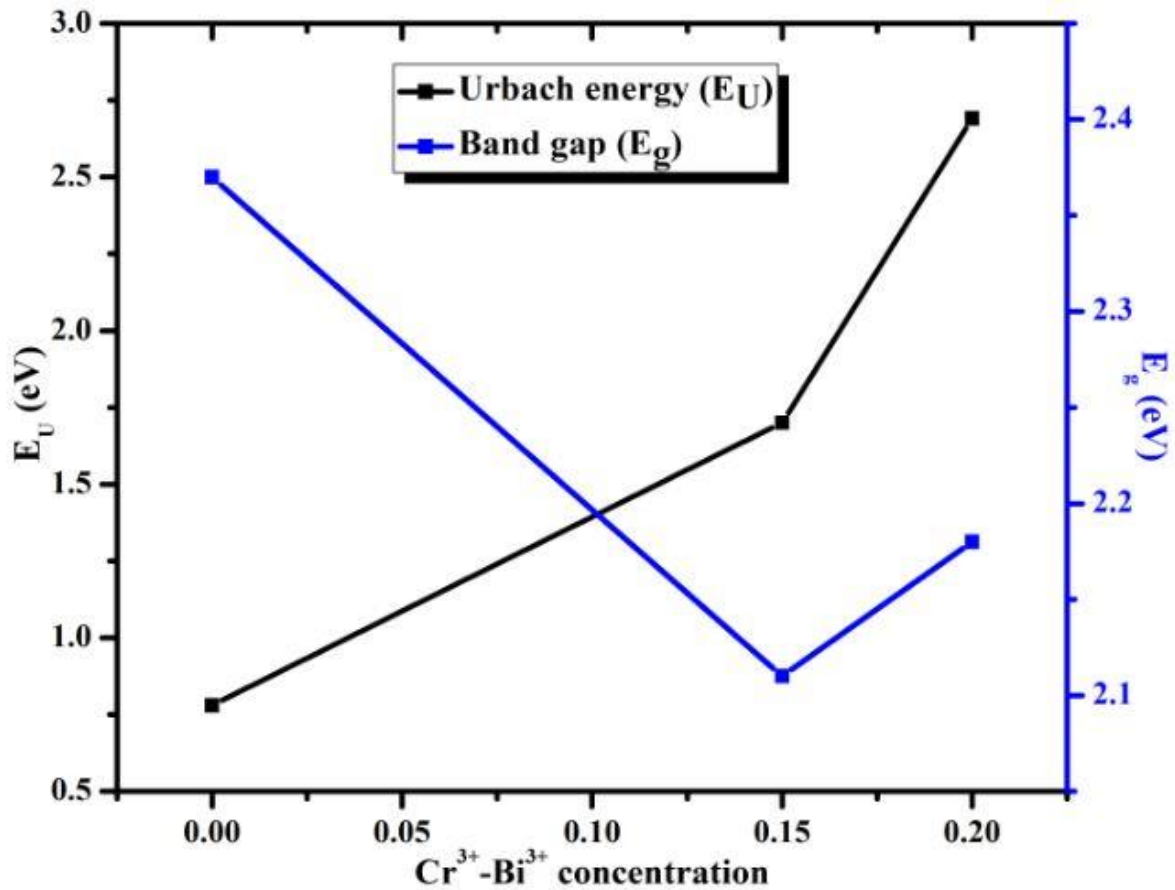
Fig. 5.34 Variation of band gap and Urbach energy with Cr^{3+}-Bi^{3+} concentration

It can be observed that all samples have H_c values higher than 1200 Oe, this makes them useful for magnetic recording media of high density [88, 92]. The value of M_s and M_r was observed to increase gradually with increase in Cr^{3+}-Bi^{3+} concentration. M_s was found to vary between 18.55-64.73 emu/g and M_r varies in the range 9.95-34.27 emu/g. The value of M_s was observed to be highest for x=0.2 (M_s=64.73 emu/g) which is 95.6% of the theoretical value (M_s=67.7 emu/g), this is higher than those observed in other synthesis method (50-60 emu/g) [138, 140]. The observed increase in M_s and M_r can be explained by the distribution of magnetic moments of Cr^{3+}-Bi^{3+} ions on the Fe^{3+} sites which are one tetrahedral sublattice ($4f_1$), one bipyramidal sublattice (2b) and three octahedral sublattice (12k, 2a, and $4f_2$) [115]. In the hexagonal lattice, 12k, 2a and 2b sites have spin up while $4f_1$ and $4f_2$ sites have spin down [93]. It was reported that Cr^{3+} ions with $3\mu_B$ choose to occupy $4f_2$ (down), 12k (up) and 2a (up) sites [143]. Additionally, the increase in M_s and M_r may be explained by the fact that Cr^{3+} ions prefer to occupy $4f_2$ sites in preference to 12k and 2a sites which increased the magnetic moment and therefore the M_s and M_r. However, the preference of occupation of Cr^{3+} ions in 12k, 2a and $4f_2$ site is much influenced by Cr^{3+} ions concentration. Roohani reported that when the concentration of Cr^{3+} ions is less than 0.25, then Cr^{3+} ions move to $4f_2$

sites in preference to 12k and 2a sites and the contrary happens when the Cr^{3+} ions concentration is greater than 0.25 [120]. Unlike Cr^{3+} ions, Bi^{3+} ions are diamagnetic with magnetic moment equal to zero [144]. Hence, no positive contribution to magnetic parameters will be observed. However, the contribution of Bi^{3+} ions to the increase in Ms and Mr values is such as during the heating process, Bi^{3+} ions oxidize to Bi^{5+} ions which move to $4f_1$ sites (spin down) preferentially[145]. The ratio between M_r and M_s has been calculated and values are given in **Table 5.11**. It is observed that M_r/M_s ratio is between 0.503-0.536 which specifies that all prepared samples are in single magnetic domain [32, 47]. Magnetic moment (n_B) and anisotropic constant (K) have been calculated by equations (5.37) and (5.38) respectively [89]:

$$n_B = \frac{M \times M_S}{5585} \tag{5.37}$$

$$2K = \mu_0 M_s H_c \tag{5.38}$$

From **Table 5.11**, we can see that n_B is ranges between 3.53-12.6 μ_B and the values of K found in the range 5.88-9.49. On another hand, both of n_B and K increase with the increasing Cr^{3+}-Bi^{3+} concentration. Equation (5.37) shows the direct proportionality relationship between M_s and n_B, it is observed that magnetic moment increases with saturation magnetization, this scenario can be verified in **Table 5.11**.

Table 5.11 Magnetic parameters for prepared samples

x	Ms (emu/g)	Mr (emu/g)	Hc (Oe)	M_r/M_s	n_B (μ_B)	K (HA^2/Kg)
0.0	18.55	9.95	6339.31	0.536	3.53	5.88
0.15	26.17	13.17	2759.04	0.503	5.08	7.22
0.2	64.73	34.27	2932.42	0.529	12.65	9.49
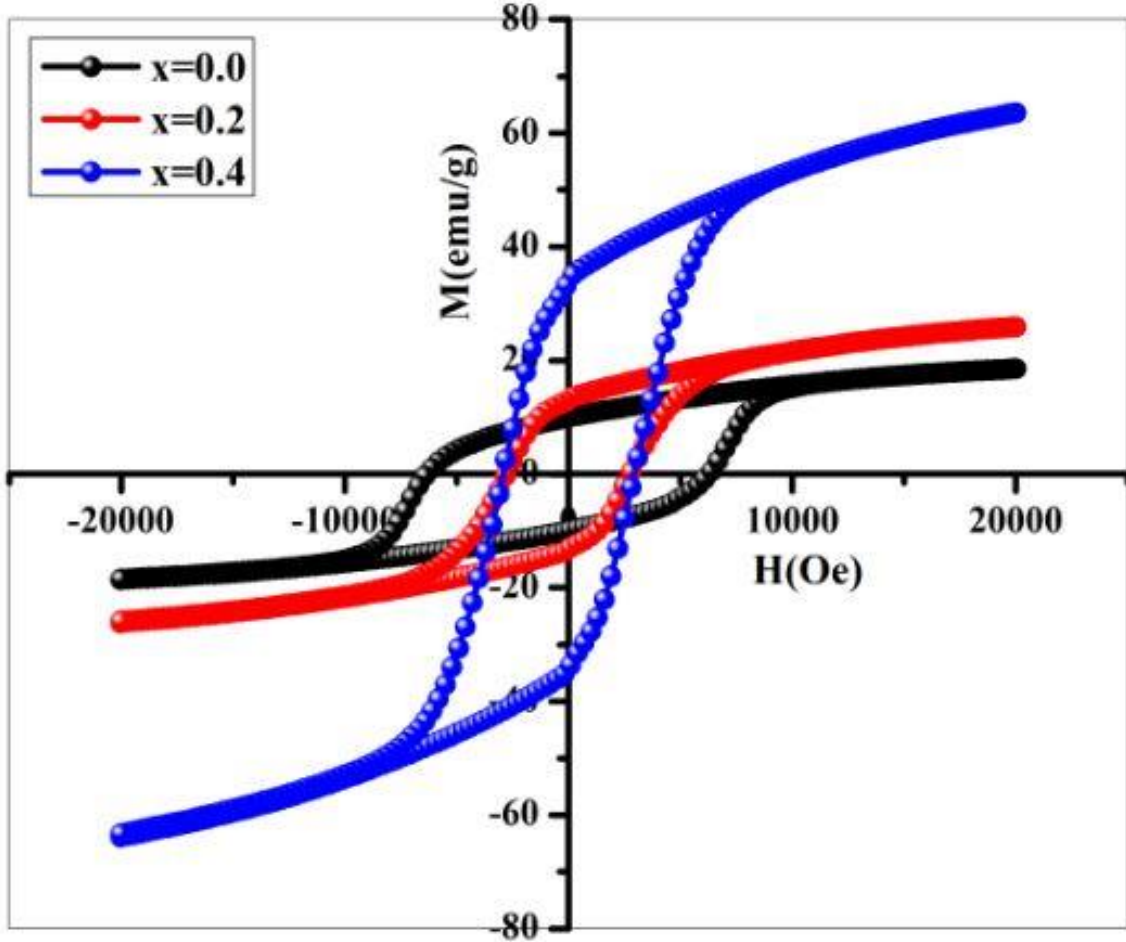
Fig. 5.35 M-H hysteresis loop of $SrFe_{12-2x}Cr_xBi_xO_{19}$ (x=0.0-0.2)

5.3.7 Electrical and dielectric properties

Impedance spectroscopy was employed in order to analyze the dielectric response of the prepared samples. Dielectric constant (ε') of synthesized samples was evaluated using the expression below [32]:

$$\varepsilon' = \frac{Ct}{\varepsilon_0 S} \tag{5.39}$$

Where C is measured in capacitance, ε_0 is permittivity in vacuum space and S represents the surface area of pellet. **Fig. 5.36 and 5.37** gives the variation of dielectric constant (ε') and loss tangent (tan δ_e) versus log of frequency at room temperature of synthesized samples in the frequency range of 100 KHz-120MHz. These figures reveal that dielectric parameters (ε' and tan δ_e) are higher at lower frequencies then decrease with the increase in frequency. This behaviour may be a consequence of two reasons: on the first hand it may be assigned to dipolar and interfacial polarization [89] and on the second hand it may be due to the rapid

variation of applied electrical field which logically increase the polarization. According to Koop, the effectiveness of grain boundaries is more important at lower frequencies whereas that of the grains is more important at higher frequencies which are responsible of the increase in polarization with frequency [108]. Higher values of ε' and tan δ_e observed at lower frequencies can be assigned to the heterogeneity of sample structure caused by Fe^{2+} ions, voids, grain boundary defects and interfacial dislocations [37, 108]. At lower frequencies, the dielectric constant decrease with the increase in frequency of applied field, this observed behavior could be due to space charge polarization as predicted by Maxwell-Wagner and Koop's theory [146]. The dielectric response is a normal behavior for ferrite materials which has been observed by several authors [99, 147]. It is worthy to note that ε' and tan δ_e are related to the stoichiometry, types and number of charge carriers and so on, which in turn depend strongly on factors such as synthesis method of sample, heating treatment, doping and concentration of the dopants [14].
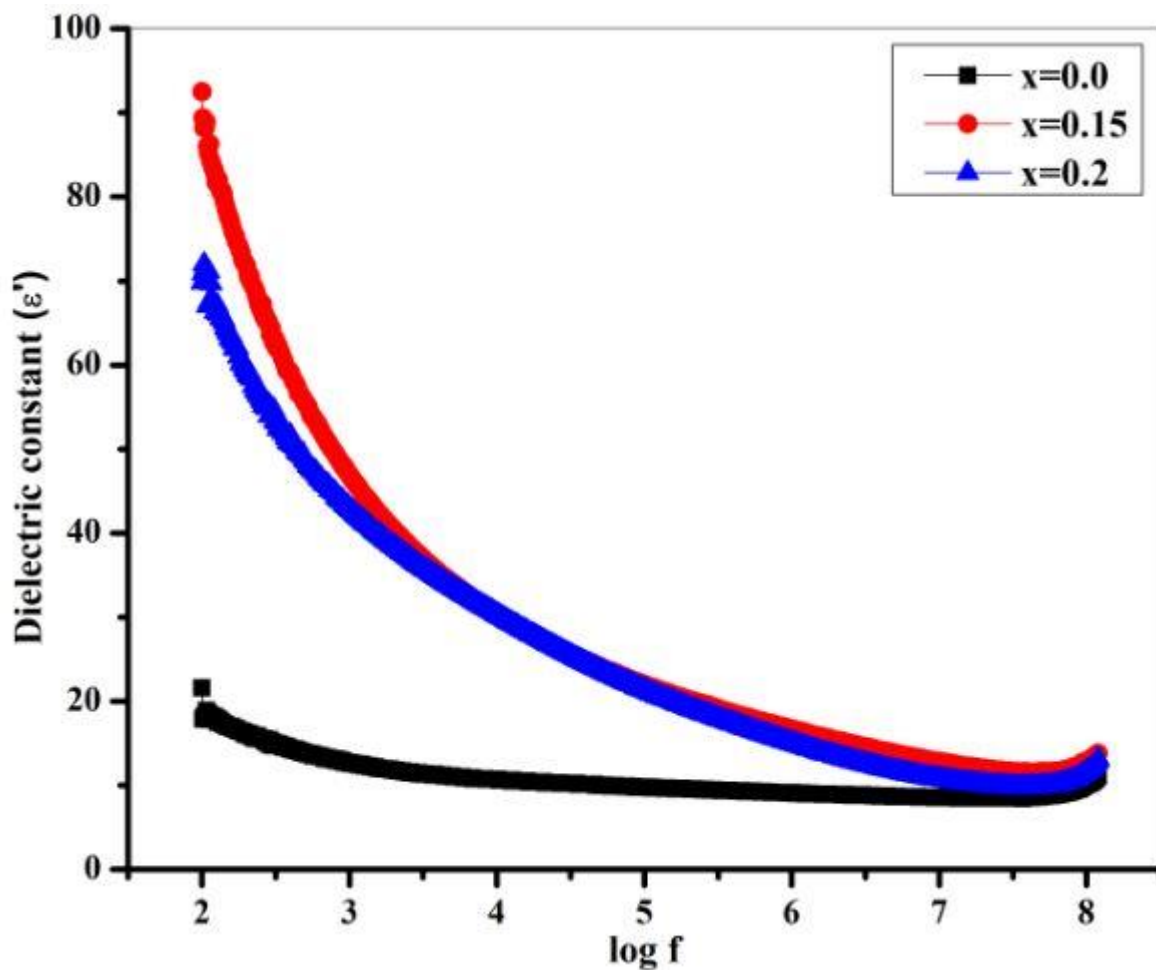
Fig.5.36 Dielectric constant (ε') of $SrFe_{12-2x}Cr_xBi_xO_{19}$ (x=0.0-0.2)

M. Anis-Ur-Rehman has reported the porosity of the material also enhances $\tan \delta_e$ which certainly due to humidity absorbed by the pores [148]. It was also found that ε' increases for $x \leq 0.15$ then decreased. The higher value of dielectric constant (ε') at lower frequency is obtained for $x=0.15$ indicating that with this doping the material is most resistive. The relation below has been used to evaluate AC electrical conductivity (σ_{AC}) of the samples:

$$\sigma_{AC} = \varepsilon_0 \varepsilon' \omega \tan\delta_e \tag{5.40}$$

Where, $\omega = 2\pi f$ is the angular frequency and f the applied field frequency. AC conductivity (σ_{AC}) in ferrites occurs from conduction mechanism. Indeed, the conduction mechanism and dielectric behaviour of ferrites are strongly correlated to the phenomenon of dielectric polarization which is similar to the electric conduction process as mentioned by Iwauchi and Rezlescu [149, 150].
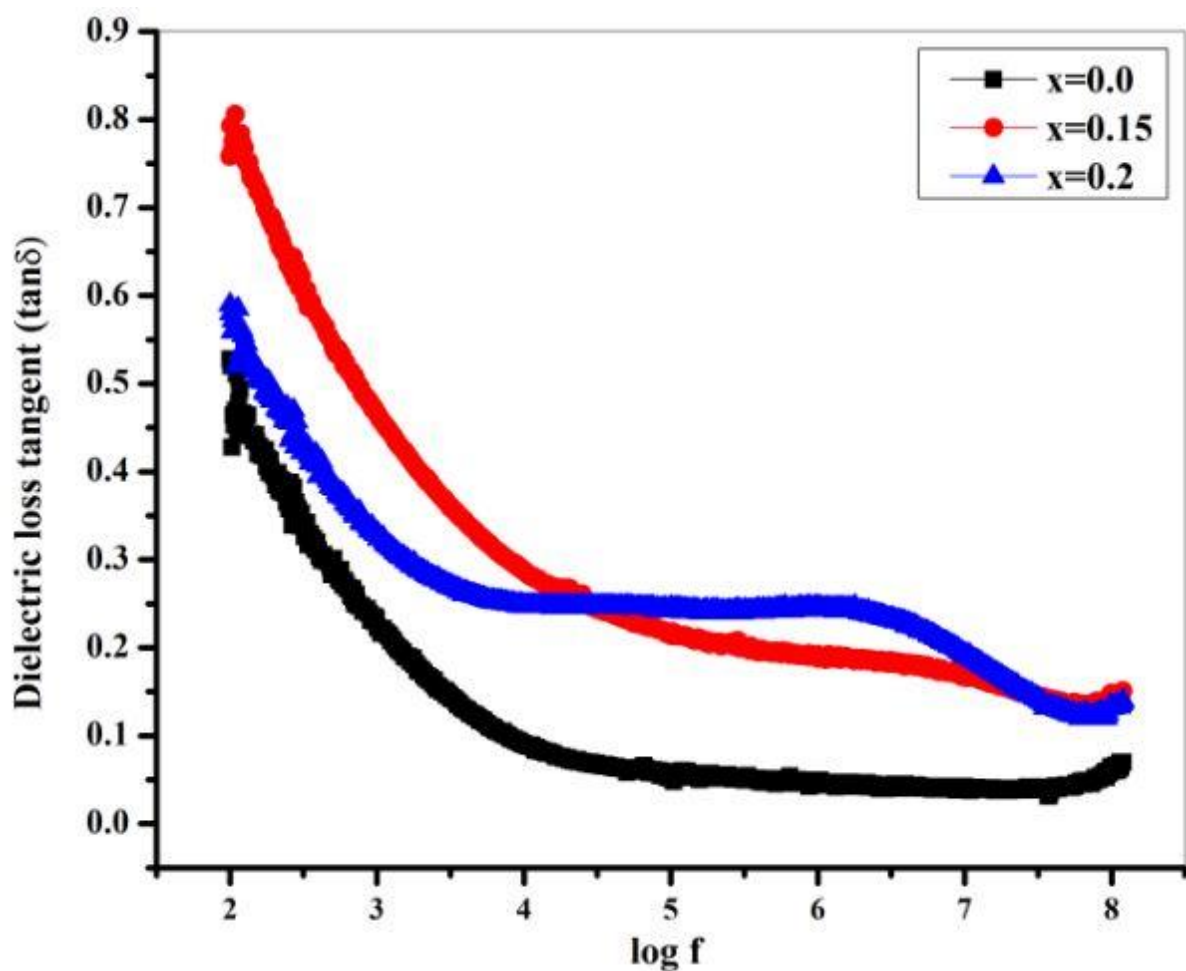
Fig. 5.37 Dielectric tangent loss (tan δ) of $SrFe_{12-2x}Cr_xBi_xO_{19}$ ($x=0.0$-0.2)

The polarization in ferrites originate from heterogeneity of the which result from electron transfer between ferric (Fe^{3+}) and ferrous (Fe^{2+}) ions at the octahedral sites according to the reaction below:

$$Fe^{2+} \leftrightarrow Fe^{3+} + e^-$$
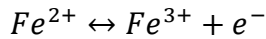
Fig. 5.38 displays the evolution of AC conductivity against logarithm of the frequency of prepared samples in the range 100 KHz-120MHz. It was observed that the conductivity is frequency independent at lower and intermediate frequencies. However, it abruptly increases at higher frequencies. The main reason of this behavior of conductivity is associated to electron exchange between Fe^{3+} and Fe^{2+} ions which increases with applied electrical field. The highest value of conductivity was obtained for x=0.15 indicating that $SrFe_{12-2x}Cr_xBi_xO_{19}$ (x=0.15) is most conductive. This increase in conductivity can also be a direct result of the decrease observed in dielectric constant. The total conductivity is defined as the sum of two terms given below [96, 151]:

$$\sigma_T = \sigma_{DC} + \sigma_{AC} \tag{5.41}$$

where the first part $\sigma_{DC} = \sigma(T)$ indicate the DC conductivity as a function of temperature and can be expressed according to the Arrhenius relation [152]:

$$\sigma_{DC} = \sigma_0 e^{-E/kT} \tag{5.42}$$

Here E represents the energy of activation, k is constant of Boltzmann and σ_0 as pre-exponential constant. This conductivity refers to the drift mobility of free charge carriers. The second part $\sigma_2 = \sigma(\omega, T)$ is temperature and frequency dependent function which represents AC conductivity and can be defined as [153, 154]:

$$\sigma_{AC} = A\omega^s \tag{5.43}$$

$$ln\sigma(\omega, T) = pln\omega + lnA(T) \tag{5.44}$$

$\omega = 2\pi f$ is angular frequency, $A(T)$ is a temperature and intrinsic property dependent constant of the material, $s(T)$ is a temperature dependent variable varying between 0 and 1 [155]. The estimation of exponent 's' can be done by plotting $\ln \sigma(\omega, T)$ as a function of $\ln \omega$ according to the equation (15).
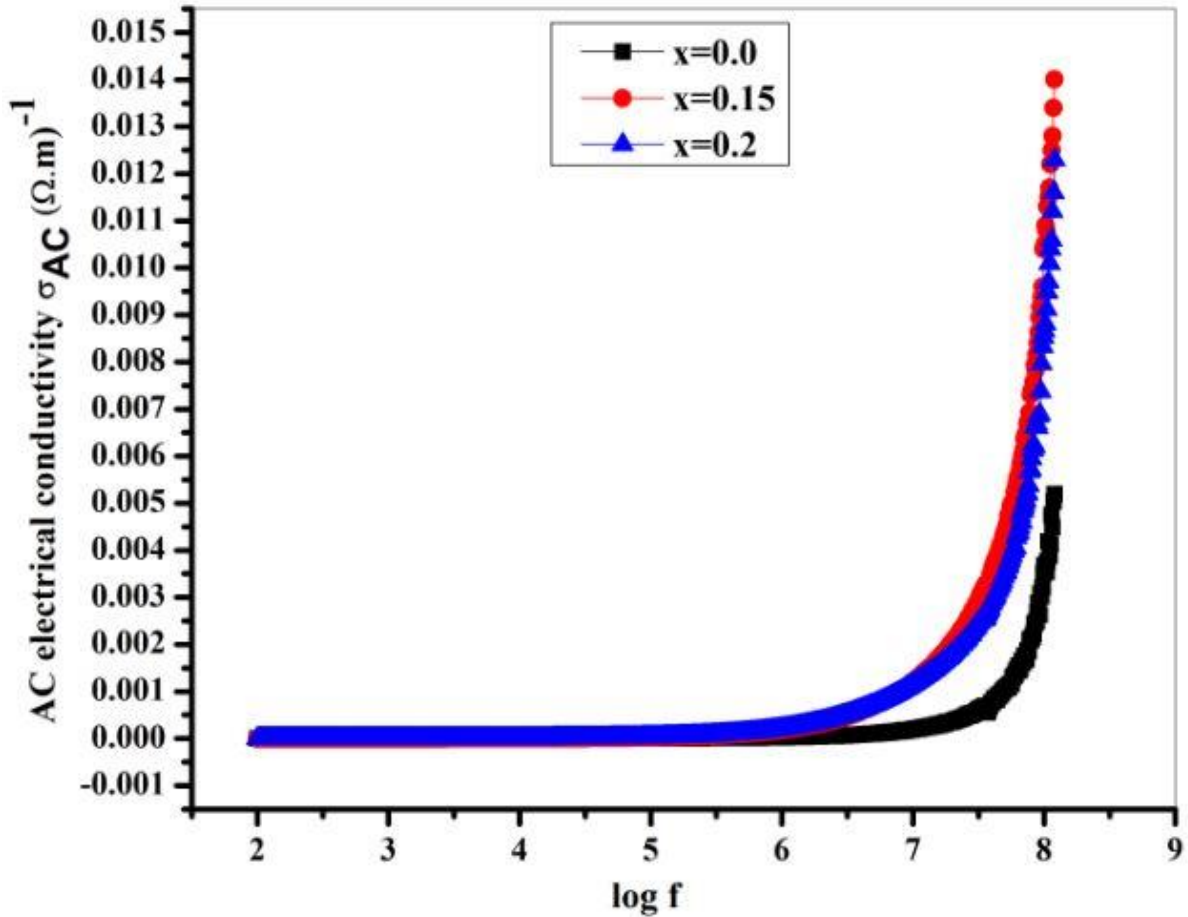
Fig. 5.38 AC conductivity (σ_{AC}) of $SrFe_{12-2x}Cr_xBi_xO_{19}$ (x=0.0-0.2)

Fig. 5.39 shows the plot of $\ln \sigma_{AC}$ with $\ln \omega$. It can be observed that obtained plots are an almost straight line which is confirmed by equation (16). From equation (16), exponent 's' represents the slope of the straight line and $\ln A(T)$ is the intercept with vertical axis ($\ln\omega$=0). According to the value of 's', it is possible to know the origin of conduction. If $s = 0$, the electrical conduction originate from DC conduction and if $s \neq 0$, the electrical conduction originate from AC conduction [24]. From **Fig. 5.39**, exponent 's' was observed to be 0.785, 0.744 and 0.779 for x=0.0, x=0.15 and x=0.2 respectively. Hence it can be deduced that the domination of the conductivity in the samples occurs from AC conduction which is linked to electron transfer between Fe^{3+} and Fe^{2+} ions.

Fig. 5.40 and **5.41** present the present the real (Z') and imaginary (Z'') part of complex impedance of prepared samples at room temperature as a function of applied field frequency in the range 100 KHz-120MHz also called Nyquist plots of impedance. Both Z' and Z'' for all samples was showing a decrease at lower frequencies, then became unchangeable from intermediate to higher frequencies with rising of applied frequency.
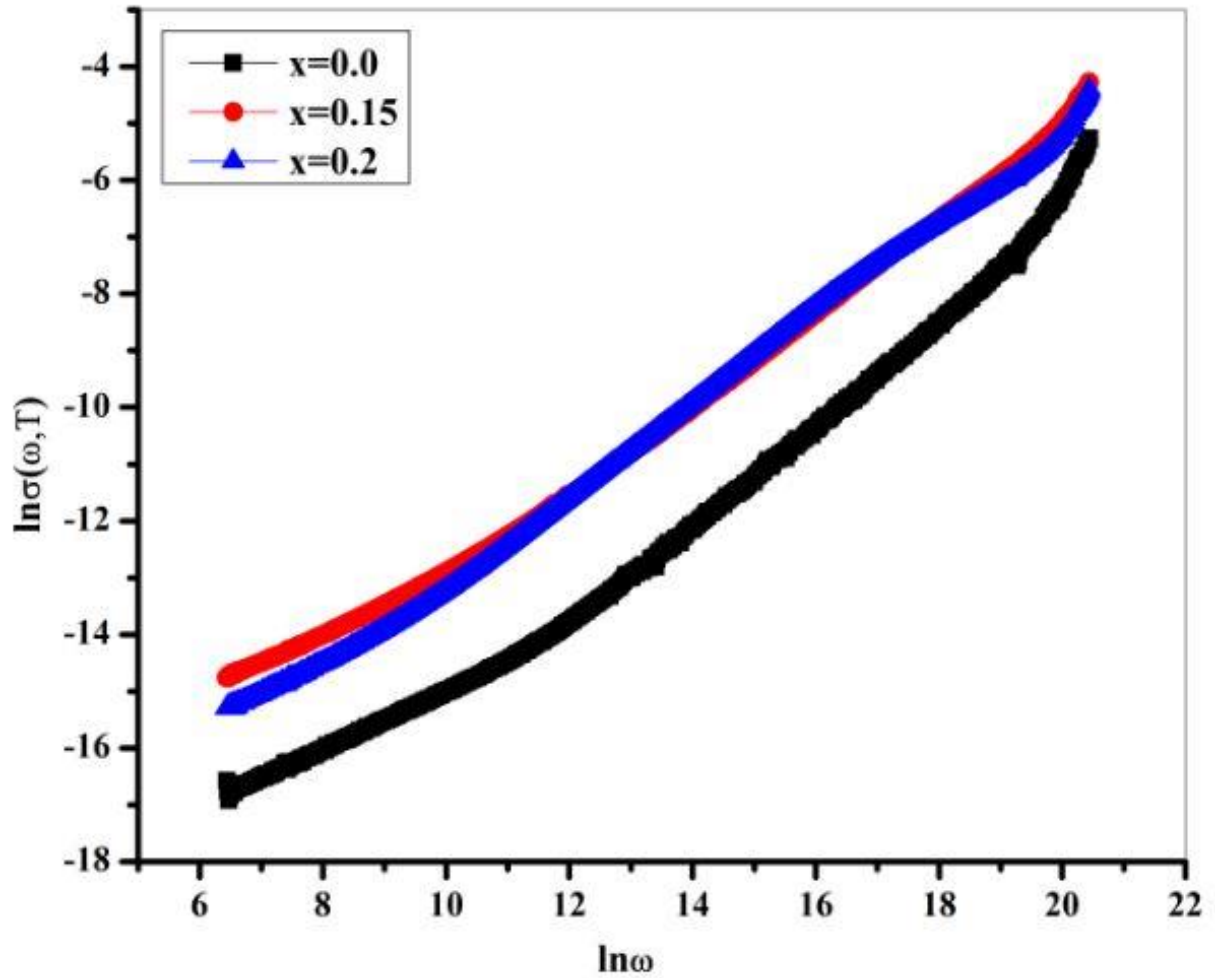
Fig. 5.39 Variation of ln $\sigma(\omega, T)$ with lnω for SrFe$_{12-2x}$Cr$_x$Bi$_x$O$_{19}$ (x=0.0-0.2)

This decrease in complex impedance (Z*) shows the probability of increase in AC conductivity. Within a heterogeneous structure, the contribution of grain boundaries for electrical properties can be well appreciated by Nyquist plot. **Fig. 5.42** presents Nyquist plots of impedance (Z'' vs Z') of prepared samples. In general, Nyquist plot consist of three semicircles where the semicircle at the left side (higher frequencies) shows the contribution of grain, the semicircle on the middle (intermediate frequencies) represents the contribution of grain boundaries while the semicircle at the right side (lower frequencies) gives the contribution of interface [156]. The radii of semicircles gives the resistance of grains, grain boundaries and interface according to the region of the sample [157]. In the present work, we did not observed three semicircles. The contribution of grains cannot be observed because of very weak presence of semicircles at higher frequency of applied field. The observed arcs at

103

lower frequencies can be assigned to grain boundaries resistance contribution and therefore, only grain boundaries are responsible for the high dielectric constant at lower frequencies. This lead to deduce that Nyquist plot reveal the insulating behavior of samples at lower frequencies which become semiconductor at higher frequencies [158]. Comparing the radii of semicircles, it was observed that the grain boundaries resistance contribution declines then rise with Cr^{3+}-Bi^{3+} concentration.
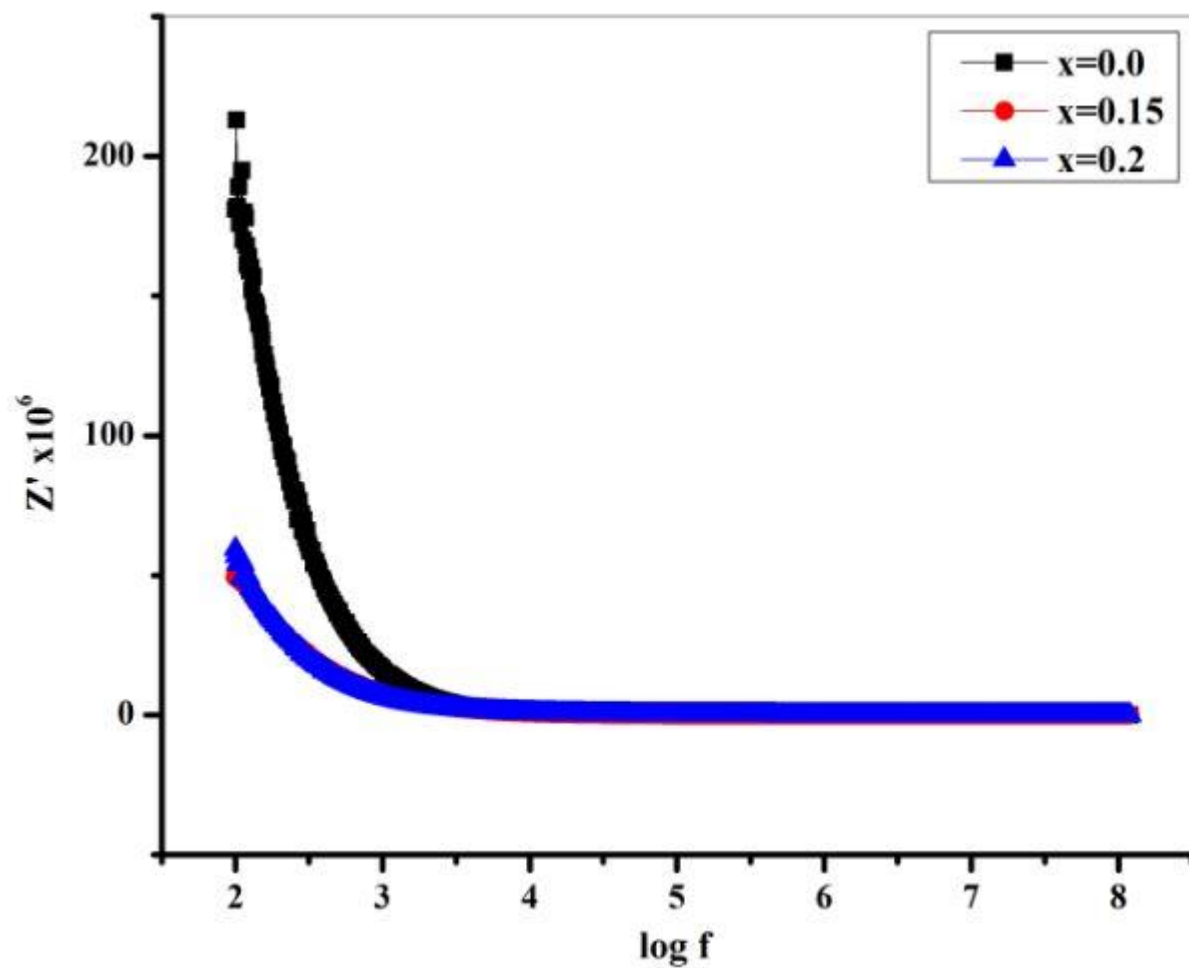
Fig. 5.40 Real part of complex impedance (Z') for $SrFe_{12-2x}Cr_xBi_xO_{19}$ (x=0.0-0.2)
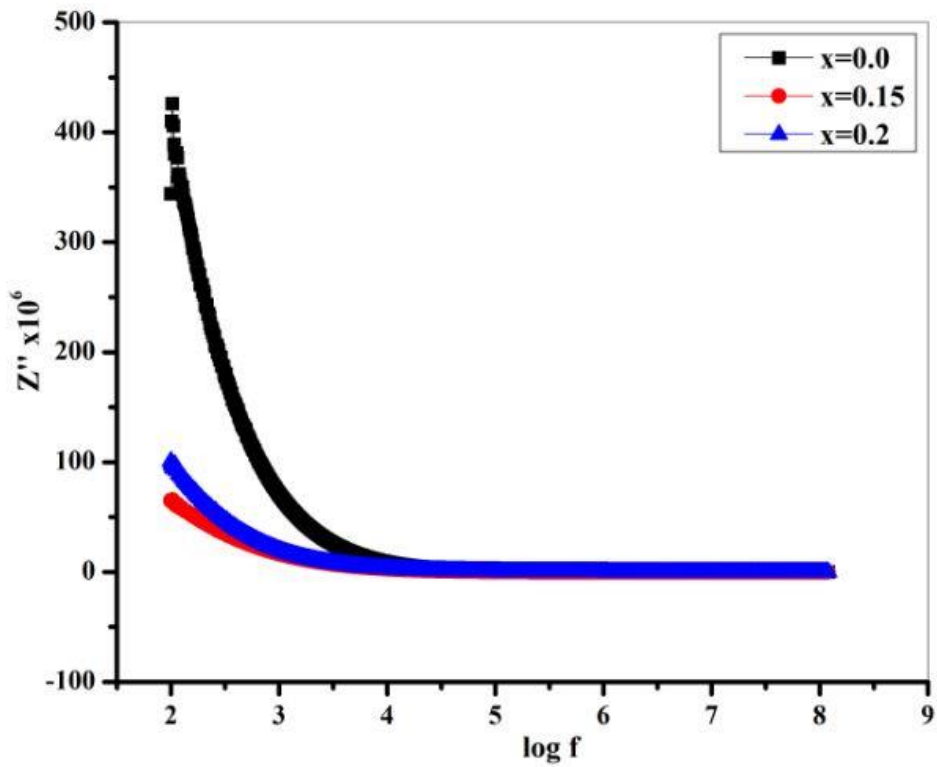
Fig. 5.41 Imaginary part of complex impedance (Z'') for $SrFe_{12-2x}Cr_xBi_xO_{19}$ (x=0.0-0.2)
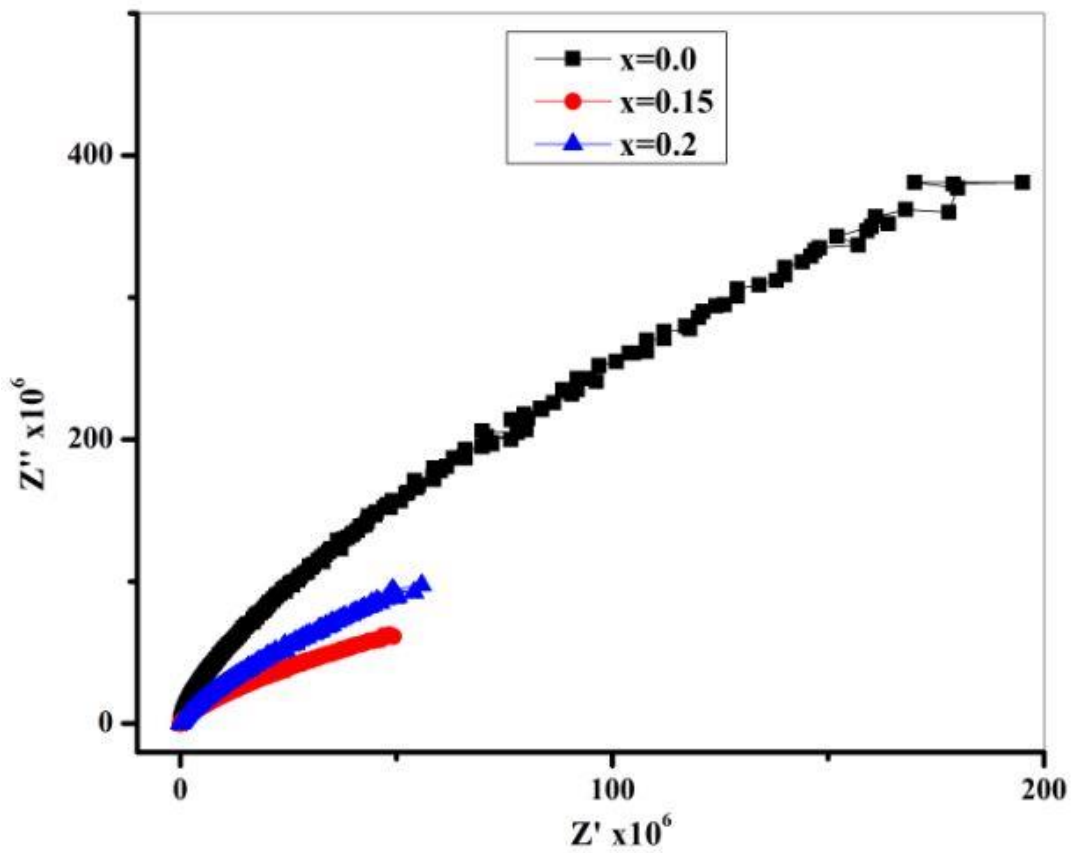
Fig. 5.42 Nyquist plots of $SrFe_{12-2x}Cr_xBi_xO_{19}$ (x=0.0-0.2)

5.4 Effect of Cr-Ni substitution on optical, electrical and magnetic properties of Co₂Y barium hexaferrite

5.4.1 XRD analysis

XRD patterns of Co₂Y hexaferrite $Ba_{2-2x}Cr_xNi_xCo_2Fe_{12}O_{22}$ (x=0.0-0.15) is given in **Fig. 5.43**. The observed diffraction peaks in this figure have been indexed using as JCPDS card: 440206 [159]. These peaks correspond to diffraction planes (0012), (110), (113), (1013), (116), (119), (0210) and (0315) in which certain peaks were reported by R. Jotania and P. Patel [160]. These obtained planes refer to Y-type hexaferrite phase with R-3m as space group. It can be noticed that all sintered samples show a single phase which is confirmed by the absence of any impurity. The lack of any second phase in XRD patterns can indicate that substituted ions have perfectly occupied crystallographic sites of Ba^{2+} ions. In order to confirm these results, Rietveld refinement was carried out in the goal to confirm the purity of prepared samples revealed by XRD patterns. It can be observed that the diffraction planes of experiment data obtained from XRD analysis (Ycal) match with and the theoretical data (Yobs) which confirm the single phase of the structure. The parameters that justify the accuracy of fit were found to be $1.10 \leq GoF \leq 1.30$, $16.60\% \leq R_p \leq 20.40\%$, $14.40\% \leq R_{wp} \leq 18.80\%$, $12.90\% \leq R_{exp} \leq 14.30\%$ (**Table 1**). In the background (blue line) of Rietveld refinement, a peak can be observed at around 35.42°. This peak is the diffraction plane (0015) which is also a plane of the Y-type hexaferrite structure as revealed by the XRD diffraction. It was observed that the intensity of (0015) peak increases with Cr^{3+}-Ni^{2+} concentration which may indicate that Cr^{3+}-Ni^{2+} ions favor the formation of that plane (**Fig. 1**). Others information such as unit cell constant (a, c) and volume (V_{cell}) were estimated by hexagonal formulae [161]:

$$\frac{1}{d_{hkl}^2} = \frac{4}{3}\left(\frac{h^2+hk+k^2}{a^2}\right) + \frac{l^2}{c^2} \tag{5.45}$$

$$V_{cell} = a^2 c \, sin\gamma \tag{5.46}$$

In these formulae, d and hkl represent d-spacing between two consecutive planes and miller indices respectively, $\gamma = 120$ which is angle between x and y-axis in the representation (x, y, z).

Lattice parameters and volume of unit cell are reported in **Table 5.12**. It can be observed that *a, c* and *V* were found to be between 5.8611-5.8648 Å, 43.5088-43.398 Å and 1294.381-1292.727 Å³ respectively. These results are close to those reported by M. Zhang et al. [162].

It is observed that *a* parameter increases whereas *c* parameter decreases. This observed fluctuation in parameters *a* and *c* led to a decrease in volume of unit cell which result from substituted ions. Indeed, after a substitution, the crystal structure generally undergoes a distortion (shrinkage or stretching) because of ionic radii of dopants. In the present research work, Ba^{2+} ions ($r_{Ba^{2+}}$=1.49 Å [163]) was replaced by Cr^{3+} ($r_{Cr^{3+}}$=0.52 Å [164]) and Ni^{2+} ($r_{Ni^{2+}}$=0.83 Å [165]) ions which caused the observed decrease in *V*. It was also observed that the intensity of peaks slightly decrease with Cr-Ni concentration. The calculation of *c/a* ratio is worth to confirm the Y-type hexagonal structure. The *c/a* ratio of prepared samples was found to be 7.39-7.43 which is in agreement with values reported by Ali et al [166].

The crystallite size (*D*), calculated density (d_x), experimental density (d_m), porosity (*P*) and specific surface area (*S*) were estimated by below formulae:

$$D = \frac{k\lambda}{\beta \cos \theta} \tag{5.47}$$

$$d_m = \frac{m}{V_p} \tag{5.48}$$

$$d_x = \frac{nM}{N_A V} \tag{5.49}$$

$$P = (1 - {d_m}/{d_x}) \times 100 \tag{5.50}$$

$$S = \frac{6000}{D d_x} \tag{5.51}$$

where *k*=0.94 is the Sherrer's constant [167], *m* and V_P are respectively the mass and volume of pellet, *n*=3 (for Y-type hexaferrite), and *M* are respectively the number of atom per unit cell, molecular weight of sample.

From **Table 5.12**, it is observed that d_x from 5.444 to 5.356 g/cm³ decreases with Cr-Ni content. These values are closed to those found by S. Bierlich and J. Topfer [168]. The calculated density of undoped sample is 0.11% less than theoretical density (5.45 g/cm³) reported by G.F.M. Pires Júnior et al. [169]. This observed decrease is related to the fact that the molecular weight of pure Co_2-Y type hexaferrite ($Ba_2Co_2Fe_{12}O_{22}$) decreases after replacing Ba^{2+} ions by Cr^{3+} and Ni^{2+} ions. This is especially due to atomic weights of Cr (52.01amu) and Ni (58.69amu) which are smaller than that of Ba (137.36amu) [170]. The experimental density was found to be between 2.5-3.1g/cm³. It is noticed that d_m is smaller

than d_x. The reason of this can be explained by the appearance of pores during the heating process [166]. The porosity of sample has been estimated and found to increase from 47.58 to 57.93%. The crystallite size and specific surface area were found to vary between 31.73-34 nm and 32.43-35.13 cm^2/g respectively. It can be observed that slighter the crystallite size, larger the surface area, which indicates there are more atoms present on the surface. This observation has been reported by Talwinder [40].
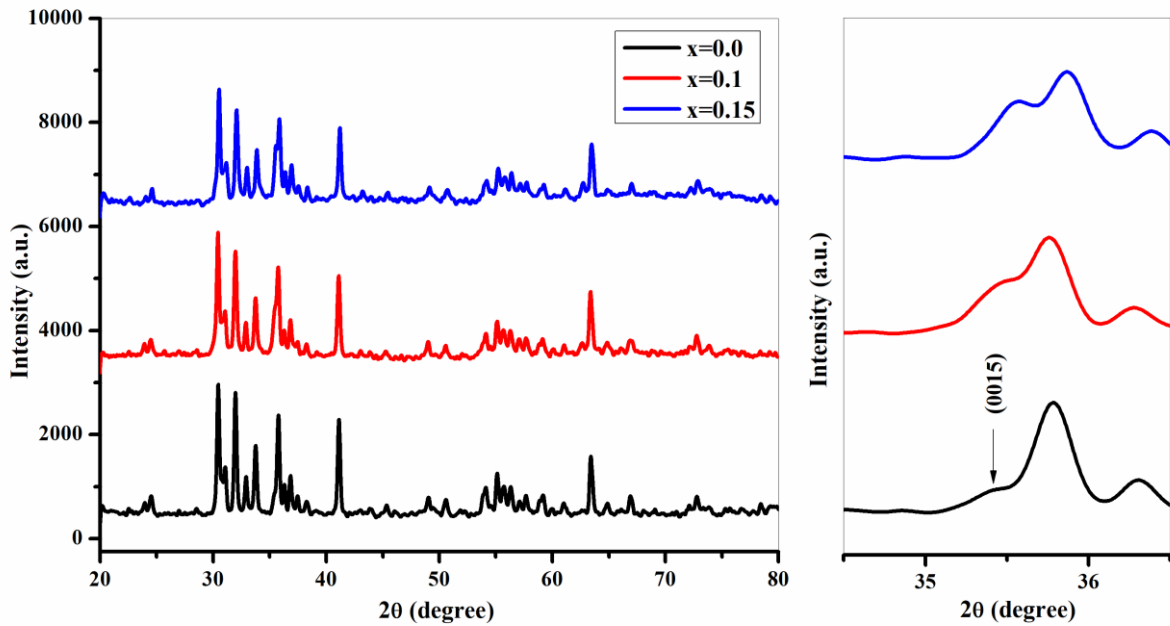
Fig. 5.43 XRD of Ba$_{2-2x}$Cr$_x$Ni$_x$Co$_2$Fe$_{12}$O$_{22}$ (x=0.0, 0.1, 0.15)

5.4.2 FTIR analysis

Fig. 5.45 gives FTIR spectra of prepared Y-type hexaferrite sintered for 6 hours at 1100°C in the wavenumber range 400-4000 nm. As spinel and M-type hexagonal ferrites, characteristic absorption bands of formation of Y-type hexaferrite also appear between 400-600 nm ranges. This is probably due to the fact that, even Y-type hexaferrite also contains spinel block. The signature of formation of Y-type hexaferrite Ba$_{2-2x}$Cr$_x$Ni$_x$Co$_2$Fe$_{12}$O$_{22}$ (x=0.0,0.1,0.15) were observed exactly at 408 and 590 cm^{-1} wavenumber which refer to the metal-oxygen stretching vibration at tetrahedral and octahedral lattice sites [30].
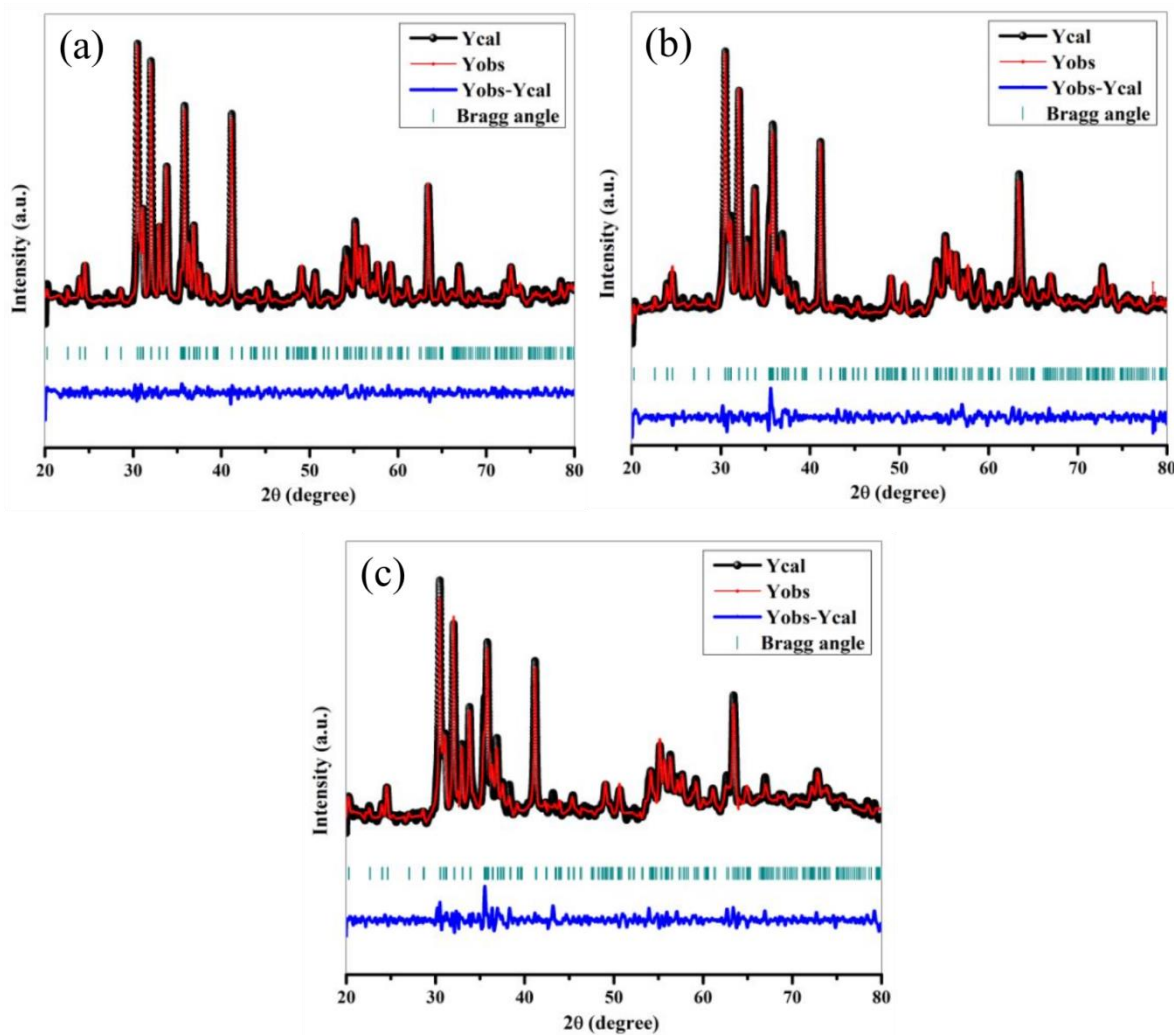
Fig. 5.44 Rietveld refinement (a) x=0.0, (b) x=0.1 and (c) x=0.15 of Ba$_{2-2x}$Cr$_x$Ni$_x$Co$_2$Fe$_{12}$O$_{22}$ (x=0.0, 0.1, 0.15)

Indeed, the band observed at 408 cm^{-1} refers to Fe-O vibration in Fe-O$_4$ (tetrahedral sites) whereas the absorption band at 590 cm^{-1} corresponds to Fe-O vibration in Fe-O$_6$ (octahedral sites) [55, 171]. FTIR spectra also reveal the presence of small absorption band at around 1581 cm^{-1} which indicates the anti-symmetrical vibration of CO$_2^-$ group [172] which certainly occurs from citric acid used. The absence of the vibration of HO$^-$ group between 3200 cm^{-1} and 3500 cm^{-1} confirms that there is no presence of water in the sample.

Table 5.12 Lattice parameters, densities, crystallite size, porosity, surface area and reliability factors of $Ba_{2-2x}Cr_xNi_xCo_2Fe_{12}O_{22}$ ($x=0.0, 0.1, 0.15$)

x	0.0	0.1	0.15
D (nm)	33.99	31.73	32.82
a (Å)	5.8611	5.8615	5.8648
c (Å)	43.5088	43.4824	43.398
V_{cell} (Å³)	1294.381	1293.769	1292.727
c/a	7.4233	7.4183	7.399
a (Å) (Rietveld)	5.860573	5.861522	5.856658
c (Å) (Rietveld)	43.499847	43.483006	43.393703
V_{cell} (Å³) (Rietveld)	1293.894(0.021)	1293.812(0.029)	1289.012 (0.120)
c/a (Rietveld)	7.422456	7.418381	7.409294
R_{bragg} (%)	5.10	6.73	8.26
R_p (%)	16.60	18.90	20.40
R_{wp} (%)	14.40	16.50	18.80
R_{exp} (%)	12.90	13.70	14.30
GoF	1.10	1.20	1.30
χ^2	1.235	1.44	1.721
Number of phase	1	1	1
ρ_{cal} (g/cm³)	5.444	5.383	5.356
ρ_{exp} (g/cm³)	2.853	2.5	3.102
P (%)	47.585	53.56	57.93
$S \times 10^7$ (cm²/g)	32.43	35.128	34.13

5.4.3 Raman spectroscopy

In order to confirm the observed single phase of Y-type hexaferrite $Ba_{2-2x}Cr_xNi_xCo_2Fe_{12}O_{22}$ ($x=0.0, 0.1, 0.15$) revealed by XRD analysis, Raman spectroscopy has been done. It is very important to know that Raman spectroscopy is a very sensitive technique to vibrational states. Raman spectra of prepared samples are given in **Fig. 5.46**. From this figure, different peaks were observed at 760, 686[1], 482, 409, 377, 340, 308, 237, 189 and 173 cm^{-1}. According to our researches, we noticed that there is very less investigations on Raman spectroscopy of Y-type hexaferrite. Then, it is very difficult to attribute the majority of previous wavenumbers to vibrational modes. However, the observed peaks in **Fig. 5.46** were found to be close to those found by Khanduri et al. [173] where peaks at 189 and 173 cm^{-1} correspond to the vibration of spinel block with E_{1g} symmetry as reported Kreisel and Jibrin [102, 133]. These peaks observed at 189 and 173 cm^{-1} are justified by the fact that Y-type hexaferrite consist of

spinel block. Moreover, it is noticed that, by adding of Cr-Ni concentration, peaks slightly shift towards high wavenumber values (blue shift) as shown in **Fig. 5.46**.
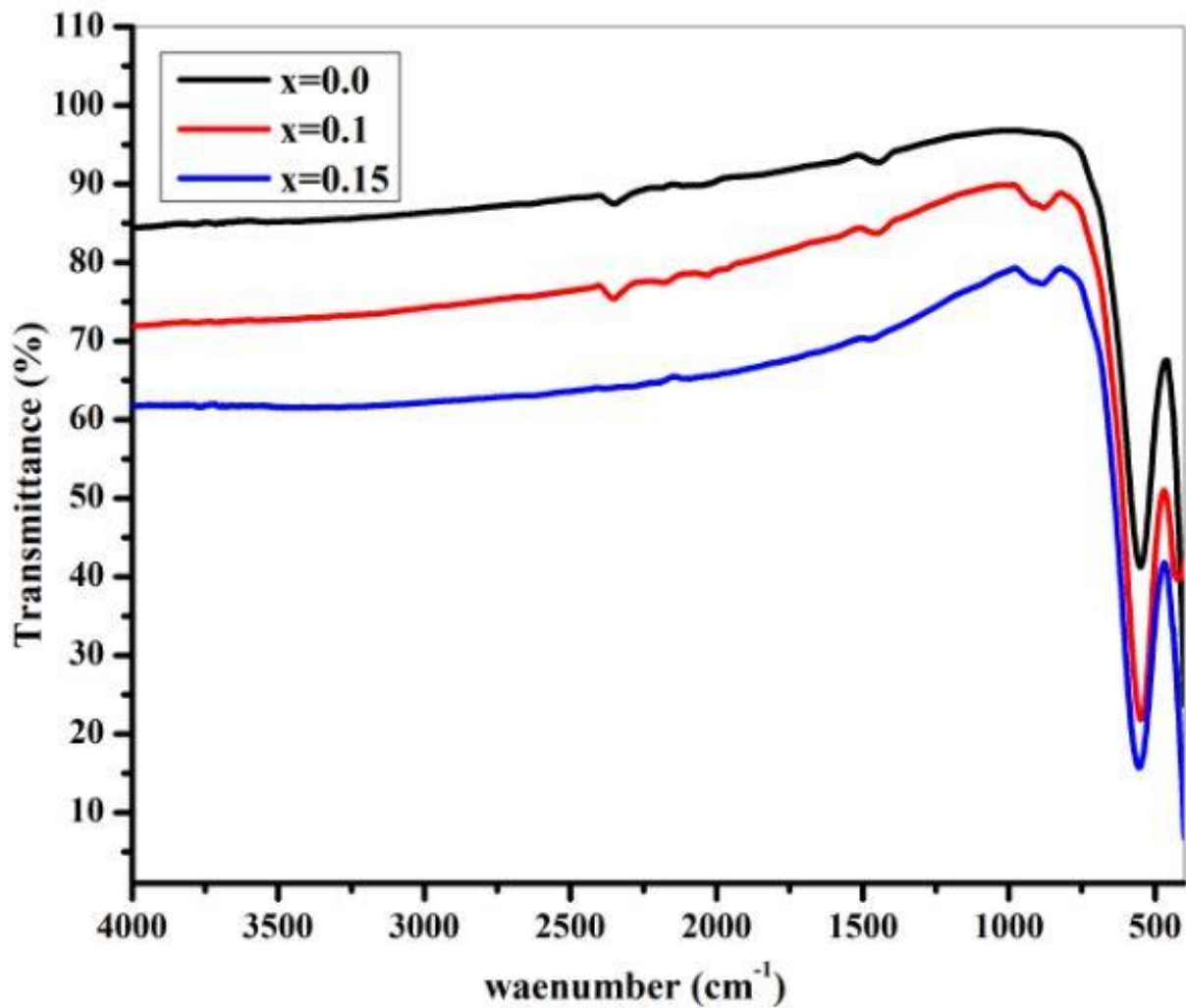
Fig. 5.45 FTIR spectra of $Ba_{2-2x}Cr_xNi_xCo_2Fe_{12}O_{22}$ (x=0.0, 0.1, 0.15)
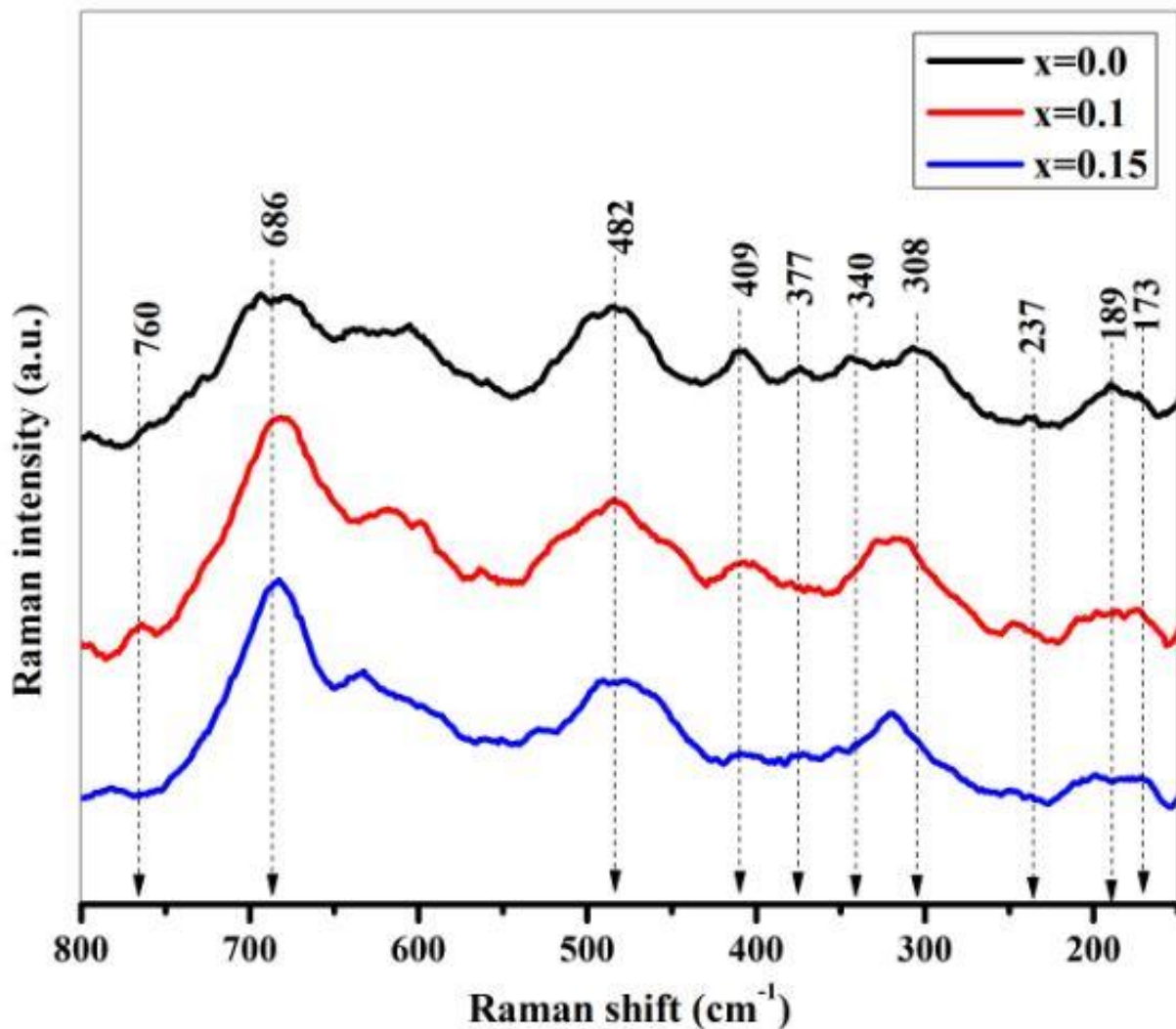
Fig. 5.46 Raman spectra of $Ba_{2-2x}Cr_xNi_xCo_2Fe_{12}O_{22}$ (x=0.0, 0.1, 0.15)

5.4.4 FESEM, EDX and mapping analysis

Fig. 5.47 (a-c) presents FESEM images for Y-type hexaferrite $Ba_{2-2x}Cr_xNi_xCo_2Fe_{12}O_{22}$ (x=0.0 and x=0.15) prepared at $1100°$ C for 6 hours. First of all, it is noticed that the prepared samples show a flat hexagonal shape and non-uniform of particles. This similar shape of Y-type hexaferrite was reported by O. Mirzaee who reported that this kind of observed shape of particles is crucial in Y-type hexaferrite applications [174]. Then, a homogeneous distribution of particles is observed, this is one of the advantages of using sol-gel method. Magnetic interactions and high temperature should be the origin of the agglomeration of particles as presented in micrographs. From FESEM images, particles size has been evaluated. **Fig. 5.47**

(b-d) shows that particles follow a normal distribution with an average particles size of 0.167 µm and 0.165 µm for x=0.0 and x=0.15 respectively. It is deduced that particles size decreases with Cr-Ni concentration. EDX and Mapping analysis were carried out to study the composition of samples. From **Fig. 5.48**, it can observed that only chemical elements that constitute $Ba_{2-2x}Cr_xNi_xCo_2Fe_{12}O_{22}$ (x=0.0 and x=0.15) are showing with their weight percent. The presence of no extra element confirms the purity revealed by XRD analysis.
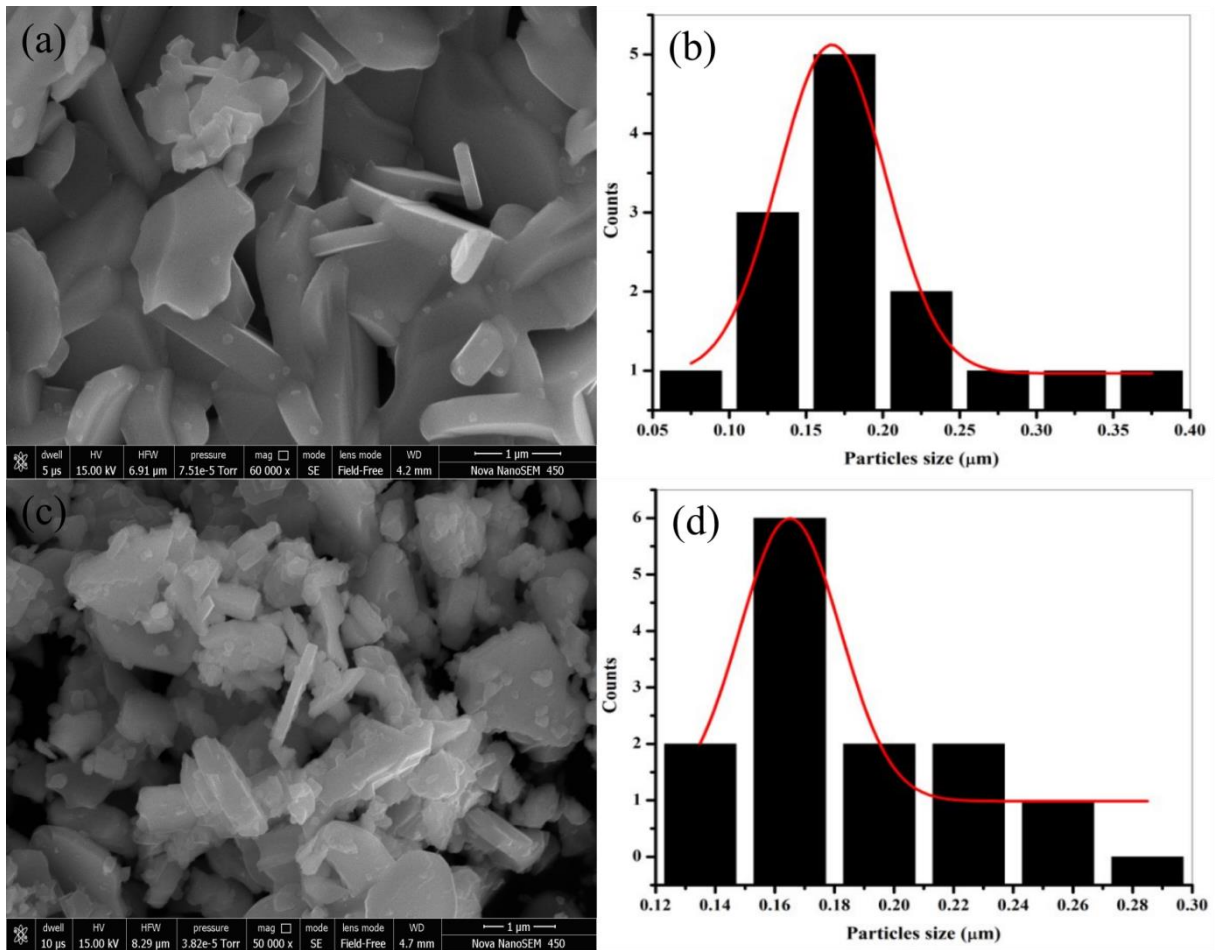
Fig. 5.47 FESEM micrographs (a) x=0.0 and (c) x=0.15 and particles distribution (b) x=0.0 and (d) x=0.15 of $Ba_{2-2x}Cr_xNi_xCo_2Fe_{12}O_{22}$
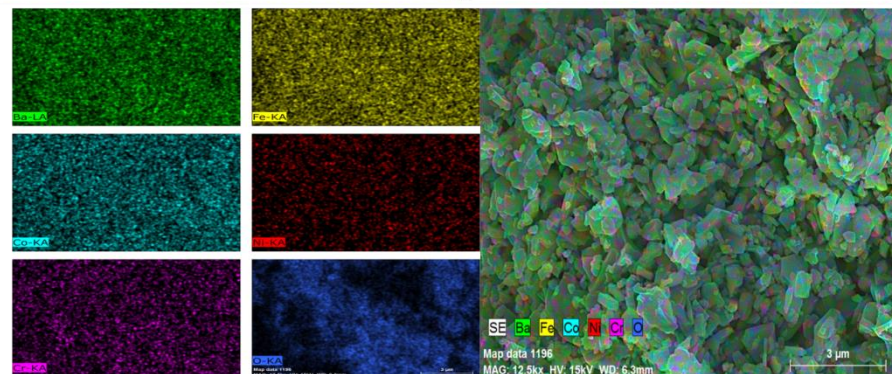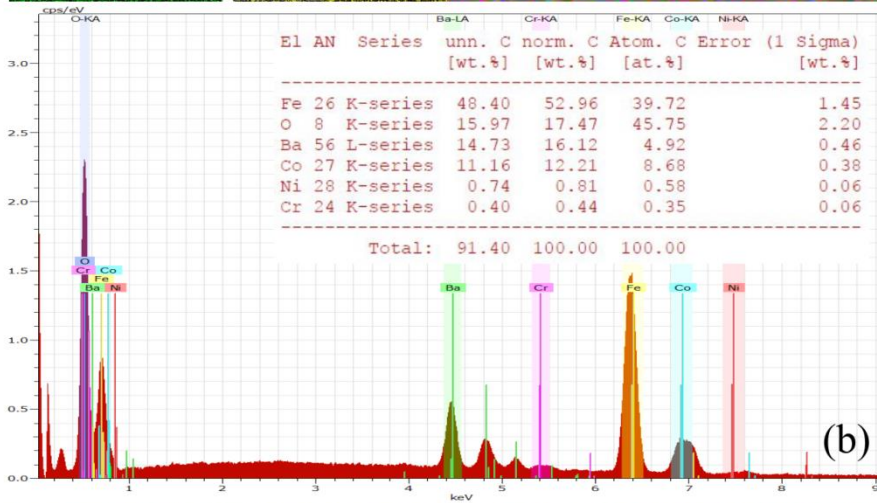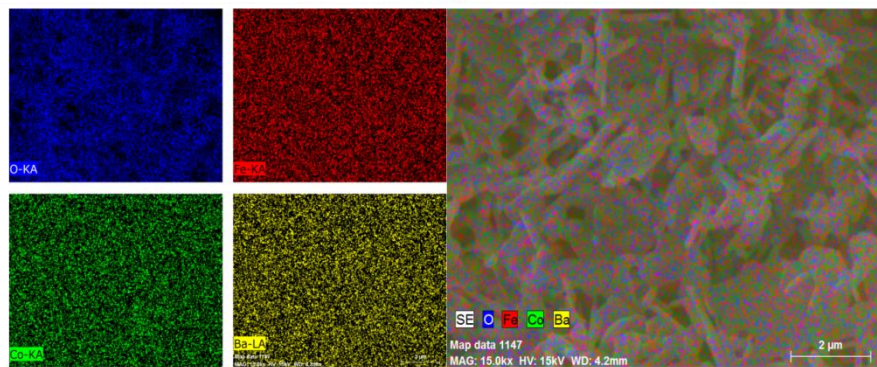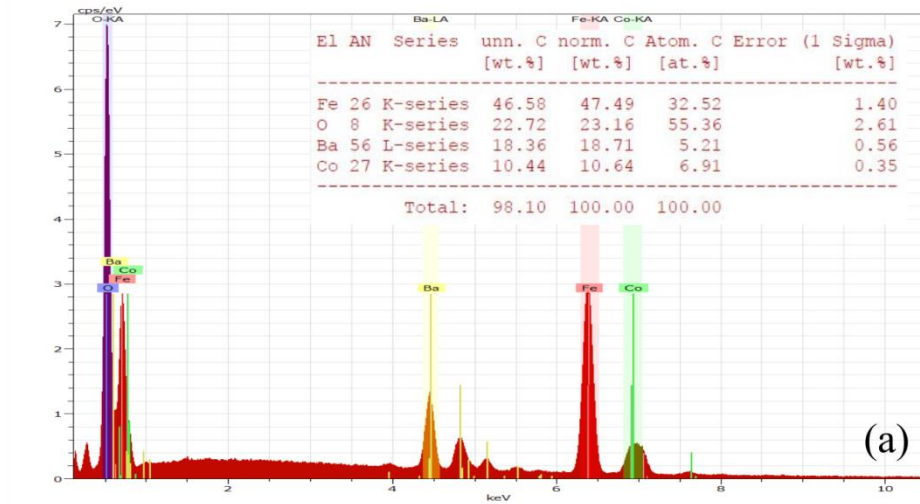
Fig. 5.48 EDX spectra and mapping of $Ba_{2-2x}Cr_xNi_xCo_2Fe_{12}O_{22}$ (a) x=0.0 and (b) x=0.15

5.4.5 Optical analysis

Optical properties especially energy of band gap of Y-type hexaferrite $Ba_{2-2x}Cr_xNi_xCo_2Fe_{12}O_{22}$ was estimated by UV-Vis-NIR spectroscopy. **Fig. 5.49** shows the band gap energy (E_g) plots of prepared samples. Indeed, E_g represents the distance between lowest unoccupied molecular orbital of conduction band (LUMO) and highest occupied molecular orbital (HOMO) of valence band .
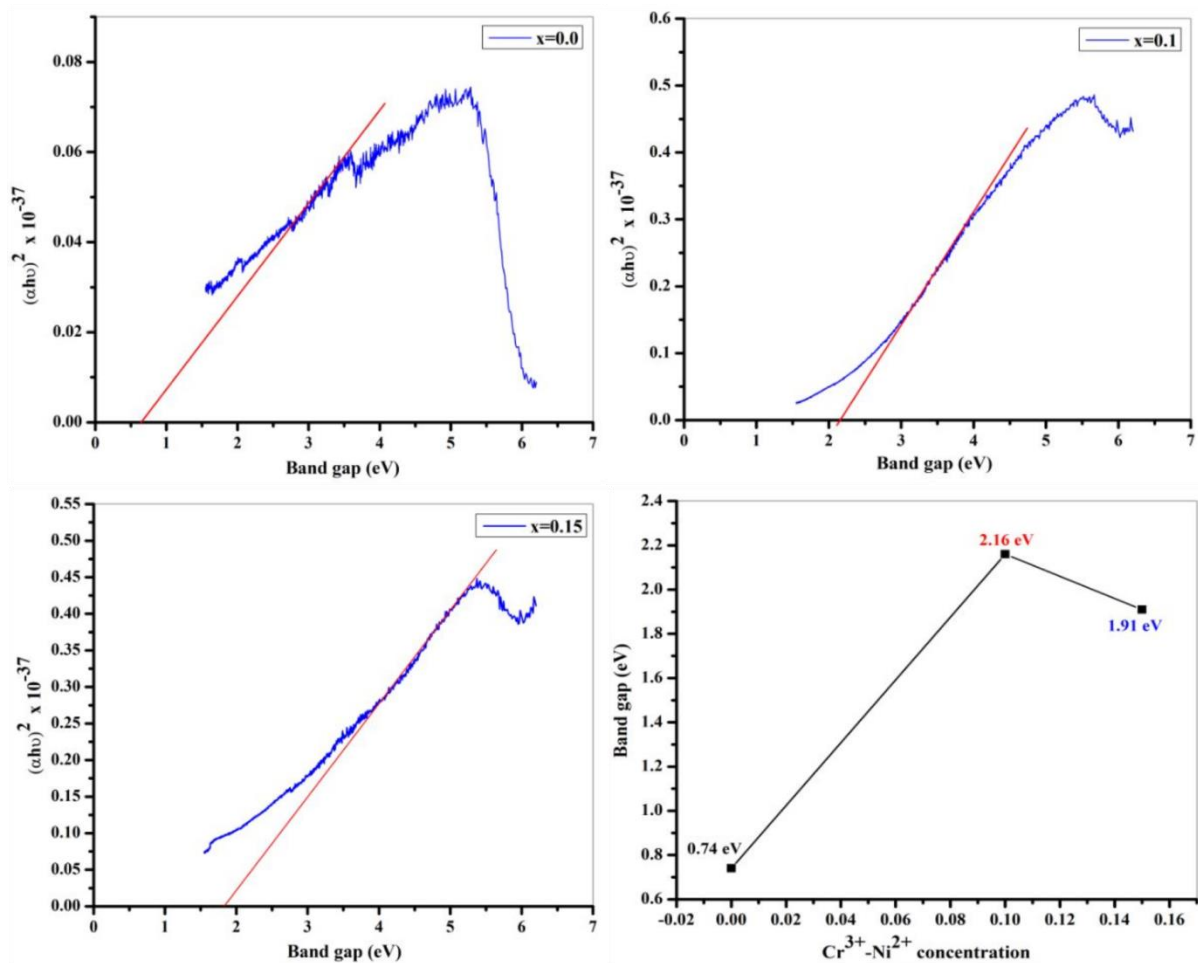
Fig. 5.49 Band gap of $Ba_{2-2x}Cr_xNi_xCo_2Fe_{12}O_{22}$ (x=0.0, 0.1, 0.15) and band gap variation with Cr^{3+}-Ni^{2+} concentration

According to that distance, materials are classified as insulator, semiconductor and conductor. However, the transition of the electron from valence band to conduction band can be done either vertically (direct band gap) or obliquely (indirect band gap). In order to estimate the band gap energy of prepared samples, Tauc relation (eq. 5.52) was used [28].

$$\frac{\alpha h v}{A} = (h v - E_g)^n \tag{5.52}$$

Here α is absorption coefficient, h designates the constant of Planck, v designates the frequency of incident photon and A designates a constant that depends on the type of transition. In this formula, the exponent 'n' can get specific values which indicate the type of transition especially 1/2, 3/2, 2 and 3 respectively for allowed direct, forbidden direct, allowed indirect and forbidden indirect transition. In this research work, we used allowed direct transition (n=1/2) toestimate E_g of prepared samples. From graphs, E_g was observed to be 0.74, 2.16 and 1.91 eV for respectively x=0.0, x=0.1 and x=0.15. According to our knowledge, less work has been done on optical properties of Y-type hexaferrite materials. Values of E_g for x=0.1 and 0.15 are comparable to those obtained by Tchouank and Auwal for M-type hexaferrite [103, 133]. Sample with x=0.0 shows the lowest value of E_g (0.74 eV) which is very close to that of germanium (0.76 eV). Due to the obtained values of E_g , the prepared Y-type hexaferrite can be used in various electronic applications.

5.4.6 Magnetic analysis

The observed curves in **Fig. 5.50** represent M-H hysteresis loop for Y-type hexaferrite $Ba_{2-2x}Cr_xNi_xCo_2Fe_{12}O_{22}$ sintered for 6 hours at 1100℃. It was found that the magnetic behaviour of prepared samples is similar to ferrimagnetic materials. From hysteresis loop characteristic parameters including saturation magnetization (Ms), remanence (Mr) and coercivity (Hc) were estimated. In the present case, Ms corresponds to the asymptote which has equation y=c (where c=Ms), Mr and Hc correspond to the intercept between the curve and axis especially x=a for H_c and y=b for M_r. It was found that Ms and M_r vary from 33.6 to 49.3 emu/g and 11.5 to 18.7 emu/g respectively whereas Hc increases from 134.8 to 268.8 Oe. Compared to M-type hexaferrite which generally shows high coercivity [55, 175, 176], it is noticed that prepared Y-type hexaferrite shows low values of H_c. Due to their low coercivity, Y-type hexaferrite materials generally present soft magnetic behavior [177]. O. Mirzaee et M. Ahmad have reported that $Sr_2Ni_2Fe_{12}O_{22}$ hexaferrite has as coercivity Hc=840 Oe and Hc=350 Oe at 1000℃ and 1100℃ respectively and presents soft magnetic behavior [174, 178]. In our case, Hc is smaller than those found by Mirzaee and Ahmad so, it can be deduced that the prepared samples are soft magnetic materials. M. Ahmad also revealed that $Sr_2Ni_2Fe_{12}O_{22}$ hexaferrite heated at 1100℃ shows Ms=61.5 emu/g [178] which is greater than the one reported in our work. However, the obtained Ms values of $Ba_{2-2x}Cr_xNi_xCo_2Fe_{12}O_{22}$

(x=0.0, 0.1, 0.15) are greater to those found by G. Murtaza [179]. Because of the increase in Hc, the soft magnetic character observed in prepared samples declines with the rise in Cr^{3+}-Ni^{2+} substitution. This soft behavior make them suitable for chip soft-magnetic components such as multi- layer chip inductors (MLCI) and chip EMI filters [48, 177, 180].

The highest values of M_s and M_r parameters were found to be 49.23 emu/g and 18.64 emu/g for respectively for x=0.1. Several factors such as synthesis process, concentration of dopant, heat-treatment may affect magnetic properties of hexaferrite. However, the parameter Ms is strongly influenced by the occupation of crystallographic sites by substituted ions. Y-type hexaferrite $A_2Me_2Fe_{12}O_{22}$ contains six sub-lattices such as $6c_{IV}$, $3a_{VI}$, $18h_{VI}$, $6c_{VI}$, $6c^{*}_{IV}$ and $3b_{VI}$ occupied by metallic ions Me^{2+} and Fe^{3+} which h are responsible of magnetism due to their magnetic moment [181, 182]. These sub-lattices are distributed into two types: octahedral sites ($3a_{VI}$, $3b_{VI}$, $18h_{VI}$ and $6c_{VI}$) and tetrahedral sites ($6c_{IV}$ and $6c^{*}_{IV}$) which possess spin up and down as presented in **Table 5.13** [183]. By doping in these sites, magnetic properties of the material may change. It has been noticed that even after doping Ba^{2+} ions by Ni^{2+} ($2.3\mu_B$ [184]) and Cr^{3+} ($3\mu_B$ [133]) ions in undoped Y-type hexaferrite $Ba_2Co_2Fe_{12}O_{22}$, Ms an M_r parameters changed. These observed fluctuations in M_s and M_r may be due to super exchange interactions between magnetic ions which result from the coupling of magnetic moments of transition metal ions [185]. Albanese reported that T-block contains a non-magnetic in the central of octahedral sites which show a strong impact on the magnetic structure of the crystal and are sources of the super exchange interactions [182].

From **Table 5.13**, it is observed that the squareness ratio (M_r/M_s) is around 0.35 of all prepared samples and less than 0.5 which specifies that prepared samples are in multi magnetic domain structure [121, 179]. The coercivity H_c was observed to rise with substitution of Cr-Ni. This behavior was observed by Khanduri [173]. The increase in H_c may be due to the increase in c/a ratio. This scenario was reported by Ali and Xu [184, 186]. In addition, the increase in Hc can be a consequence of increase in porosity. It was reported that if the porosity is high, the coercivity will be also high [142]. The coercivity also depends on the structure of material. If the material presents a single magnetic domain, then coercivity is only controlled by the domain rotation [187]. This situation is generally observed in M-type hexaferrite materials. But if the material presents a multi magnetic domain, the coercivity is controlled by wall displacement [187]. Hence, the coercivity of prepared samples is dominated by magnetic wall motion. It is well know that the H_c strongly depends on particle size. In the situation of wall displacement (multi domain), H_c trend to decreases when the

particle size increases as reported Globus [188]. As mentioned previously, H_c increases with the substitution whereas the particle size decreases as it was found in FESEM analysis. The anisotropy constant (K) was calculated using eq. 5.53 and values are listed in **Table 5.13**. It was found that K increases with increase in Cr^{3+}-Ni^{2+} concentration.

$$2K = \mu_0 M_s H_c \tag{5.53}$$

Table 5.13 Magnetic parameters for prepared samples

x	M_s (emu/g)	M_r (emu/g)	Hc (Oe)	M_r/M_s	K (HA^2/Kg)
0.0	33.61	11.58	134.86	0.344	0.23
0.1	49.23	18.64	141.63	0.379	0.35
0.15	35.47	12.47	268.71	0.352	0.95
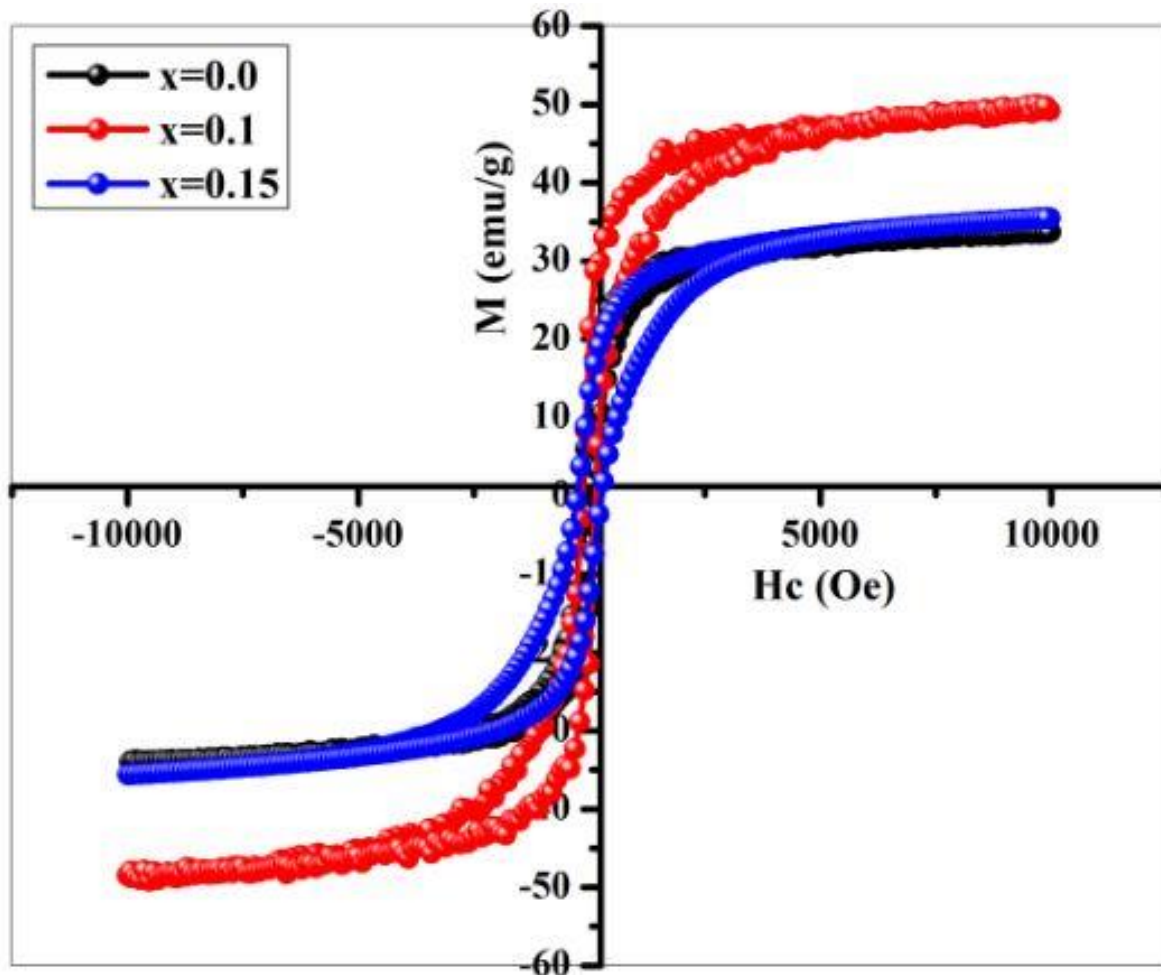
Fig. 5.50 M-H hysteresis loop of $Ba_{2-2x}Cr_xNi_xCo_2Fe_{12}O_{22}$ (x=0.0, 0.1, 0.15)

5.4.7 Impedance and dielectric analysis

The real and imaginary part of complex impedance Z* were calculated in the 100-120MHz frequency range at room temperature using the following expressions:

$$Z^* = Z' - jZ'' \tag{5.54}$$

$$Z' = |Z|cos\theta \tag{5.55}$$

$$Z'' = |Z|sin\theta \tag{5.56}$$

Where j^2=-1, Z is the modulus of complex impedance and θ the phase angle.
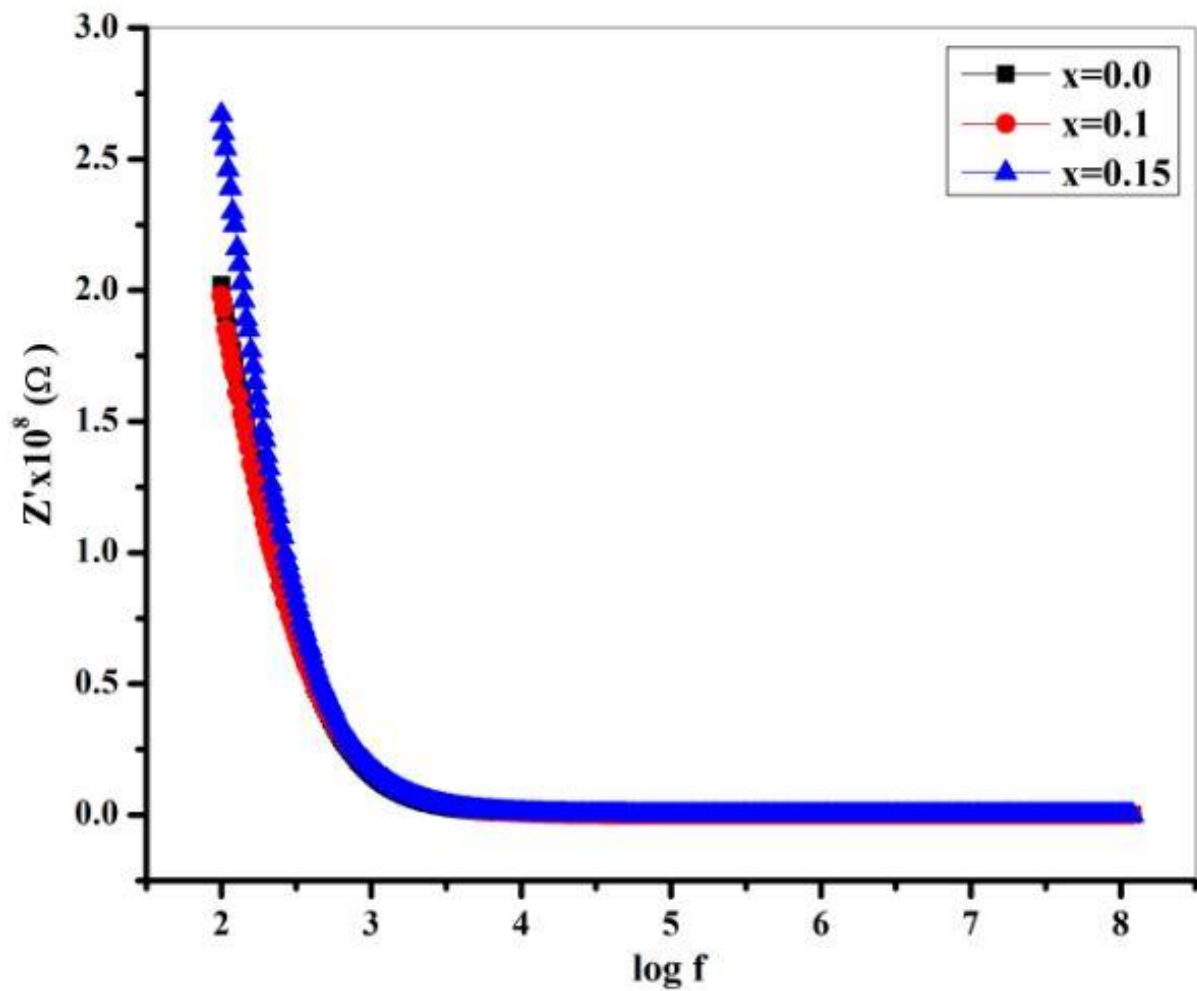
Fig. 5.51 Real part (Z') of complex impedance for $Ba_{2-2x}Cr_xNi_xCo_2Fe_{12}O_{22}$ (x=0.0, 0.1, 0.15)
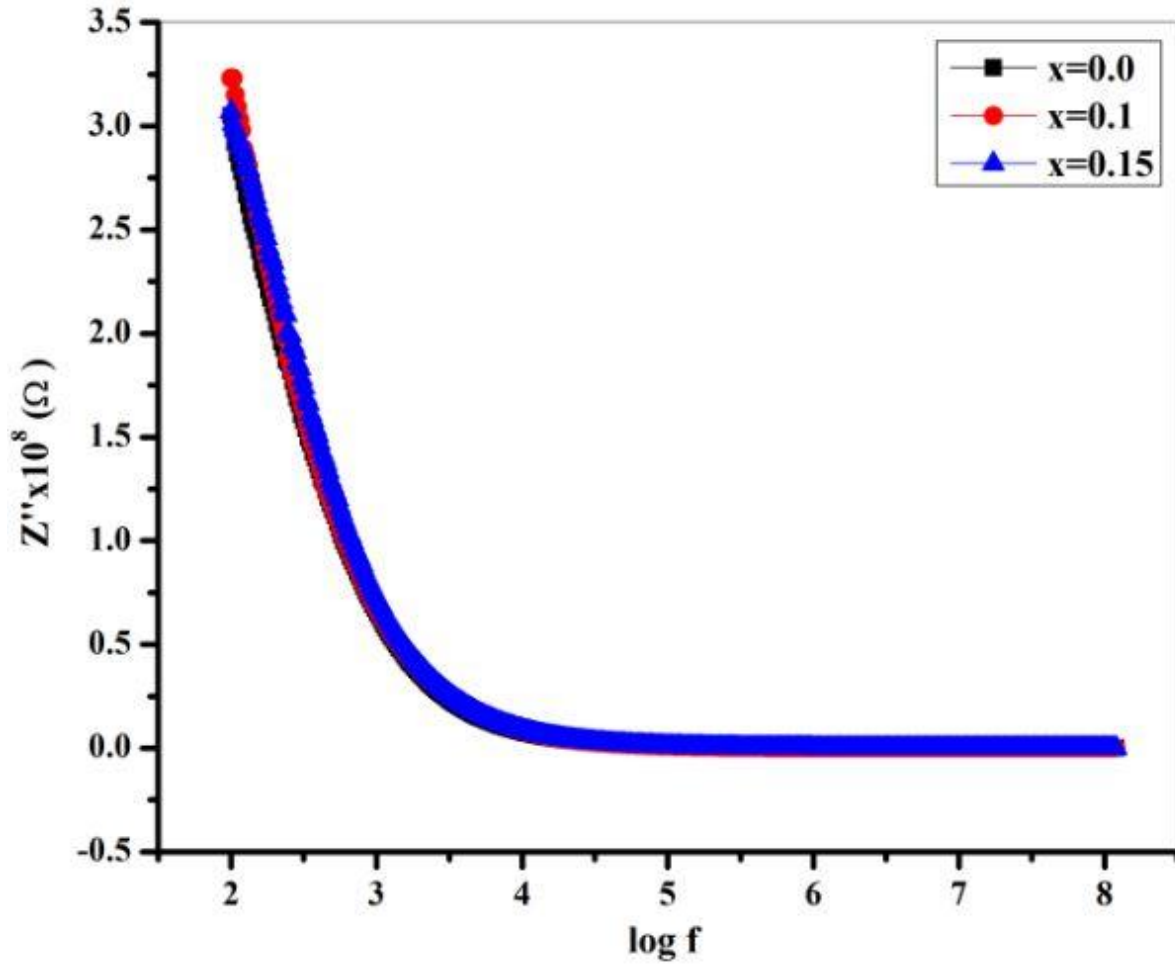
Fig. 5.52 Imaginary part (Z'') of complex impedance for $Ba_{2-2x}Cr_xNi_xCo_2Fe_{12}O_{22}$ (x=0.0-0.15)

Fig. 5.51 and **5.52** show the variation of Z' and Z'' against logarithmic frequency (log f). It can be realised that both of Z' and Z'' decline with the frequency up to around 10^3 Hz and then become unchangeable. Similar scenario was also observed by I. Odeh et al. [189].

The dielectric behavior of all prepared samples was examined by calculating quantities including dielectric constant (ε'), dielectric loss (ε'') and dielectric loss tangent (tan δ_e). The Formulae below were used:

$$\varepsilon' = \frac{Z''}{\omega C_0 Z^2} \qquad (5.57)$$

$$\varepsilon'' = \frac{Z'}{\omega C_0 Z^2} \qquad (5.58)$$

$$\varepsilon'' = \varepsilon' \times tan\delta_e \qquad (5.59)$$

The variation in dielectric parameters (ε', ε'' and tan δ_e) as a function of log f is displayed in **Fig. 5.53** and **5.54 (a)**. First of all, a decrease with the frequency can be observed in all three parameters at lower frequencies then from intermediate frequencies, ε'' and tan δ_e became constant. However a slight decrease is observed at intermediate frequencies in ε'. This observed decrease in ε' is a typical dielectric behavior of ferrimagnetic materials as reported Ravinder et al. [190]. This decrease in ε' at lower and intermediate frequencies may be assigned to interfacial and dipolar polarization as explained by the two-layer model of Maxwell and Wagner [133, 191]. From 32MHz, it can be seen an increase in ε' which is attributed to electronic polarization. The high values of ε' at lower frequencies appear as a result of inhomogeneity of the sample structure which include Fe^{2+} ions, oxygen vacancies, defects, voids, grain boundary and interfacial dislocations which increase the value of ε' at low frequency [37, 108]. When external electrical field is applied, a displacement of charge carriers from their initial position is observed forming a dipolar moment which causes the polarization of the structure. This polarization is due to the electron exchange between ferrous and ferric ions and increases with the increase in applied electric field. The decrease in ε' originate from the polarization at lower frequencies but at higher frequencies, any species contributing to the polarization lag behind the electrical applied field as reported by Elahi et Tchouank [133, 191]. The dielectric constant value is influenced by the condition of synthesis (synthesis method, heating temperature, heating time, doping and concentration of doping) [14]. The highest value of ε' was found to be 12.4 at 100 Hz for x=0.0.

Generally the observed behavior in constant dielectric is familiar to heterogeneous material. However it is not always similar for tan δ_e. Sometimes, tan δ_e can show a resonance peak which can be clarified by the Debye relaxation theory [192]. This resonance peak appears when the frequency of external applied electric field and that of electron hopping are matching i.e. when the condition $\omega_{max}\tau=1$ is verified, where τ represents the relaxation time. The relaxation phenomenon is due to orientation polarization occurring from oxygen defects in the material [96].

Grains and grain boundaries contribute to dielectric properties in heterogeneous material. Nyquist plot (Z'' vs Z') permits to separate their contribution. R. Pattanayak reported that Nyquist plot ideally presents three semicircles which represent the contribution of grains (left side), contribution of grain boundaries (semicircle on the middle) and the contribution of interface (right side) which correspond to higher, intermediate and lower frequencies respectively [156]. The radii of these semicircles respectively refer to the resistance of grains,

grain boundaries and interface [157]. **Fig. 5.54 (b)** shows Nyquist plots of impedance of prepared Co_2Y barium hexaferrite in the 100 Hz-120 MHz frequency range at room temperature. It can be clearly noticed that plots are not displaying entire semicircles. This kind of plots was obtained by M. Wu et al. at room temperature [193]. Since in Nyquist plots of impedance the frequency increases from left to right side, it is easy to deduce that the observed semi-circular arcs correspond to grain boundaries contribution which indicates that the grain contribution is negligible to that of grain boundaries. This is due to the fact that small grain size and large number of grain boundaries characterize nanocrystalline sample [23]. From **Fig. 5.54 (b)**, the highest value grain boundaries resistance is obtained for x=0.1.
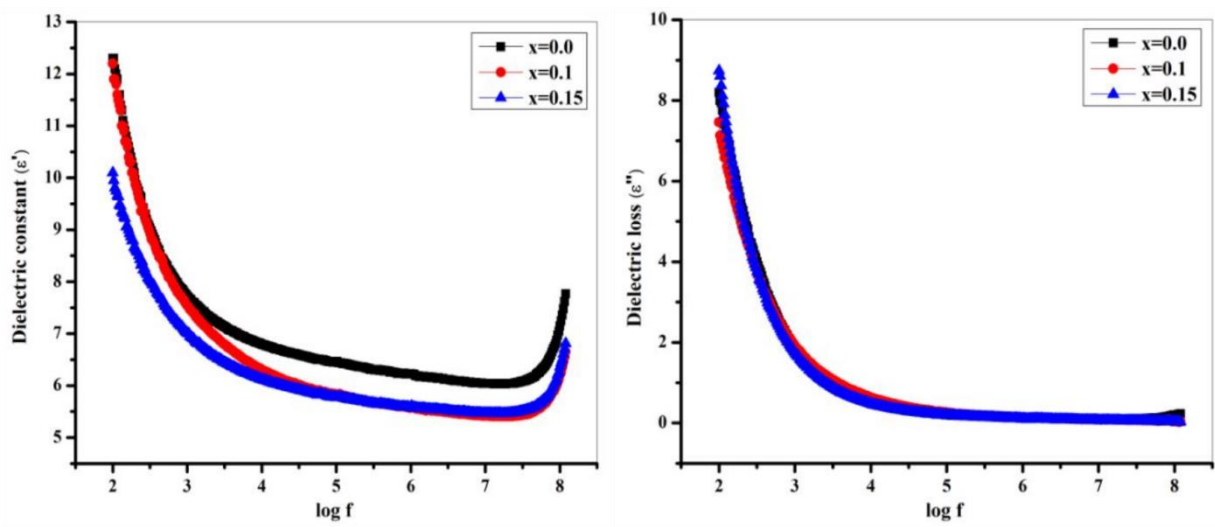
Fig. 5.53 Dielectric constant (ε') dielectric loss of $Ba_{2-2x}Cr_xNi_xCo_2Fe_{12}O_{22}$ (x=0.0, 0.1, 0.15)
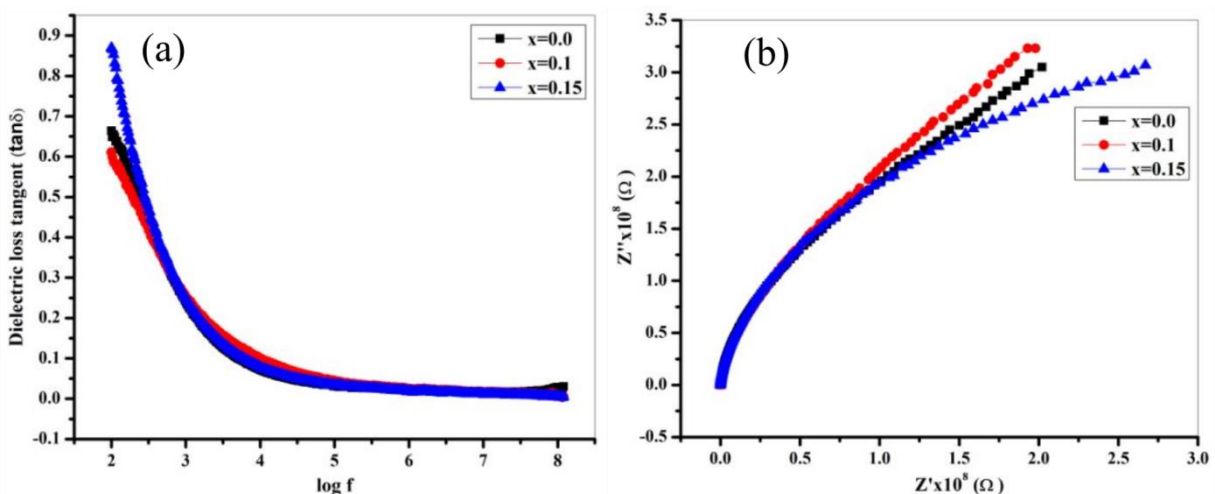
Fig. 5.54 (a) Dielectric loss tangent (tanδ) and (b) Nyquist plots of $Ba_{2-2x}Cr_xNi_xCo_2Fe_{12}O_{22}$ (x=0.0-0.15)

5.4.8 AC electrical conductivity analysis

AC electrical conductivity (σ_{AC}) of prepared Co_2Y barium hexaferrite was estimated using the relation below:

$$\sigma_{AC} = \varepsilon_0 \omega \varepsilon'' \tag{5.60}$$

Where, ε_0 is permittivity of the free space. **Fig. 5.55** shows the plot of AC electrical conductivity of the prepared samples at room temperature in the frequency range 100 Hz-120 MHz. It was observed that σ_{AC} remains unchangeable and not dependant on doping for lower and intermediate frequencies, but increases abruptly at higher frequencies. The conduction phenomenon in ferrite is related to electron hopping between ferrous (Fe^{2+}) and ferric (Fe^{3+}) ions at the octahedral sites according to the equation: ($Fe^{2+} \leftrightarrow Fe^{3+} + e$). The conduction mechanism and dielectric polarization are much correlated [149]. So the observed increase in σ_{AC} at higher frequencies appears as a consequence of decrease in dielectric constant and decreases with Cr^{3+}-Ni^{2+} concentration. Highest values of σ_{AC} was found to be 1.54 $(\Omega.cm)^{-1}$ for x=0.0.

Generally the conductivity is given by the following relation [133]:

$$\sigma_t = \sigma_{DC} + \sigma_{AC} \tag{5.61}$$

Where, σ_{DC} is DC electrical conductivity. The expression of AC electrical conductivity (σ_{AC}) can also be written as [133]:

$$\sigma_{AC} = A\omega^s \tag{5.62}$$

Where s is a temperature dependent variable without dimension, A is a temperature dependent constant which also depend on intrinsic material properties. The values of s lie between 0.0 and 1 [155]. By transforming eq. 5.62 we obtained:

$$ln\sigma_{AC} = s\,ln\omega + lnA \tag{5.63}$$

This equation resembles to the straight line equation with s as slope. The variation of ln σ_{AC} against ln ω is displayed in **Fig. 5.56**. The observed plots are almost straight lines as expected. The s values was observed to be 0.706, 0.664 and 0.633 for x=0.0, x=0.1 and x=0.15 respectively.
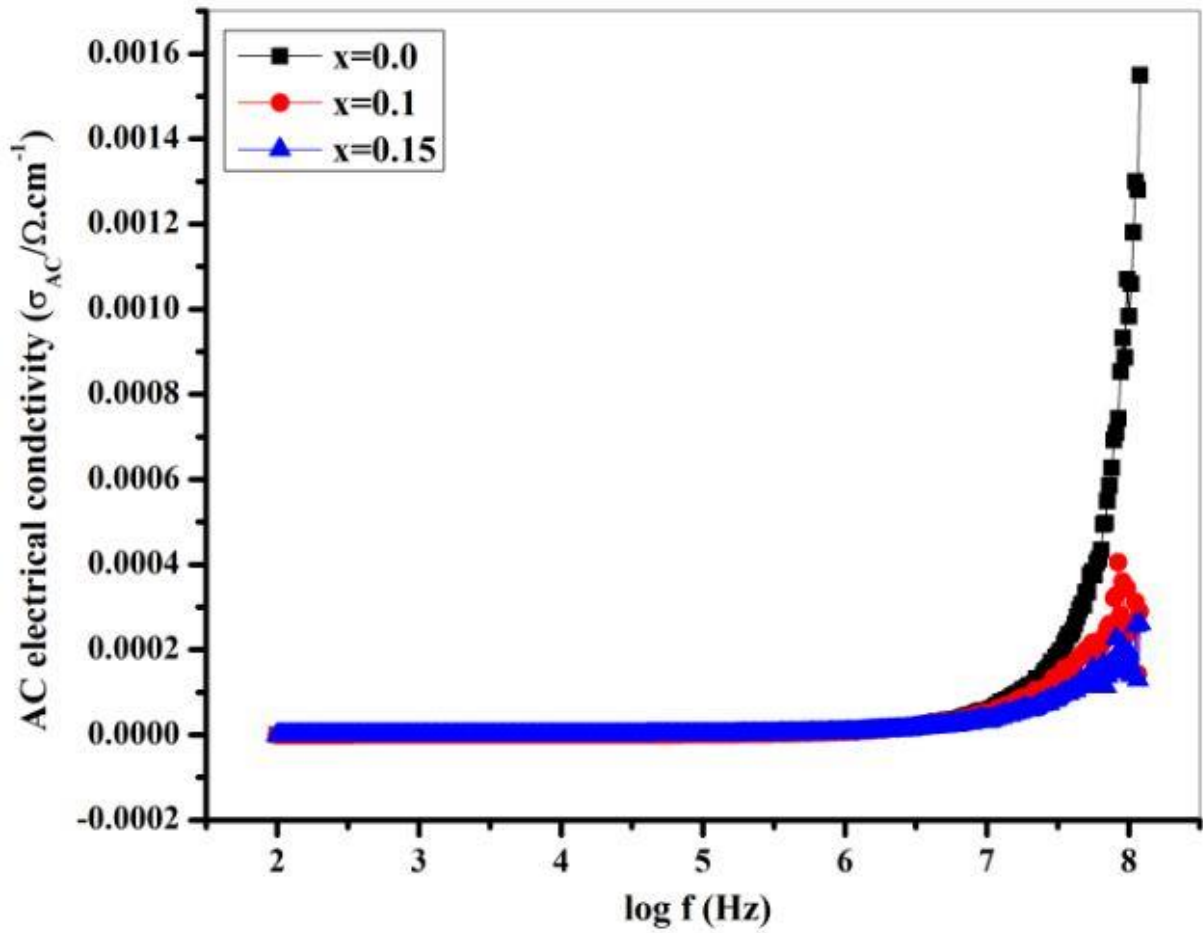
Fig. 5.55 AC conductivity (σ_{AC}) of $Ba_{2-2x}Cr_xNi_xCo_2Fe_{12}O_{22}$ (x=0.0, 0.1, 0.15)

M. Irfan et al.   reported that the electrical conductivity of the material is frequency independent (σ_{DC}) when s=0 and frequency dependent when $s{\neq}0$ [24]. In this work $s{\neq}0$, so it can be deduced that the conduction of prepared samples is dominated by the AC electrical conductivity (σ_{AC}).
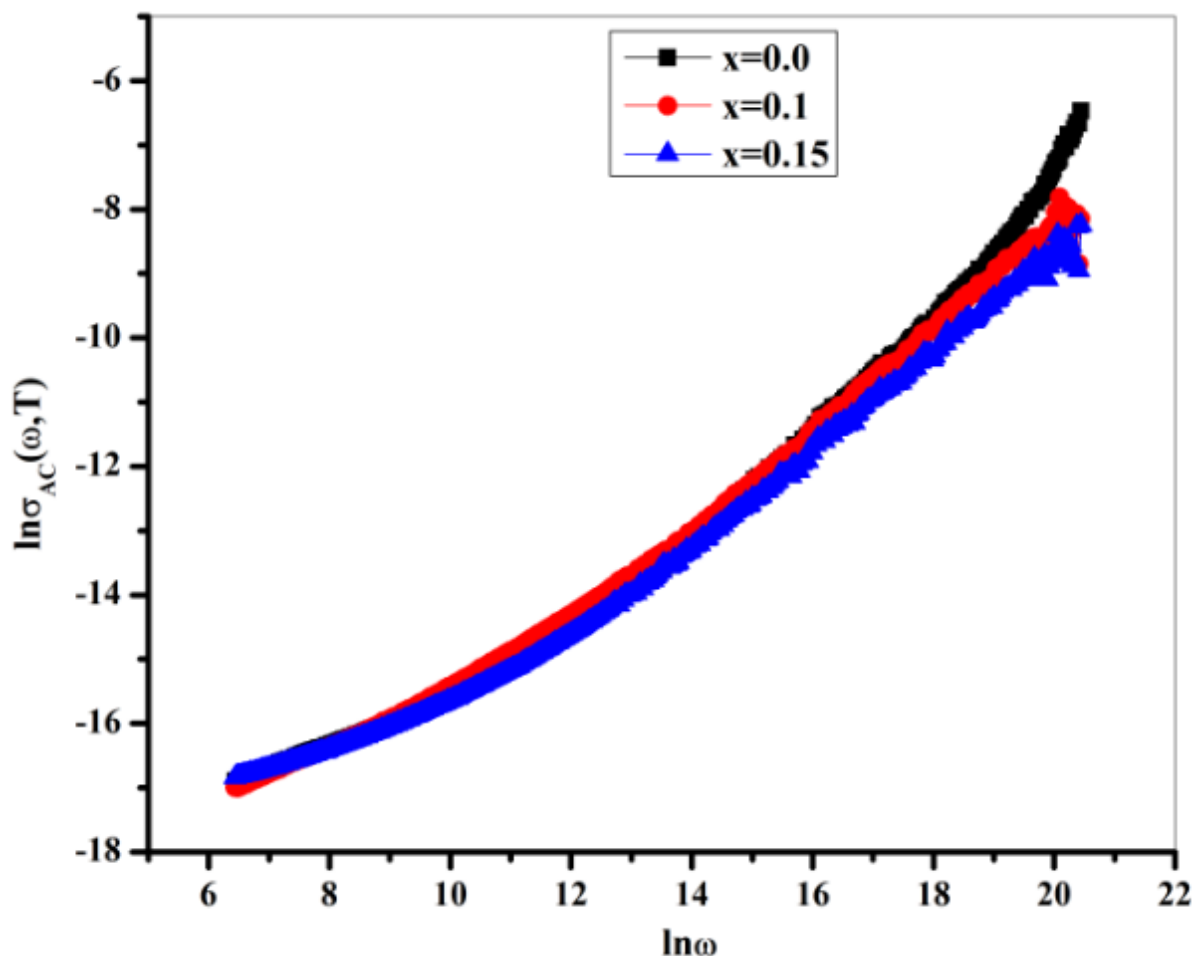
Fig. 5.56 Variation of ln $\sigma(\omega, T)$ with $\ln\omega$ for $Ba_{2-2x}Cr_xNi_xCo_2Fe_{12}O_{22}$ (x=0.0, 0.1, 0.15)

5.5 Crystal structure refinement, optical properties, dielectric and impedance spectroscopy of Ni^{2+}-Co^{2+} substituted bismuth copper titanate (BCTO)

5.5.1 XRD analysis

Fig. 5.57 shows the XRD patterns of $Bi_{2/3}Cu_{3-2x}Ni_xCo_xTi_4O_{12}$ (x=0.0, 0.1, 0.2) calcined for 7 hours at 900 ℃ temperature. The observed peaks in the XRD spectra was indexed according to standard data (JCPDS number: 80-1343), the single phase was observed for all synthesized samples with perovskite structure having *Im-3* as space group with the absence of secondary phase such as TiO_2, Cu_2O, and CuO and related oxides [58]. The lack of secondary phase in the XRD spectra indicates that the substituted cations have occupied the different crystallographic sites of the prepared samples. The lattice parameters (a) and unit cell volume (V_{cell}) were calculated using following formulae [194]

125

$$d_{hkl} = a(h^2 + k^2 + l^2)^{-1/2} \tag{5.64}$$

$$V_{cell} = a^3 \tag{5.65}$$

The values of a and V_{cell} were respectively found to be in the range 7.37-7.41Å and 401-406Å^3 and are in agreement with values earlier reported in literature [195-197]. It can be observed that a and V_{cell} values increases with the concentration of doping (**Table 5.14**). This increase in a and V_{cell} can be due to the slight deformation of crystal structure of the prepared samples caused by the larger ionic radii of Co^{2+} ($r_{Co^{2+}} = 0.074$ nm) and Ni^{2+} ($r_{Ni^{2+}} = 0.072$ nm) as compared to that of Cu^{2+} ($r_{Cu^{2+}} = 0.069$ nm). Furthermore, increase in d-spacing could also be the reason behind the increase in the values of a and V_{cell}. Fullprof Suite Software was employed to refine the lattice parameters of synthesized samples. The modelling of the background was carried out using linear-interpolation method while the shape of the peaks was refined using pseudo-Voigt function. Furthermore, parameters such as atomic positions, zero correction, unit cell parameters, half width parameters (U, V, and W), background, atomic occupancy and scale factor were varying throughout the refinement process. The black line represents the calculated fitted data, the black line is for the experimental data, and the blue line is for the difference between calculated fitted data and experimental data (**Fig. 5.58**). The crystallite size (D) was evaluated by the equation below [58, 133, 198]

$$D = \frac{0.9\lambda}{\beta cos\theta} \tag{5.66}$$

With, λ being the wavelength of the X-ray, θ being the Bragg angle, and β being the full width at half maximum (FWHM). The average values of D was found to be between 41-47 nm. From **Fig. 5.57**, a slight displacement of peak to lower diffraction angle can be observed in the (220) peak when the substitution content increases, similar scenario was observed by X. Huang et al. [199]. This slight shift is a consequence of the changes in lattice parameter caused by the substituted cations (**Table 5.14**). Surface area (S), X-ray density (d_x), bulk density (d_m) and porosity (P) have been determined using [200]

$$S = \frac{6000}{d_x D} \tag{5.67}$$

$$d_x = \frac{ZM}{VN_A} \tag{5.68}$$

$$d_m = \frac{4m}{\pi d^2 t} \qquad (5.69)$$

$$P = \left(1 - \frac{d_m}{d_x}\right) \times 100 \qquad (5.70)$$

Where m is pellet weight, d is pellet diameter, t pellet thickness, M is sample molecular weight, N A is the constant of Avogadro (6.023×1023 mol-1), and Z is the number of atoms per unit cell. It was discovered that the surface area of the prepared pellets was 22-24.7 cm^2/g. The lower the value of D, the bigger the surface area, can be noted.

This indicates that the number of atoms is more important at the surface when the particles size is small. The X-ray and bulk densities decrease as the concentration of cations is increased (**Table 5.15**), this could be due to reduction in the molecular weight of the electroceramic caused by the atomic weights of Ni^{2+} (58.69) and Co^{2+} (58.94) [88, 170]. In addition, the reduction in bulk density may also be due to the existence of pores in the sample resulting from heat treatment or synthesis process. The distinction between X-ray density and bulk density characterizes this. **Table 5.15** lists the calculated sample porosity. It can be observed that with crystallite size I the porosity differ inversely i.e. the more porous, the crystal is, the smaller its size [201].
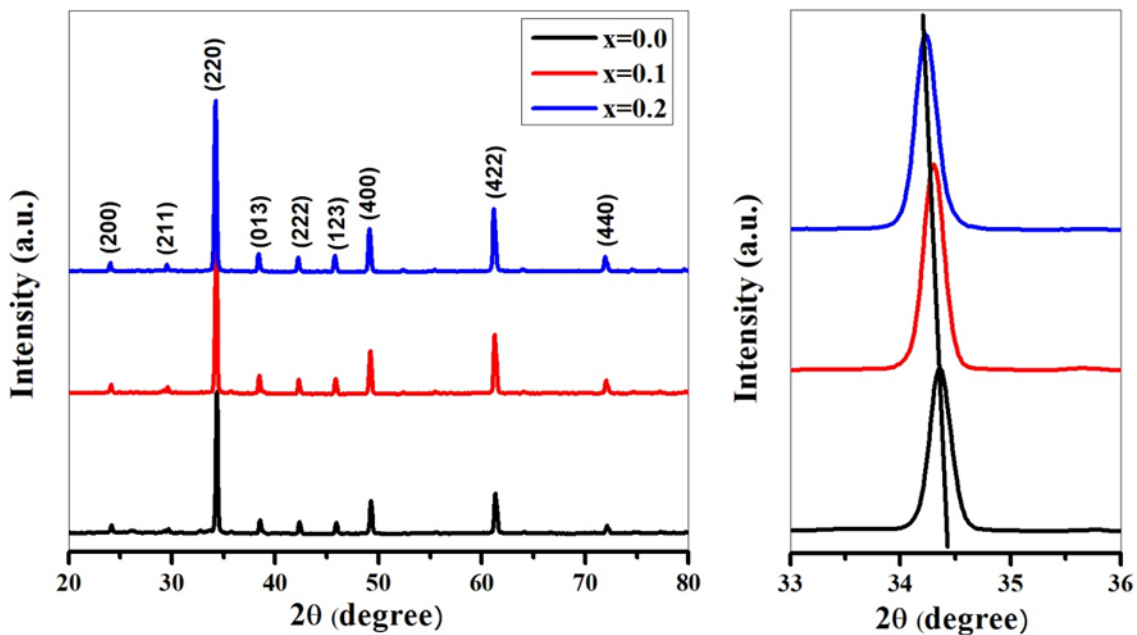
Fig. 5.57 XRD pattern of $Bi_{2/3}Cu_{3-2x}Ni_xCo_xTi_4O_{12}$ (x=0.0, 0.1, 0.2)

Table 5.14 Diffraction angle (2θ), d spacing (d), full width at half maxima (β), lattice constants (a) volume of cell (V) for $Bi_{2/3}Cu_{3-2x}Ni_xCo_xTi_4O_{12}$ (x=0.0, 0.1, 0.2) and reliability factors

x	$2\theta(°)$	$\beta(°)$	d (Å)	D (nm)	a (Å)	V (Å^3)	Reliability factors
0.0	34.36	0.183	2.6079	45.44	7.3763	401.336	R_p=18.8 R_{exp}=13.4 R_{wp}=20.9 R_{Bragg}=6.19 GoF=1.5 χ^2=2.406
0.1	34.31	0.179	2.6116	46.45	7.3867	403.046	R_p=13.9 R_{exp}=11.0 R_{wp}=23.4 R_{Bragg}=6.69 GoF=2.1 χ^2=4.568
0.2	34.23	0.199	2.6178	41.77	7.4043	405.924	R_p=14.3 R_{exp}=10.7 R_{wp}=23.5 R_{Bragg}=6.97 GoF=2.2 χ^2=4.8

Table 5.15 X-ray density (d_x), bulk density (d_m), porosity (P), crystallite size (D), phase present, surface area (S) for $Bi_{2/3}Cu_{3-2x}Ni_xCo_xTi_4O_{12}$ (x=0.0, 0.1, 0.2)

x	d_x (g/cm³)	d_m (g/cm³)	P (%)	D (nm)	Phase	$S \times 10^7$ (cm²/g)
0.0	5.901	4.044	31.472	45.44	BCC	22.374
0.1	5.869	4.039	31.166	46.45	BCC	22.011
0.2	5.819	3.535	39.257	41.77	BCC	24.682

5.5.2 FTIR analysis

Fig. 5.59 demonstrates the $Bi_{2/3}Cu_{32x}Ni_xCo_xTi_4O_{12}$ FTIR spectra (x=0.0, 0.1, 0.2) from 400 to 4000 cm-1. The major characteristics bands of bismuth copper titanate ceramics were observed at 430, 509, and 588 cm⁻¹, these bands could be attributed to regions of Ti^{4+} ion as a result of v_{Ti-O}= 653-550 cm⁻¹ and $v_{Ti-O-Ti}$= 495- 436 cm⁻¹ [57, 202]. The bands at 430 and 588 cm⁻¹ specifically corresponds to Ti-O stretching vibration, this band signify the formation of perovskite phase of the bismuth copper titanate ceramic [203, 204]. In general, Absorption bands appearing between 380 and 700 cm⁻¹ are usually observed as a result of mixed vibrations of CuO_4 and TiO_6 octahedron [56, 59, 205]. The band observed at 1121 and 1409 cm⁻¹ could be assigned to stretching vibrations of C-N and C-H respectively [206]. The faint absorption band at 1580 cm⁻¹ and the broad absorption band observed at around 3414 cm⁻¹ could be assigned to O-H vibrations of water molecules and C-H vibrations of alkyl group present in the precursors [207, 208].
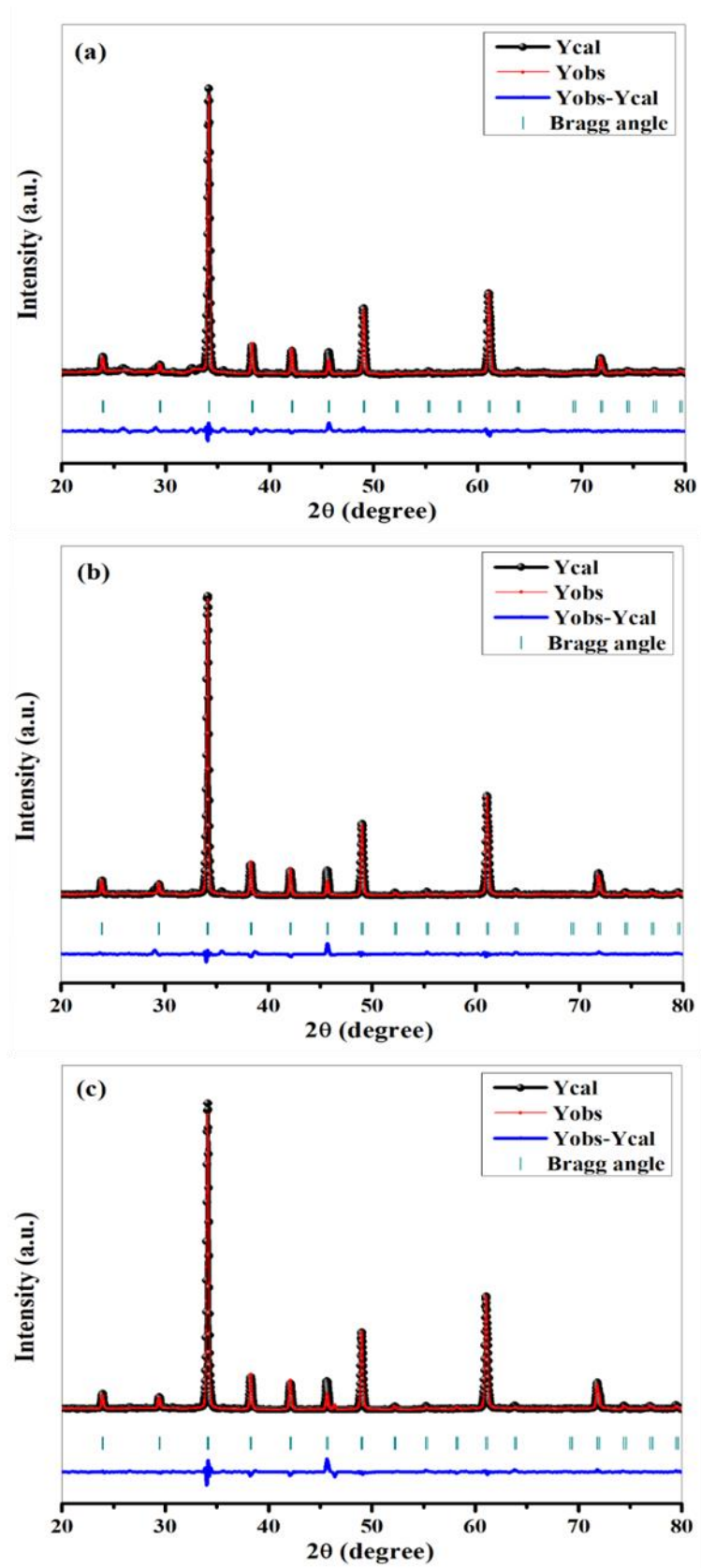
Fig. 5.58 Rietveld refinement of XRD pattern of $Bi_{2/3}Cu_{3-2x}Ni_xCo_xTi_4O_{12}$ (x=0.0, 0.1, 0.2)
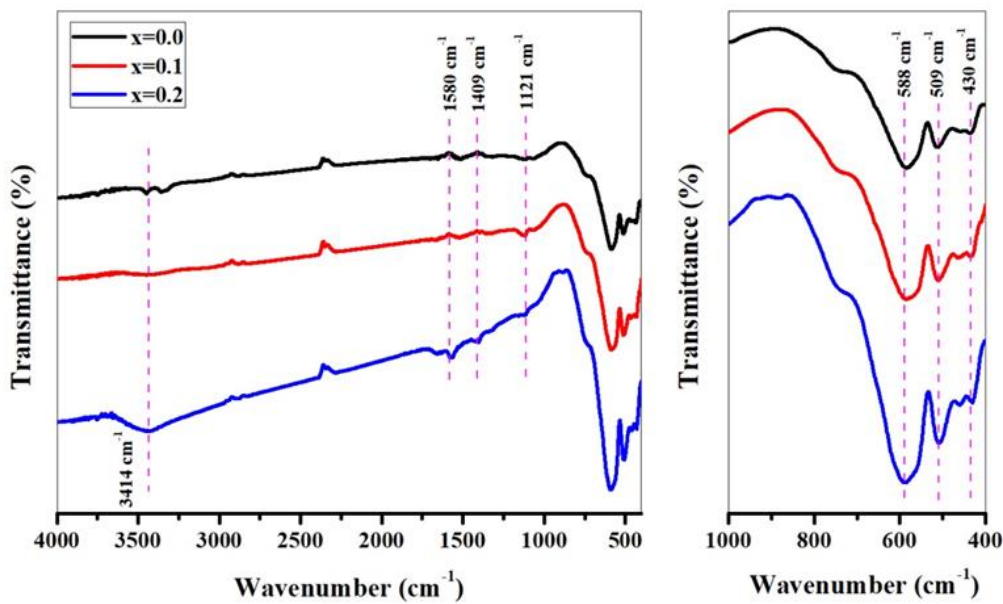
Fig. 5.59 FTIR spectra of $Bi_{2/3}Cu_{3-2x}Ni_xCo_xTi_4O_{12}$ (x=0.0, 0.1, 0.2)

5.5.3 Raman spectroscopy

Fig. 5.60 shows the $Bi_{2/3}Cu_{3-2x}Ni_xCo_xTi_4O_{12}$ Raman spectra (x=0.0, 0.1, 0.2) collected in the 200-800 cm^{-1} range. The Raman spectra show several modes at 233, 246, 281, 312, 434, 511, 572, 645, 687, and 751 cm^{-1} whose intensity decrease with the substitution of Ni^{2+}-Co^{2+}. The rotation-like mode of the TiO_6 octahedron which is usually accompanied by antistretching mode of Ti-O-Ti causes the appearance of modes at 434 and 511cm^{-1} as a result of A_g symmetry; interestingly, the Ti-O-Ti antistretching mode results in the occurrence of modes at 572 cm^{-1} [96, 202]. The appearance of these modes (434, 511, and 572 cm^{-1}) are a confirmation of the bismuth titanate phase of the prepared samples. Additionally, lattice dynamic calculations (LCD's) assigned the appearance of Raman active mode at 318 cm-1 to TiO_6 octahedron rotation-like mode as a consequence of E_g symmetry [209]. However, in our Raman spectra, this mode was noted at 312 cm^{-1}. As a consequence of F_g symmetry, the Ti-O-Ti stretching vibration mode could also be ascribed to the appearance of a very weak mode at 751 cm^{-1} as a result of F_g symmetry [122, 210]. According to LCD's, the mode responsible for Ti-O-Ti stretching vibrational mode is to appear at 708 cm^{-1} [209]. However, this mode can shift to higher wave numbers as reported by C. Mu et al. [211]. The weak mode at 246 cm-1 could be ascribed to the CuO phase [122], this contradicts the XRD result because other phases apart from bismuth copper titanate phase were not observed in the XRD pattern. This contradiction stems from the fact that Raman spectroscopy is more sensitive than XRD. The

131

Raman active mode 281 cm^{-1} occur due to F_g symmetry and is attributed to rotation-like mode of the TiO$_6$ octahedron, the modes at 233, 645, and 687 cm^{-1} have not been reported by LCD's or observed in any experiment to the best of our knowledge. In general, the appearance of Ti-O-Ti stretching vibrational mode could trigger density distribution of delocalized charges which may prompt the appearance of other modes in the spectra [211].
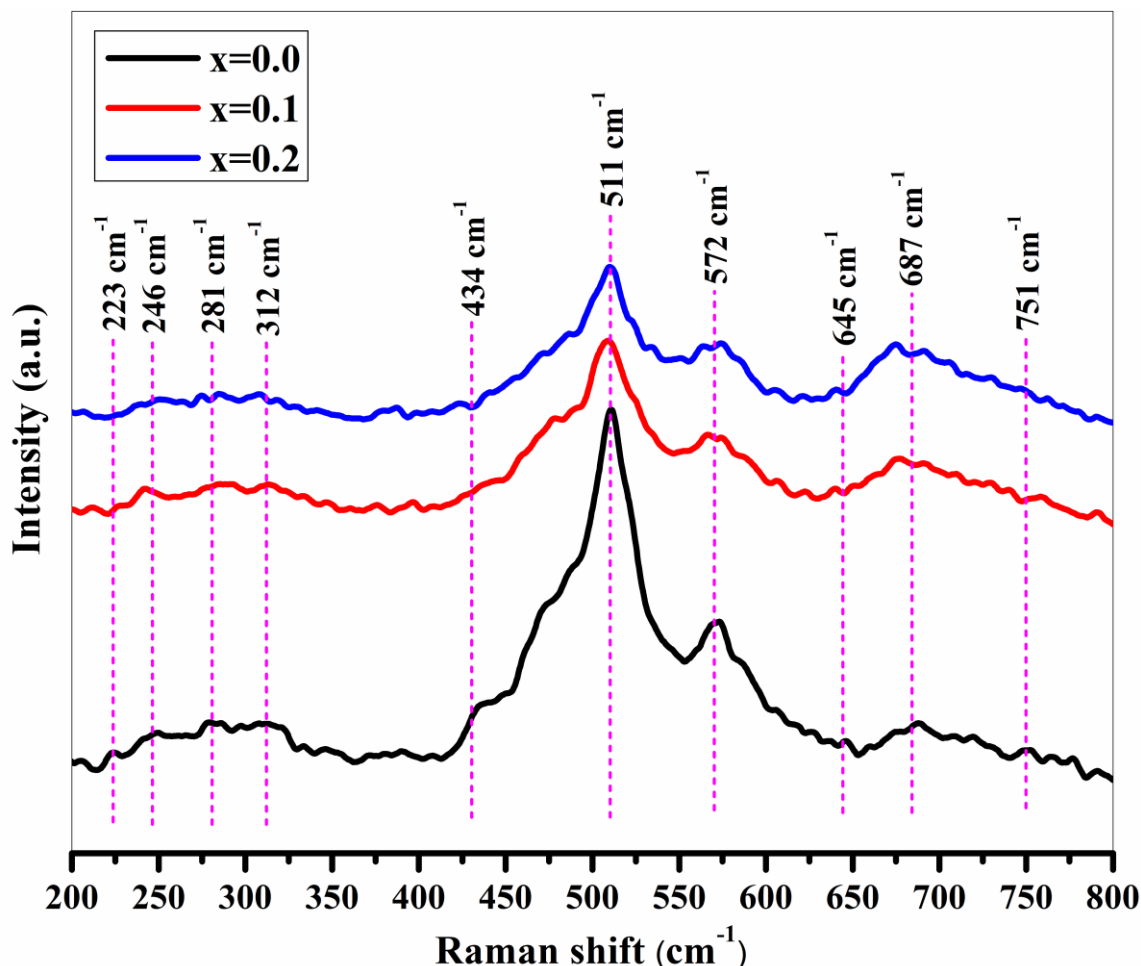
Fig. 5.60 Raman spectra of Bi$_{2/3}$Cu$_{3-2x}$Ni$_x$Co$_x$Ti$_4$O$_{12}$ (x=0.0, 0.1, 0.2)

5.5.4 Morphology analysis

Fig. 5.61 (a) and **(c)** shows Bi$_{2/3}$Cu$_{3-2x}$Ni$_x$Co$_x$Ti$_4$O$_{12}$ FESEM micrographs and particle distribution (x=0.0, 0.2). It can be noted that most particles display cubic-like shapes with non-uniformity in particle size which represents the BCTO structure. The average particle size was 0.22µm and 0.11µm respectively for x=0.0 and x=0.2 (**Fig. 5.61 (b)** and **(d)**). This decrease in average particle size is supported by XRD analysis where it has been observed that the crystallite size also decreases. EDX and mapping analysis were used to identify the composition of the prepared sample. **Fig. 5.62** presents the EDX spectra and mapping for

$Bi_{2/3}Cu_{3-2x}Ni_xCo_xTi_4O_{12}$ (x=0.0 and 0.2). Clearly, all the host and substituted cations (Bi, Cu, Ni, Co, Ti and O) have been observed in the prepared samples. This observation therefore confirms the stoichiometry and no impurity in the samples prepared. This also promotes the purity of the samples from XRD assessment observed.
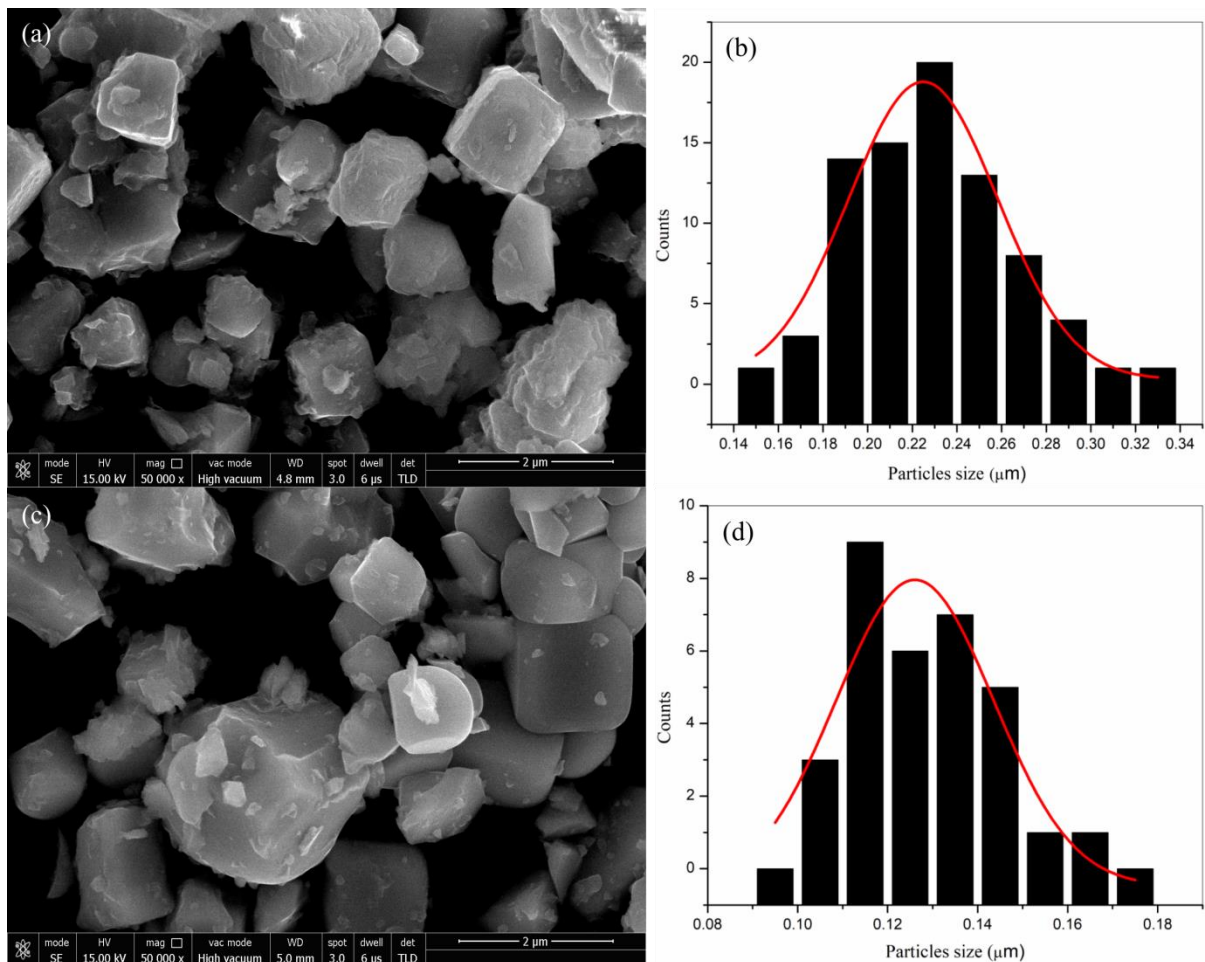
Fig. 5.61 FESEM micrograph and particles size distribution of $Bi_{2/3}Cu_{3-2x}Ni_xCo_xTi_4O_{12}$ (a-b) x=0.0 and (c-d) x=0.2
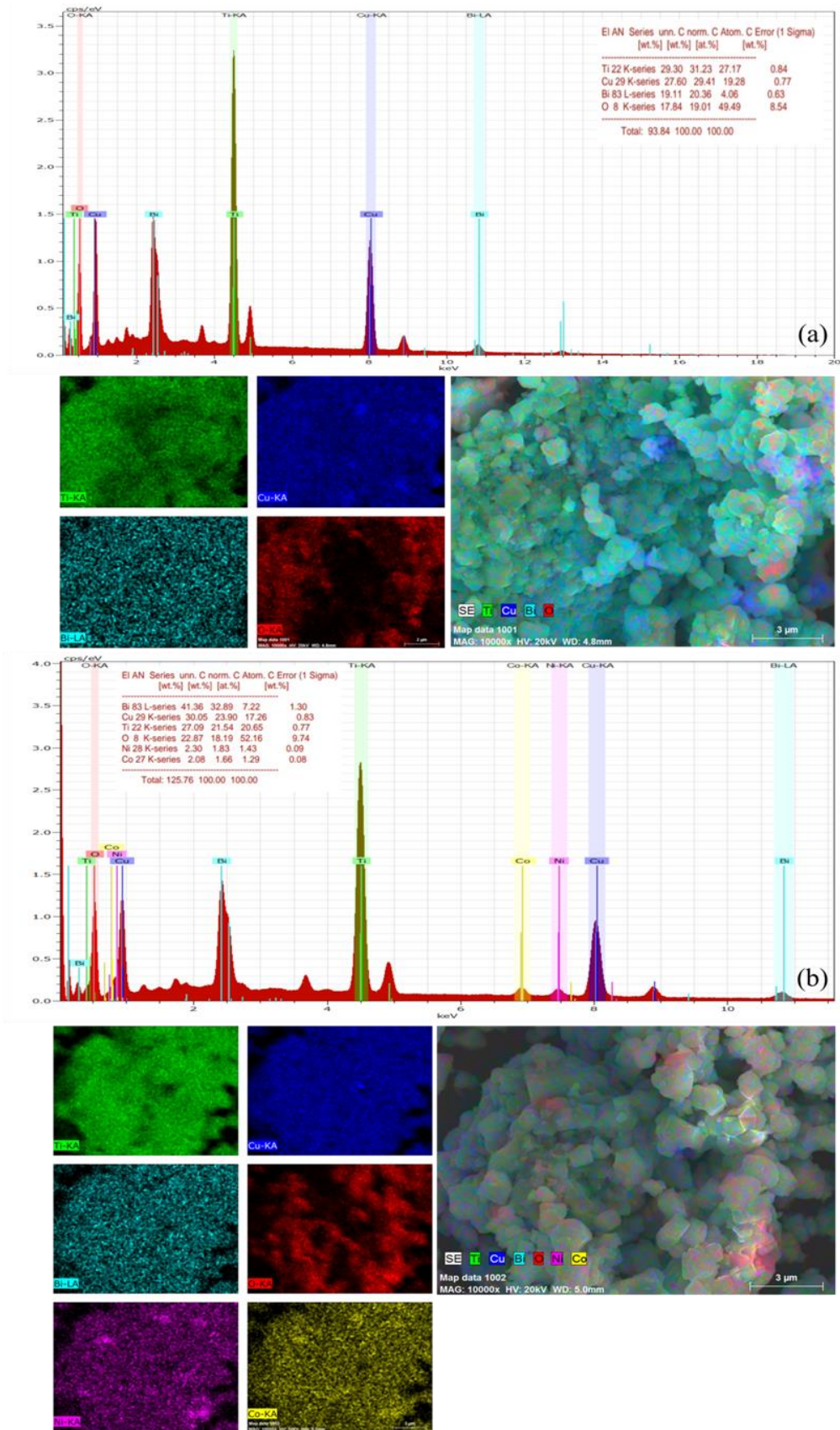
Fig. 5.62 EDX spectra and mapping of $Bi_{2/3}Cu_{3-2x}Ni_xCo_xTi_4O_{12}$ (a) $x=0.0$ and (b) $x=0.2$

5.5.5 Band gap and Urbach energy analysis

Using UV-Vis-NIR spectroscopy over the 220-1320 nm region, $Bi_{2/3}Cu_{3-2x}Ni_xCo_xTi_4O_{12}$ (x=0.0, 0.1, 0.2) optical assessment was conducted. The band gap (E_g) which is defined by the difference between the valence-band and conduction-band couple with semiconducting nature of the sample was evaluated using the Kubelka-Munk absorbance spectra by using the Tauc relation [27, 212]

$$\alpha h\upsilon = A\left(h\upsilon - E_g\right)^n \tag{5.71}$$

Where α represents the absorption coefficient which is proportional to the Kubelka-Munk function denoted by $F(r)$, A is a parameter which define a certain transition and its values rely on the values of n which are 1/2 (allowed direct transition), 2 (allowed indirect transition), 3/2 (forbidden direct transition), and 3 (forbidden indirect transition) values, υ is the incident photons frequency and h is the constant of Planck. **Fig. 5.63** shows the plot of absorbance spectra of $Bi_{2/3}Cu_{3-2x}Ni_xCo_xTi_4O_{12}$ (x=0.0, 0.1, 0.2). Clearly, five absorption peaks can be observed in the absorbance spectra between 225-1320 nm, specifically at 270, 368, 692, 808, and 936 nm. The strong absorption peak at 808 nm become more pronounced after the initiation of the substitution of Ni^{2+}-Co^{2+}, this could be attributed to the occupation of Ni^{2+} and Co^{2+} at Cu^{2+} site. The absorption peaks at 270, 368, 692, and 936 nm correspond to $\sigma - \sigma^*, n - \sigma^*, \pi - \pi^*$ and $n - \pi^*$ transitions respectively. Reflections peaks are observed at around 318 and 607 nm, the intensity of the reflection peak at 607 nm decreases with the increase in concentration of Ni^{2+}-Co^{2+}, this indicates that the replacement of Ni^{2+}-Co^{2+} increases the sample intake. Similar observation was made in the absorbance spectra of our previous research [96]. **Fig. 5.64** depicts plots of $(\alpha h\upsilon)^2$ as opposed to E_g for each BCTO electroceramic sample by extrapolating the linear portion of the graph and was found to be 3.64, 3.69 and 3.67 eV respectively for the x=0.0, x=0.1 and x=0.2 BCTO electroceramic samples (**Table 5.16 and Fig. 5.66**). The optical band gap varies inversely with the size of the crystallite, it was reported that the optical properties of the nanomaterials depend on the size of the crystallite, i.e. the larger the size of the crystallite, the smaller the band gap, Rashad et al reported similar situation [213].

The electrical properties of nanomaterials are influenced by the presence of defect states in the nanomaterials [212]. These defect states can be understood by investigating the spectral

dependence of the α at the region of lower photon energy which is much less than E_g, this region of lower photon energy is called the Urbach tail and is given by the equation [214]

$$\alpha = \alpha_0 \exp\left(\frac{hv}{E_U}\right) \tag{5.72}$$

Where α_0 is a constant, hv is the energy of the incident radiation, and E_U is the Urbach energy. We can obtain an equation of a straight line by taking the log of Eqn. 5.72 as thus

$$\ln \alpha = \left(\frac{1}{E_U}\right) hv + \ln \alpha_0 \tag{5.73}$$

Fig. 5.65 presents the graph of $\ln \alpha$ against hv for $Bi_{2/3}Cu_{3-2x}Ni_xCo_xTi_4O_{12}$ (x=0.0, 0.1, 0.2). The Urbach energy (E_U) of the samples was determine by linear fitting of the graph of $\ln \alpha$ against hv and taking the reciprocal of the slope. The values of E_U for the BCTO electroceramic samples was found to be 2.798 for x=0.0, 2.588 for x=0.1, and 2.590 for x=0.2 eV (**Table 5.16 and Fig. 5.66**). Deficiencies have been recorded and disorders can lead to the creation of localized states in or near the conductive band, thus improving the E_U bandwidth [215]. Hence, the observed values of E_U could be attributed to structural defects caused by the substitution of the host cation (Cu^{2+}) with larger ionic radii cations (Co^{2+} and Ni^{2+}), this structural defects have been observed in XRD analysis.

Table 5.16 Urbach energy and band gap of $Bi_{2/3}Cu_{3-2x}Ni_xCo_xTi_4O_{12}$ (x=0.0, 0.1, 0.2)

x	Urbach energy (eV)	Band gap (eV)
0.0	2.798	3.64
0.1	2.588	3.69
0.2	2.590	3.67
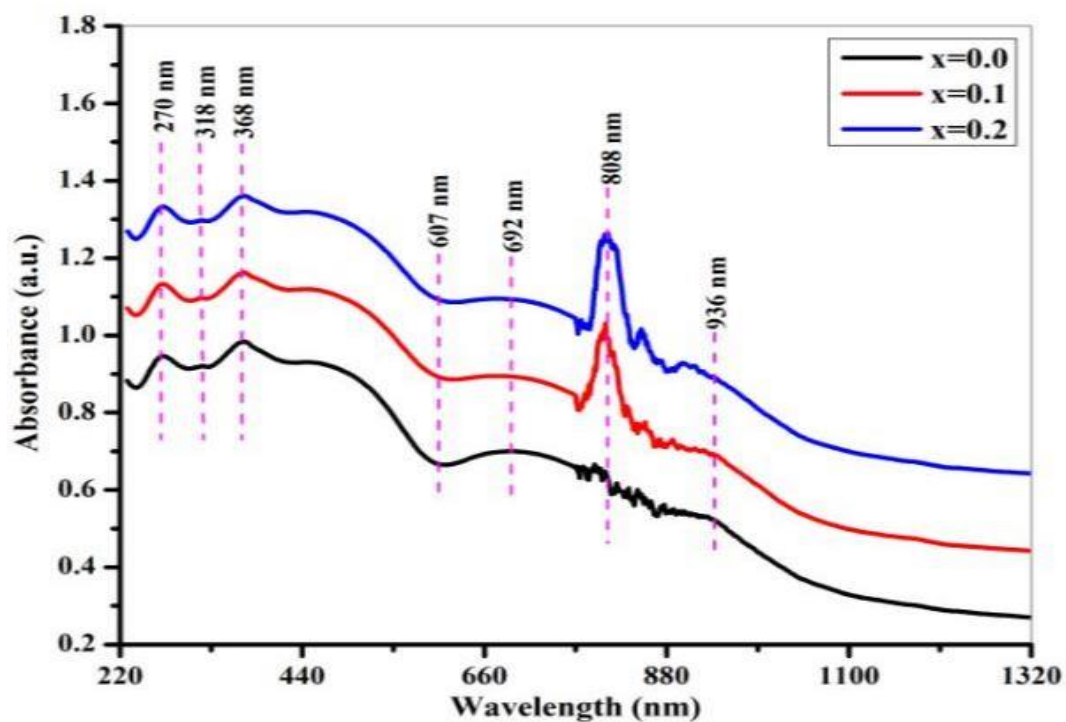
Fig. 5.63 Variation of absorbance with wavelength for $Bi_{2/3}Cu_{3-2x}Ni_xCo_xTi_4O_{12}$ (x=0.0, 0.1, 0.2)
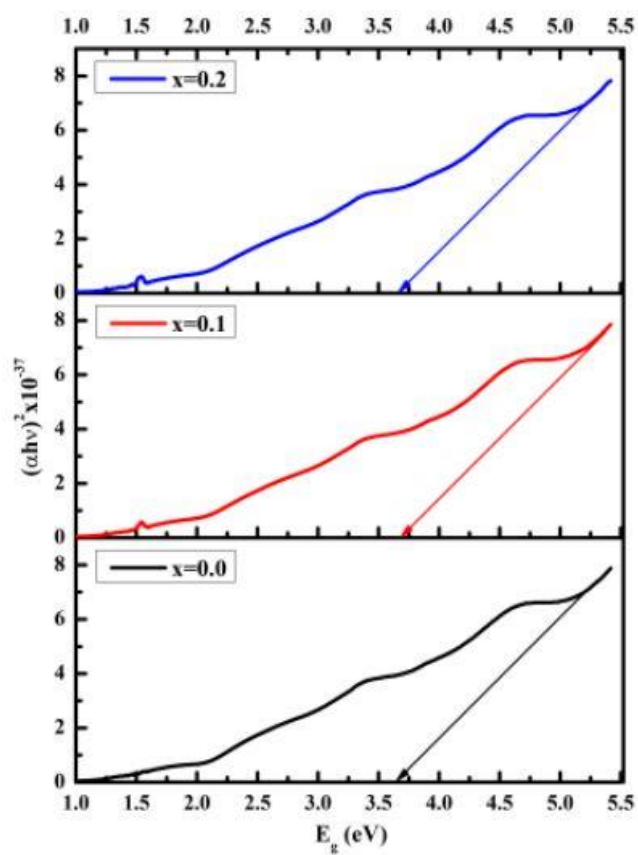
Fig. 5.64 Optical band gap for $Bi_{2/3}Cu_{3-2x}Ni_xCo_xTi_4O_{12}$ (x=0.0, 0.1, 0.2)
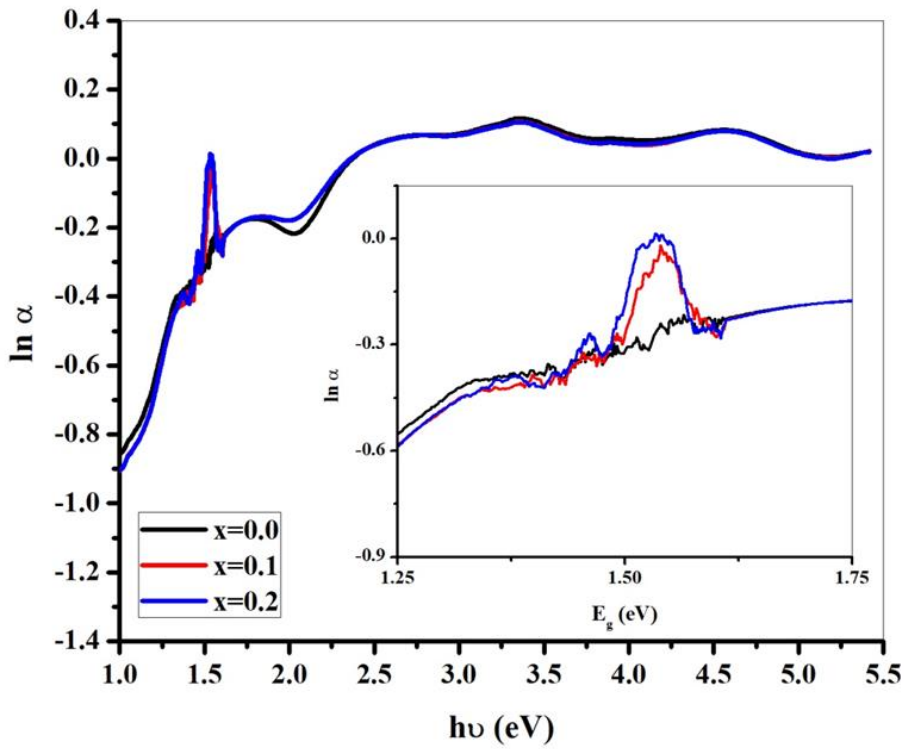
Fig. 5.65 Urbach energy for $Bi_{2/3}Cu_{3-2x}Ni_xCo_xTi_4O_{12}$ (x=0.0, 0.1, 0.2)
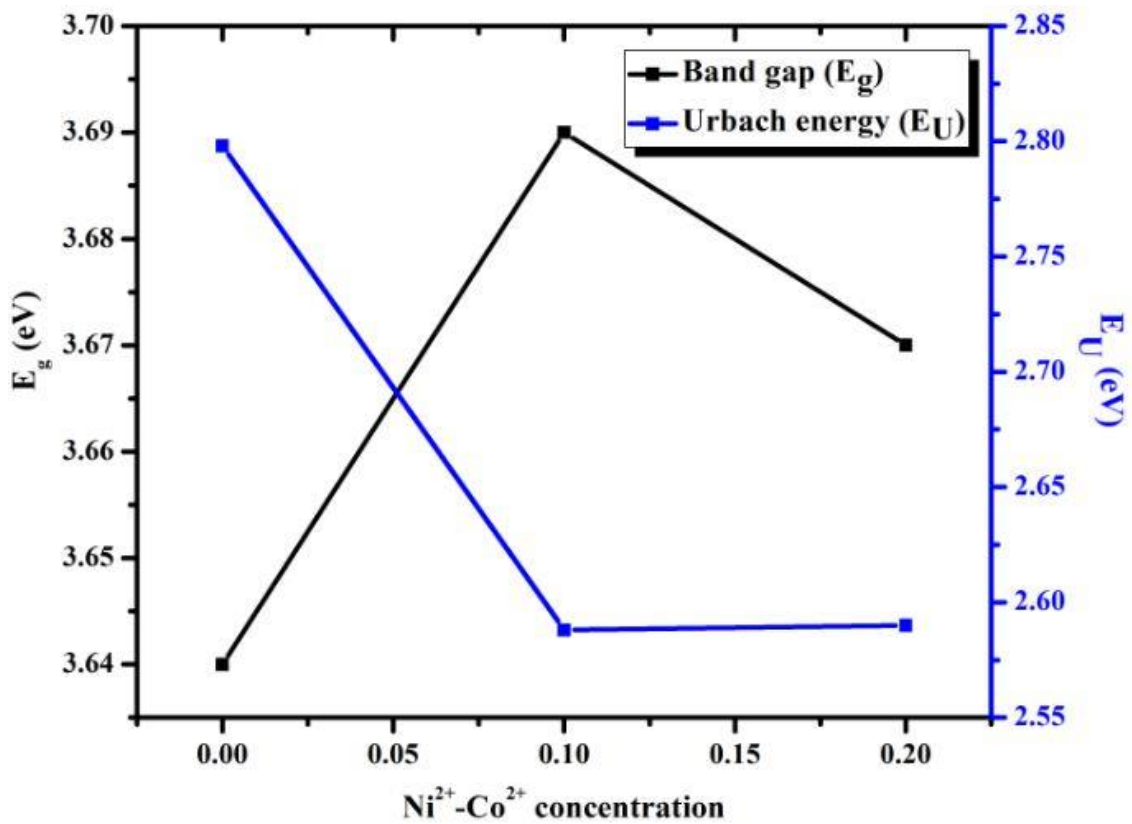
Fig. 5.66 Variation of band gap and Urbach energy against Ni^{2+}-Co^{2+} concentration for $Bi_{2/3}Cu_{3-2x}Ni_xCo_xTi_4O_{12}$ (x=0.0, 0.1, 0.2)

5.5.6 Dielectric response

Material dielectric properties rely on variables such as preparation technique, heating temperature and time, cation replacement and concentration in the sample. These factors determine the nature of the ionic, dipolar, electronic, and interfacial polarization mechanism. Complex permittivity (ε^*) determines the dielectric reaction of the prepared specimens which is written as

$$\varepsilon^* = \varepsilon' - j\varepsilon'' \tag{5.74}$$

With $j = \sqrt{-1}$ being a complex number, ε' being the real part of complex permittivity and ε'' being the imaginary part of complex permittivity which are expressed as

$$\varepsilon' = \frac{Z''}{\omega C_0 Z^2} \tag{5.75}$$

$$\varepsilon'' = \frac{Z'}{\omega C_0 Z^2} \tag{5.76}$$

Where Z' and Z'' are the real and imaginary parts of complex impedance respectively, $\omega = 2\pi f$ being the frequency and C_0 being the geometrical capacitance. The dielectric tangent loss can be written as a ratio of ε'' and ε' as

$$\tan \delta_e = \frac{\varepsilon''}{\varepsilon'} \tag{5.77}$$

Fig. 5.67 and **5.68** are the plots of the variation of dielectric constant (ε') and dielectric tangent loss ($\tan \delta$) against logarithmic frequency for $Bi_{2/3}Cu_{3-2x}Ni_xCo_xTi_4O_{12}$ (x=0.0, 0.1, 0.2). From **Fig. 5.67**, it can be noted that, at reduced frequencies, the prepared samples display large ε'. The values of ε' are 3800 for x=0.0, 2200 for x=0.1, and 2700 for x=0.3. The appearance of high dielectric constant at lower frequencies signify the possibility of accumulation of charge carriers on the interface of grains and grain boundary which result in space charge polarization [216]. This explanation is based on Maxwell-Wagner model which states that dielectric materials having heterogeneous structure can be assumed to comprise of grains which are conducting and grain boundaries which are insulating, this situation causes the appearance of space charge polarization when the applied field drop across the grain boundaries [217]. Clearly, low concentration of Ni^{2+} and Co^{2+} decrease the values of ε' as seen in the BCTO electroceramic having x=0.1. As the concentration of Ni^{2+} and Co^{2+} is increased (BCTO electroceramic having x=0.2), the values of ε' increases. The ε' values

decreases as the frequency is increased, this is obvious for all samples at reduced, intermediate and higher frequencies except for BCTO electroceramic with x=0.0 where autonomous behaviour was observed at higher frequencies. Similar to ε', $\tan \delta_e$ decreases as the frequency is increased at lower frequencies for the BCTO electroceramic having x=0.01 and x=0.2, this could be due to the polarization of the interfacial space charge as already stated in the analysis of ε'. Nonetheless, $\tan \delta_e$ steadily increase at higher frequencies due to structural defects which cause electronic polarization [96, 218]. The sample with x=0.0 shows a Debye-type relaxation peak at intermediate frequencies, this could be attributed to dipolar or ionic/atomic polarization [219, 220].
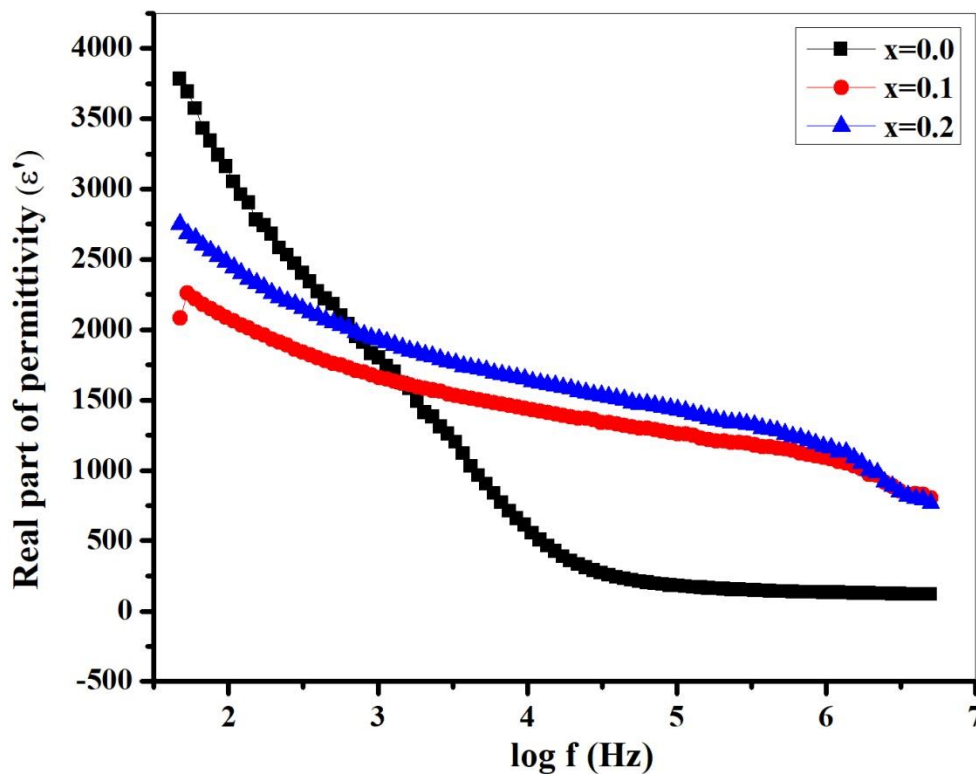
Fig. 5.67 Variation of dielectric constant with frequency for $Bi_{2/3}Cu_{3-2x}Ni_xCo_xTi_4O_{12}$ (x=0.0-0.2)
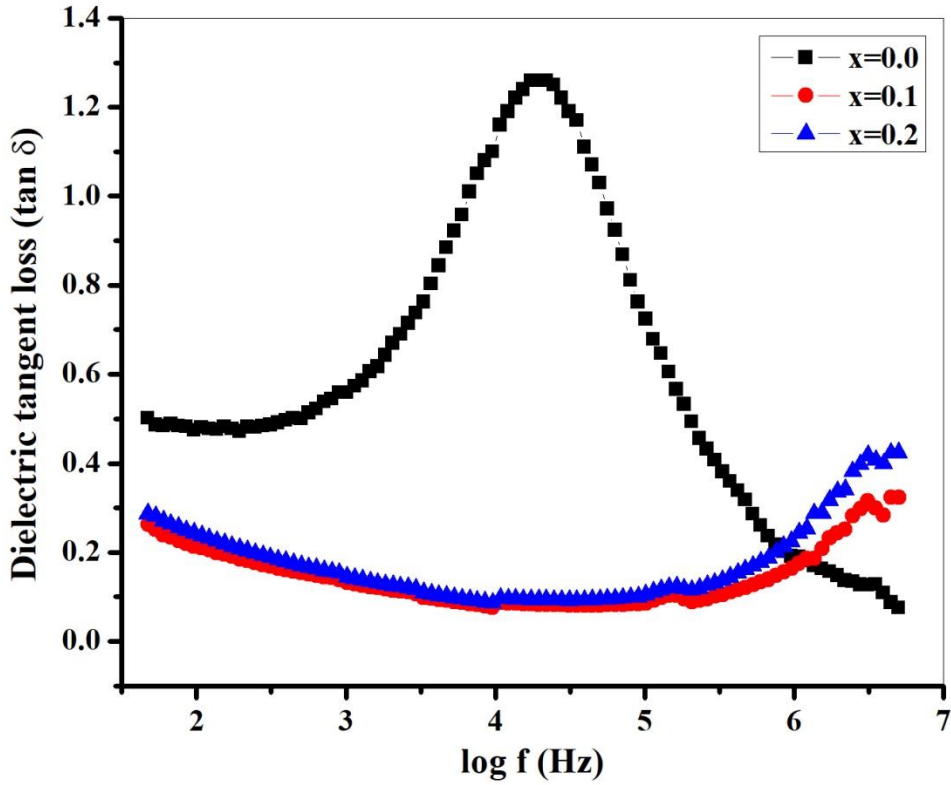
Fig. 5.68 Variation of dielectric loss tangent with frequency for $Bi_{2/3}Cu_{3-2x}Ni_xCo_xTi_4O_{12}$ (x=0.0, 0.1, 0.2)

5.5.7 Impedance and modulus spectroscopy

Usually, heterogeneous polycrystalline materials give more than one electrical response and show both grain and grain boundary contribution [221]. The grain resistance (R_g) and grain boundary resistance (R_{gb}) contributions to the dielectric response can be determined from the nature of the semi-circular arc obtained in the plot of Z'' against Z', also called Nyquist plot. Complex impedance (Z^*) can be describes as a function of real (Z') and imaginary (Z'') parts of complex impedance as [65]

$$Z^* = Z' - jZ'' \tag{5.78}$$

Where

$$Z' = \frac{R_g}{1+(\omega R_g C_g)^2} + \frac{R_{gb}}{1+(\omega R_{gb} C_{gb})^2} \tag{5.79}$$

and

$$Z'' = \frac{\omega R_g^2 C_g}{1+(\omega R_g C_g)^2} + \frac{\omega R_{gb}^2 C_{gb}}{1+(\omega R_{gb} C_{gb})^2} \tag{5.80}$$

Where C_g is the grain capacitance, C_{gb} is grain boundary capacitance, $\omega = 2\pi f$ is the angular frequency and $j^2 = -1$ is complex number. Similarly, the complex electric modulus (M^*) can be written as a function of real (M') and imaginary (M'') parts of complex electric modulus as [222]

$$M^* = M' + jM'' \tag{5.81}$$

Where

$$M' = \omega C_0 Z'' \tag{5.82}$$

and

$$M'' = \omega C_0 Z' \tag{5.83}$$

Where $C_0 = \varepsilon_0 S/t$ is capacitance of free space, ε_0 is the permittivity of free space, S is the surface area of pellet sample and t is the thickness of pellet of sample. **Fig. 5.69** presents the Nyquist plot of complex impedance for $Bi_{2/3}Cu_{3-2x}Ni_xCo_xTi_4O_{12}$ (x=0.0, 0.1, 0.2). Generally, Nyquist plot present three semicircle arcs, the semicircle arc from the left side (higher frequency) displays the R_g contribution which corresponds to intrinsic property of the material while the one at intermediate frequency gives the contribution of R_{gb} and semicircle arc in the right side correspond to the contribution of the grain-interface which corresponds to extrinsic property of the material [156]. From the inset of **Fig. 5.69**, it can be observed that two semicircle arcs were observed for the BCTO electroceramic having x= 0.0 whereas the BCTO electroceramic having x≠0.0 were not observed as a result of very small radii of the semicircle arcs. The grain and grain boundary resistances can be evaluated from the intercept of the semicircle with Z'-axis at higher and lower frequency respectively [96]. It was noticed that that grain boundary resistance R_g increased and then decreases with the concentration of Ni^{2+}-Co^{2+} substitution. As observed, the grain boundary resistance R_{gb} is higher than grain resistance ($R_{gb} \gg R_g$), this was also obse

rved by Z. Yang et al. [60]. To correlate the relationship between microstructure and electrical properties, data are generally modelled by an ideal equivalent electrical circuit consisting of resistance and capacitance as shown in **Fig. 5.69**. The electric modulus formalism is often associated with impedance formalism so as to determine the different microscopic processes accountable for localized dielectric relaxations as well as long-range conductions [152]. Indeed, the electric modulus is very important for electrical relaxation processes and is based capacitance effects. Nyquist plot of complex electric modulus for $Bi_{2/3}Cu_{3-2x}Ni_xCo_xTi_4O_{12}$ (x=0.0, 0.1, 0.2) is shown in **Fig. 5.70**. Unlike Nyquist plot for complex impedance (Z'' vs Z'), the semicircle arc from left side correspond to the contribution of grain boundary capacitance (C_{gb}) at lower frequency and the semicircle on right side correspond to the contribution grain capacitance (C_g) at higher frequency, it can be seen that the radius of the arc decreases then increase with increase in frequency and concentration of Ni^{2+}-Co^{2+} substitution. This clearly indicates that the observed semicircle arcs in **Fig. 5.70** are attributed to contribution of grain and grain boundary effect [156].
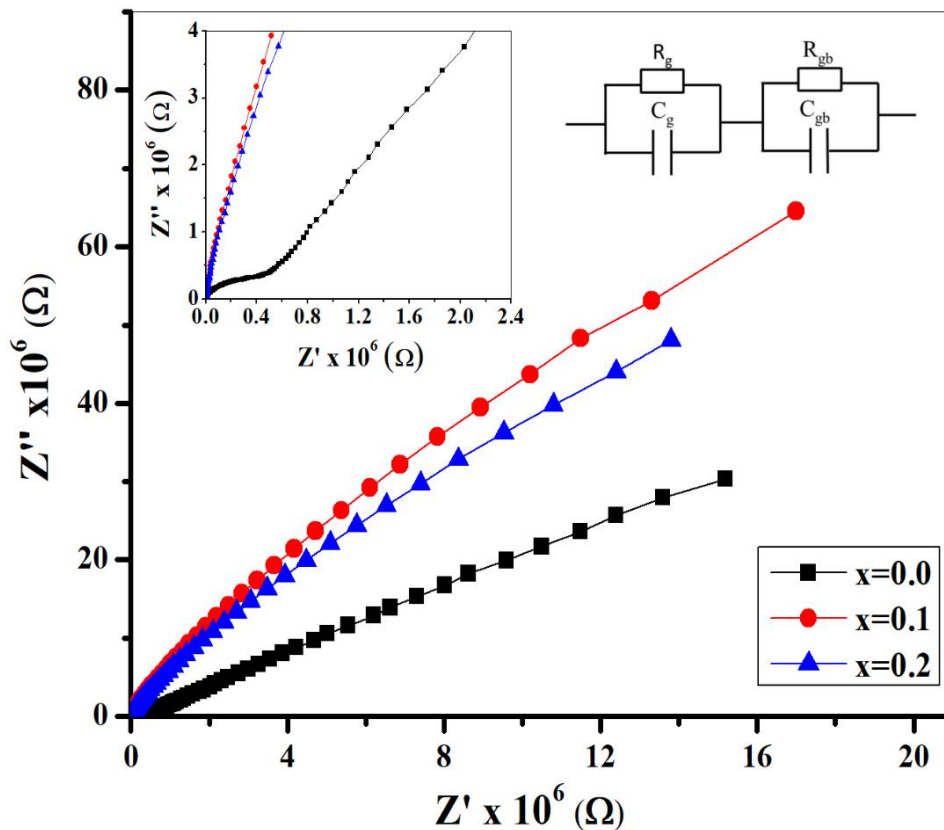
Fig. 5.69 Nyquist plot of complex impedance for $Bi_{2/3}Cu_{3-2x}Ni_xCo_xTi_4O_{12}$ (x=0.0, 0.1, 0.2)
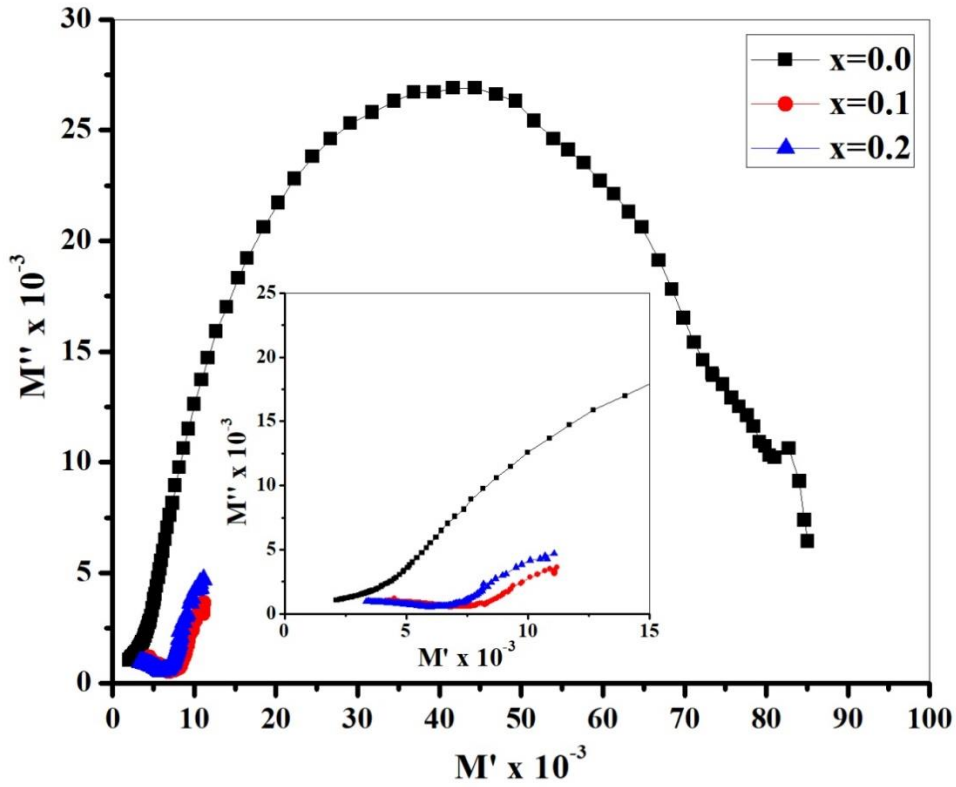
Fig. 5.70 Nyquist plot of complex electric modulus for $Bi_{2/3}Cu_{3-2x}Ni_xCo_xTi_4O_{12}$ (x=0.0, 0.1, 0.2)

5.5.8 AC electrical conductivity analysis

The total conductivity (σ_t) in the material is consisted of two terms and can be defined by [94, 96]

$$\sigma_t = \sigma_{AC} + \sigma_{DC} \tag{5.84}$$

Where $\sigma_{DC} = \sigma_0 e^{-E_a/kT}$ represents the frequency independent part of conductivity and $\sigma_{AC}(\omega, T) = A\omega^s$ being the frequency and temperature dependent part of conductivity, σ_0 is a pre-exponential constant, E_a is the activation energy for electrical conduction, T is temperature, k is Boltzmann's constant, A is a temperature-dependent constant, s is a numerical constant and $\omega = 2\pi f$ is the angular frequency with f as frequency. Additionally, the AC conductivity can be calculated using the following formula

$$\sigma_{AC} = \varepsilon_0 \omega \varepsilon'' = \varepsilon_0 \omega \varepsilon' tan\delta_e \tag{5.85}$$

Fig. 5.71 displays for the $Bi_{2/3}Cu_{3-2x}Ni_xCo_xTi_4O_{12}$ frequency AC conductivity variation (x=0.0, 0.1, 0.2). AC conductivity shows similar behaviour with the other dielectric parameters. AC conductivity values indicates frequency-independent behaviour at reduced and intermediate frequencies and rise at greater frequencies abruptly. Hopping, tunnelling of charges or free band conduction could be the reason for the abrupt increase of conductivity at higher frequencies [96]. The highest value of AC conductivity was found to be 0.08 S.cm^{-1} for x=0.2. **Fig. 5.72** shows the variation of ln σ_{AC} with ln ω for $Bi_{2/3}Cu_{3-2x}Ni_xCo_xTi_4O_{12}$ (x=0.0, 0.1, 0.2), which is frequency and temperature dependent and can be written as

$$\sigma_{AC}(\omega, T) = A\omega^s \tag{5.86}$$

We can modify Eqn. 5.86 to get an equation of a straight line by taking the log of the equation

$$\ln \sigma_{AC}(\omega, T) = s \ln \omega + \ln A \tag{5.87}$$

The value of s is the slope of the straight line graph represented by Eqn. 5.87. The values of s falls between 0 and 1 and it determine the nature of the conductivity of the samples. The conductivity is frequency independent when $s = 0$, whereas it is frequency dependent for $s \leq 1$ [24]. From **Fig. 5.72**, the values of 0.53, 0.92 and 0.93 were respectively for x=0.0, x=0.1, and x=0.2. Since $s \neq 0$, then we can conclude that the AC conduction is the dominant conductivity in the sample.
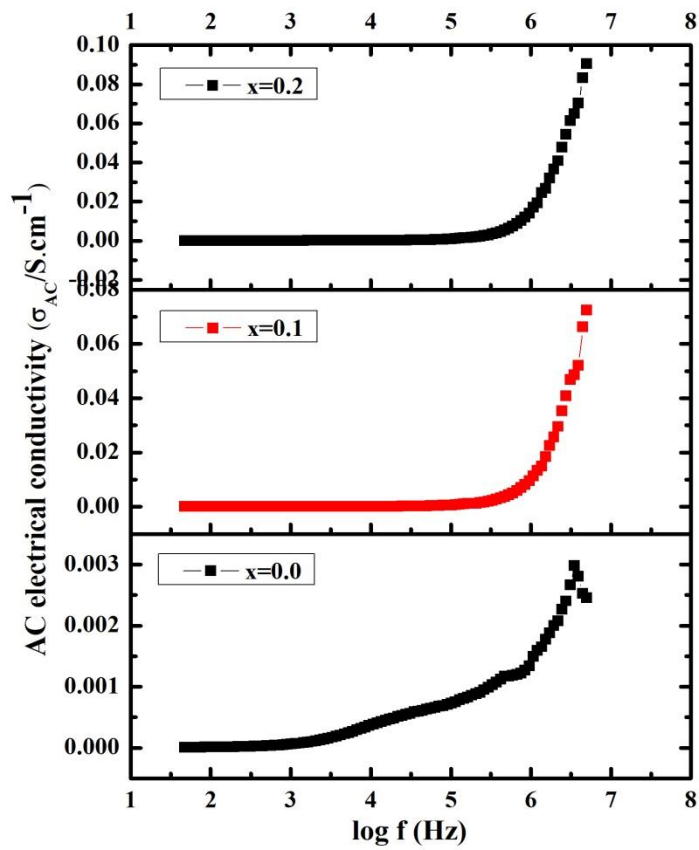
Fig. 5.71 Variation of Ac conductivity with frequency for $Bi_{2/3}Cu_{3-2x}Ni_xCo_xTi_4O_{12}$ (x=0.0, 0.1, 0.2)
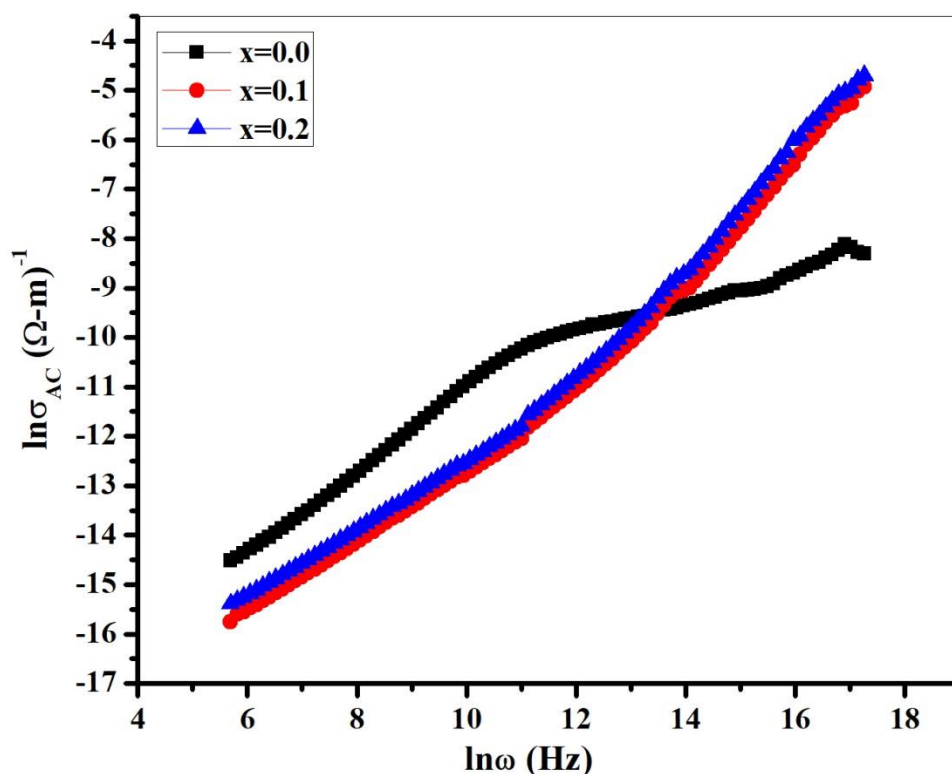
Fig. 5.72 Variation of ln σ_{ac} with ln ω for $Bi_{2/3}Cu_{3-2x}Ni_xCo_xTi_4O_{12}$ (x=0.0, 0.1, 0.2)

5.6 Structural and optical properties of $BaFe_{11.8}Bi_{0.1}Al_{0.1}O_{19}$ embedded in polyaniline (PANI) for electronic devices

5.6.1 XRD analysis

Using X-ray diffraction, the crystal structure of $BaFe_{11.8}Bi_{0.1}Al_{0.1}O_{19}$-PANI nanocomposites was studied. XRD sample patterns are shown in **Fig. 5.73**. The observed peaks in this figure have been indexed using 39-1433 as JCPDS card [30] and correspond to reflection planes of $BaFe_{11.8}Bi_{0.1}Al_{0.1}O_{19}$ which are matching to the specific diffraction angles . It was found that all these peaks correspond to diffraction planes of pure M-type barium hexagonal ferrite with *P63/mmc* as space group. The absence of second phase confirms the single crystal phase of $BaFe_{11.8}Bi_{0.1}Al_{0.1}O_{19}$ which indicates that Al^{3+} and Bi^{3+} ions occupied perfectly crystallographic sites of Fe^{3+} ions. Generally in M-type hexaferrite, the second phase (α-Fe_2O_3) appear at around 2θ=33.13 and correspond to (103) diffraction plane. From **Fig. 5.73**,

147

the presence of PANI in the composite is materialized by the large peak observed at around 2θ=25.12-25.46; this is supported by J. Luo and C. L. Yuan [7, 8]. Rietveld refinement of the crystal structure of $BaFe_{11.8}Bi_{0.1}Al_{0.1}O_{19}$ has been done by the use of FULLPROF suite package. The diffraction peaks were modelled with Thompson-Cox-Hastings pseudo-Voigt * Axial divergence asymmetry function and linear interpolation method was used to model the background. During the refinement, parameters such as occupancy of all atoms, background, atomic positions, unit cell, half-width and zero position were varying throughout the process. This refinement has confirmed that the observed peaks in XRD patterns are those of M-type hexaferrite with space group *P63/mmc* (**Fig. 5.74**). The quality of refinement is justified by reliability factors (R_p, R_{wp}, R_{exp}, χ^2 and GoF) given in **Table 5.17**. GoF (Good of fit) has been found to be between 1.6-1.8. Crystallite size (D), unit cell parameters (a and c) and volume (V) were calculated using the following formulae and summarized in **Table 5.17**:

$$\frac{1}{d_{hkl}^2} = \frac{4}{3}\left(\frac{h^2+hk+k^2}{a^2}\right) + \frac{l^2}{c^2} \tag{5.88}$$

$$V_{cell} = \frac{\sqrt{3}}{2}a^2c \tag{5.89}$$

$$D = \frac{0.9\lambda}{\beta\cos\theta} \tag{5.90}$$

Where, d_{hkl} refers to d-spacing, hkl are the miller indices, λ =1.54056 Å is the wavelength of incident X-ray, β is full width at half maxima (in radian), θ is the Bragg angle. The crystallite size of prepared composite were found to be between 37-41 nm while lattice parameters a, c and Vcell were found to be in the range 5.86-5.89 Å, 23.11-23.17 Å and 689.37-694.56 Å^3. It was observed that a, c and Vcell increase with amount of PANI. This can be due to the fact that after adding PANI, the crystal structure of $BaFe_{11.8}Bi_{0.1}Al_{0.1}O_{19}$ has undergone some distortions. This distortion (stretching) of the structure can be justified by the shifting of diffraction angle (2θ) toward small values (**Fig. 5.73**). Bulk density (d_m) of sample has been estimated. It was found to be between 1.09-1.18g/cm^3. These values are very small compared to the bulk density of M-type barium hexaferrite ($BaFe_{12}O_{19}$) which is around 3.23g/cm^3 as reported by Tchouank et al.[133]. The reason of this difference in d_m may be due to the fact that PANI is less dense than M-type hexaferrite material.

Table 5.17 Structural parameters and reliability factors

x	HP1	HP2	HP3
$\beta(^\circ)$	0.224	0.225	0.194
Crystallite size (D) nm	37.108	35.307	40.949
Lattice parameter (a) Å	5.868	5.872	5.884
Lattice parameter (c) Å	23.114	23.114	23.163
Volume of unit cell (V) Å^3	689.37	690.122	694.55
Bulk density (d_m) g/cm^3	1.111	1.175	1.094
R_{bragg}	5.57	6.72	5.13
R_P	13.2	14.0	12.6
R_{wp}	21.7	22.9	20.7
R_{exp}	12.1	14.2	12.4
χ^2	3.229	2.608	2.792
GoF	1.8	1.6	1.7
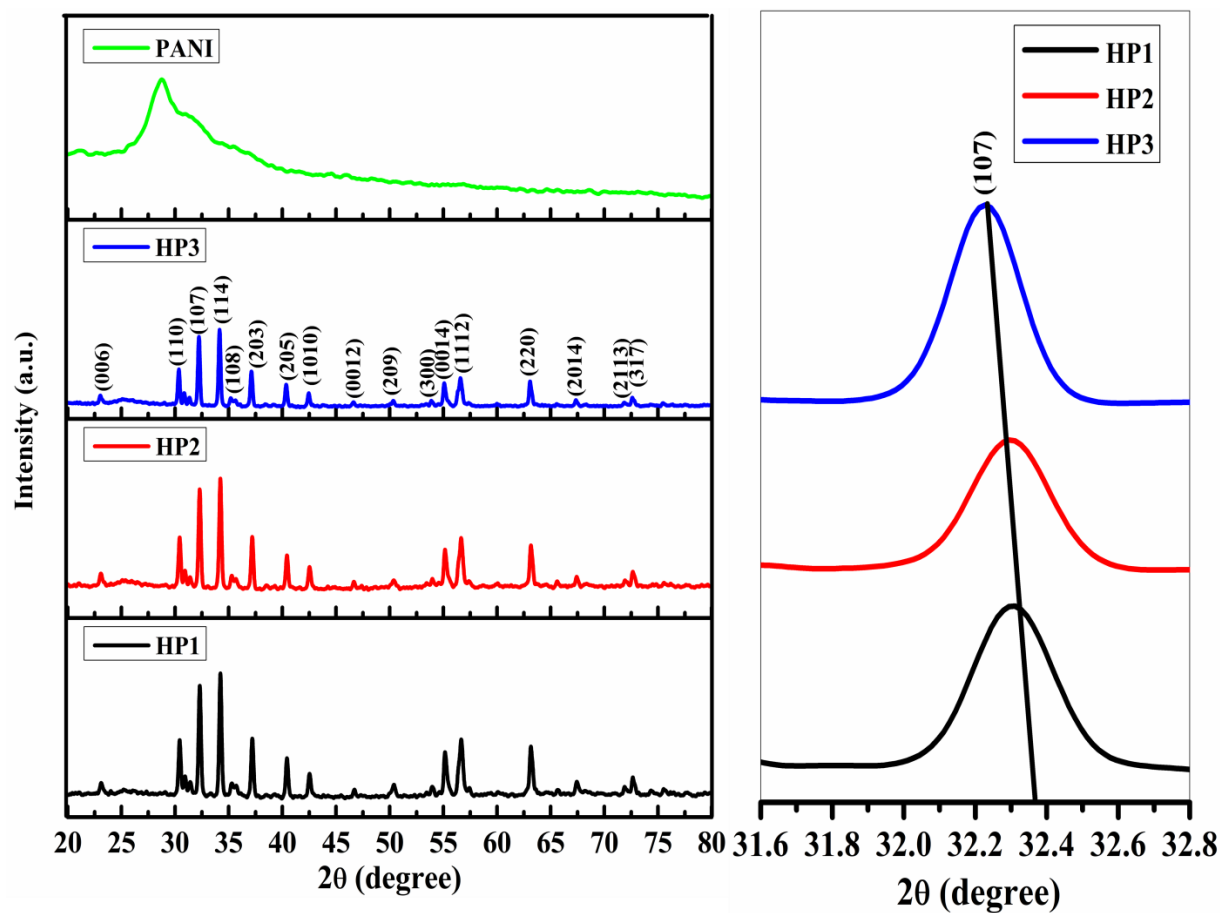
Fig. 5.73 XRD patterns of $BaFe_{11.8}Bi_{0.1}Al_{0.1}O_{19}$-PANI composite
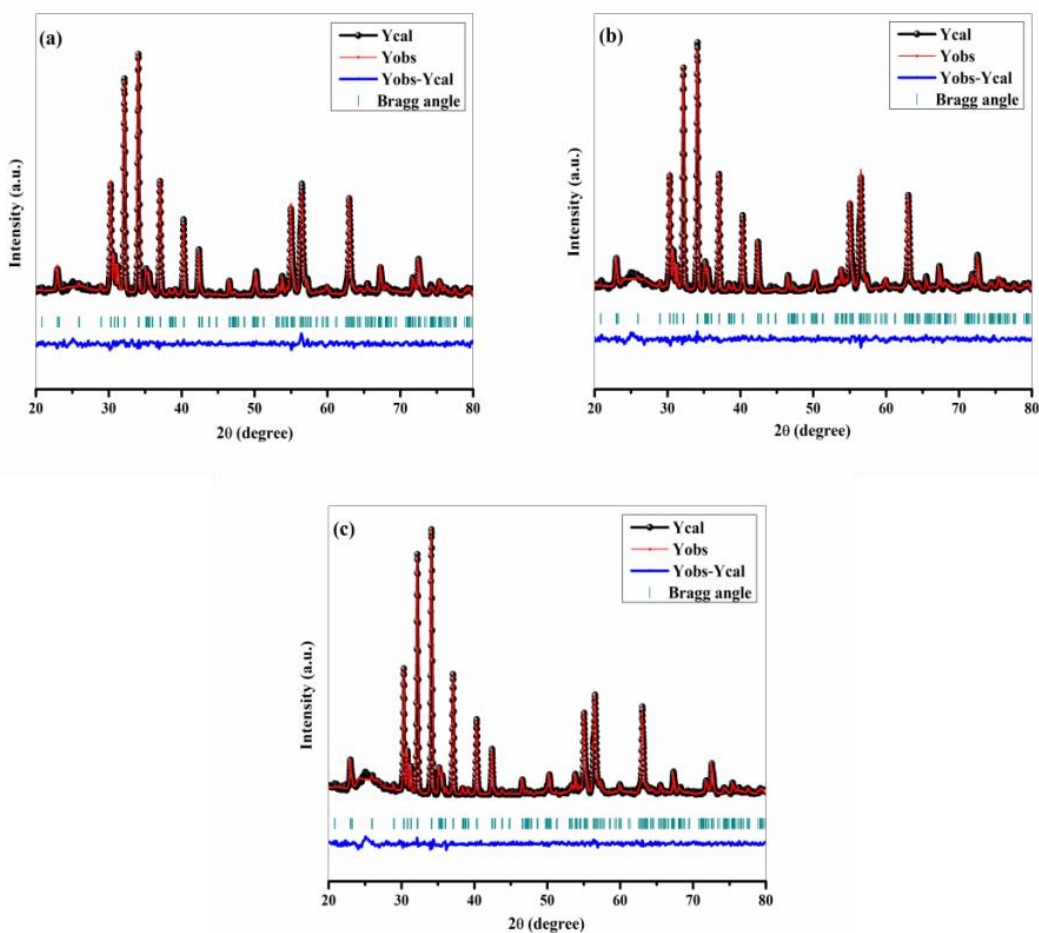
Fig. 5.74 Rietveld Refinement of $BaFe_{11.8}Bi_{0.1}Al_{0.1}O_{19}$-PANI composite (a) HP1, (b) HP2 and (c) HP3

5.6.2 FTIR analysis

FTIR spectroscopy was used to determine functional groups in prepared samples. For analysis, thin pellets of KBr with the prepared samples in the ratio 10:1 respectively have been made. **Fig. 5.75** shows FTIR spectra of PANI and $BaFe_{11.8}Bi_{0.1}Al_{0.1}O_{19}$-PANI composites recorded in the wavenumber range 400-4000 cm^{-1}. FTIR spectrum of PANI is given in **Fig. 5.75(d)** and its characteristic absorption peaks were found at around 804 cm^{-1} (out-of plane deformation vibration of benzene ring), 1123 and 1601 cm^{-1} (vibration band of N=Q=N) indicating the formation of PANI, 1297 cm^{-1} (N-H bending band of benzenoid rings) and 1486 cm^{-1} (C=N stretching of quinoid ring) [223-228]. **Fig. 5.75(a-c)** displays HP1, HP2 and HP3 FTIR spectra respectively. In these figures, it can be noted there are all distinctive peaks of PANI that can indicate the coating of $BaFe_{11.8}Bi_{0.1}Al_{0.1}O_{19}$ particles with PANI in HP1, HP2 and HP3 samples. The characteristic peaks of $BaFe_{11.8}Bi_{0.1}Al_{0.1}O_{19}$ are defined by Fe-O bond vibration at 442 and 587 cm^{-1} [30]. The peak observed at 2356 cm^{-1}

refers to the presence of CO_2 in the sample which was absorbed from the atmosphere and the wide band at 3429 cm^{-1} refers to the vibration of –OH group.
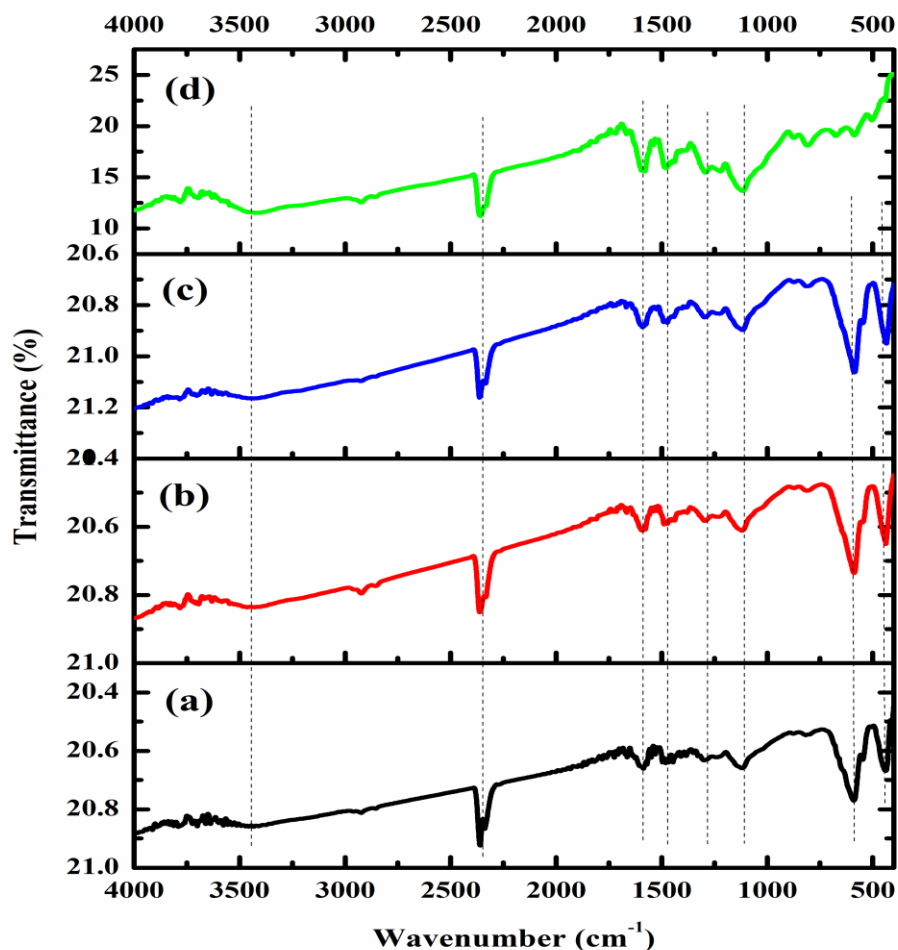
Fig. 5.75 FTIR spectra of (a) PANI, (b) HP1, (c) HP2 and (d) HP3

5.6.3 Morphological analysis

FESEM micrograph of $BaFe_{11.8}Bi_{0.1}Al_{0.1}O_{19}$-PANI composite especially HP1 is given in **Fig. 5.76**. In this image, it can be noticed that PANI has coated hexaferrite particles and the size of observed spherical particles was found to be 25-50 nm. The composition of sample presented by FESEM micrograph has been examined by EDX analysis given in **Fig. 5.77**. The weight percent of each chemical element is showing in **Fig. 5.77** (inset). All chemical elements that constitute both $BaFe_{11.8}Bi_{0.1}Al_{0.1}O_{19}$ and PANI are presents what confirm the homogenous distribution and results revealed by XRD analysis.
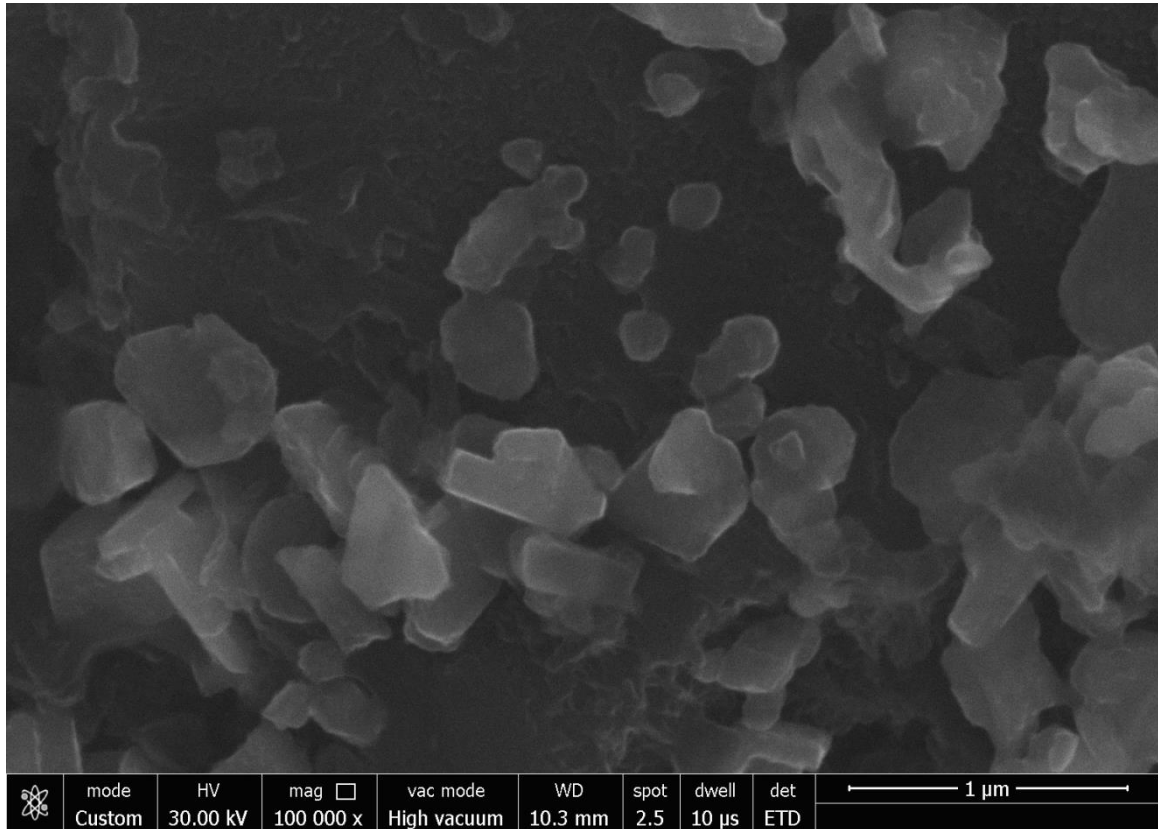
Fig. 5.76 FESEM micrographs of $BaFe_{11.8}Bi_{0.1}Al_{0.1}O_{19}$-PANI composite

El	AN	Series	unn. C [wt.%]	norm. C [wt.%]	Atom. C [at.%]	Error (1 Sigma) [wt.%]
C	6	K-series	61.75	61.75	68.45	7.92
O	8	K-series	23.73	23.73	19.74	4.17
N	7	K-series	11.82	11.82	11.24	3.15
Fe	26	K-series	1.97	1.97	0.47	0.11
Ba	56	L-series	0.42	0.42	0.04	0.06
Bi	83	L-series	0.23	0.23	0.01	0.09
Al	13	K-series	0.08	0.08	0.04	0.04
		Total:	100.00	100.00	100.00	
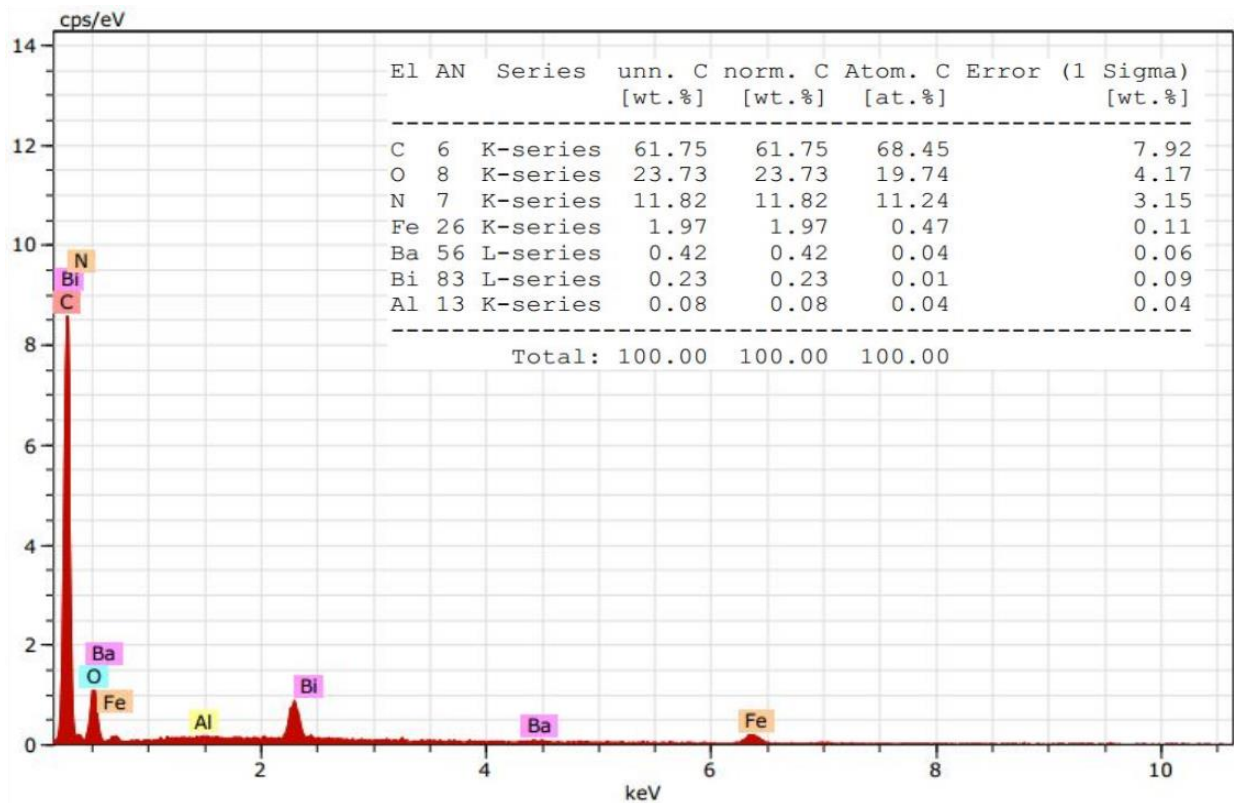
Fig. 5.77 EDXS spectra of $BaFe_{11.8}Bi_{0.1}Al_{0.1}O_{19}$-PANI composite

152

5.6.4 Optical analysis

UV-vis spectroscopy was employed to examine the $BaFe_{11.8}Bi_{0.1}Al_{0.1}O_{19}$-PANI composite optical properties. **Fig. 5.78** exhibits the absorption spectra of prepared sample in the range 200-780nm. According to the literature, PANI presents two characteristic absorption bands in UV-vis spectrum especially at around 336nm and 600 nm which are allocated to the phenyl ring ($\pi - \pi^*$) and benzenoid to quinoid ($n - \pi^*$) transitions respectively [226, 229]. In the present case, the UV-vis spectra are also showing to two large absorption peaks indicating the presence of PANI. Those two absorption bands were found to be (323 nm and 580nm) for HP1, (323 nm and 584 nm) for HP2 and (323 nm and 585 nm) for HP3.
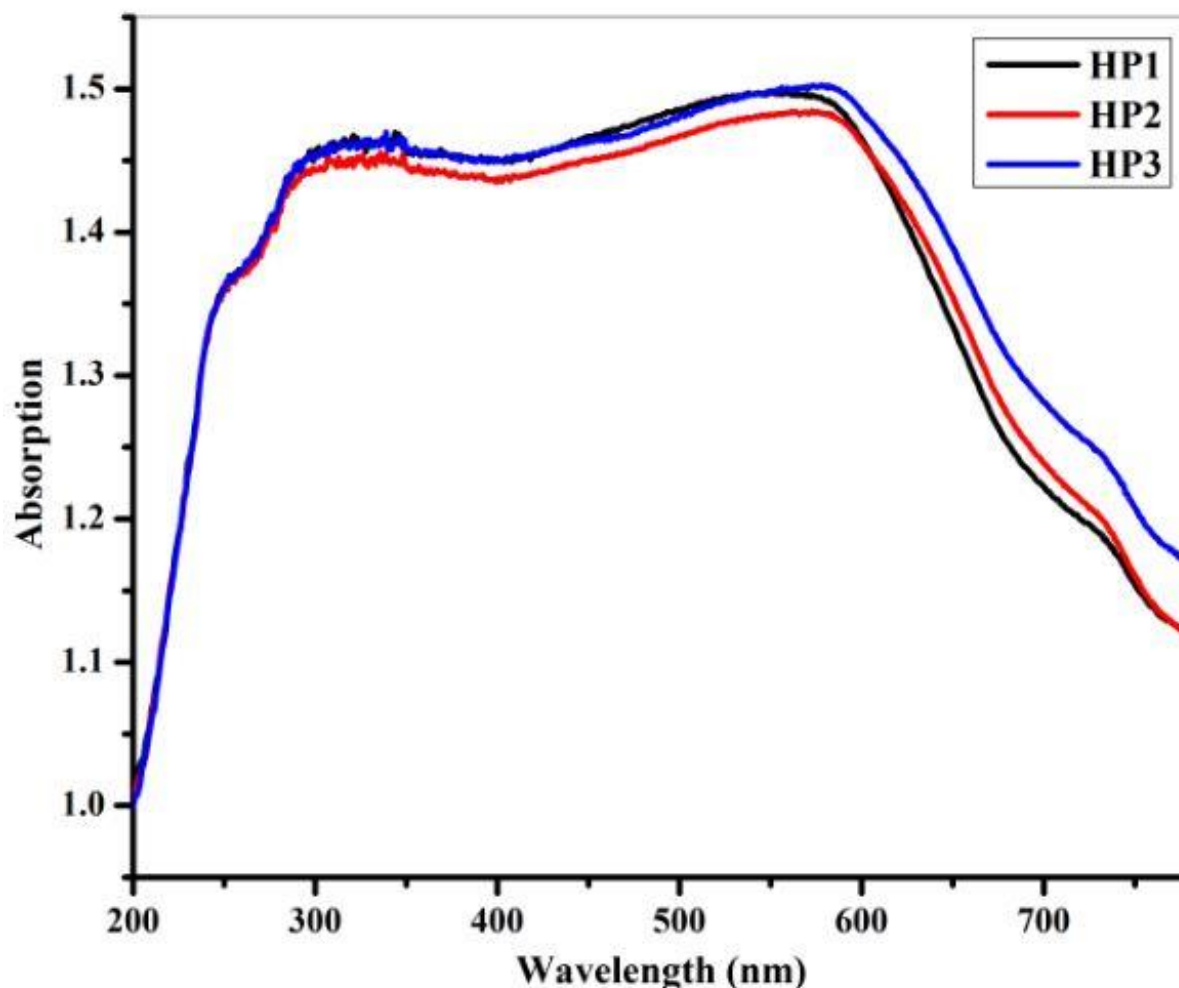
Fig. 5.78 UV plots of $BaFe_{11.8}Bi_{0.1}Al_{0.1}O_{19}$-PANI composite

Compared to the absorption bands of PANI, it was noticed that peaks of HP1, HP2 and HP3 show blue shift (hypsochromic shift) which appear as a result of the interaction of –NH in PANI and oxygen in hexaferrite particles[227]. These absorption bands indicate the passage from valence band to the band of conduction. The transition require an energy defined by the band gap energy (E_g) calculated from the following equation [55]:

$$(\alpha h\nu)^2 = A(h\nu - E_g) \tag{5.91}$$

Where A is a constant, E_g is the energy of the band gap and h is the constant of Planck. **Fig. 5.79** shows Eg plots of prepared sample.
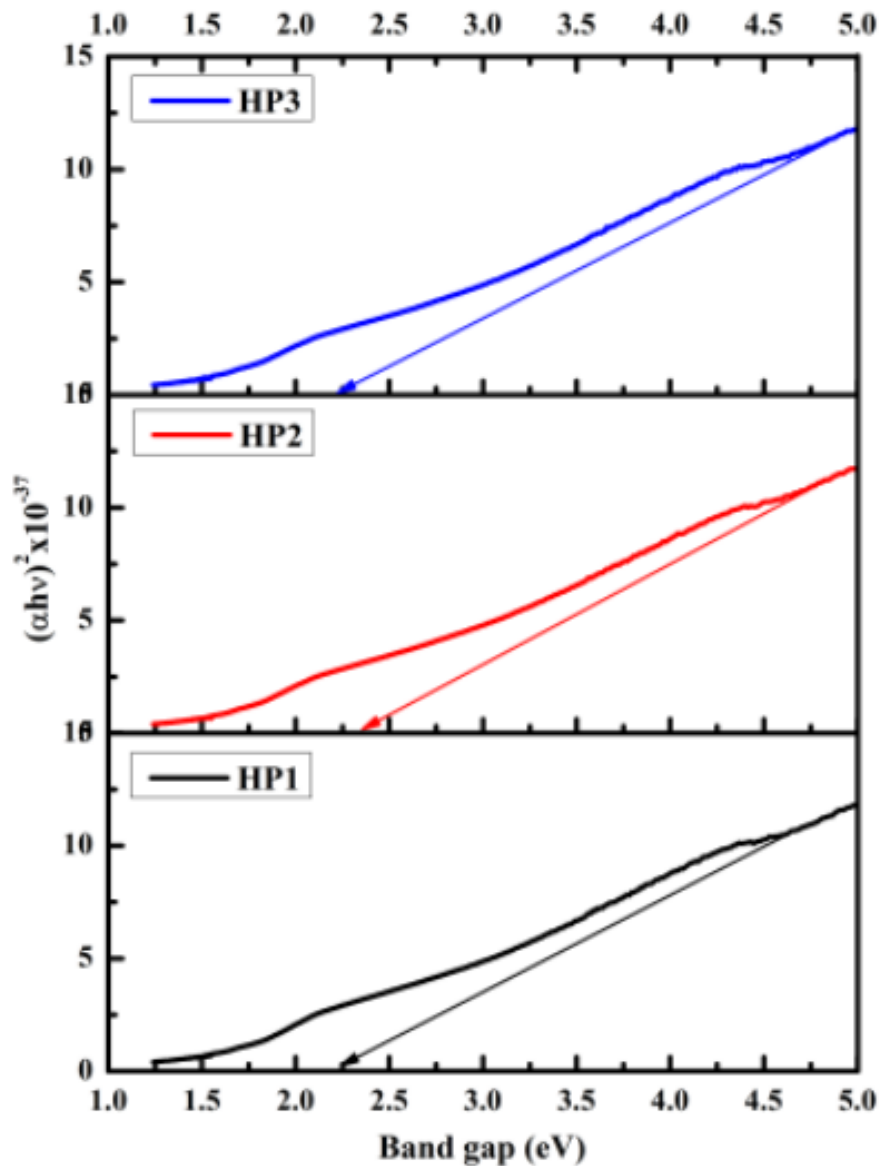
Fig. 5.79 Optical band gap of $BaFe_{11.8}Bi_{0.1}Al_{0.1}O_{19}$-PANI composite

After an extrapolation of linear part of the curve of $(\alpha h\nu)^2$ against E_g, band gap energies of prepared samples have been estimated and were found to be 2.24, 2.36 and 2.21 eV for HP1, HP2 and HP3 respectively. For all the samples the values of E_g were found to be lesser than 3.18 eV [132]. It can be noticed that the band gap values and crystallite size vary inversely that means higher the crystallite size smaller the band gap. This can be explained by quantum confinement effects [104].

5.7 Structural and optical properties of $Ba_{0.7}Dy_{0.3}Fe_{11.4}Cr_{0.3}O_{19}$/polyaniline (PANI) nanocomposites for optoelectronics

5.7.1 Structural analysis

X-ray diffraction patterns were used to carry out the structural properties of nanocomposites consisted by $BaFe_{11.8}Bi_{0.1}Al_{0.1}O_{19}$-PANI. **Fig.5.80** exhibits the XRD patterns of prepared sample. The observed peaks in this figure were found using as JCPDS number: 39-1433[30]. The diffraction angles 23.49, 30.35, 30.79, 32.18, 34.13, 35.61, 37.09, 40.35, 54.03, 55.07, 56.51, 57.55, 62.41, 63.07, 63.93, 71.88 and 75.40 are equivalent to (006), (110), (008, (107), (114), (108), (203), (205), (300), (0014), (2011), (218), (1015), (220), (0016), (2113) and (403) diffraction planes of magnetoplumbite structure with space group *P63/mmc* respectively. Moreover, the presence of second phase (α-Fe_2O_3) can be observed. The related peaks to second phase were indexed using 72-0469 as JCPDS card [147]. The diffraction planes (012), (104), (024) and (018) observed at 2θ=24.14, 33.13, 49.42 and 57.54 indicate the presence of impurity which may be due to the synthesis conditions of $Ba_{0.7}Dy_{0.3}Fe_{11.4}Cr_{0.3}O_{19}$. In fact the presence of an impurity phase can be explained by the fact that the reaction between reactions was incomplete [32]. The peak at around 2θ=25.37 indicates the presence of PANI in the composite; this observation was also reported by C. L. Yuan and J. Luo [7, 8]. It is also observed that peak intensity decreases progressively from sample HP11 to HP33, indicating here the strong presence of the amorphous compound (PANI) in the composite.

Crystallite size (D), lattice constants (a and c) and volume of unit cell (V) were calculated according to the formulae below and values are tabulated in **Table 5.18:**

$$\frac{1}{d_{hkl}^2} = \frac{4}{3}\left(\frac{h^2+hk+k^2}{a^2}\right) + \frac{l^2}{c^2} \qquad (5.92)$$

$$V_{cell} = \frac{\sqrt{3}}{2}a^2c \tag{5.93}$$

$$D = \frac{0.9\lambda}{\beta \cos \theta} \tag{5.94}$$

where d_{hkl} represents the distance between two consecutive planes, hkl represent the diffraction plane, β is full width at half maxima (in radian), $\lambda(1.54056 \text{ Å})$ being the wavelength of the X-ray incident, θ being the angle of deviation.

Table 5.18 Crystallite size (D), lattice parameters (a and c) and volume of unit cell (V) of $Ba_{0.7}Dy_{0.3}Fe_{11.4}Cr_{0.3}O_{19}$ in prepared composite

Sample code	Peak	$2\theta(°)$	$\beta(°)$	d-spacing	a (Å)	c (Å)	V (Å³)	D (nm)
HP11	(300)	54.03	0.104	1.6959	5.8748	23.2768	695.7218	85.7408
HP22	(300)	54.02	0.097	1.6962	5.8758	23.28	696.0637	91.9242
HP33	(300)	53.84	0.115	1.7013	5.8935	23.2736	700.0632	77.4741
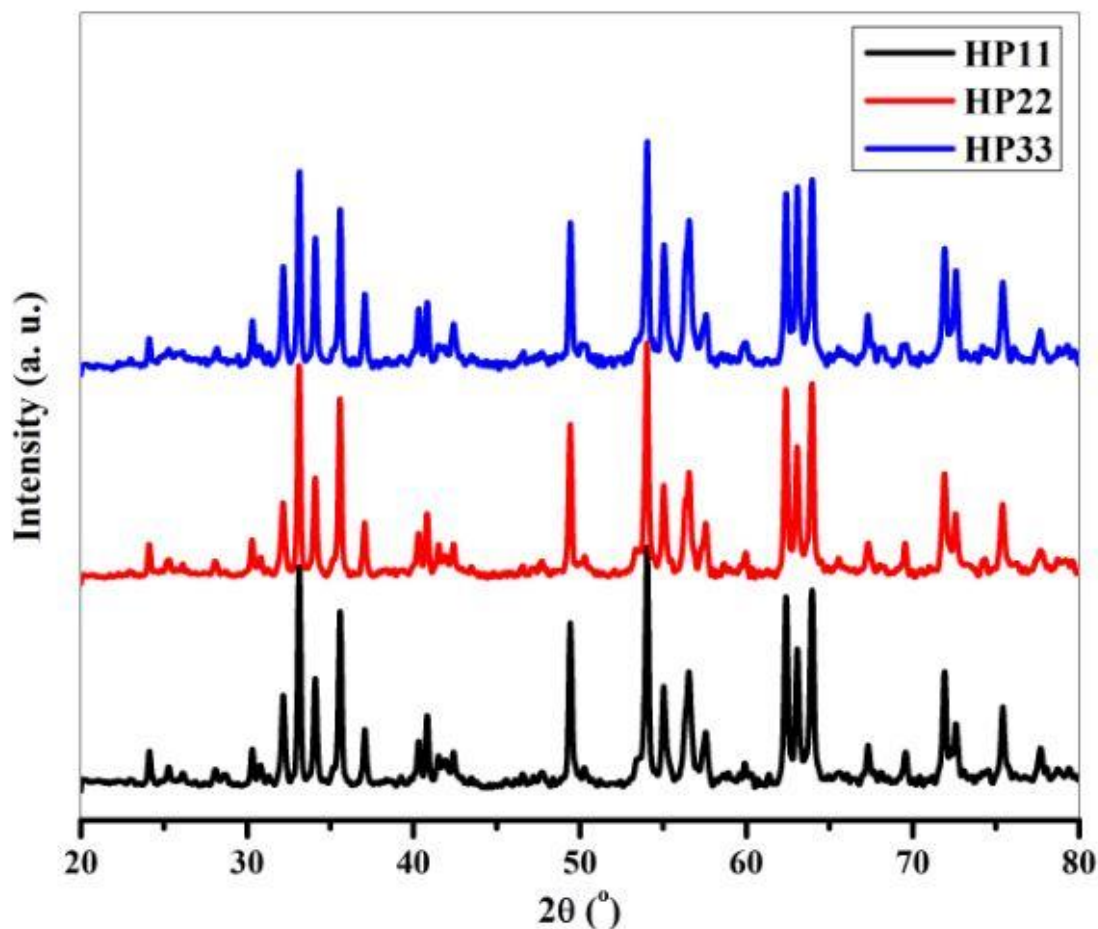
Fig. 5.80 XRD patterns of $Ba_{0.7}Dy_{0.3}Fe_{11.4}Cr_{0.3}O_{19}$/PANI composite

The crystallite size of prepared composite was found to be between 24.16-42.18 nm while lattice parameters (a and c) and unit cell volume were found to decrease from (5.886 to 5.880 Å) and (23.214 to 23.186 Å) and from 696.443 to 694.243 Å^3 respectively.

5.7.2 FTIR analysis

To identify the different functional groups in the sample, FTIR spectroscopy has been used. Before FTIR analysis, some amount of the prepared sample has to be mixed with potassium bromide (KBr) in the ratio 1:10. Then the mixture powder was transformed into pellet using KBr press. FTIR spectra were recorded between 400 and 4000 cm^{-1}.
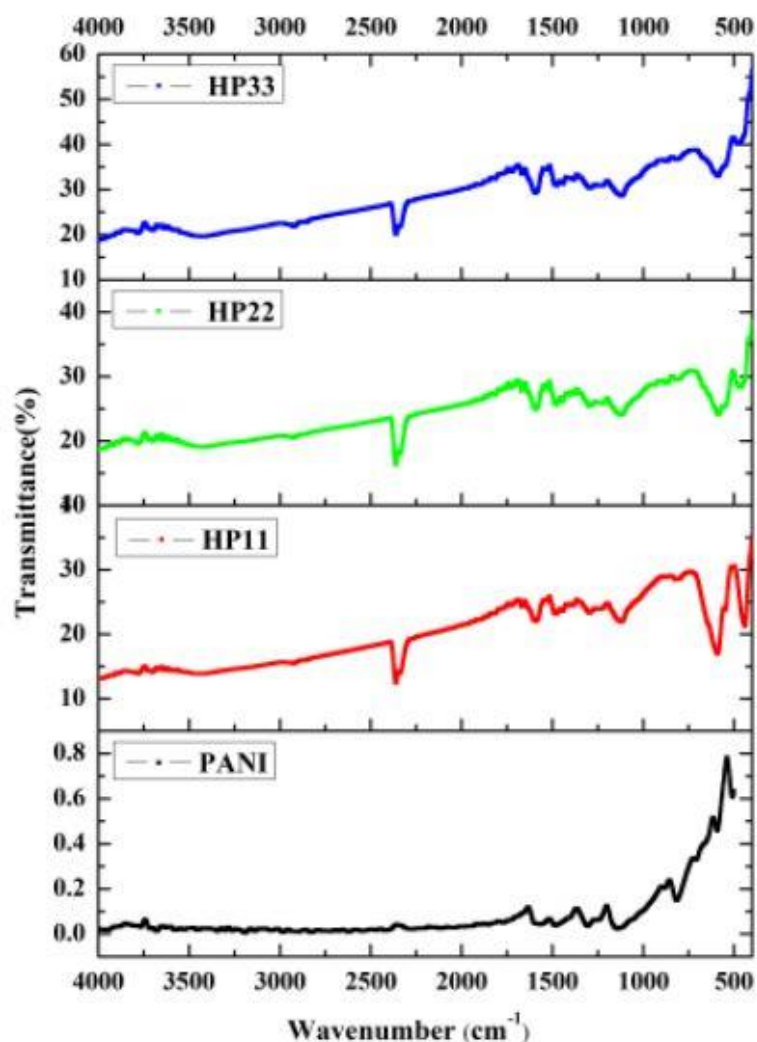
Fig. 5.81 FTIR spectra of (a) PANI, (b) HP11, (c) HP22 and (d)HP33

Fig. 5.81 shows FTIR spectra for polyaniline (PANI) and $Ba_{0.7}Dy_{0.3}Fe_{11.4}Cr_{0.3}O_{19}$/PANI composites in the range 400-4000 cm^{-1}. In all FTIR spectra, PANI peaks can be observed in

the range 800-1600 cm^{-1}. At around 1567 cm^{-1} and 1486 cm^{-1}the observed peaks are assigned to C=C stretching vibration of quinoid and benzenoid rings. Absorption bands at 1306 cm^{-1} and 1253 cm^{-1} are assigned to N-H bending and asymmetric C-N stretching modes of the benzenoid ring whereas the peak at 1142 cm^{-1} correspond to vibrational modes of N=Q=N (Q represents quinonic ring). The C-H out plane vibration of benzene ring is observed at around 804 cm^{-1} [7, 223, 224, 230]. Two important peaks are observed at around 437 cm^{-1} and 590 cm^{-1} indicating the formation of hexaferrite [30]. These bands refer to the crystallographic site ferric. Hydroxyl (OH) groups are allocated to the large absorption peak with low intensity observed in 3200-3600 cm^{-1} wavenumber in composites. It can be noticed that the intensity of peaks between 400-600 cm^{-1}gradually decrease (**Fig. 5.81(b-d)**), this may be a consequence of the strong presence of PANI in the composite.

5.7.3 Morphological analysis

Fig. 5.82 shows FESEM micrographs of Ba$_{0.7}$Dy$_{0.3}$Fe$_{11.4}$Cr$_{0.3}$O$_{19}$/PANI composite. It can be well observed that all hexagonal particles are coated indicating the presence of PANI. It was noticed that particles exhibit a homogeneous distribution. **Fig. 5.83** presents EDX spectra of prepared composite. From this figure, all elements that are present is sample can be observed. The weight percent of these elements is given in **Fig. 5.83**(inset). The detection of each chemical element by EDX support the fact that the formation of hexaferrite and PANI was obtained as revealed by XRD analysis.

5.7.4 Optical analysis

Optical properties of Ba$_{0.7}$Dy$_{0.3}$Fe$_{11.4}$Cr$_{0.3}$O$_{19}$/PANI composite were carried out using UV-visible absorption spectra. **Fig. 5.84** shows absorption spectra of prepared sample in the range 200-800nm. J. Deng and P. K. Khanna have reported that PANI shows two large absorption bands in UV-vis spectroscopy at around 336 nm and 600 nm that correspond to $\pi - \pi^*$ transition phenyl ring and $n - \pi^*$ transition benzenoid to quinoid respectively [226, 229]. In this work, we also obtained two broad bands close to those values especially at around 345 and 545 nm. It is observed that the absorption region of The Ba$_{0.7}$Dy$_{0.3}$Fe$_{11.4}$Cr$_{0.3}$O$_{19}$/PANI composite was comprised between 200-600 nm for HP11, 200-650 nm for HP22 and 200-700 nm for HP33. More the amount of PANI increase, more the absorption region shows a slight redshift (bathochromic shift).

Fig. 5.82 FESEM micrographs of $Ba_{0.7}Dy_{0.3}Fe_{11.4}Cr_{0.3}O_{19}$/PANI composite

El	AN	Series	unn. C [wt.%]	norm. C [wt.%]	Atom. C [at.%]	Error (1 Sigma) [wt.%]
Fe	26	K-series	28.59	30.99	10.85	0.84
O	8	K-series	27.91	30.26	36.96	4.30
C	6	K-series	26.83	29.09	47.33	4.38
Ba	56	L-series	5.13	5.56	0.79	0.21
N	7	K-series	2.36	2.56	3.57	0.97
Cr	24	K-series	1.15	1.24	0.47	0.08
Dy	66	M-series	0.28	0.31	0.04	0.07
		Total:	92.25	100.00	100.00	
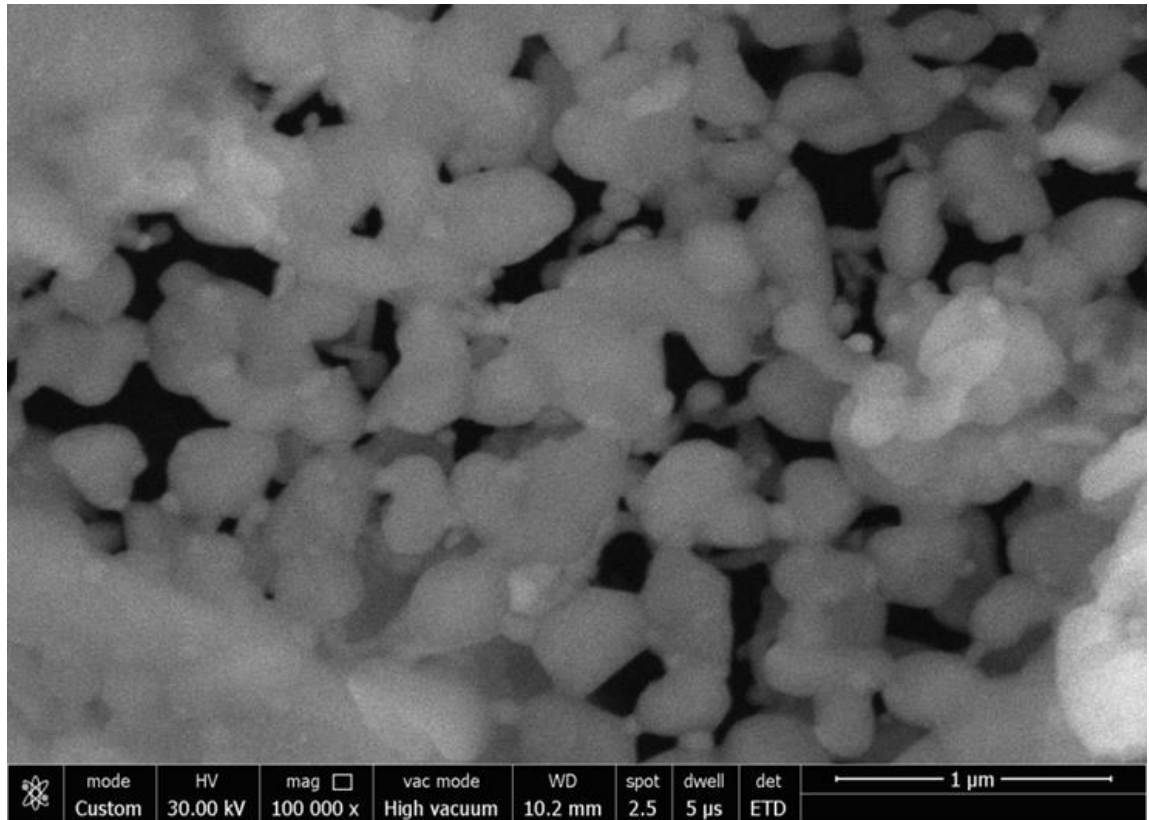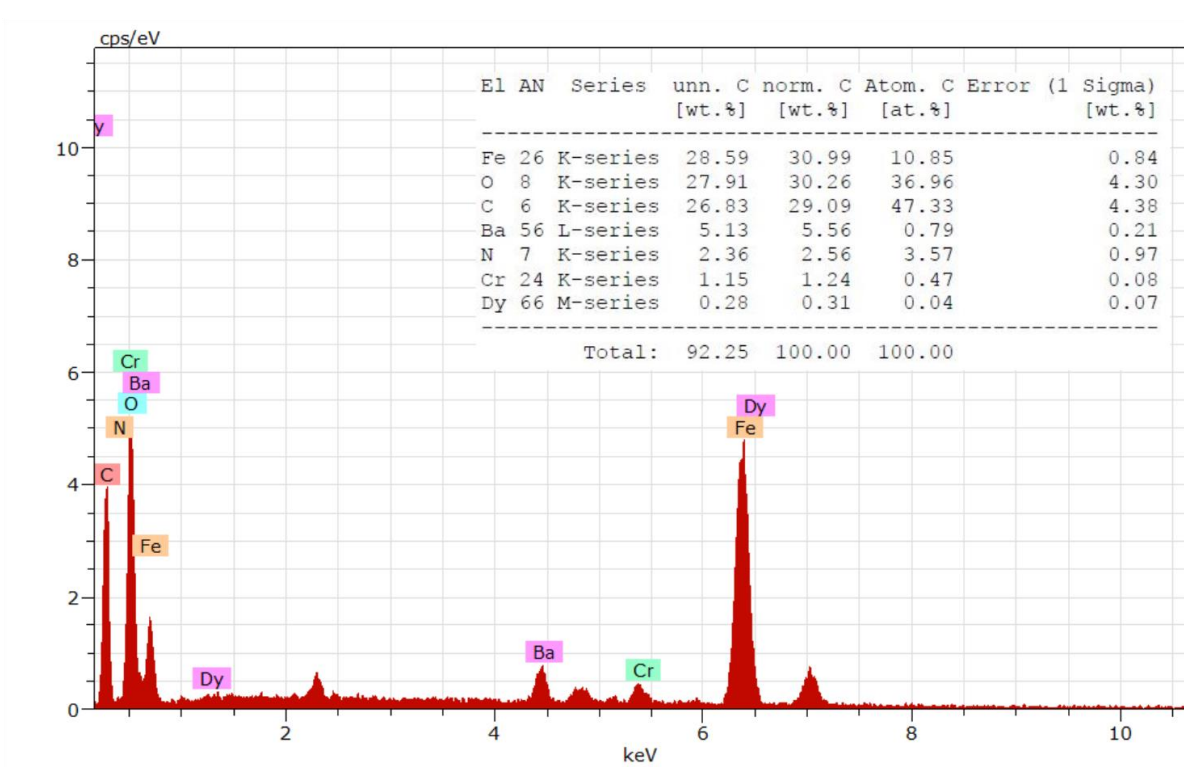
Fig. 5.83 EDX spectra of $Ba_{0.7}Dy_{0.3}Fe_{11.4}Cr_{0.3}O_{19}$/PANI composite

The transition of electrons from the valence band to the conduction band characterizes this absorption. The energy needed for this transition is describes by the energy of the band gap Eg expressed by the following relation [55].

$$(\alpha h v)^2 = A(h v - E_g) \tag{5.95}$$

With A being a constant, E_g being the band gap energy and h being the Planck's constant. **Fig. 5.85** shows Eg plots of prepared sample. The values of E_g were determined by extrapolating the linear part of the graph of $(\alpha h v)^2$ against E_g.
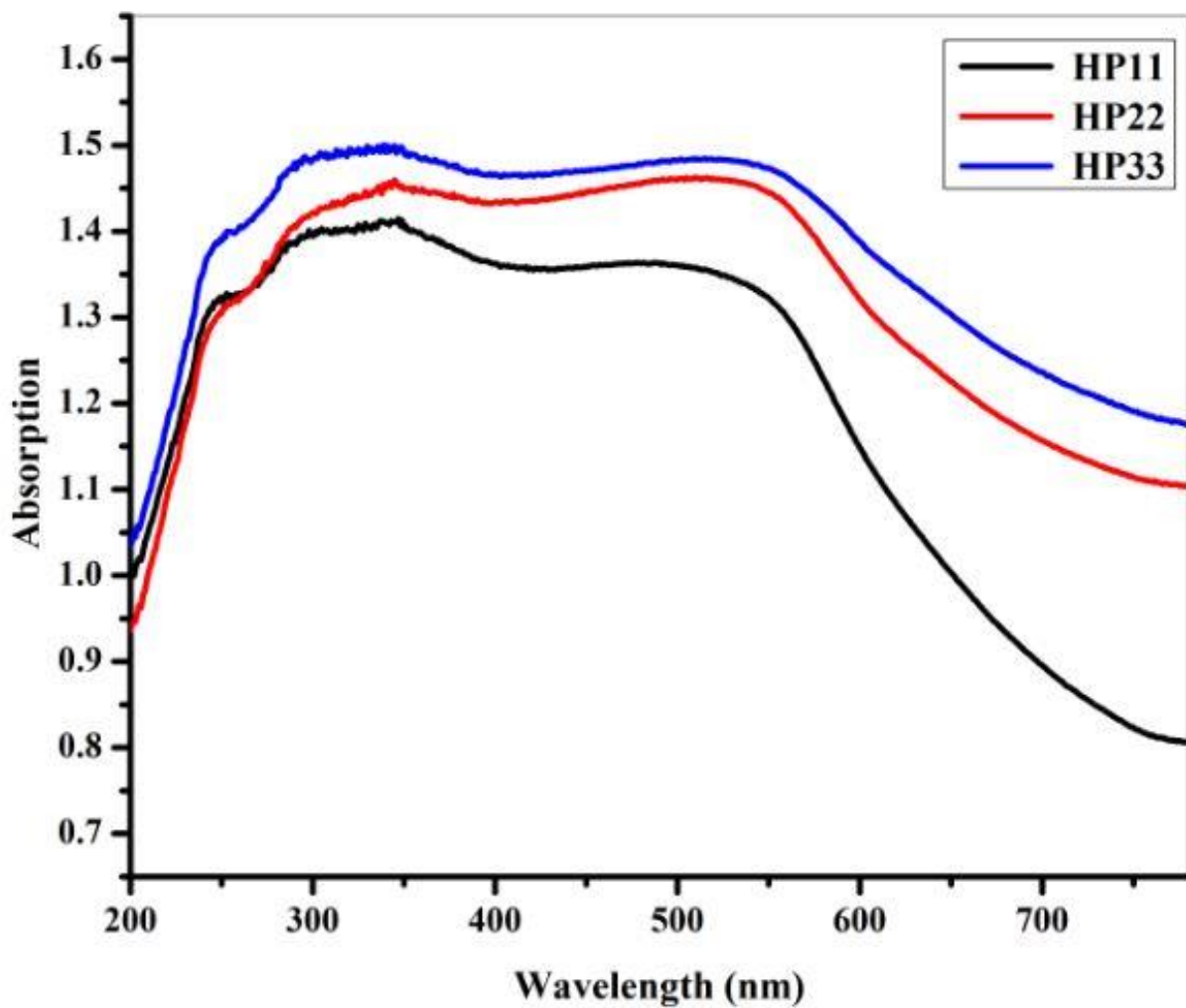
Fig. 5.84 UV-Vis plots of $Ba_{0.7}Dy_{0.3}Fe_{11.4}Cr_{0.3}O_{19}$/PANI composite
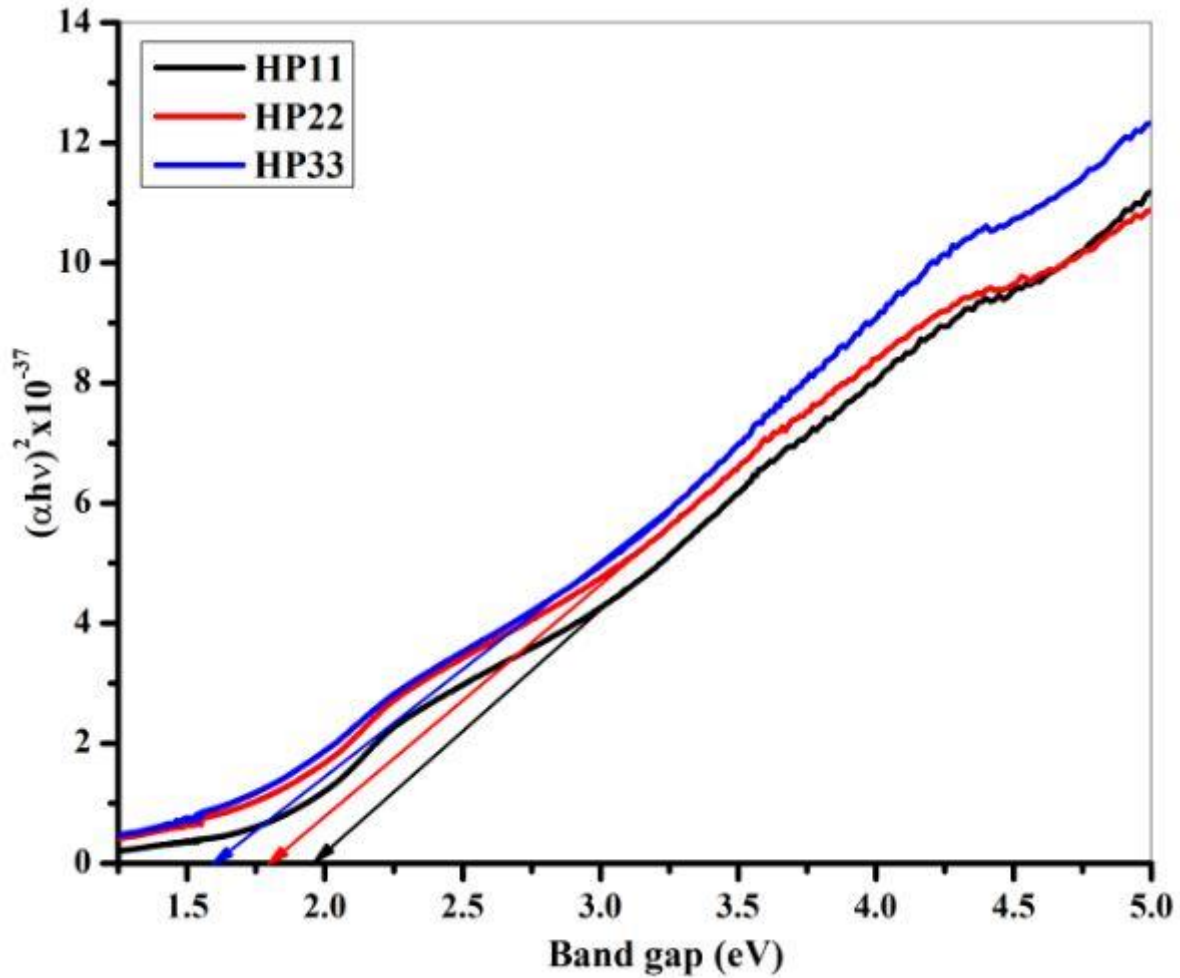
Fig. 5.85 Optical band gap of $Ba_{0.7}Dy_{0.3}Fe_{11.4}Cr_{0.3}O_{19}$/PANI composite

Band gap energy values were found to be 1.96, 1.80 and 1.59eV for HP11, HP22 and HP33 respectively. It can be remarked that the value of band gap decrease with the increase in amount of PANI. This scenario was expected because due to the conductive nature of PANI the composite became more conductive with the increase in PANI amount and therefore the band gap value decrease. These obtained values are less than pure M-type barium hexagonal ferrite revealed by the literature (3.18 eV) [132].

5.8 Structural, magnetic and optical properties of combination of Hexagonal ferrite, bismuth copper titanate and polypyrrole

5.8.1 XRD analysis

X-ray diffraction analysis was utilized to study the material structural properties. XRD patterns of BBPY1, BBPY2 and BBPY3 nanocomposite are shown in **Fig. 5.86**. For BBPY1 sample with space group $P6_3/mmc$, the XRD pattern is given in **Fig. 5.86(a)**. The observed peaks have been indexed using 39-1433 as JCPDS card [89]. It can be observed that only the hexaferrite peaks at $2\theta = 22.97°$, $30.29°$, $30.77°$, $31.26°$, $32.15°$, $34.08°$, $35.13°$, $37.05°$, $40.29°$, $42.39°$, $50.26°$, $53.84°$, $55.03°$, $56.52°$, $63.06°$, $67.29°$, and $72.56°$ corresponding respectively to the (006), (110), (008), (112), (107), (114), (200), (203), (205), (206), (209), (300), (217), (2011), (220), (2014), and (317) diffraction planes are showing. This indicates that prepared BBPY1 material is in single crystal. Generally the second phase in hexaferrite is characterized by the presence of hematite (α-Fe_2O_3) at around $33.13°$ with (102) as reflection plane [147]. Similarly, diffraction planes in **Fig. 5.86(b)** have been indexed using JCPDS card: 80-4313 [58]. The diffraction peaks have been show at $2\theta = 23.88°$, $34.09°$, $38.28°$, $42.11°$, $45.67°$, $49.04°$, $61.11°$ and $71.90°$ respectively matching to the (200), (220), (013), (222), (123), (400), (422), and (440) hkl planes. These observed peaks were found to define the crystal structure of BCTO with space group *Im-3*. It is noticed that even BBPY2 is pure sample. During the formation of bismuth copper titanate (BCTO), it is often possible to get the formation of CuO and TiO_2 which appear as second phases. **Fig. 5.86(c)** presents the XRD pattern of BBPY3 composite. It can be noticed that characteristic peaks of BBPY1 and BBPY2 materials previously cited are also mentioned in the composite. The presence of no impurities indicates that all dopants have been inserted into crystallographic sites. The Presence of amorphous material (PPY) is detected by the presence of the peak at around $25°$ which is revealed in literature [6]. It is also observed that BBPY3 composite shows the intensity of peaks lower than the intensity of BBPY1 and BBPY2 peaks. This may be due to the fact that the PPY has coated BBPY1 and BBPY2 nanoparticles.

Crystallite size (D), volume (V_{cell}), and unit cell constants (a and c) of BBPY1 sample were calculated on the base of the following relations:

$$\frac{1}{d_{hkl}^2} = \frac{4}{3}\left(\frac{h^2+hk+k^2}{a^2}\right) + \frac{l^2}{c^2} \tag{5.96}$$

$$V_{cell} = 0.8666a^2c \tag{5.97}$$

$$D = \frac{0.9\lambda}{\beta \cos \theta} \tag{5.98}$$

with d_{hkl} being the distance between two consecutive planes, *hkl* being the miller indices, β being the full width at half maximum (in radian), θ being the angle of reflection and λ is the wavelength X-ray incident (1.54056Å). Values of *a*, *c* and *V* of prepared BBPY1 sample were found to be 5.8976 Å, 23.2051 Å and 698.98 Å^3 respectively (**Table 5.19**). These results are close to those reported by M. C. Dimri [13]. The hexagonal structure of M-type hexaferrite material can be also supported by *c/a* ratio which has to be smaller than 3.98 as reported by K. M. U. Rehman [101]. In the present case, *c/a* ratio has been found to be 3.93 which confirm the hexagonal structure of prepared BBPY1 sample. X–ray density (d_x) and surface areas (S) have been determined using following equations [133]:

$$d_x = \frac{Z \times Molecular\ mass}{VN_A} \tag{5.99}$$

$$S = \frac{6000}{d_x D} \tag{5.100}$$

Where z is number of atom per unit cell and N_A is Avogadro's number (6.023×10^{23}). It was found that $S = 28.33 \times 10^7$ cm^2/g and $d_x = 5.43$ g/cm^3.

Similarly, volume (*V*) and unit cell parameters (*a*) of BBPY2 ceramic were evaluated by below equations:

$$d_{hkl} = \frac{a}{\sqrt{h^2+k^2+l^2}} \tag{5.101}$$

$$V = a^3 \tag{5.102}$$

Lattice constant and volume of unit cell were found to be 7.433 Å and 410.6402 Å^3 respectively. Value of *a* was found to be around 0.23% higher than that reported by Gautam for pure bismuth copper titanate (BCTO) [231]. This observed difference is due to the substitution of Bi^{3+} ions by La^{3+} ions. Indeed, ionic radius of La^{3+} ions ($r_{La^{3+}}=1.22$Å [232, 233]) is larger than ionic radius of Bi^{3+} ions ($r_{Bi^{3+}}=1.17$Å [123]). In general, since the ionic radius varies from one atom to another, the crystalline structure undergoes stretching or shrinkage depending on whether the radius of the substituted atom is larger or smaller. Crystallite (*D*), X-ray density (d_x) and surface area (*S*) of prepared BBPY2 have been

estimated by eqn. (5.98), eq. (5.99) and eq. (5.100) respectively and values are listed in **Table 5.20**.
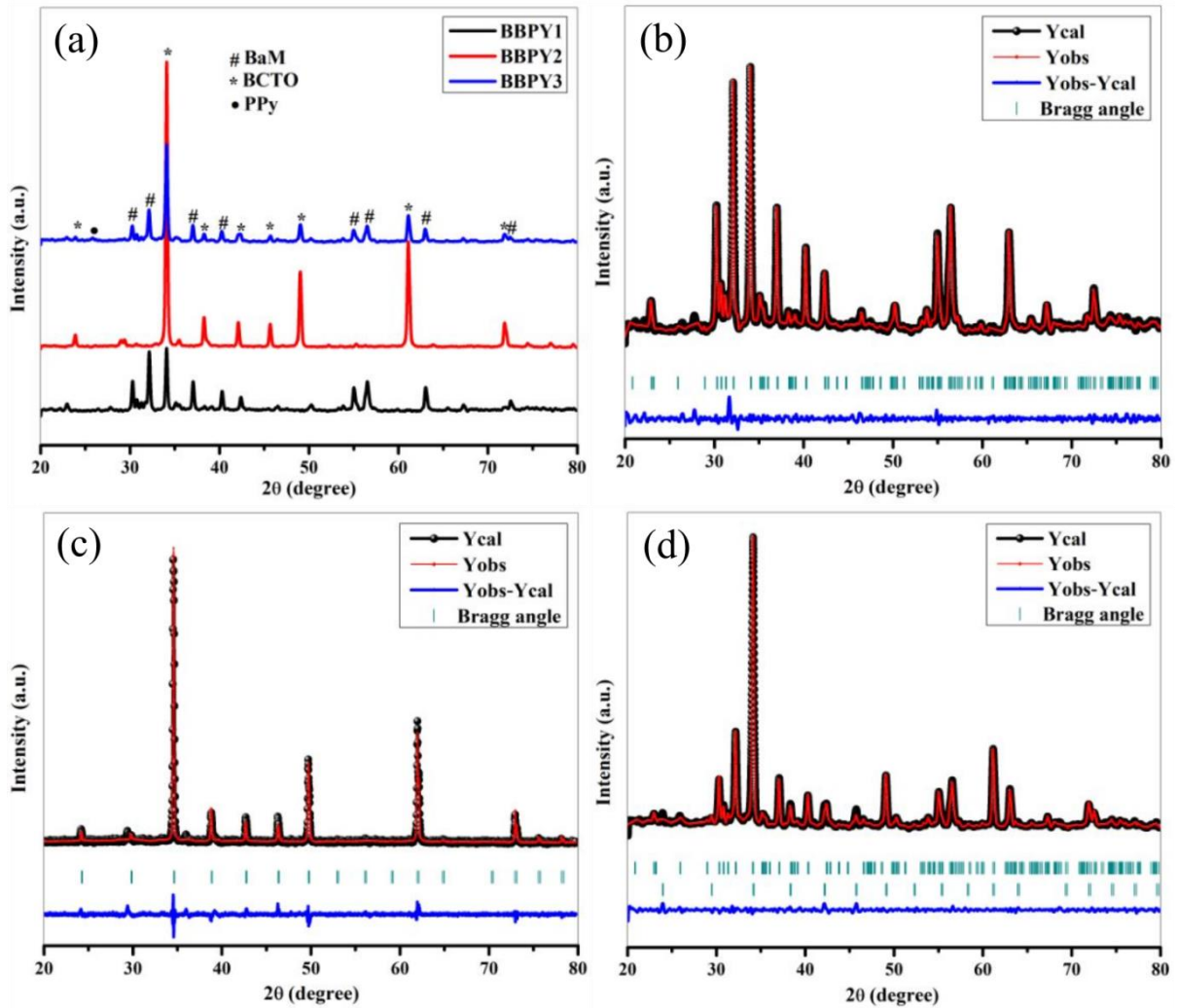
Fig. 5.86 (a) XRD patterns of prepared samples and Rietveld refinement of (b) BBPY1 sample, (c) BBPY2 ceramic and (d) BBPY2 composite

Table 5.19 Lattice parameters (a and c), volume of unit cell (V), full width at half maxima (β), crystallite size (D), X-ray density (d_x) and specific surface area (S) of BBPY1, BBPY2 and BBPY3

Concentration (x)	BBPY1	BBPY2	BBPY3	
			Hexaferrite phase	BCTO phase
β (°)	0.213	0.220	-	-
D (nm)	39.0096	37.7694	-	-
d (Å)	2.6287	2.6279	-	-
a (Å)	5.8976	7.433	5.9054	7.4340
c (Å)	23.2051	-	23.2496	-
c/a	3.9347	-	3.9370	-
V (Å^3)	698.98	410.6402	702.1740	410.8278
a (Å) *(Rietveld)*	5.899464	7.329851	5.894159	7.420128
c (Å) *(Rietveld)*	23.237938	-	23.208855	-
c/a *(Rietveld)*	3.9390	-	3.9376	-
V (Å^3)*(Rietveld)*	700.412(0.008)	393.809(0.003)	698.278(0.029)	408.540(0.017)
d_x(g/cm^3)	5.43	5.69	-	-
$S \times 10^7$(cm^2/g)	28.33	27.92	-	-

Table 5.20 Conditions for refinement, reliability factor (R_p, R_{wp}, R_{exp}), refined half-width parameters (U, V, W) chi-square (χ^2) and good of fit (GoF) of BBPY1, BBPY2 and BBPY3

Concentration (x)	BBPY1	BBPY2	BBPY3	
λ(Å)	1.54056	1.54056	1.54056	
Cycles of refinement	30	30	30	
Step (°)	0.005	0.005	0.005	
Profile function	P-Voigt * Axial divergence asymmetry	P-Voigt * Axial divergence asymmetry	P-Voigt * Axial divergence asymmetry	
R_p (%)	14.9	30.1	13.1	
R_{wp} (%)	13.9	20.7	12.4	
R_{exp} (%)	11.9	12.1	12.1	
χ^2	1.360	2.948	1.046	
GoF	1.2	1.7	1.0	
			Hexaferrite phase	BCTO phase
U	0.252775	-0.012804	-0.035023	-0.045552
V	-0.254427	-0.021350	0.046936	0.015598
W	0.118113	0.038507	0.045836	0.068434
Space group	P6$_3$/mmc	Im-3	P6$_3$/mmc	Im-3

5.8.2 FTIR analysis

FTIR spectroscopy technique was used to determine the presence of functional groups and residual chemicals in the synthesis process. **Fig. 5.87** exhibits FTIR spectra of PPY, BBPY1, BBPY2 and BBPY3 samples in the range 400-4000 cm^{-1}. For PPY (**Fig. 5.87(a)**), the peaks observed at these wavenumbers 804 and 1108 cm^{-1} correspond to C-H out-of plane and C-H in plane deformation vibration [75], at 1282 cm^{-1} represents (=C-H)in plane vibration [6]. The peak observed at around 1400 cm^{-1} wavenumber represents C-N stretching vibration and bands around 1587-1695 cm^{-1} represent the functional vibrations of polypyrrole rings [234]. The broad band at 3162 cm^{-1} corresponds to C-H stretching. The FTIR spectroscopy

spectrum of BBPY1 sample is given in **Fig. 5.87(b)**. In this figure, two significant peaks between 400 and 600 cm^{-1} especially at around 431 and 592 cm^{-1} can be observed. These peaks are assigned to stretching Fe-O vibration in octahedral and tetrahedral sites indicating the hexagonal ferrite formation [30, 128]. For prepared BBPY2 ceramic (**Fig. 5.87(c)**), observed peaks at around 579, 511 and 431cm^{-1} represent absorption bands for Ti ion which are attributed to v_{T_i-O} =653-550 cm^{-1} and $v_{T_i-O-T_i}$ =495-435 cm^{-1} [57]. **Fig. 5.87(d)** shows the FTIR spectrum of BBPY3 composite. In this figure, the characteristic peaks of each sample are shown. The absorption band presents at 2356 cm^{-1} in **Fig. 5.87(a)** and **5.87(d)** is assigned to the CO$_2$ absorption from the air [54].
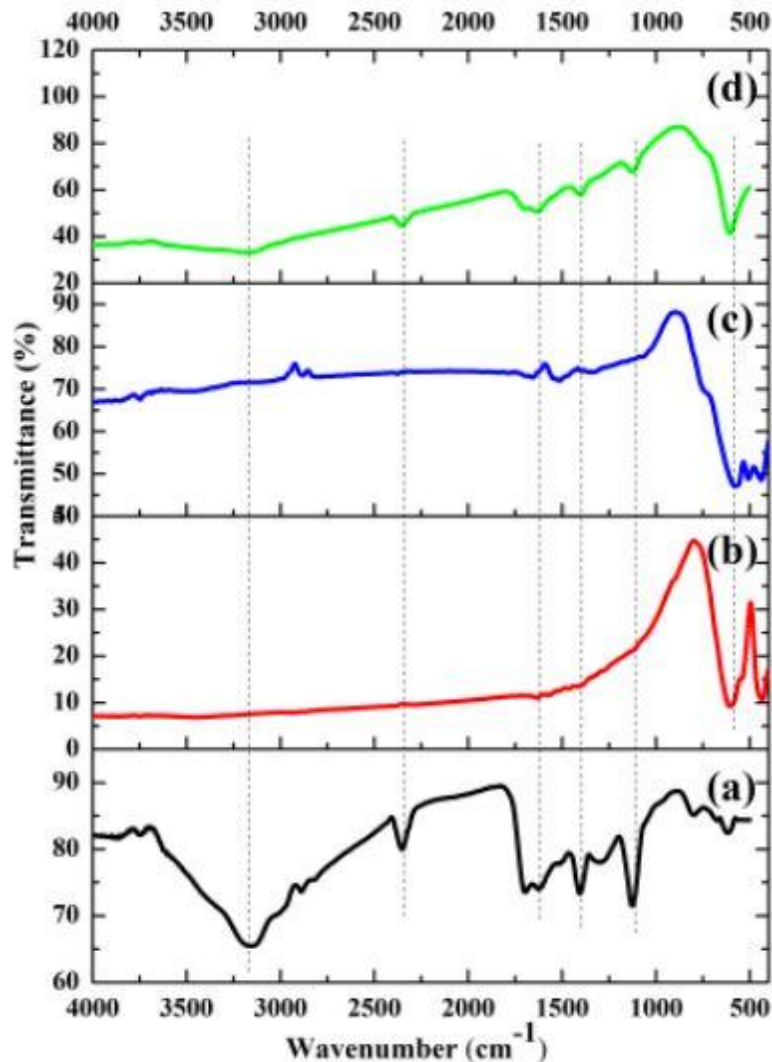
Fig. 5.87 FTIR spectra of (a) PANI (b) BBPY1 sample, (c) BBPY2 ceramic and (c) BBPY2 composite

5.8.3 Raman spectroscopy

Raman spectroscopy is a very useful characterization technique that permits to determine the different vibration modes present in a sample. **Fig. 5.88** shows Raman spectra for BBPY1, BBPY2 and BBPY3 samples recorded in the range 150-2000 cm^{-1}. The different characteristic peaks of BBPY1 and BBPY2 ceramic are revealed between 150 and 800 cm^{-1}. For prepared BBPY1, it is well known that the unit cell of barium hexagonal ferrite possess 64 atoms and 42 active ramen modes including $11A_{1g}+14 E_{1g}+ 17E_{2g}$ [40, 129]. The Raman spectrum presented in **Fig4. 5.88(a)** shows different dispersion bands of prepared BBPY1 sample. Raman modes for prepared BBPY1 sample have been observed at around178, 325, 408, 472, 527, 614 and 683 cm^{-1}. The peaks at 472, 614 and 408 cm^{-1} correspond to the A_{1g} vibration of octahedral site with symmetry 4f1 and 12k, the peak at 683 cm^{-1} is assigned to the A_{1g} vibration at the bipyramidal site (2b), at 527 and 325 cm^{-1} the vibration of Fe-O bond corresponding to 12k, 2a and 4f2 is observed whereas the band at 178 cm^{-1} corresponds to the E_{1g} of the whole spinel blocks [40, 102].

Raman spectrum is given in **Fig. 5.88(b)** for BBPY2ceramic. The crystal structure of perovskite with *Im-3* as space group present eight (8) Raman active modes including $2A_g+2E_g+4F_g$ [209]. In **Fig 5.88(b)**, Raman modes are observed at 299, 499, 565 and 702 cm^{-1}. The band at 702 cm^{-1} can be assigned to *Ti-O-Ti* stretching mode (F_g (4) symmetry) [211]. The band at 565 cm^{-1} of F_g(3) symmetry can be certainly attributed to O-Ti-O anti –stretching whereas bands at 499 and 299 cm^{-1} with E_g (2) and F_g (1) symmetries respectively refer to TiO_6 rotation-like modes [209, 235, 236].

Unlike prepared BBPY1 and BBPY2 ceramic, the main characteristic peaks of PPY appear above 900 cm^{-1}.The main peaks of PPY have been observed at 943, 992, 1051, 1318, 1417 and 1580 cm^{-1}. These peaks correspond to Raman modes for PPY reported in literature [237-240]. The 1580 peak is associated to C=C stretching ring vibration [241]. The observed bands at 943, 992 and 1051 cm^{-1} can be attributed to C-H out-of –plane deformation, ring deformation and C-H in-plane deformation respectively whereas the peaks at 1318 and 1417 cm^{-1} correspond to C-C and C-N stretching vibrations [242-246].
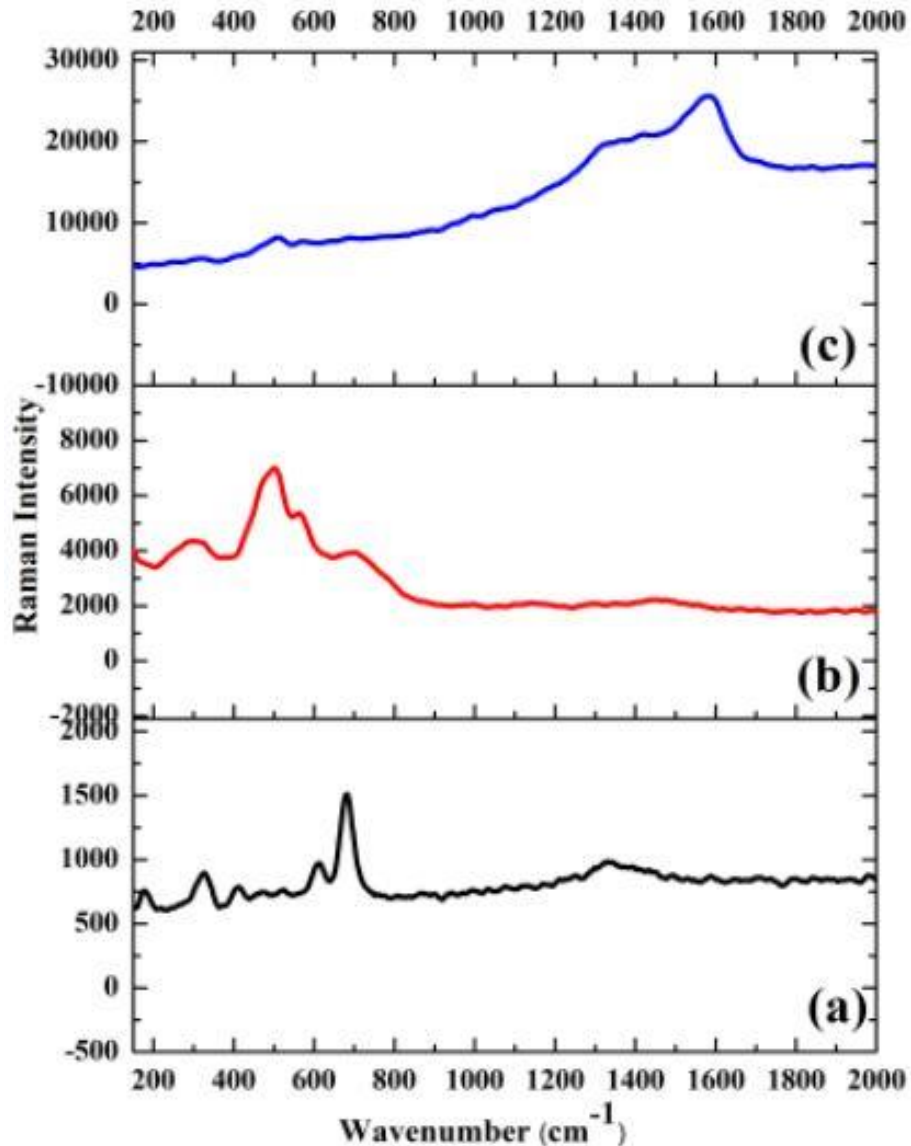
Fig. 5.88 Raman spectra for (a) BBPY1 sample, (b) BBPY2 ceramic and (c) BBPY2 composite

5.8.4 FESEM/EDX analysis

FESEM and EDX studies have been done to analyze the morphology and elemental composition of prepared samples. FESEM micrographs of BBPY1 (**Fig. 5.89(a)**) shows homogeneous distribution and hexagonal shape of particles. Similarly, a homogeneous distribution of particle is also revealed by FESEM micrographs of BBPY2 ceramic (**Fig. 5.89(b)**) and particles present cubic like shape. In these two cases, it was observed that particles agglomerated which can be as a result of the synthesis method used. The particles distribution of BBPY1 sample and BBPY2 ceramic follow the normal distribution law and

the average particle sizes were found to be 0.19 and 0.163µm respectively. **Fig. 5.89(c)** presents FESEM micrographs of BBPY3 composite.
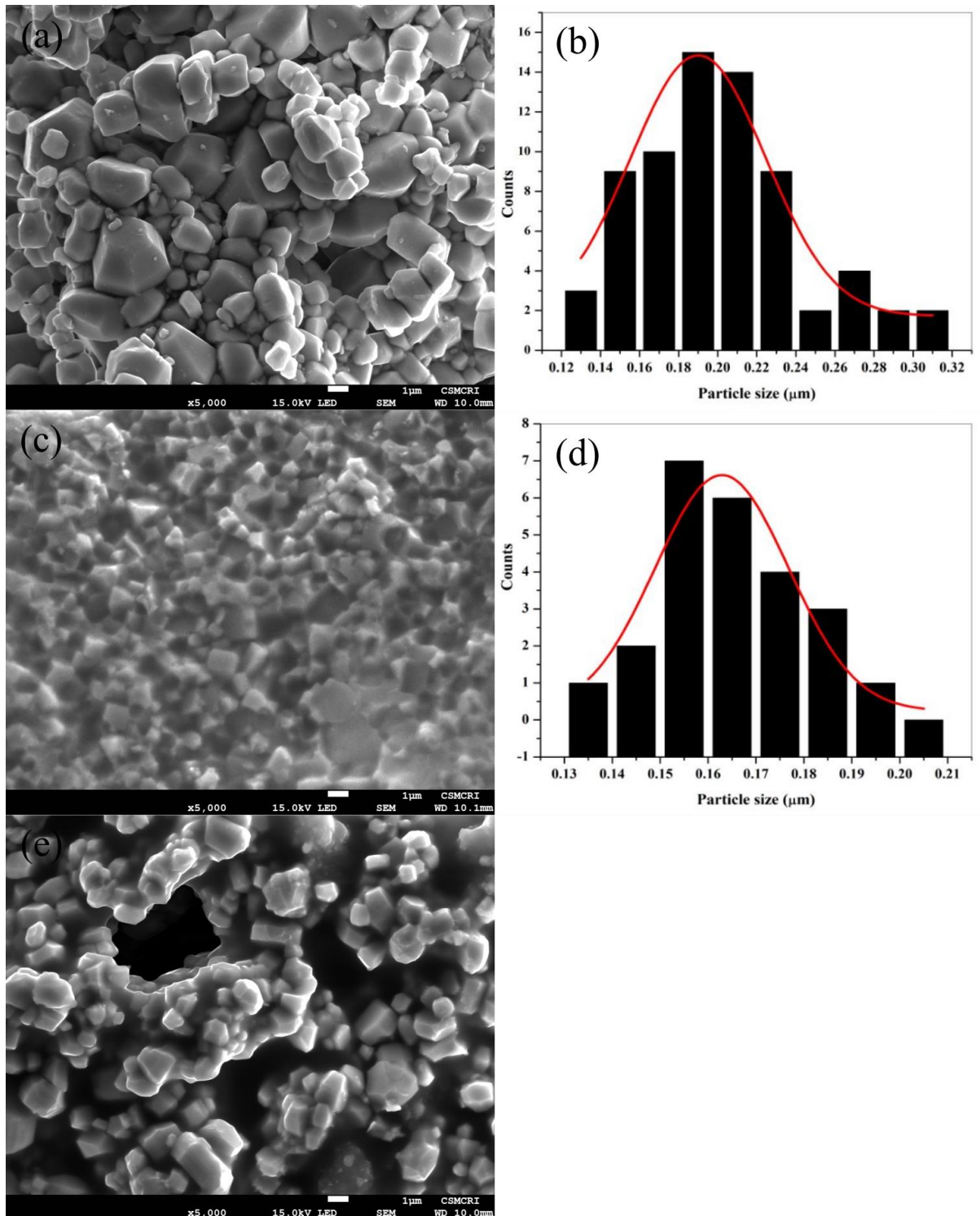
Fig. 5.89 FESEM micrograph for (a) BBPY1, (c) BBPY2, (e) BBPY3 and particles size distribution for (b) BBPY1, (d) BBPY2
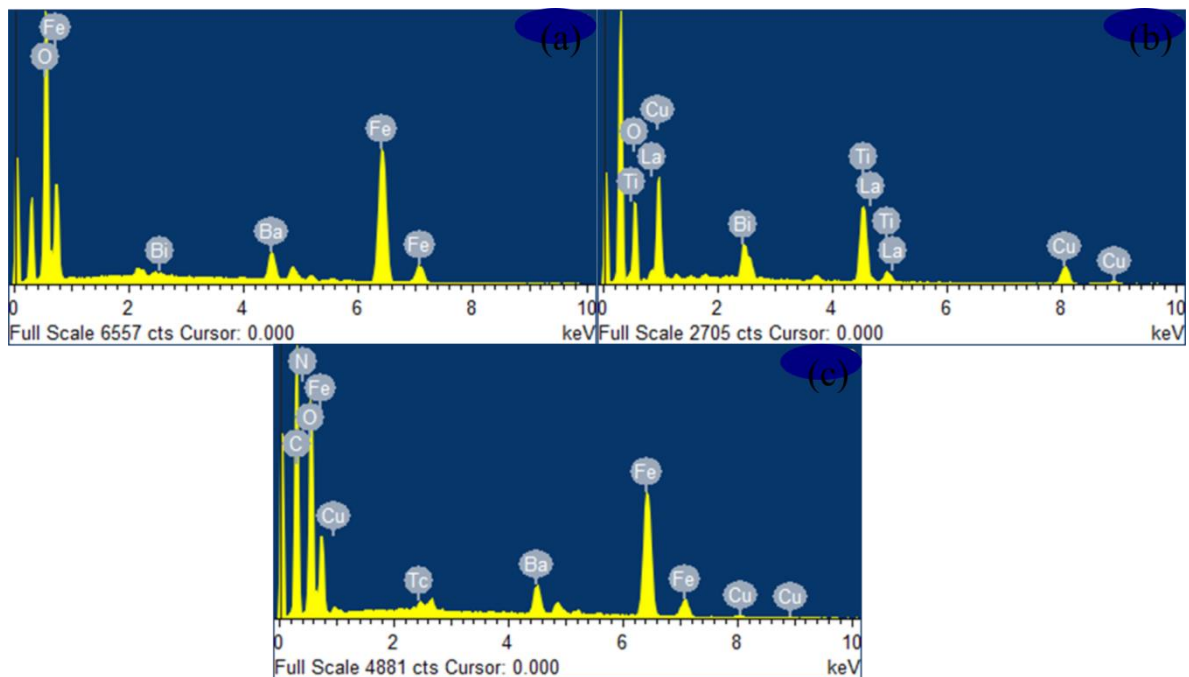
Fig. 5.90 EDX spectra for (a) BBPY1 sample, (b) BBPY2 ceramic and (c) BBPY2 composite

In this figure, the presence of PPY can be clearly observed (transparent sheet) and it is noticed that BBPY1 and BBPY2 particles are embedded in PPY. **Fig. 5.90a-c** exhibit EDX spectra of BBPY1, BBPY2 and BBPY3 samples respectively. The chemical elements present in the prepared samples were observed in the EDX spectra; this confirms the composition of the samples and the absence of any impurity which justifies the results revealed by the XRD analysis.

5.8.5 Optical analysis

Using UV-Vis-NIR spectroscopy in the range 200-1900 nm, the analysis of optical properties of prepared samples was taken out. UV region is defined from 200 to 800nm. In this region, it is noticed that all samples show four absorption peaks such as 293, 385,480 and 660 nm for BBPY1, 291, 388, 470 and 724 nm for BBPY2, 283, 366, 470 and 724 nm for BBPY3 (**Fig. 5.91**). These absorption peaks occur from $\sigma - \sigma^*, n - \sigma^*, \pi - \pi^*$, and $n - \pi^*$ transitions respectively [54]. At around 636 nm for BBPY2 ceramic, a slight reflection peak is observed.

The optical band gap energy (E_g) has been calculated using the formula below:

$$(\alpha h\upsilon)^{1/n} = A(h\upsilon - E_g) \tag{5.103}$$

Where α is the absorption coefficient, h is the Planck's constant ($6.6260 \times 10^{-34} \, J.s$), υ is the frequency of incident photon and A is a characteristics constant that depends on n. The

exponent *n* take values such as 1/2, 3/2, 2 and 3 for allowed direct, forbidden indirect, allowed direct and forbidden direct transitions respectively [40]. **Fig. 5.92** displays plots of E_g for prepared samples. These plots were obtained assuming the allowed direct transition (n=1/2) and the values of E_g were determined using an extrapolation of the plot ($(\alpha h v)^2 = 0$). Values of E_g were found to be 3.47, 3.83 and 2.36 eV for BBPY1, BBPY2 and BBPY3 respectively. It can be noticed that E_g value of BBPY3 composite is smaller than those of BBPY1 and BBPY2 samples. This can be explained by the presence of PPY which is a conducting polymer that certainly increase the conductivity in the material and therefore decrease the band gap energy. The low band gap of BBPY3 compared to that of BBPY2 and BBPY2 indicates the high semiconductor nature of BBPY3 which makes it an appropriate material for electronic applications.
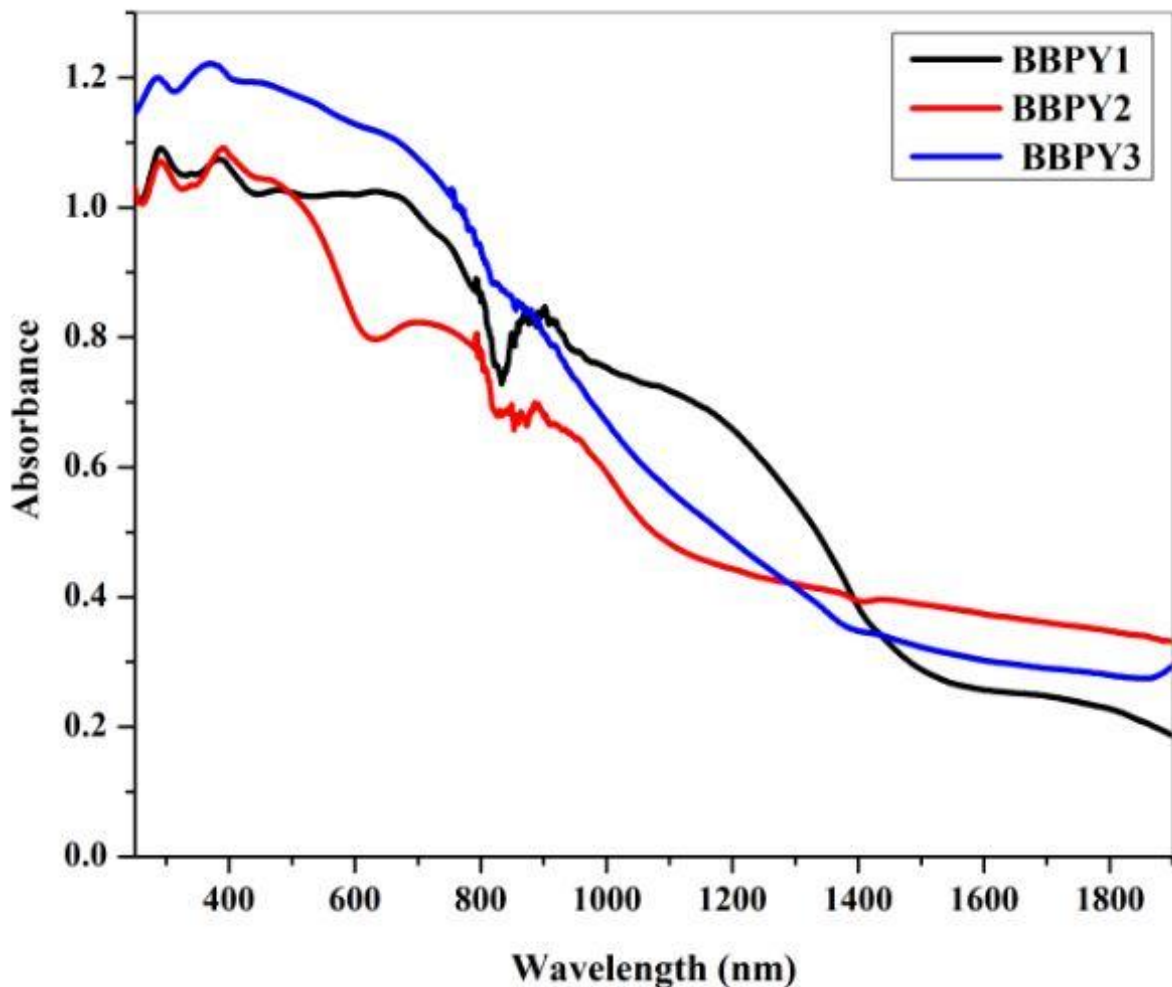
Fig. 5.91 Variation of absorbance with wavelength for BBPY1 sample, BBPY2 ceramic and BBPY3 composite
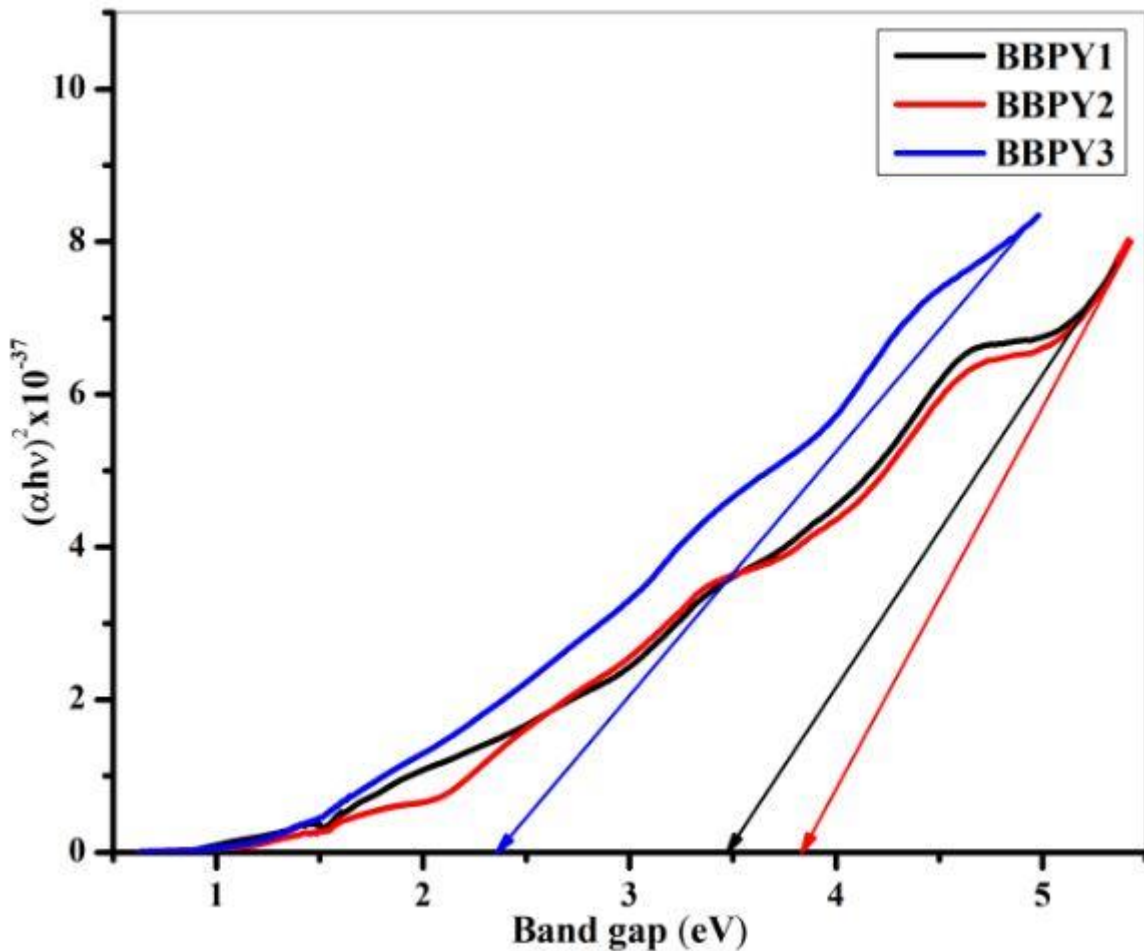
Fig. 5.92 Optical band gap for BBPY1 sample, BBPY2 ceramic and BBPY3 composite

5.8.6 Magnetic analysis

Fig. 5.93 exhibits the field-dependent magnetization of BBPY1 sample, BBPY2 ceramic and BBPY3 composite at room temperature. In the first observation, it can be noticed that BBPY1 and BBPY3 samples showed a hysteresis loop indicating the ferromagnetic behaviour of the material while BBPY2 sample showed a horizontal straight line demonstrating the non-ferromagnetic behaviour of BBPY2 ceramic. The saturation magnetization (M_s), coercivity (H_c) and remnant magnetization (M_r) were estimated from curves and values are listed in **Table 5.21**. The Fe^{3+} ions which have $5\mu_B$ as magnetic moments are responsible of magnetism in M-type hexaferrite. These ions are distributed at fives crystallographic sites including 12k, 2a, and 4f2 which are octahedral, 4f1 and 2b which are tetrahedral and bipyramidal [115]. These different sites contain spins in the upward and downward direction as reported in **Table 5.22**. Basically, it can be thought that by replacing Fe3+ ions with diamagnetic ions such as Bi3+, the saturation magnetization of the material will always decrease. However, as reported by S. Shakoor et al., during the heating period, Bi^{3+} ions

173

oxidize to Bi^{5+} ions which shift to 4f1 sites (down) preferentially and contribute to the increase in saturation magnetization [145]. In the same way, Mossbauer spectroscopy also revealed that except 4f1 sites, the others sites are hardly influenced by Bi^{3+} ions [103]. It was found that the obtained M_s for BBPY1 sample less than that of $BaFe_{12}O_{19}$ reported by A. Mali and A. Ataie [90]. The reason of that is certainly related to the conditions of synthesis. The values of Ms and Mr for BBPY1 under an applied of magnetic field were found to be 32.134 emu/g and 17.692 emu/g respectively. After adding BBPY2 ceramic and Polypyrrole (PPY), these two parameters decreased considerably as expected. This result indicates that only BBPY1 material contribute for the magnetization in BBPY3 composite. The observed decrease in M_s parameters of BBPY1 can be explained by the non-magnetic behaviour of BBPY2 ceramic (**Fig. 5.93**) but also by the weak magnetic behaviour of PPY [247]. Many other reasons can be attributed to the decrease in M_s especially the weak magnetic super-exchange interaction, presence of interfacial interaction between magnetic and dielectric particles, lattice defects and random orientation of spin on the surface of nanoparticles in BBPY3 composite [248, 249]. It is noticed that the coercivity of the composite is larger than that of M-type hexaferrite. This can be explained by the fact that after coating hexaferrite particles with Polypyrrole, the particle size will increase. indeed, structural properties can affect the magnetic properties of a sample especially the coercive field which inversely varies with the particle size [141]. The prepared magnetic materials (BBPY1 and BBPY3) proves to be useful for high-density perpendicular magnetic recording media due to their high coercivity (>1200 Oe) [133]. The anisotropy constant (*K*) and squareness ratio (*SR*) were estimated using equations (5.104) and (5.105) respectively [30]:

$$SR = \frac{M_r}{M_s} \tag{5.104}$$

$$2K = \mu_0 M_s H_c \tag{5.105}$$

Where $\mu_0 = 4\pi \times 10^{-7} \, H/m$ is the permeability in empty space. It is noticed that SR values of BBPY1 and BBPY3 composite were found to be 0.551 and 0.626 respectively which indicating that they are in single magnetic domain [6].
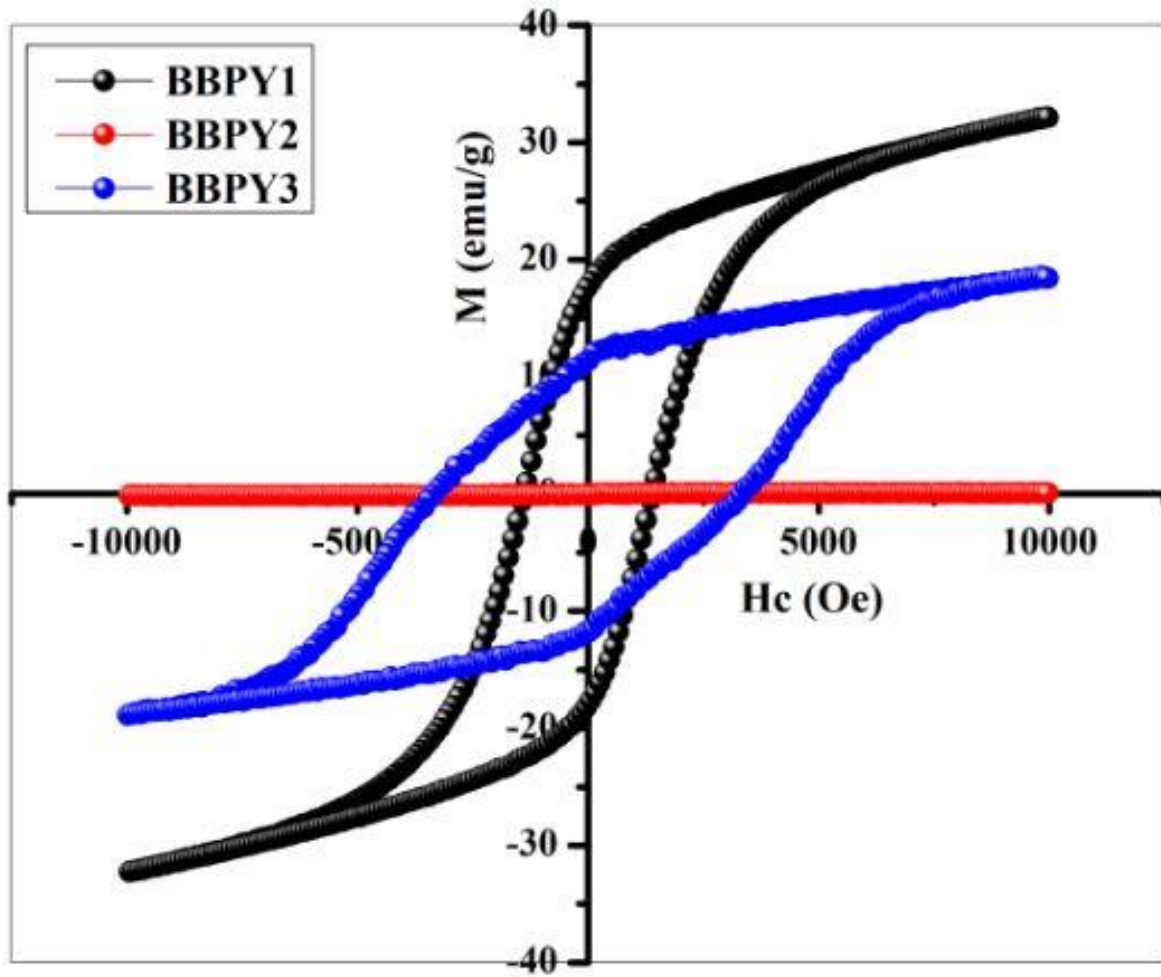
Fig. 5.93 M-H hysteresis loop of BBPY1, BBP2 and BBPY3

Table 5.21 Coercivity (H_c), remnant magnetization (M_r), saturation magnetization (M_s), squareness ratio (*SR*), and anisotropy constant (*K*) for BBPY1 and BBPY3 composite

Sample code	H_c (Oe)	M_r (emu/g)	M_s (emu/g)	SR (M_r/M_s)	K (HA^2/kg)
BBPY1	1374.53	17.692	32.134	0.551	1.218
BBPY3	3320.87	11..378	18.181	0.626	1.891

Table 5.22 Distribution in crystallographic sites of M-type hexaferrite, spin orientation and number of Fe^{3+} ions

Sublattice	Spin orientation	Crystallographic sites	Number of ions
12k	↑	Octahedral	6
4f2	↓	Octahedral	2
2a	↑	Octahedral	1
2b	↑	Bipyramidal	1
4f1	↓	Tetrahedral	2

5.9 X-band Shielding of Electromagnetic Interference (EMI) and optical sensing properties of Co_2Y hexaferrites/BCTO/PANI nanocomposites

5.9.1 XRD analysis

The XRD spectra of PANI, BCTO, Co_2Y, and Co_2Y/BCTO/PANI nanocomposites are shown **Fig. 5.94** The most intense diffraction peaks having *hkl* values (110), (113), (0012), (1013), (116), (0114), (119), (205), (2113), (1214), (220), (2026), and (1313) corresponds to the Co_2Y hexaferrite. These diffraction peaks were indexed according to the JCPDS card no. 440206 and were found to correspond to pure single crystalline phase of Co_2Y hexaferrite with space group R-3m. The diffraction peaks showing the presence of any impurity or secondary phase have not been observed. The lattice parameters (*a* and *c*), crystallite size (*D*), and volume of unit cell (V_{cell}) were determined by using the formula [28]

$$\frac{1}{d_{hkl}^2} = \frac{4}{3}\left(\frac{h^2 + hk + k^2}{a^2}\right) + \frac{l^2}{c^2} \tag{5.106}$$

$$V_{cell} = 0.8666a^2c \tag{5.107}$$

$$D = \frac{k\lambda}{\beta\cos\theta} \tag{5.108}$$

where, *hkl* are the miller indices and d_{hkl} is the inter planar spacing, θ is the Braggs angle, *k* is the shape factor ($k = 1$), β is the full width at half maximum (in radian), and λ is the wavelength of the X-ray (1.54056 Å). Similarly, the most intense diffraction peaks with *hkl*

values (110), (200), (211), (220), (013), (222), (321), (400), (422), and (440) were compared with the JCPDS card no. 801343. These diffraction peaks were found to be identical to the pure single crystalline phase of BCTO electroceramic with space group *Im-3*. The purity of the BCTO electroceramic was ascertained by the absence of impurity or secondary phases such as TiO_2 and CuO. The lattice constant (*a*) as well as the volume of unit cell (V_{cell}) were determined by using the formula [96]

$$a = d_{hkl} \sqrt{h^2 + k^2 + l^2} \tag{5.109}$$

$$V_{cell} = a^3 \tag{5.110}$$

The calculated values of *a, c, D,* and V_{cell} for both the Co_2Y and BCTO are presented in **Table 5.23**. These values are in agreement with literature [162, 250]. The XRD spectra for Co_2Y/BCTO/PANI nanocomposites show the successful coating of Co_2Y and BCTO with PANI.

Table 5.23 Values of lattice parameters (*a* and *c*), crystallite size (*D*), and volume of unit cell (V_{cell}) for BCTO and Co_2Y hexaferrite

Sample	2θ	$\beta(°)$	d (Å)	a (Å)	c (Å)	V (Å³)	D(nm)	D_x(g/cm³)	$S \times 10^7$(cm²/g)
BCTO	34.21	0.2	2.6193	7.4085	7.4085	406.6218	41.558	5.7878	24.9445
Co_2Y	30.66	0.302	2.9139	5.8210	43.7085	1282.6019	28.487	5.1261	41.0870
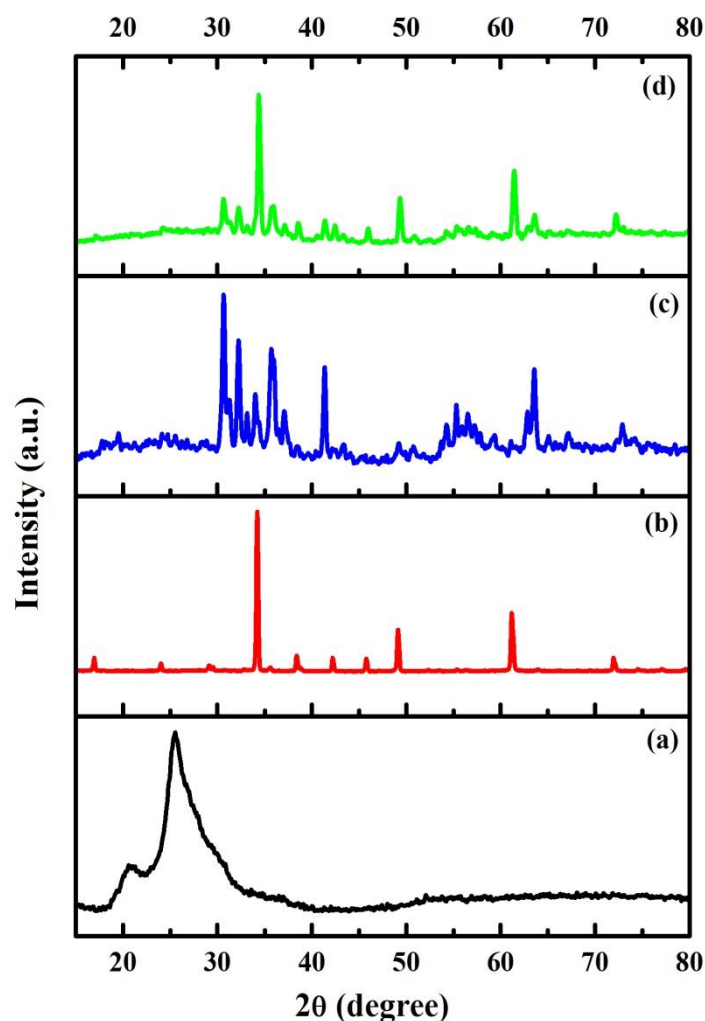
Fig. 5.94 XRD patterns of $Co_2Y/BCTO/PANI$ nanocomposites for (a) PANI, (b) BCTO, (c) Co_2Y, and (d) $Co_2Y/BCTO/PANI$

5.9.2 FTIR analysis

The FTIR spectra of PANI, BCTO, Co_2Y, and $Co_2Y/BCTO/PANI$ nanocomposites **Fig. 5.95 (a)**, **(b)**, **(c)**, and **(d)** respectively recorded in the range 350 to 2000 cm^{-1}. The spectrum of PANI shows seven absorption bands at 1620, 1504, 1342, 1186, 882, and 585 cm^{-1} (**Fig. 5.95 (a)**). These absorption bands are characteristics band of PANI and therefore confirm the formation PANI. The bands 1620 and 1504 cm^{-1} appear as a result of C=N (quinoid ring) and C=C (benzenoid ring) stretching mode [59, 251]. at The absorption bands at 1342 and 1186 cm^{-1} could be respectively attributed to C-N stretching vibrations of secondary amine and C-H out of plane stretching vibrations whereas those at 882 and 585 cm^{-1} are observed as a result of C-H stretching vibrations [252, 253]. The spectra of BCTO shows characteristics

178

absorption bands at 545 and 448 cm^{-1} while that of Co$_2$Y appear at 557 and 418 cm^{-1} [28] [231]. These appearance of these bands in BCTO electroceramic signify the Cu-O (CuO$_4$) and Ti-O-Ti (TiO$_6$ octahedral) stretching vibrations [122]. In the Co$_2$Y structure, the characteristics bands usually occur due to stretching vibrations of Fe-O at octahedral and tetrahedral crystallographic sites [54]. All the characteristics absorption bands of PANI, BCTO, and Co$_2$Y have been observed in the Co$_2$Y/BCTO/PANI nanocomposite, this confirms the formation of the Co$_2$Y/BCTO/PANI nanocomposite material. The characteristic bands of BCTO and Co$_2$Y are not clearly observed in the Co$_2$Y/BCTO/PANI nanocomposite as a result of peak mixing. Also, the characteristics band of PANI shifted to higher wavenumber due to the presence of BCTO and Co$_2$Y.
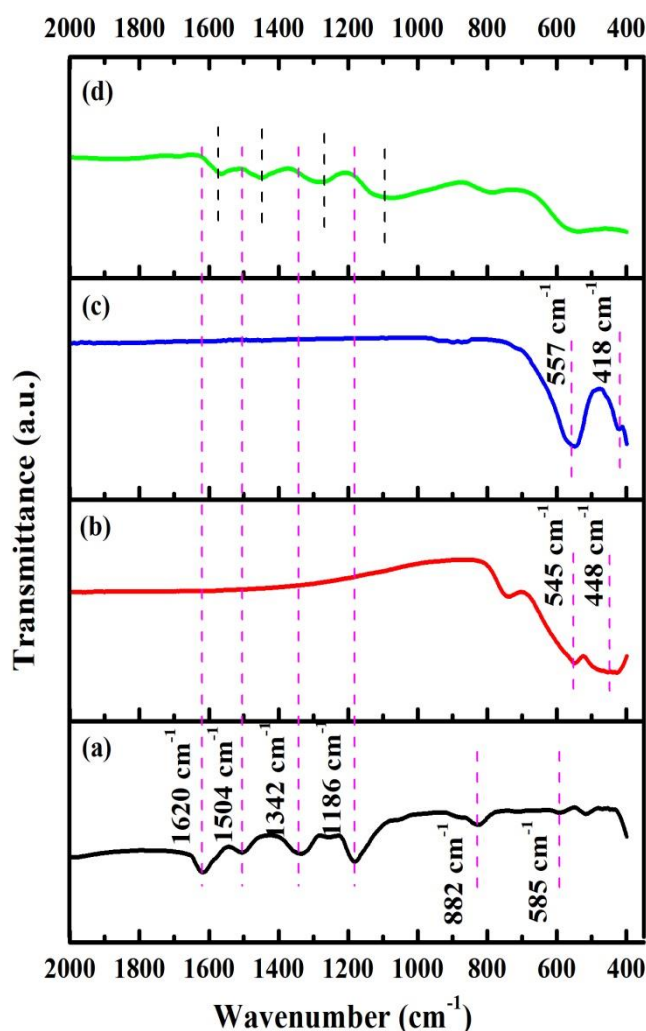
Fig. 5.95 FTIR spectra of Co$_2$Y/BCTO/PANI nanocomposites for (a) PANI, (b) BCTO, (c) Co$_2$Y, and (d) Co$_2$Y/BCTO/PANI

5.9.3 Morphology analysis

Fig. 5.96 (a-c) presents the FESEM micrograph of PANI, BCTO, and Co_2Y. Clearly, the PANI nanoparticles have irregular shapes; the particles tend to stick to each other and form an agglomerated morphology (**Fig. 5.96 (a)**). On one hand, the FESEM images of the BCTO electroceramics shows particles of various sizes with well-defined cubic shape as well as clear grain boundary and the absence of agglomeration. On the other hand, the FESEM micrographs of Co_2Y shows particles in agglomerated form, this agglomeration is usually observed in magnetic nanoparticles as a result of magnetic interaction between the nanoparticles [27, 28]. **Fig. 5.100 (a-c)** shows the particle size distribution of PANI, BCTO, and Co_2Y. Clearly, the particle distribution follows Gaussian distribution and the average particle size was found to be 0.036, 0.074, and 0.053 μm for PANI, BCTO, and Co_2Y respectively. The EDX spectra and mapping of PANI, BCTO, and Co_2Y are presented in (**Fig. 5.97, 5.98, and 5.99**). The EDX spectra and mapping shows the substituted and host element of the samples. Hence, we can assume the confirmation of the stoichiometry and purity of the PANI, BCTO, and Co_2Y samples since no other element have been observed. The FESEM micrograph, EDX spectra and mapping of Co_2Y/BCTO/PANI nanocomposite are respectively presented in **Fig. 5.96 (d)** and **5.100 (d)**. The presence of PANI, BCTO, and Co_2Y nanoparticles can be vividly observed in the micrograph. This confirms the presence and the successful intercalation of the various components of the Co_2Y/BCTO/PANI nanocomposite. Also, the stoichiometry of the as well as purity can be ascertained since all the various elements of the component of the nanocomposite are clearly observed in the EDX spectra and mapping.
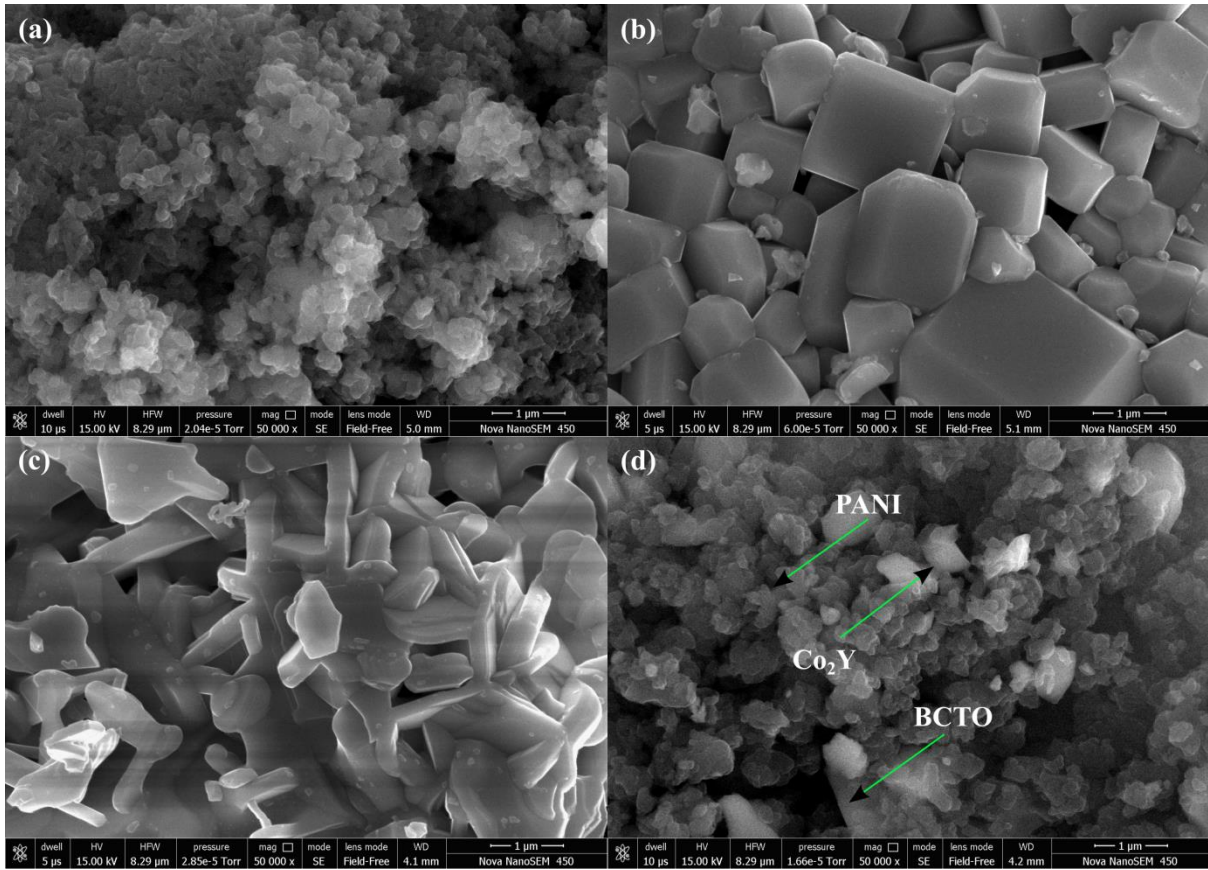
Fig. 5.96 FESEM micrograph of Co$_2$Y/BCTO/PANI nanocomposites for (a) PANI, (b) BCTO, (c) Co$_2$Y, and (d) Co$_2$Y/BCTO/PANI
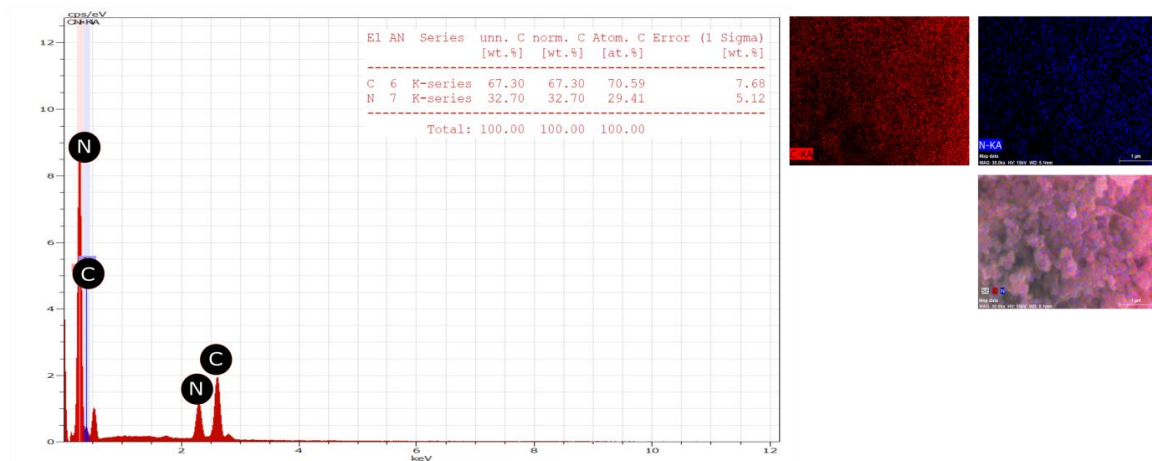
Fig. 5.97 EDX spectra and mapping of PANI
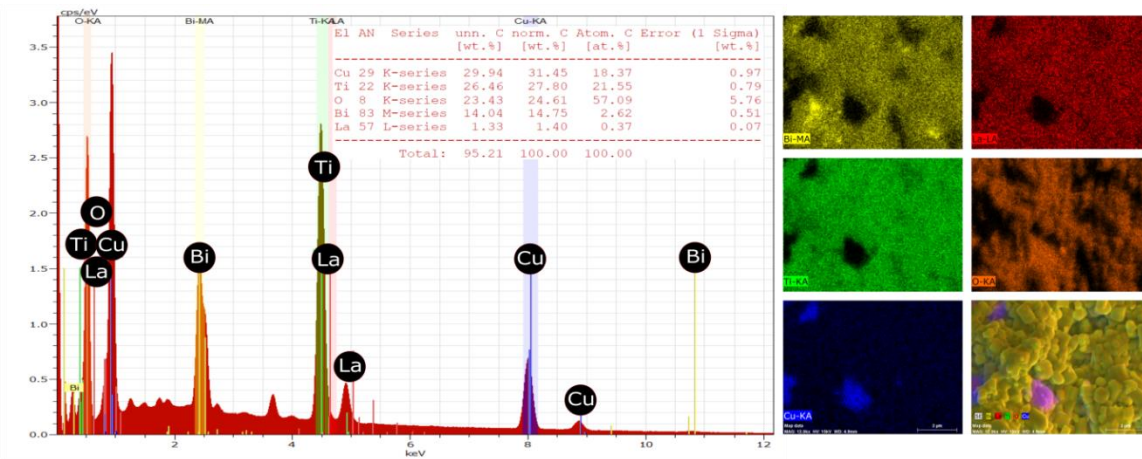
Fig. 5.98 EDX spectra and mapping of BCTO
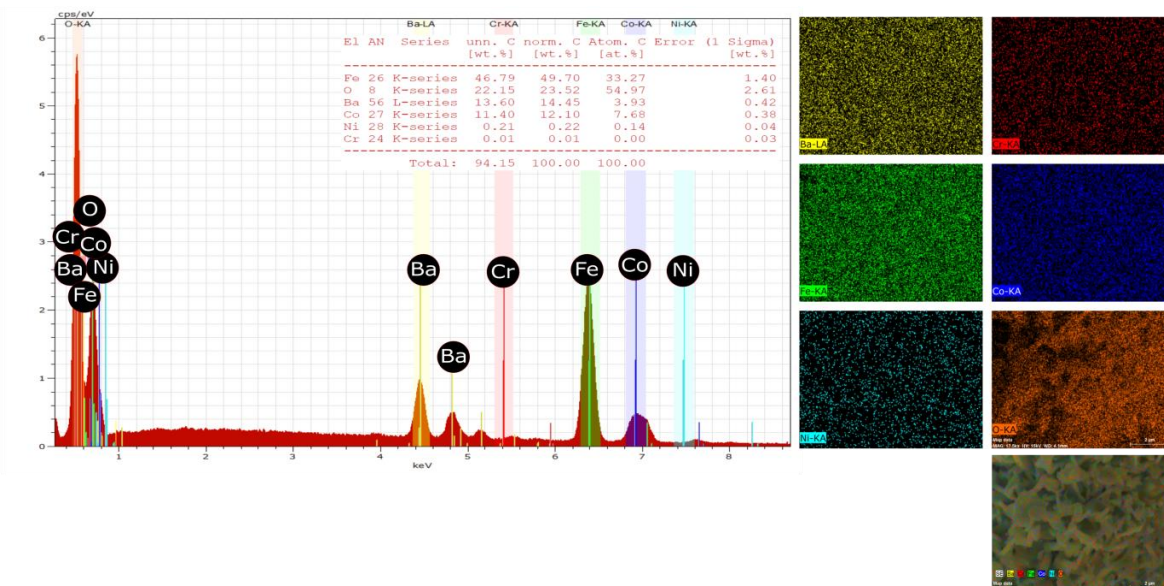
Fig. 5.99 EDX spectra and mapping of Co$_2$Y
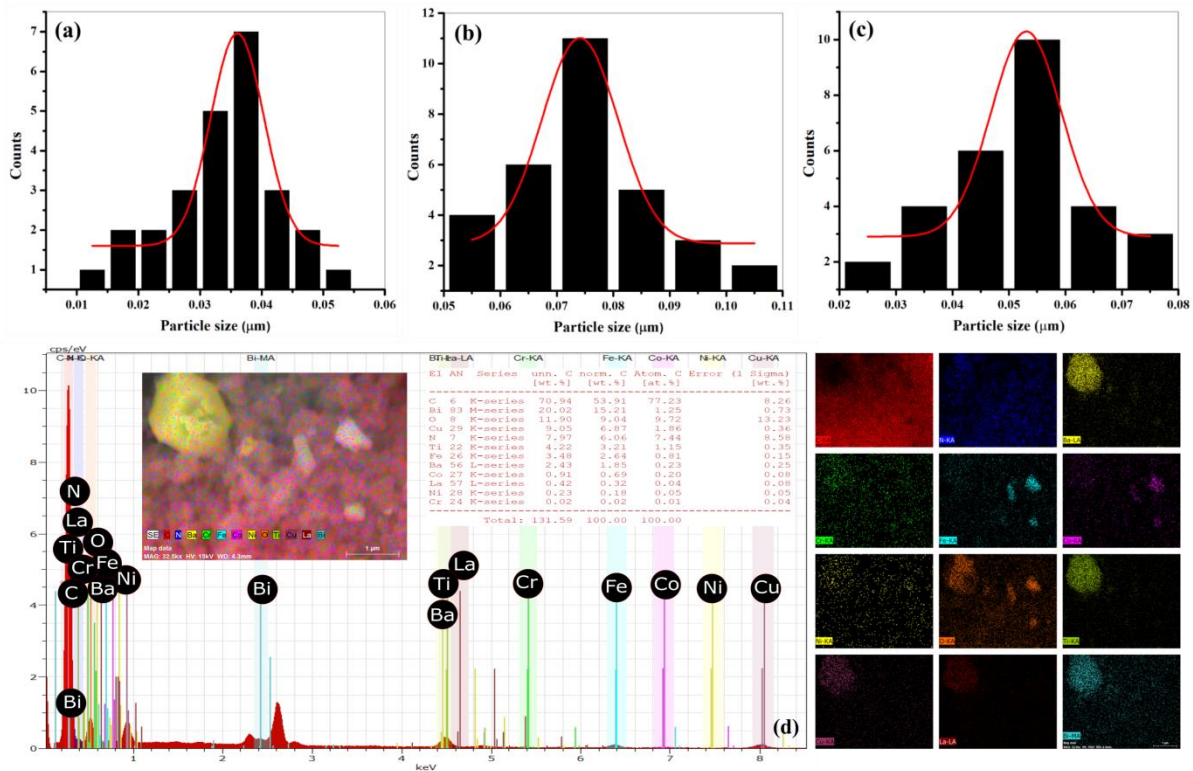
Fig. 5.100 Particle size distribution of (a) PANI, (b) BCTO, (c) Co_2Y and EDX spectra/mapping of (d) Co_2Y/BCTO/PANI nanocomposites

5.9.4 Magnetic analysis

The M-H hysteresis loop of BCTO, Co_2Y, and Co_2Y/BCTO/PANI nanocomposite is presented in **Fig. 5.101**. The values of H_c, M_s, and M_r were estimated from the M-H hysteresis loop and reported in **Table 5.24**. It can be observed that Co_2Y and Co_2Y/BCTO/PANI nanocomposite shows paramagnetic behaviour whereas BCTO shows a horizontal straight line indicating the absence of any magnetic parameters such as coercivity (H_c), saturation magnetization (M_s), and remnant magnetization (M_r), this is no surprise as BCTO is a non-magnetic material. As observed in **Fig. 5.101**, the values of M_s and M_r for the Co_2Y/BCTO/PANI nanocomposite was found to be 11.602 emu/g and 3.422 emu/g respectively, this values are smaller than that of Co_2Y barium hexaferrites nanoparticles (M_s=44.658 emu/g and M_r=19.088 emu/g). This decrease is due to the presence of nonmagnetic BCTO microparticles and PANI, this indicates that Co_2Y barium hexaferrites nanoparticles contributes most to the magnetic properties of Co_2Y/BCTO/PANI nanocomposite. Additionally, this may be the consequence of interfacial polarization between Co_2Y and BCTO nanoparticles, the presence of lattice defects, weakening of super-exchange

interactions as result of the presence of nonmagnetic BCTO particles and PANI, and random orientation of spin at the surface of Co_2Y/BCTO/PANI composite [54].

PANI in the composite plays the role of matrix i.e. Co_2Y and BCTO nanoparticles are embedded in PANI. Then, this can imply that the particles size in composite is certainly larger than that of Co_2Y particles due to presence of BCTO microparticles which have large particle size. In addition, it is known that the coercive field is strongly influenced by the particles size which decrease when the particle size increase as reported by Globus [188]. From **Table 5.24**, it can be noticed that H_c decreases from 433.167 to 340.141 Oe which may be a consequence of coating of BCTO and Co_2Y nanoparticles with PANI as explained above. Compared to M-type hexaferrite which shows high coercivity, the obtained values for Co_2Y and composite are low which indicate that they are soft materials. The squareness ratio (*SR*) and anisotropy constant (*K*) were evaluated using the relations below:

$$SR = \frac{M_r}{M_s} \tag{5.111}$$

$$H_c = \frac{2K}{\mu_0 M_s} \tag{5.112}$$

Where $\mu_0 = 4\pi \times 10^{-7}$ H/m represents the permeability in vacuum. The structure of material is defined by the value of *SR*. It has been reported that if *SR* is greater or equal to 0.5 then the material is in single magnetic domain and if it is less than 0.5 the material exhibits a multi magnetic domain [133]. In the present work, the squareness ratio was found to be 0.427 and 0.295 for Co_2Y and composite respectively. Since these values are less than 0.5, it can be deduced that Co_2Y and Co_2Y/BCTO/PANI nanocomposite exhibit multi magnetic domain. The value of anisotropy constant has been observed to decrease from 0.969 to 0.198 after the addition of BCTO nanoparticles and PANI; this is a consequence of lack of magnetism in PANI and BCTO microparticles.
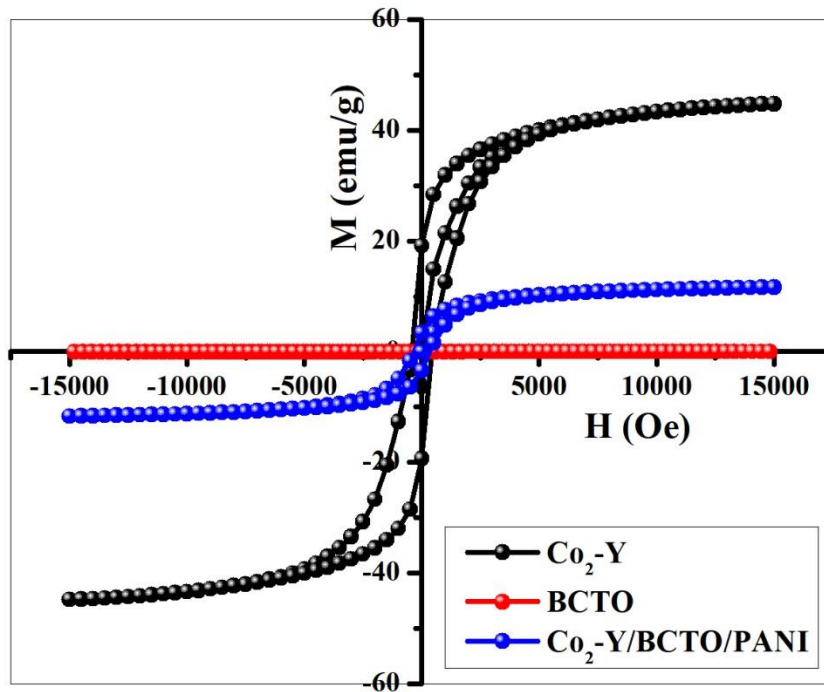
Fig. 5.101 *M-H* hysteresis loop for $Co_2Y/BCTO/PANI$ nanocomposite

Table 5.24 Values of coercivity (H_c), saturation magnetization (M_s), remnant magnetization (M_r) squareness ratio (M_r/M_s), and anisotropy constant (K).

Samples	$M_s(emu/g)$	$M_r(emu/g)$	$H_c(Oe)$	$SR(M_r/M_s)$	$K(HA^2/Kg)$
Co_2Y	44.658	19.088	433.167	0.427	0.969
Co_2Y /BCTO/PANI	11.602	3.422	340.141	0.295	0.198

5.9.5 Magnetic and dielectric loss mechanism

The degree of attenuation and reflection characteristics of nanomaterials that can be used for the shielding of EM wave can be determined from the complex permittivity ($\varepsilon^* = \varepsilon' - j\varepsilon''$) and complex permeability ($\mu^* = \varepsilon' - j\varepsilon''$) with the real part of complex permittivity (ε') and imaginary part of complex permittivity (ε'') contributing to the dielectric losses and the real part of complex permeability (μ') and the imaginary part of complex permeability (μ'') contributing to the magnetic losses [54]. On one hand, the electric energy storage ability is

185

usually indicated by the extent of ε' whereas that of magnetic energy storage can be evaluated from μ', on the other hand the ε'' and μ'' represents the losses in dielectric and magnetic energy [254]. The dielectric loss tangent ($\tan \delta_e$) and magnetic loss tangent ($\tan \delta_m$) which respectively measures the attenuation of the electric field and magnetic field by the EM wave absorber is written as [54, 122]

$$\tan \delta_e = \frac{\varepsilon''}{\varepsilon'} \tag{5.113}$$

$$\tan \delta_m = \frac{\mu''}{\mu'} \tag{5.114}$$

Where δ_e is the dielectric loss angle and δ_m is the magnetic loss angle. In general, the more the value of δ_e and δ_m, the more the attenuation of the wave as it passes through the EM wave absorber. Therefore, both the components of ε^* and μ^* contribute to the compression of EM wave inside the material. The values of ε', ε'', μ', μ'', $\tan \delta_e$, and $\tan \delta_m$, for the Co_2Y and BCTO samples are almost independent of frequency (**Fig. 5.102, 5.103, and 5.104**). However, the Co_2Y/BCTO/PANI nanocomposite shows multiple resonance peaks with varying intensities over the whole frequency range. Specifically, ε' and ε'' dominate the lower frequency region whereas the higher frequency region is dominated by μ' and μ''. Polarization is of four kinds, namely interfacial, dipolar, atomic, and electronic polarization. Interfacial and electronic polarizations are dominant at lower and intermediate frequencies respectively, the intermediate frequency is mostly dominated by the effects of dipolar and atomic polarization [254]. Hence, we could attribute the occurrence of relaxation peaks at lower and higher frequency to the presence of interfacial and electronic polarization respectively and those occurring at intermediate frequency to dipolar and atomic polarization. The values of ε', ε'', μ', and μ'' for the Co_2Y/BCTO/PANI nanocomposite are higher than those of Co_2Y and BCTO nanoparticles. This came with no surprise as the combination of a material with excellent magnetic property (i. e. Co_2Y) with that of giant dielectric constant material (i. e. BCTO) should yield a composite material with high ε', ε'', μ', and μ''. Additionally, the conductivity of PANI coupled with its abundant dipoles also plays great role at ensuring the occurrence of orientation polarization and electron hopping which in turn increase the dielectric properties [255]. Clearly, both the values of ε' and ε'' are greater than those of μ', and μ'', this is due to the fact that PANI is also a dielectric absorbent just like BCTO and therefore contributes to the dielectric losses in the material [256]. Additionally, the Co_2Y nanoparticles contributes to the values of ε' and ε'' in accordance with Koop's

phenomenological theory which states that interfacial polarization occur in ferrites materials due the presence of low conducting grains separated by high resistive grain boundary [257]. Interestingly enough, the abrupt increase in the values of μ', and μ'' at higher frequency could be tied to relaxation effects between the PANI chain and the Co_2Y nanoparticles [258]. The plot of $\tan\delta_e$ and $\tan\delta_m$ also shows relaxation peaks with the values of $\tan\delta_\varepsilon$ being greater than those of $\tan\delta_m$ by almost 50%.

Having discussed the mechanism of magnetic losses, it is paramount to understand where these losses are originating from. Magnetic losses usually appear due to resonance of the domain wall, magnetic hysteresis losses, effect of eddy current, exchange resonance and natural resonance. In hexaferrites, resonance of the domain wall usually occur at low frequency (< 1 GHz) and in materials that are multi-domain in nature, hence we can assume that resonance of the domain has no contribution to the observed magnetic losses. Magnetic hysteresis loss occurs when the magnetization vector lags behind applied EM field vector, and in the frequency range 2 to 18 GHz, it is negligible for hexaferrites and therefore has no contribution in this case. The magnetic losses due to effects of eddy current is evaluated using the equation [54]

$$C_0 = \mu''\left(\mu'\right)^{-2} f^{-1} = 2\pi\mu_0\sigma t \tag{5.115}$$

Where μ_0 is the permeability of vacuum, σ is the conductivity whereas t is the thickness of the EM wave absorber. If the magnetic losses occurs only due to effect of eddy current, then the graph of C_o against frequency should remain constant and frequency independent in accordance with the skin-effect criterion [259]. Clearly, the higher frequency region of the graph of Co_2Y nanoparticles and $Co_2Y/BCTO/PANI$ nanocomposite as well as the intermediate frequency region of the $Co_2Y/BCTO/PANI$ nanocomposite remains constant and frequency independent (**Fig. 5.105**), thus we can assume the contribution of the effects of eddy current in this region. The lower and intermediate frequency region of the BCTO and Co_2Y nanoparticles as well as the higher frequency region of the BCTO nanoparticles are well adorn by the presence of resonance peaks which could be exchange resonance or natural resonance. However, exchange resonances usually occur at higher frequency region than natural resonance in accordance with Aharoni's theory. Hence, we can assume that the peaks of resonance observed at lower frequency are due to natural resonance whereas those observed at higher frequency region are due to exchange resonance [122].
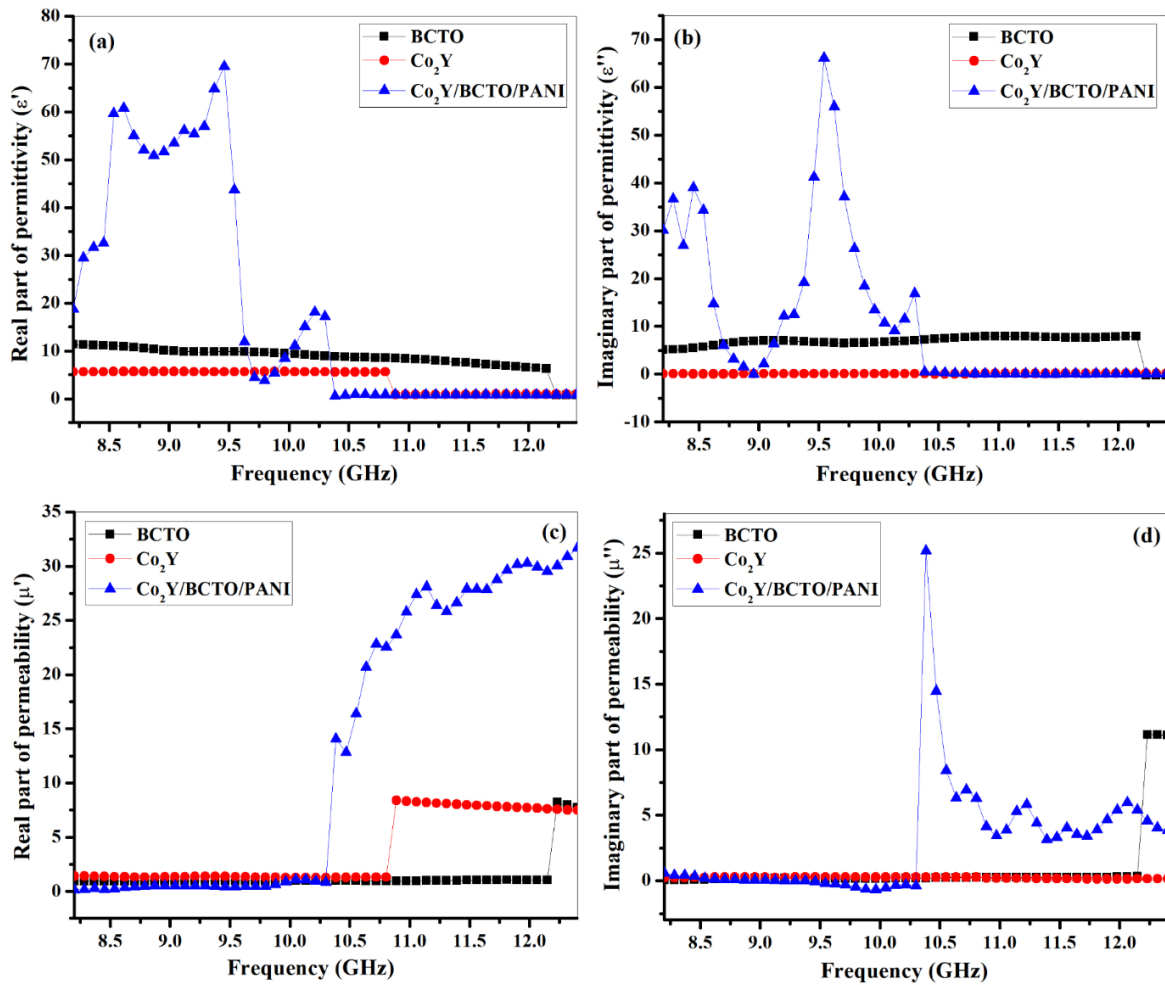
Fig. 5.102 Plot of (a) real part of complex permittivity, (b) imaginary part of complex permittivity (c) real part of complex permeability, and (d) imaginary part of complex permeability with frequency for $Co_2Y/BCTO/PANI$ nanocomposite
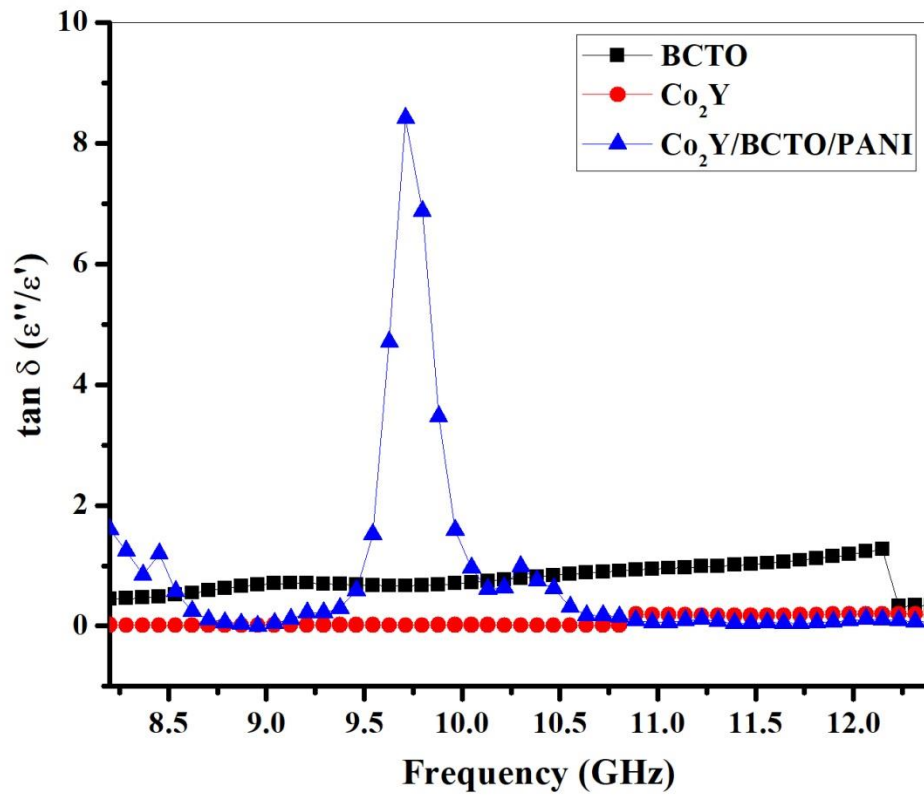
Fig. 5.103 Variation of dielectric tangent loss with frequency for Co₂Y/BCTO/PANI nanocomposite
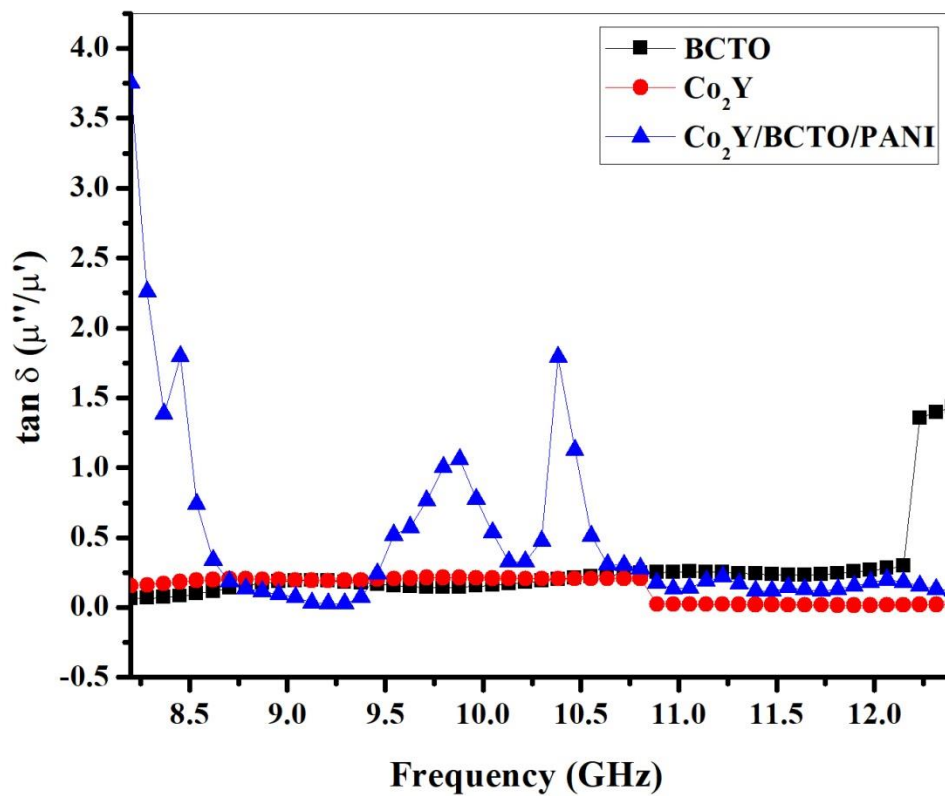
Fig. 5.104 Variation of magnetic tangent loss with frequency for Co₂Y/BCTO/PANI nanocomposite
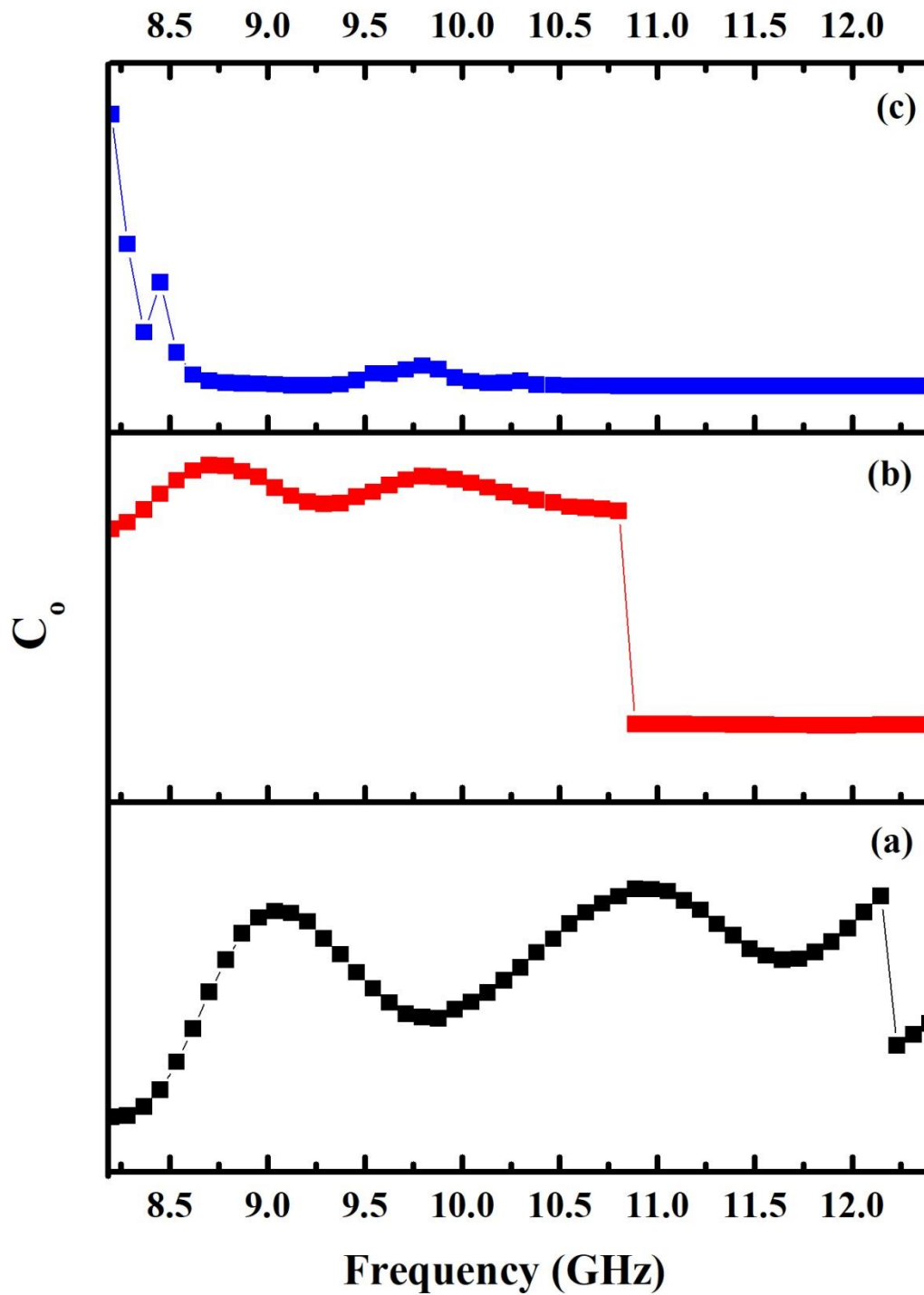
Fig. 5.105 Variation of C_o with frequency for $Co_2Y/BCTO/PANI$ nanocomposite (a) BCTO, (b) Co_2Y, and (c) $Co_2Y/BCTO/PANI$

5.9.6 EMI shielding mechanism and performance

The EMI shielding mechanism and performance which include shielding effectiveness due to absorption (SE_A), shielding effectiveness due to reflection (SE_R), shielding effectiveness due to multiple internal reflection (SE_M), and total shielding (SE_T) were evaluated from the obtained S parameters (S_{11} or S_{22} and S_{12} or S_{21}) as well as reflection coefficient (R) and transmission coefficient (T) which are given as [260]

$$R = |S_{11}|^2 = |S_{22}|^2 \qquad\qquad (5.116)$$

$$T = |S_{12}|^2 = |S_{21}|^2 \qquad\qquad (5.117)$$

$$SE_R = -10\log(1 - R) \qquad\qquad (5.118)$$

$$SE_A = -10\log\left(\frac{T}{1-R}\right) \qquad\qquad (5.119)$$

$$SE_T = SE_A + SE_R + SE_M \qquad\qquad (5.120)$$

The SE_M in equation 13 can be neglected when $SE_T > 10\ dB$ and therefore equation 13 can be simplified as

$$SE_T = SE_A + SE_R \qquad\qquad (5.121)$$

The EMI shielding material must be able to provide efficient shielding against incident electromagnetic (EM) wave, this is usually achieved by ensuring the electric charge carriers and magnetic dipoles interact with the incident EM wave. Hence, conductivity is of paramount importance when it comes to ensuring efficient shielding of EM waves. Therefore, the microwave conductivity and skin depth for BCTO, Co_2Y, and Co_2Y/BCTO/PANI nanocomposite are evaluated and presented in **Fig. 5.106** and **5.107**. The variation of SE_A and SE_R for BCTO, Co_2Y, and Co_2Y/BCTO/PANI nanocomposite in the frequency range 8.2 to 12. 4 GHz are respectively shown in **Fig. 5.108** and **5.109**. The highest values of SE_A and SE_R were observed in the Co_2Y/BCTO/PANI nanocomposite and are respectively found to be 14.30 and 17.66 both at 10.30 GHz, these values indicate that SE_R dominates and therefore most of the incident EM wave is reflected rather than absorbed. This claim is further supported by the observed low values of skin depth (**Fig. 5.107**). The variation of SE_T for BCTO, Co_2Y, and Co_2Y/BCTO/PANI nanocomposite in the frequency range 8.2 to 12. 4 GHz are shown in **Fig. 5.110**.The maximum value of SE_T for BCTO, Co_2Y, and Co_2Y/BCTO/PANI nanocomposite was found to be 23.10, 27.39, and 31.97 dB at 10.47, 9.62, 10.30 GHz respectively. Clearly, the Co_2Y/BCTO/PANI nanocomposite show better

SE_T as compared with BCTO and Co_2Y. This is simple because heterogeneous system presents a situation in which virtual charges accumulate at the interface two materials have different dielectric property and conductivity, this in turn result in the appearance of interfacial (Maxwell-Wagner) polarization [261]. This is further validated by the observed high values of conductivity (**Fig. 5.106**). This accumulation of charges results in charge carrier mobility and increase the conductivity of the material, therefore SE_T values for $Co_2Y/BCTO/PANI$ nanocomposite turn out to be higher than those observed in BCTO and Co_2Y. A comparative table of SE_T values of our synthesized nanocomposites with other composites reported in literature is shown in **Table 5.25**. It can be observed that $Co_2Y/BCTO/PANI$ nanocomposite offer better EMI shielding performance in comparison. This research has demonstrated the efficiency of incorporating dielectric and magnetic material in a conduction polymer in EMI shielding.
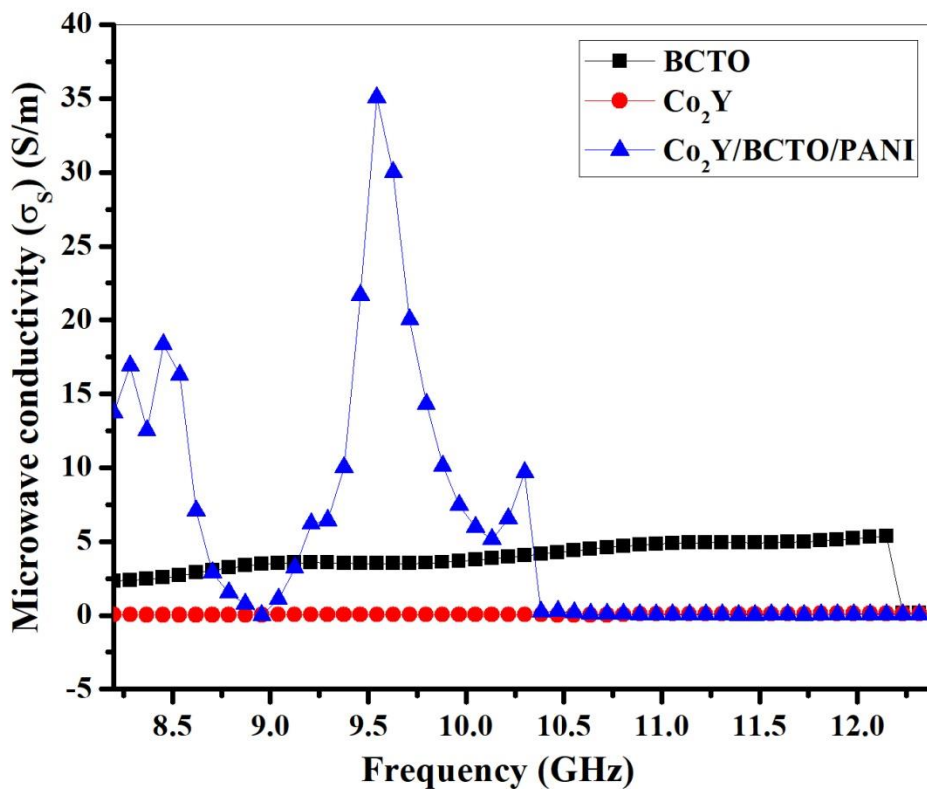
Fig. 5.106 Variation of microwave conductivity with frequency for $Co_2Y/BCTO/PANI$ nanocomposite
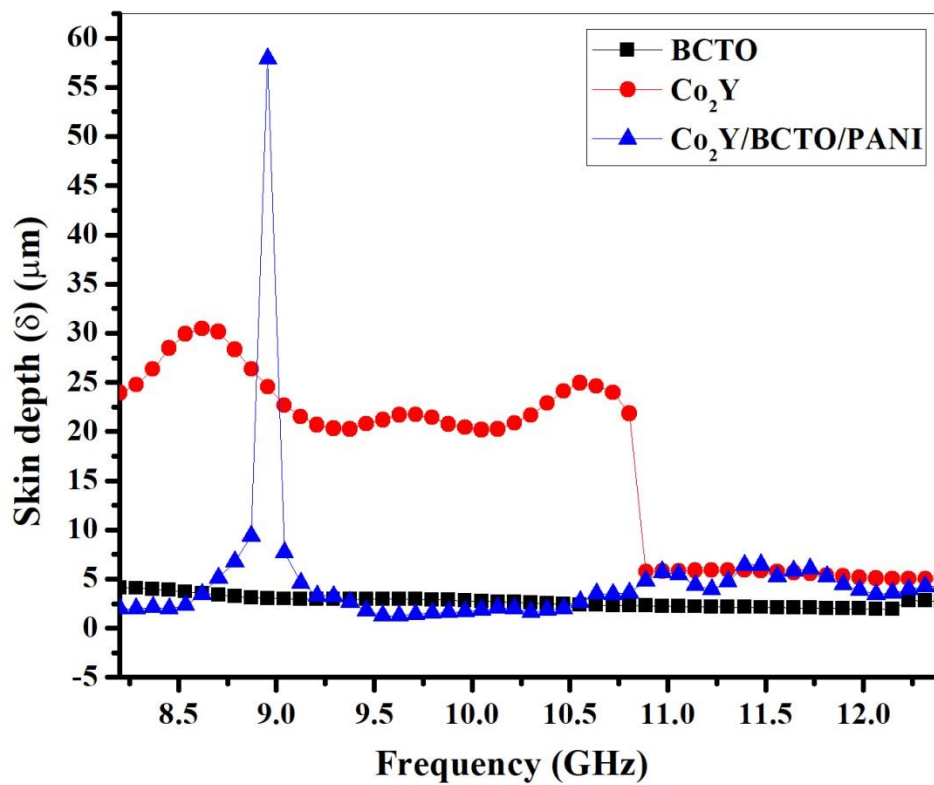
Fig. 5.107 Variation of skin depth with frequency for $Co_2Y/BCTO/PANI$ nanocomposite
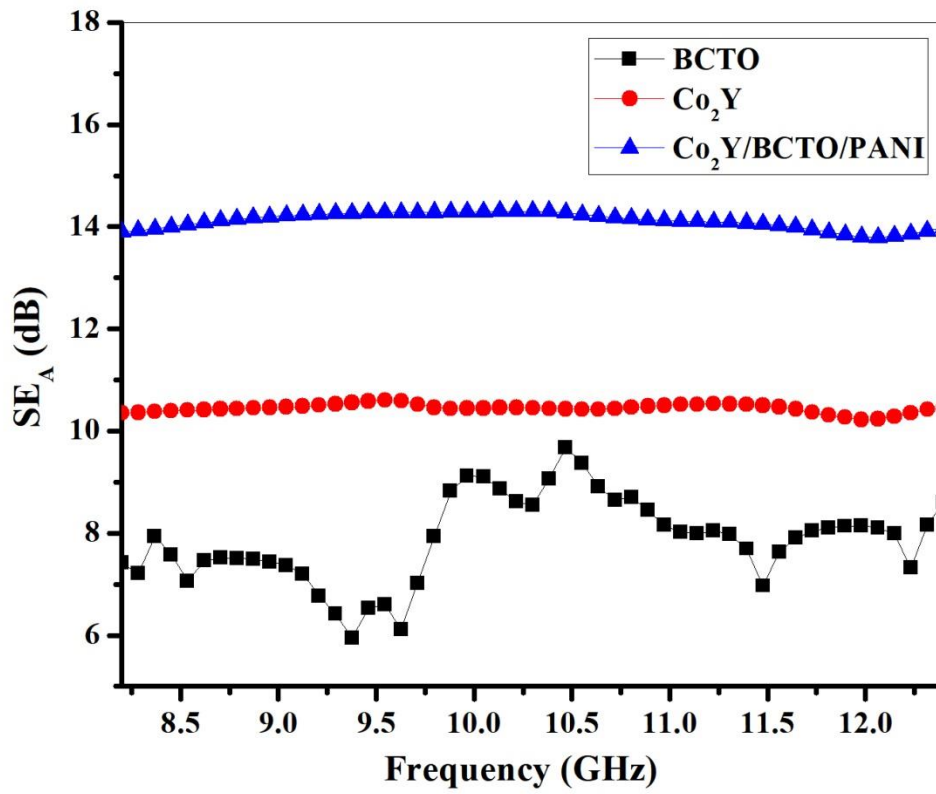
Fig. 5.108 Variation of shielding effectiveness for absorption with frequency for Co$_2$Y/BCTO/PANI nanocomposite
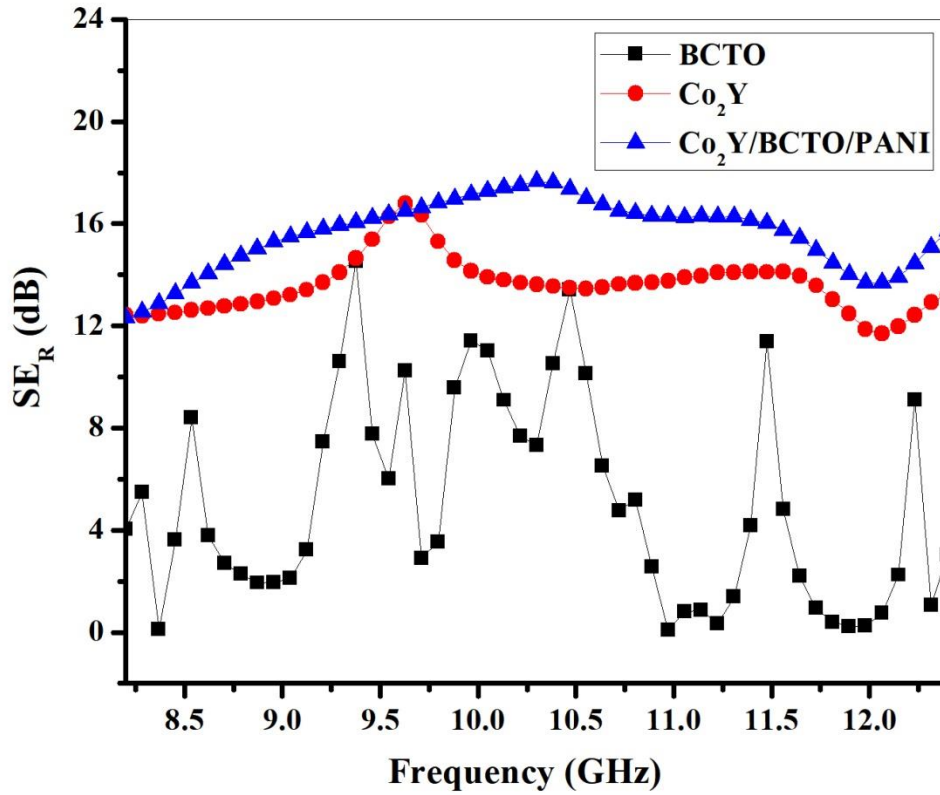
Fig. 5.109 Variation of shielding effectiveness for reflection with frequency for $Co_2Y/BCTO/PANI$ nanocomposite
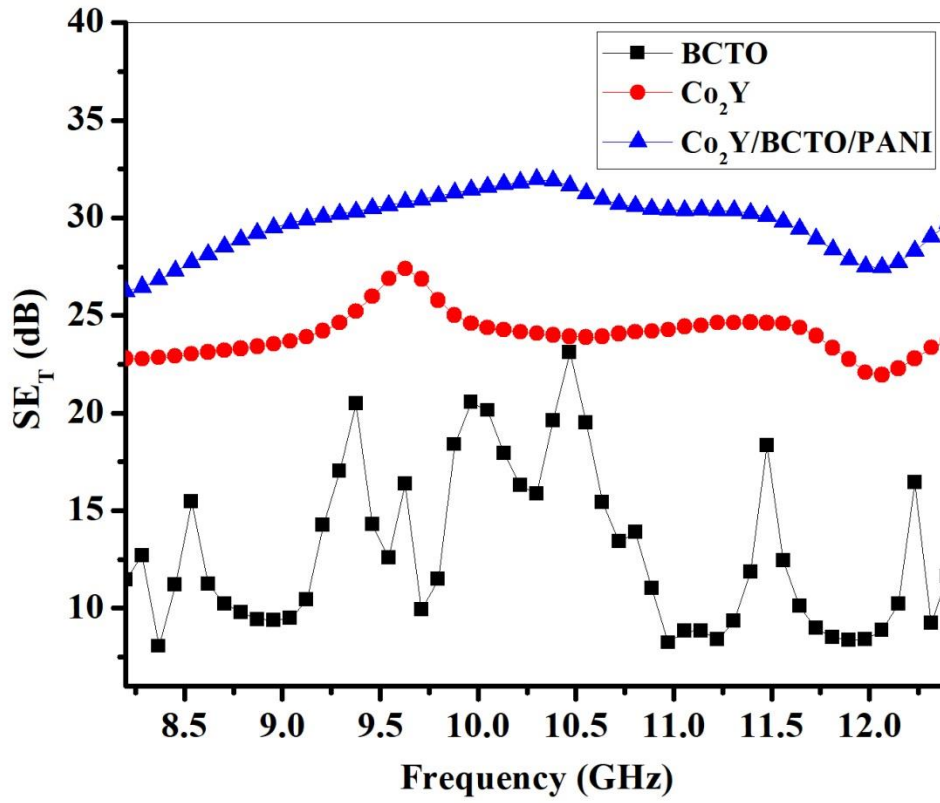
Fig. 5.110 Variation of total shielding effectiveness with frequency for $Co_2Y/BCTO/PANI$ nanocomposite

Table 5.25 Comparison of SE_T values for BCTO, Co_2Y, and Co_2Y/BCTO/PANI nanocomposite with other composites

Composites	Pellet thickness (t) (mm)	Maximum total shielding effectiveness (SE_T) (dB)	Frequency (GHz)	References
PLLA/MWCNT nanocomposites foams	2.5	23.00	8.2-12.4	[262]
MoS2-rGO/Fe3O4 nanocomposites	-	8.27	8.2-12.4	[263]
Porous superhydrophobic polymer and carbon composites	2	28.50	8.2-12.4	[264]
PI/RGO/MWCNTs nanocomposite	0.5	18.20	8.2-12.4	[265]
Strontium hexaferrites	2	27.40	18	[126]
Polypropylene and carbon fibre composite foams	3.2	24.90	8.2-12.4	[266]
BCTO	2	23.10	10.47	This work
Co_2Y	2	27.39	9.62	This work
Co_2Y/BCTO/PANI nanocomposite	2	31.97	10.30	This work

Chapter 6

Summary and conclusion

In summary, it is important to remember that the purpose of this thesis was that of the synthesis of a nano material capable of absorbing electromagnetic waves in the X band. For this, we proceeded to the synthesis and characterization of hexaferrite materials, dielectric and conductive polymer. Characterization techniques such as XRD, FTIR, FESEM, EDX, Raman, impedance analyzer, VSM and VNA have been used. Because of their advantages compared to others methods, sol-gel auto combustion method was used for the synthesis of Hexaferrite and BCTO nanoparticles while oxidative polymerization was used with success for the synthesis of conductive polymers.

Sol-gel auto combustion technique has been used with success to prepare M-type hexaferrite $Ba_{1-x}Al_xFe_{12-y}Mn_yO_{19}$ ($x = 0.6$ and y = 0.3). XRD analysis revealed the formation of pure M-type hexaferrite phase with the presence of hematite as secondary phase at $1050^{\circ}C$. Crystallite size showed an increase with increasing of heating temperature. Also, an increase of particle size from 47 nm to 167 nm for $950^{\circ}C$ and $1050^{\circ}C$ was observed in FESEM micrographs. Saturation magnetization was found to increase from 6.78 to 33.97emu/g with the increase in the heating temperature. However the highest value of coercivity (7779.94 Oe) was obtained at $850^{\circ}C$. Dielectric study showed that ε' and tan δ parameters decrease with the increase in temperature. ε'' increased for the high values of frequencies. The AC conductivity σ_{AC} was also increased at high frequency. UV-Vis-NIR spectroscopy showed that the absorption region for prepared samples is 200-600 nm.

Al-Cr barium hexagonal ferrites were successfully prepared by sol-gel auto combustion method. The observed XRD patterns indicate the formation of single phase M-type barium hexaferrites for all compositions whereas FTIR spectra give the idea of the formation of hexagonal ferrite structure. Dielectric parameters such as dielectric constant, dielectric tangent loss and AC conductivity show response of typical ferrites material. Saturation and remnant magnetization decrease (for x=0.2) as result of replacement of Fe^{3+} ion by Al^{3+} ion. Cr^{3+} ion prefer to occupy 12k, 2a and $4f_2$ sites, Similarly, saturation and remnant magnetization increase (for x=0.4) due to the fact that more Cr^{3+} ions ($3\mu_B$) replaces Fe^{3+} ions at $4f_2$ site. The calculated values of the squareness ratio suggest that the sample x=0.0 is multi-domain whereas the samples having x=0.2 and x=0.4 are single domain. The improvement of dielectric constant at high frequency and low dielectric makes the material

useful in electronics devices. Moreover, the magnetic parameters also show that the prepared material may be useful for high-density perpendicular magnetic recording media.

$SrFe_{12-2x}Cr_xBi_xO_{19}$ (x=0.0-0.2) nanoparticles have been prepared using of sol gel auto combustion method successfully. X-ray analysis revealed the single crystal phase of samples with $P6_3/mmc$ as space group and no impurity which was confirmed by Rietveld refinement. FTIR spectra showed vibration bands of hexaferrite at around 441, 552 and 598 cm^{-1}. Magnetic parameters (Ms and Mr) were found to increase with Cr^{3+}-Bi^{3+} concentration as a result of occupation of octahedral and tetrahedral sites by Cr^{3+} and Bi^{3+} ions. High value of coercivity (Hc) revealed that the prepared samples are useful for recording media applications. Dielectric parameters (ϵ' and tan δ) showed a decrease with increasing of applied field frequency whereas the conductivity increases at higher frequencies.

Nano sized particles $Ba_{2-2x}Cr_xNi_xCo_2Fe_{12}O_{22}$ (x=0.0, 0.1, 0.15) have been prepared with success employing sol-gel autocombustion technique. The characterizations of prepared samples revealed a lot of information: The XRD analysis revealed the diffraction planes of Co_2Y barium hexaferrite without the presence of any impurity. Those peaks were confirmed by refining XRD patterns. The morphology of the prepared samples show a flat hexagonal shape with particle size of 0.167 μm and 0.165 μm for x=0.0 and x=0.15 respectively. All substituted and host elements of prepared samples were observed in EDX spectra and mapping which confirmed XRD results. Low values of band gap (between 0.74 and 2.16 eV) were obtained from UV-Vis-NIR spectroscopy. Highest values of M_s (49.23 emu/g) was obtained for x=0.1. An increase in H_c with Cr^{3+}-Ni^{2+} concentration was observed and all prepared samples presented soft magnetic character. The highest value of dielectric constant (12.4) at 100 Hz and the highest value of Ac electrical conductivity (1.54 $(\Omega.cm)^{-1}$) at 120 MHz have been obtained in the sample with x=0.0. Nyquist plots of complex impedance show that the observed large dielectric constant originates from grain boundary contribution.

Ni^{2+}-Co^{2+} substituted $Bi_{2/3}Cu_3Ti_4O_{12}$ electroceramic have been successfully prepared using sol-gel autocombustion technique. The prepared electroceramics were subjected to various characterizations and subsequent data analysis using different software, the following observations have been made: The XRD spectra of the prepared electroceramic show explicit peaks of BCTO electroceramic with cubic perovskite structure, single crystalline phase and space group Im-3. CuO and TiO_2 secondary phases have not been observed in the spectra. However, CuO phase was observed in the Raman spectra at 246 cm^{-1}. This contradiction is

observed as a result of higher sensitivity of Raman spectroscopy as compared to XRD. The morphology of the prepared samples shows cubic particles with an average particle size of 0.22μm and 0.11μm for undoped (x=0.0) and doped (x=0.2) samples respectively. The observation of all the substituted and host elements in the EDX spectra indicates that the stoichiometry of the BCTO electroceramic is maintained. Analysis of band gap show that the sample with x=0.1 exhibit the highest value of band gap (3.69 eV). Urbach energy was calculated and we conclude that structural defects as a result of substitution of the host cation (Cu^{2+}) by larger ionic radii cations (Co^{2+} and Ni^{2+}); this explanation is supported by XRD analysis. The highest value of dielectric constant (3800) has been obtained in the sample with x=0.0 at 100 Hz. Cole-Cole plots of complex impedance and electric modulus show that the observed large dielectric constant originates from grain boundary contribution.

Nanocomposites of $BaFe_{11.8}Bi_{0.1}Al_{0.1}O_{19}$-PANI have been prepared successfully by mechanical grinding of $BaFe_{11.8}Bi_{0.1}Al_{0.1}O_{19}$ particles and PANI. Sol gel technique has been used to prepare $BaFe_{11.8}Bi_{0.1}Al_{0.1}O_{19}$ whereas oxidative polymerization was used to make PANI. XRD analysis and Rietveld refinement revealed hexagonal structure of $BaFe_{11.8}Bi_{0.1}Al_{0.1}O_{19}$ with space group *P63/mmc* without any second phase in the sample. The presence of PANI was localized at around 25°. FTIR analysis revealed all different functional groups in the prepared samples. Band gap was estimated by UV-vis analysis and values were found to be between 2.21-2.36 eV.

$Ba_{0.7}Dy_{0.3}Fe_{11.4}Cr_{0.3}O_{19}$/PANI composites have been successfully synthesized using mechanical grinding after making $Ba_{0.7}Dy_{0.3}Fe_{11.4}Cr_{0.3}O_{19}$ and PANI by sol-gel method and oxidative polymerization method respectively. The formation of hexagonal ferrites was confirmed from XRD patterns and some traces of second phase (α-Fe_2O_3) were also observed. (FTIR) spectroscopy gave information about functional groups occurred from hexaferrite and PANI by the appearance of absorption peaks between 400-600 cm^{-1} and 800-1600 cm^{-1}. The band gap decreases with the increase in PANI amount.

Sol-gel auto-combustion technique was used with success to synthesize nano sized particles of $BaFe_{11.8}Bi_{0.2}O_{19}$ (BBPY1) and $[Bi_{(1-x)}La_x]_{2/3}Cu_3Ti_4O_{12}$ (x=0.2) (BBPY2). Polypyrrole was successfully prepared using oxidative polymerization method. The BBPY3 nanocomposite was obtained by mixing all three prepared samples employing mechanical grinding method. From characterization techniques, much information were obtained for BBPY1, BBPY2 and BBPY3.

Single crystal structure of BBPY1 and BBPY2 was observed from XRD analysis indicating that the prepared samples are pure. All diffraction peaks were also observed on XRD pattern of BBPY3 indicating that the presence of each single sample. The presence of polypyrrole in BBPY3 nanocomposite was observed at around 25°. Lattice constant of BBPY1 were found to be a=5.8976Å. FESEM analysis displayed BBPY1, BBPY2 and PPY particles. The average particle size of BBPY1 and BBPY2 were found to be 0.19 and 0.163μm respectively. The MS value of BBPY1 was found to be 32.134 emu / g. this value decreased after the addition of BBPY2 and PPY and reached 18.181 emu / g for the composite. However, Hc was found to increase from 1374.53 to 3320.87 Oe.

We have successfully Co_2Y barium hexaferrites nanoparticles and BCTO microparticles using sol-gel autocombustion method. The prepared samples were mixed in a PANI matrix using mechanical blending method. The structural analysis shows the successful incorporation of Co_2Y barium hexaferrites nanoparticles and BCTO microparticles in the PANI matrix. Also, the purity of all the prepared samples has been assumed based on the structural analysis. The magnetic properties of the Co_2Y/BCTO/PANI nanocomposite show drastic reduction in magnetic parameters as result of lack of magnetism in BCTO and d PANI. The maximum value of SE_T for BCTO, Co_2Y, and Co_2Y/BCTO/PANI nanocomposite was found to be 23.10, 27.39, and 31.97 dB at 10.47, 9.62, and 10.30 GHz respectively. The fact that these values are above 20 dB indicates that the prepared samples can be used for technological application. Additionally, our samples outperform other composites materials as presented in **Table 5.25**.

Future scope

During the work of this thesis, characterization techniques such as XRD, FTIR, UV, VSM, FESEM, Impedance Analyzer, Raman and VNA were performed. But given the lack of some equipment, all the properties of the materials have not been explored. It would be interesting to complement the characterization techniques used in this work by others such as electronic paramagnetic resonance (EPR), Nuclear magnetic resonance (NMR) and Mössbauer analysis which could give more information on the properties of the material.

In this work all analysis were done at room temperature due to limited access to research equipment. Then, a variation of this temperature would lead to understand the behavior of the material in various media.

With regard to the shielding properties studied, it would be interesting to know the effect of the variation of thickness on these properties in order to know for which thickness the material has a maximum of absorption.

Bibliography

[1]   X. Li, R. Gong, Z. Feng, J. Yan, X. Shen, and H. He, "Effect of particle size and concentration on microwave-absorbing properties of $Cu_xCo_{2-x}Y$ (x=0, 1) hexaferrite composites," *J. Am. Ceram. Soc.*, **89**, 1450–1452 (2006).

[2]   R. C. Pullar, "Hexagonal ferrites: A review of the synthesis, properties and applications of hexaferrite ceramics," *Prog. Mater. Sci.*, **57**, 1191–1334 (2012).

[3]   T. Kaur, S. Kumar, S. B. Narang, and A. K. Srivastava, "Radiation losses in microwave Ku region by conducting pyrrole/barium titanate and barium hexaferrite based nanocomposites," *J. Magn. Magn. Mater.*, **420**, 336–342 (2016).

[4]   J. Zhang, L. Wang, and Q. Zhang, "A composite material based on BaZn2Fe16O27 ferrite and antimony-doped tin oxide composite with excellent microwave absorbing property and 1.06 μm reflection performance," *J. Mater. Sci. Mater. Electron.*, **26**, 6218–6223 (2015).

[5]   F. Guo, W. Zi, G. Ji, L. Zou, and S. Gan, "Polyaniline containing W-type hexaferrite composites for microwave absorption in high-frequency applications," *J. Polym. Res.*, vol. **22**, 1 (2015).

[6]   J. Jiang, L. Ai, and L. Li, "Multifunctional polypyrrole/strontium hexaferrite composite microspheres: Preparation, characterization, and properties," *J. Phys. Chem. B*, vol. **113**, 1376–1380 (2009).

[7]   J. Luo, P. Shen, W. Yao, C. Jiang, and J. Xu, "Synthesis, Characterization, and Microwave Absorption Properties of Reduced Graphene Oxide/Strontium Ferrite/Polyaniline Nanocomposites," *Nanoscale Res. Lett.*, vol. **11**, 141 (2016).

[8]   C. L. Yuan, "Polyaniline coated magnetic particles of manganese titanium substituted strontium hexaferrites composites as microwave absorbers," *J. Mater. Sci. Mater. Electron.*, **27**, 4908–4912 (2016).

[9]   C. L. Yuan, Y. S. Hong, and C. H. Lin, "Synthesis and characterization of $Sr(ZnZr)_x$ $Fe_{12-2x}O_{19}$–PANI composites," *J. Magn. Magn. Mater.*, **323**, 1851–1854 (2011).

[10]   S. Tyagi, H. B. Baskey, R. C. Agarwala, V. Agarwala, and T. C. Shami, "Development of hard/soft ferrite nanocomposite for enhanced microwave absorption," *Ceram. Int.*,

37, 2631–2641 (2011).

[11] L. Rezlescu, E. Rezlescu, P. . Popa, and N. Rezlescu, "Fine barium hexaferrite powder prepared by the crystallisation of glass," *J. Magn. Magn. Mater.*, **193**, 288–290 (1999).

[12] A. M. Balbashov, V. Y. Ivanov, A. A. Mukhin, L. D. Iskhakova, Y. F. Popov, G. P. Vorob'ev, and M. E. Voronchikhina, "Magnetic and magnetoelectric properties of M-type substitution hexaferrites $TSc_xFe_{12-x}O_{19}$ (T = Ba, Sr)," *JETP Lett.*, **101**, 489–496 (2015).

[13] M. C. Dimri, R. Stern, S. C. Kashyap, K. P. Bhatti, and D. C. Dube, "Magnetic and dielectric properties of pure and doped barium hexaferrite nanoparticles at microwave frequencies," *Phys. Status Solidi a-Applications Mater. Sci.*, **206**, 270–275 (2009).

[14] R. M. Almeida, W. Paraguassu, D. S. Pires, R. R. Corrêa, and C. W. de Araujo Paschoal, "Impedance spectroscopy analysis of BaFe12O19 M-type hexaferrite obtained by ceramic method," *Ceram. Int.*, **35**, 2443–2447 (2009).

[15] R. B. Jotania, R. B. Khomane, C. C. Chauhan, S. K. Menon, and B. D. Kulkarni, "Synthesis and magnetic properties of barium-calcium hexaferrite particles prepared by sol-gel and microemulsion techniques," *J. Magn. Magn. Mater.*, **320**, 1095–1101 (2008).

[16] M. H. Shams, S. M. A. Salehi, and A. Ghasemi, "Electromagnetic wave absorption characteristics of Mg-Ti substituted Ba-hexaferrite," *Mater. Lett.*, **62**, 1731–1733 (2008).

[17] K. K. Mallick, P. Shepherd, and R. J. Green, "Magnetic properties of cobalt substituted M-type barium hexaferrite prepared by co-precipitation," *J. Magn. Magn. Mater.*, **312**, 418–429 (2007).

[18] Y. C. Wong, J. Wang, and G. B. Teh, "Structural and magnetic studies of SrFe12O19 by sol-gel method," *Procedia Eng.*, **76**, 45–52 (2014).

[19] M. Radwan, M. M. Rashad, and M. M. Hessien, "Synthesis and characterization of barium hexaferrite nanoparticles," *J. Mater. Process. Technol.*, **181**, 106–109 (2007).

[20] A. G. Belous, O. I. V'yunov, E. V. Pashkova, V. P. Ivanitskii, and O. N. Gavrilenko, "Mössbauer study and magnetic properties of M-type barium hexaferrite doped with

Co + Ti and Bi + Ti ions," *J. Phys. Chem. B*, **110**, 26477–26481 (2006).

[21] V. V. Pankov, M. Pernet, P. Germi, and P. Mollard, "Fine hexaferrite particles for perpendicular recording prepared by the coprecipitation method in the presence of an inert component," *J. Magn. Magn. Mater.*, **120**, 69–72 (1993).

[22] F. Aen, M. F. Wasiq, M. U. Rana, H. M. Khan, and M. A. Khan, "Structural and electrical behavior evaluation of Ho-substituted Co2W hexagonal ferrites," *Ceram. Int.*, **42**, 16077–16083 (2016).

[23] M. Irfan, A. Elahi, and A. Shakoor, "Hysteresis and electric modulus analysis of Y3+ doped MnNi-Y-type hexagonal ferrite," *Ceram. - Silikaty*, **60**, 34–40 (2016).

[24] M. Irfan, M. U. Islam, I. Ali, M. A. Iqbal, N. Karamat, and H. M. Khan, "Effect of Y_2O_3 doping on the electrical transport properties of $Sr_2MnNiFe_{12}O_{22}$ Y-type hexaferrite," *Curr. Appl. Phys.*, **14**, 112–117 (2014).

[25] B. da Costa Andrade and M. A. Macedo, "Structural and Magnetoelectric Properties of a New W-Type Hexaferrite ($Sr_{0.85}Ce_{0.15}Co_2Fe_{16}O_{27-\delta}$)," *Adv. Mater. Res.*, **975**, 263–267 (2014).

[26] Z. W. Li, L. Chen, Y. Wu, and C. K. Ong, " Microwave attenuation properties of W - type barium ferrite $BaZn_{2-x}Co_xFe_{16}O_{27}$ composites ," *J. Appl. Phys.*, **96**, 534–539 (2004).

[27] J. Mohammed, H. Y. Hafeez, Tchouank Tekou Carol T., C. E. Ndikilar, J. Sharma, P. K. Maji, S. K. Godara and A. K. Srivastava, "Structural, dielectric, and magneto-optical properties of Cu^{2+}-Er^{3+} substituted nanocrystalline strontium hexaferrite," *Mater. Res. Express*, **6**, 056111 (2019).

[28] J. Mohammed, A. B. Suleiman, T. Tekou Carol Trudel, H. Y. Hafeez, J. Sharma, P. K. Maji, S. K. Godara, and A. K. Srivastava, "Enhanced dielectric and optical properties of nanoscale barium hexaferrites for optoelectronics and high frequency application," *Chinese Phys. B*, **27**, 128104 (2018).

[29] S. H. Mahmood, M. D. Zaqsaw, O. E. Mohsen, A. Awadallah, I. Bsoul, M. A. Awawdeh, and Q. I. Mohaidat, "Modification of the Magnetic Properties of Co 2 Y Hexaferrites by Divalent and Trivalent Metal Substitutions," *Solid State Phenom.*, vol.

241, no. January, pp. 93–125, 2016.

[30] T. Tekou Carol Trudel, J. Sharma, J. Mohammed, S. Kumar, and A. K. Srivastava, "Effect of temperature on the magnetic properties of nano-sized M-type barium hexagonal ferrites," *AIP Conf. Proc.*, **1860**, 020008 (2017).

[31] S. H. Mahmood, A. N. Aloqaily, Y. Maswadeh, A. Awadallah, I. Bsoul, M. Awawdeh, and H. Juwhari, "Effects of Heat Treatment on the Phase Evolution, Structural, and Magnetic Properties of Mo-Zn Doped M-Type Hexaferrites," *Solid State Phenom.*, vol. **232**,. 65–92 (2015).

[32] T. Kaur, S. Kumar, H. B. Bhat, and A. K. Srivastava, "Enhancement in physical properties of barium hexaferrite with substitution," *J. Mater. Res.*, **30**, 2753–2762 (2015).

[33] T. González-Carreño, M. P. Morales, and C. J. Serna, "Barium ferrite nanoparticles prepared directly by aerosol pyrolysis," *Mater. Lett.*, **43**, 97–101 (2000).

[34] M. Cernea, S. G. Sandu, C. Galassi, R. Radu, and V. Kuncser, "Magnetic properties of $Ba_xSr_{1-x}Fe_{12}O_{19}$(x=0.05-0.35) ferrites prepared by different methods," *J. Alloys Compd.*, **561**, 121–128 (2013).

[35] M. J. Iqbal and M. N. Ashiq, "Physical and electrical properties of Zr-Cu substituted strontium hexaferrite nanoparticles synthesized by co-precipitation method," *Chem. Eng. J.*, **136**, 383–389, 2008.

[36] V. V Soman, V. M. Nanoti, and D. K. Kulkarni, "Dielectric and magnetic properties of Mg – Ti substituted barium hexaferrite," *Ceram. Int.*, **39**, 5713–5723 (2013).

[37] I. Ali, M. U. Islam, M. S. Awan, and M. Ahmad, "Electric and dielectric properties of Cr-Ga substituted BaM hexaferrites for high-frequency applications," *J. Mater. Eng. Perform.*, **22**, 2673–2680 (2013).

[38] M. A. Rafiq, M. Waqar, T. A. Mirza, A. Farooq, and A. Zulfiqar, "Effect of Ni^{2+} Substitution on the Structural, Magnetic, and Dielectric Properties of Barium Hexagonal Ferrites ($BaFe_{12}O_{19}$)," *J. Electron. Mater.*, **46**, 241–246 (2017).

[39] J. Mohammed, J. Sharma, S. Kumar, Tchouank Tekou Carol T., and A. K. Srivastava, "Calcination temperature effect on the microstructure and dielectric properties of M-

type strontium hexagonal ferrites," *AIP Conf. Proceeding*, **1860**, 020007 (2017).

[40] T. Kaur, J. Sharma, S. Kumar, and A. K. Srivastava, "Optical and Multiferroic Properties of Gd-Co Substituted Barium Hexaferrite," *Cryst. Res. Technol.*, **52**, 1700098 (2017).

[41] M. R. Meshram, N. K. Agrawal, B. Sinha, and P. S. Misra, "Characterization of M-type barium hexagonal ferrite-based wide band microwave absorber," *J. Magn. Magn. Mater.*, **271**, 207–214 (2004).

[42] S. B. Narang and I.S. Hudiara, "Microwave dielectric properties of M-Type barium , calcium and strontium hexa- ferrite substituted with Co and Ti," *J. Ceram. Process. Res.*, 7, 113–116 (2006).

[43] F. Leccabue, R. Panizzieri, S. Garcia, N. Suarez, J. L. Sanchez, O. Ares, and X. R. Hua, "Magnetic and Mossbauer study of rare-earth- substituted M- , W- and X-type hexagonal ferrites," *J. Mater. Sci.*, **25**, 2765–2770 (1990).

[44] Y. Tokunaga, Y. Kaneko, D. Okuyama, S. Ishiwata, T. Arima, S. Wakimoto, K. Kakurai, Y. Taguchi, and Y. Tokura, "Multiferroic M-type hexaferrites with a room-temperature conical state and magnetically controllable spin helicity," *Phys. Rev. Lett.*, **105**, 17–20 (2010).

[45] J. C. Corral-Huacuz and G. Mendoza-Suárez, "Preparation and magnetic properties of Ir-Co and La-Zn substituted barium ferrite powders obtained by sol-gel," *J. Magn. Magn. Mater.*, **242**, 430–433 (2002).

[46] A. Collomb, M. A. Farhat Hadj, and J. C. Joubert, "CObalt location in the y-type hexagonal ferr1te : $BaCoFe_6O_{11}$," *Mater. Res. Bull.*, **24**, 453–458 (1989).

[47] C. Sudakar, G. N. Subbanna, and T. R. N. Kutty, "Wet chemical synthesis of multicomponent hexaferrites by gel-to-crystallite conversion and their magnetic properties," *J. Magn. Magn. Mater.*, **263**, 253–268 (2003).

[48] Y. Bai, J. Zhou, Z. Gui, Z. Yue, and L. Li, "Complex Y-type hexagonal ferrites : an ideal material for high-frequency chip magnetic components," *J. Magn. Magn. Mater.*, **264**, 44–49 (2003).

[49] S. H. Mahmood, M. D. Zaqsaw, O. E. Mohsen, A. Awadallah, I. Bsoul, M. Awawdeh,

and Q. I. Mohaidat, "Modification of the Magnetic Properties of Co_2Y Hexaferrites by Divalent and Trivalent Metal Substitutions," *Solid State Phenom.*, **241**, 93–125 (2016).

[50] A. Deriu, F. Licci, S. Rinaldi, and T. Besagni, "Y-type hexagonal ferrites containing zinc, copper and cadmium: magnetic properties and cation distribution," *J. Magn. Magn. Mater.*, **22**, 257–262 (1981).

[51] S. G. Lee and S. J. Kwon, "Saturation magnetizations and Curie temperatures of Co-Zn Y-type ferrites," *J. Magn. Magn. Mater.*, **153**, 279–284 (1996).

[52] M. A. Subramanian, D. Li, N. Duan, B. A. Reisner, and A. W. Sleight, "High dielectric constant in ACu3Ti4O12and $ACu_3Ti_3FeO_{12}$ phases," *J. Solid State Chem.*, **151**, 323–325 (2000).

[53] M. Anilkumar, S. R. Dhage, and V. Ravi, "Synthesis of bismuth titanate by the urea method," *Mater. Lett.*, **59**, 514–516 (2005).

[54] J. Mohammed, Tchouank Tekou Carol T. H. Y. Hafeez, D. Basandrai, G. R. Bhadu, S. K. Godara, G. S. Narang, and A. K. Srivastava, "Lightweight SrM/CCTO/rGO nanocomposites for optoelectronics and - K u band microwave absorption," *J. Mater. Sci. Mater. Electron.*, **30**, 4026–4040 (2019).

[55] J. Mohammed, A. B. Suleiman, H. Y. Hafeez, Tchouank Tekou Carol T., J. Sharma, G. R. Bhadu, S. K. Godara, and A. K. Srivastava, "Effect of heat-treatment on the magnetic and optical properties of Sr0.7Al0.3Fe11.4Mn0.6O19," *Mater. Res. Express*, **5**, 086106 (2018).

[56] H. S. Kushwaha, P. Thomas, and R. Vaish, "Polyaniline/$CaCu_3Ti_4O_{12}$ nanofiber composite with a synergistic effect on visible light photocatalysis," *RSC Adv.*, **5**, 87241–87250 (2015).

[57] C. Masingboon, P. Thongbai, S. Maensiri, T. Yamwong, and S. Seraphin, "Synthesis and giant dielectric behavior of $CaCu_3Ti_4O_{12}$ ceramics prepared by polymerized complex method," *Mater. Chem. Phys.*, **109**, 262–270 (2008).

[58] P. Gautam, S. S. Yadava, A. Khare, and K. D. Mandal, "Dielectric and magnetic studies of $0.5Bi_{2/3}Cu_3Ti_4O_{12}$- $0.5Bi_3LaTi_3O_{12}$ nano-composite ceramic synthesized by semi-wet route," *Ceram. Int.*, **43**, 3133–3139 (2017).

[59] J. Mohammed, B. F. Abubakar, K. U. Yerima, H. Hamisu, U. T. Isma, A. Muhammad, U. F. Zulatu, A. Abubakar, N. M. Salihu, Mubarak S. Abubakar, Y. Saidu, Tchouank Tekou Carol T., and A. K. Srivastava, "Biodegradable polymer modified rGO / PANI / CCTO nanocomposites : Structural and dielectric properties," *Mater. Today Proc.*, **5**, 28462–28469 (2018).

[60] Z. Yang, L. Zhang, X. Chao, L. Xiong, and J. Liu, "High permittivity and low dielectric loss of the $Ca_{1-x}Sr_xCu_3Ti_4O_{12}$ ceramics," *J. Alloys Compd.*, **509**, 8716–8719 (2011).

[61] J. Liu, C. G. Duan, W. G. Yin, W. N. Mei, R. W. Smith, and J. R. Hardy, "Large dielectric constant and Maxwell-Wagner relaxation in $Bi_{2/3}Cu_3Ti_4O_{12}$," *Phys. Rev. B - Condens. Matter Mater. Phys.*, **70**, 144106 (2004).

[62] B. Rivas-Murias, M. Sanchez-Andujar, J. Rivas, and M. A. Senaris-Rodriguez, "Influence of high levels of Nb and Ti doping on the dielectric properties of $CaCu_3Ti_4O_{12}$ type of compounds," *Mater. Chem. Phys.*, **120**, 576–581 (2010).

[63] U. S. Rai1, L. Singh, K. D. Mandal, and N. B. Singh, "An Overview on Recent Developments in the Synthesis , Characterization and Properties of High Dielectric Constant Calcium Copper Titanate Nano-Particles," *Nanosci. Technol. Open access*, **1**, 1–17 (2014).

[64] Y. Q. Tan, J. L. Zhang, W. T. Hao, G. Chen, W. B. Su, and C. L. Wang, "Giant dielectric-permittivity property and relevant mechanism of $Bi_{2/3}Cu_3Ti_4O_{12}$ ceramics," *Mater. Chem. Phys.*, **124**, 1100–1104 (2010).

[65] Z. Yang, P. Liang, L. Yang, P. Shi, X. Chao, and Z. Yang, "Synthesis, dielectric properties of $Bi_{2/3}Cu_3Ti_4O_{12}$ ceramics by the sol–gel method," *J. Mater. Sci. Mater. Electron.*, **26**, 1959–1968 (2015).

[66] L. Yang, X. Chao, Z. Yang, N. Zhao, L. Wei, and Z. Yang, "Dielectric constant versus voltage and non-Ohmic characteristics of $Bi_{2/3}Cu_3Ti_4O_{12}$ ceramics prepared by different methods," *Ceram. Int.*, **42**, 2526–2533, (2016).

[67] P. Liang, Y. Li, F. Li, X. Chao, and Z. Yang, "Effect of the synthesis route on the phase formation behavior and electric property of $Na_{0.5}Bi_{0.5}Cu_3Ti_4O_{12}$ ceramics," *Mater. Res. Bull.*, **52**, 42–49 (2014).

[68] K. Gurunathan, D. P. Amalnerkar, and D. C. Trivedi, "Synthesis and characterization of conducting polymer composite (PAn/TiO$_2$) for cathode material in rechargeable battery," *Mater. Lett.*, **57**, 1642–1648 (2003).

[69] N. G. Deshpande, Y. G. Gudage, R. Sharma, J. C. Vyas, J. B. Kim, and Y. P. Lee, "Studies on tin oxide-intercalated polyaniline nanocomposite for ammonia gas sensing applications," *Sensors Actuators, B Chem.*, **138**, 76–84 (2009).

[70] C. Peng, S. Zhang, D. Jewell, and G. Z. Chen, "Carbon nanotube and conducting polymer composites for supercapacitors," *Prog. Nat. Sci.*, **18**, 777–788 (2008).

[71] A. Olad, M. Barati, and H. Shirmohammadi, "Conductivity and anticorrosion performance of polyaniline/zinc composites: Investigation of zinc particle size and distribution effect," *Prog. Org. Coatings*, vol. **72**, 599–604 (2011).

[72] S. Sathiyanarayanan, V. Karpakam, K. Kamaraj, S. Muthukrishnan, and G. Venkatachari, "Sulphonate doped polyaniline containing coatings for corrosion protection of iron," *Surf. Coatings Technol.*, **204**, 1426–1431 (2010).

[73] A. C. Aks, N. Onar, M. F. Ebeoglugil, I. Birlik, E. Celik, and I. Ozdemir, "Electromagnetic and Electrical Properties of Coated Cotton Fabric with Barium Ferrite Doped Polyaniline Film," *J. Appl. Polymer Sci.*, **113**, 358-366 (2009).

[74] M. A. Chougule, S. G. Pawar, P. R. Godse, R. N. Mulik, S. Sen, and V. B. Patil "Synthesis and Characterization of Polypyrrole (PPy) Thin Films," *Soft Nanoscience Letters*, **1**, 6–10 (2011).

[75] H. J. Kharat, K. P. Kakde, P. A. Savale, K. Datta, P. Ghosh, and M. D. Shirsat, "Synthesis of polypyrrole films for the development of ammonia sensor," *Polymers adv. Techno.*, **18**, 397–402 (2007).

[76] Maciej Sniechowski, "Structure and Dynamics of conducting polyanaline based compounds," (2005).

[77] M. Hatamzadeh, A. Mahyar, and M. Jaymand, "Chemical modification of polyaniline by N-grafting of polystyrenic chains synthesized via nitroxide-mediated polymerization," *J. Braz. Chem. Soc.*, **23**, 1008–1017 (2012).

[78] P. Saini, V. Choudhary, B. P. Singh, R. B. Mathur, and S. K. Dhawan, "Enhanced

microwave absorption behavior of polyaniline-CNT/polystyrene blend in 12.4-18.0 GHz range," *Synth. Met.*, **161**, 1522–1526 (2011).

[79] H. W. Ott, "Electromagnetic compatibility engineering," (2009).

[80] J. Zhang, L. Wang, and Q. Zhang, "Electromagnetic properties and microwave-absorption properties of $BaTiO_3/BaZn_2Fe_{16}O_{27}$ composite in 2–18 GHz," *J. Mater. Sci. Mater. Electron.*, **25**, 5601–5605 (2014).

[81] T. Kaur, S. Kumar, J. Sharma, and A. K. Srivastava, "Radiation losses in the microwave Ku band in magneto-electric nanocomposites," *Beilstein J. Nanotechnol.*, **6**, 1700–1707 (2015).

[82] F. Mohd. Idris, M. Hashim, Z. Abbas, I. Ismail, R. Nazlan, and I. R. Ibrahim, "Recent developments of smart electromagnetic absorbers based polymer-composites at gigahertz frequencies," *J. Magn. Magn. Mater.*, vol. **405**, 197–208 (2016).

[83] V. Choudhary, S. K. Dhawan, and P. Saini, "Polymer based nanocomposites for electromagnetic Interference (EMI) Shielding," (2012).

[84] K. C. Honeychurch, "Printed thick-film biosensors," *Print. Film. Mater. Sci. Appl. Sensors, Electron. Photonics*, 366–409 (2012).

[85] M. A. Mohamed, J. Jaafar, A. F. Ismail, M. H. D. Othman, and M. A. Rahman, "Fourier Transform Infrared (FTIR) Spectroscopy," 3-29 (2017).

[86] S. Foner, "Versatile and sensitive vibrating-sample magnetometer," *Rev. Sci. Instrum.*, **30**, 548 (1959).

[87] S. K. Chawla, R. K. Mudsainiyan, S. S. Meena, and S. M. Yusuf, "Sol – gel synthesis, structural and magnetic properties of nanoscale M-type barium hexaferrites $BaCo_xZr_xFe_{(12-2x)}O_{19}$," *J. Magn. Magn. Mater.*, **350**, 23–29 (2014).

[88] M. N. Ashiq, M. J. Iqbal, M. Najam-Ul-Haq, P. H. Gomez, and A. M. Qureshi, "Synthesis, magnetic and dielectric properties of ErNi doped Sr-hexaferrite nanomaterials for applications in High density recording media and microwave devices," *J. Magn. Magn. Mater.*, **324**, 15–19 (2012).

[89] T. Kaur, B. Kaur, B. H. Bhat, S. Kumar, and A. K. Srivastava, "Effect of calcination

temperature on microstructure, dielectric, magnetic and optical properties of $Ba_{0.7}La_{0.3}Fe_{11.7}Co_{0.3}O_{19}$ hexaferrites," *Phys. B Condens. Matter*, **456**, 206–212 (2015).

[90] A. Mali and A. Ataie, "Structural characterization of nano-crystalline BaFe12O19 powders synthesized by sol-gel combustion route," *Scr. Mater.*, **53**, 1065–1070 (2005).

[91] A. Ataie and S. Heshmati-Manesh, "Synthesis of ultra-fine particles of strontium hexaferrite by a modified co-precipitation method," *J. Eur. Ceram. Soc.*, **21**, 1951–1955 (2001).

[92] L. Yadong, R. Liu, Z. Zhang, and C. Xiong, "Synthesis and characterization of nanocrystalline $BaFe_{9.6}Co_{0.8}Ti_{0.8}M_{0.8}O_{19}$ particles," *Mater. Chem. Phys.*, **64**, 256–259 (2000).

[93] M. N. Ashiq, M. J. Iqbal, and I. H. Gul, "Structural , magnetic and dielectric properties of Zr–Cd substituted strontium hexaferrite ($SrFe_{12}O_{19}$) nanoparticles," *J. Alloys Compd.*, **487**, 341–345 (2009).

[94] I. Ali, M. U. Islam, M. S. Awan, and M. Ahmad, "Effects of Heat-Treatment Temperature on the Microstructure , Electrical and Dielectric Properties of M-Type Hexaferrites," *J. Electron. Mater.*, **43**, 512–521 (2014).

[95] Y. Bai, J. Zhou, Z. Gui, and L. Li, "Electrical properties of non-stoichiometric Y-type hexagonal ferrite," *J. Magn. Magn. Mater.*, **278**, 208–213 (2004).

[96] J. Mohammed, Tchouank Tekou Carol T., H. Y. Hafeez, B. I. Adamu, Y. S. Wudil, Z. I. Takai, S. K. Godara, and A. K. Srivastava, "Tuning the dielectric and optical properties of Pr-Co – substituted calcium copper titanate for electronics applications," *J. Phys. Chem. Solids*, **126**, 85–92 (2019).

[97] M. J. Iqbal, M. N. Ashiq, P. Hernandez-gomez, and J. M. Munoz, "Synthesis , physical , magnetic and electrical properties of Al–Ga substituted co-precipitated nanocrystalline strontium hexaferrite," *J. Magn. Magn. Mater.*, vol. **320**, 881–886 (2008).

[98] T. Kaur, R. Sethi, and A. K. Srivastava, "Influence of La-Mg on Optical-Dielectric and Magnetic Properties of Barium Hexaferrite," *Sci. Eng. Appl.*, **1**, 10–18 (2016).

[99] M. N. Ashiq, M. J. Iqbal, and I. Hussain Gul, "Effect of Al-Cr doping on the structural,

magnetic and dielectric properties of strontium hexaferrite nanomaterials," *J. Magn. Magn. Mater.*, **323**, 259–263 (2011).

[100] V. N. Dhage, M. L. Mane, A. P. Keche, C. T. Birajdar, and K. M. Jadhav, "Structural and magnetic behaviour of aluminium doped barium hexaferrite nanoparticles synthesized by solution combustion technique," *Phys. B Phys. Condens. Matter*, **406**, 789–793 (2011).

[101] K. M. U. Rehman, X. Liu, M. Li, S. Jiang, Y. Wu, C. Zhang, C. Liu, X. Meng, and H. Li, "Synthesization and magnetic properties of $Ba_{1-x}Y_xFe_{12}O_{19}$ hexaferrites prepared by solid-state reaction method," *J. Magn. Magn. Mater.*, **426**, 183–187 (2017).

[102] S. Che, J. Wang, Q. Chen, P. Condens, S. Che, J. Wang, and Q. Chen, "Soft magnetic nanoparticles of BaFe 12 O 19 fabricated under mild conditions," *J. Phys. Condens. Matter*, vol. 15, pp. L335–L339, 2003.

[103] J. Kreisel, G. Lucazeau, and H. Vincent, "Raman Spectra and Vibrational Analysis of $BaFe_{12}O_{19}$ Hexagonal Ferrite," *J. Solid State Chem.*, **137**, 127–137 (1998).

[104] I. A. Auwal, H. Güngüne, A. Baykal, S. Güner, S. E. Shirsath, and M. Sertkol, "Structural , morphological , optical , cation distribution and Mössbauer analysis of Bi 3 þ substituted strontium hexaferrite," *Ceram. Int.*, **42**, 8627–8635 (2016).

[105] A. Baykal, I. A. Auwal, S. Güner, and H. Sözeri, "Magnetic and optical properties of Zn^{2+} ion substituted barium hexaferrites," *J. Magn. Magn. Mater.*, **430**, 29–35 (2017).

[106] K. W. Wagner, "Zur Theorie der unvollkommenen Dielektrika.," *Ann. Phys.*, **345**, 817–855 (1913).

[107] A. Hooda, S. Sanghi, A. Agarwal, and R. Dahiya, "Crystal structure refinement , dielectric and magnetic properties of Ca/Pb substituted $SrFe_{12}O_{19}$ hexaferrites," *J. Magn. Magn. Mater.*, **387**, 46–52 (2015).

[108] M. N. Ashiq, S. Shakoor, M. Najam-ul-haq, M. F. Warsi, I. Ali, and I. Shakir, "Structural , electrical , dielectric and magnetic properties of Gd-Sn substituted Sr-hexaferrite synthesized by sol – gel combustion method," *J. Magn. Magn. Mater.*, **374**, 173–178 (2015).

[108] B. Want, B. H. Bhat, and B. Z. Ahmad, "Effect of lanthanum substitution on dielectric

relaxation, impedance response, conducting and magnetic properties of strontium hexaferrite," *J. Alloys Compd.*, **627**, 78–84 (2015).

[109] P. Kumar, A. Gaur, and R. K. Kotnala, "Magneto-electric response in Pb substituted M-type barium-hexaferrite," *Ceram. Int.*, **43**, 1180–1185 (2017).

[110] I. A. Auwal, B. Ünal, H. Güngüneş, S. E. Shirsath, and A. Baykal, "Dielectric properties, cationic distribution calculation and hyperfine interactions of La^{3+} and Bi^{3+} doped strontium hexaferrites," *Ceram. Int.*, **42**, 9100–9115 (2016).

[111] R. K. Panda, R. Muduli, S. K. Kar, and D. Behera, "Dielectric relaxation and conduction mechanism of cobalt ferrite nanoparticles," *J. Alloys Compd.*, **615**, 899–905 (2014).

[112] H. Sözeri, H. Deligöz, H. Kavas, and A. Baykal, "Magnetic , dielectric and microwave properties of M – Ti substituted barium," *Ceram. Int.*, **40**, 8645–8657 (2014).

[113] B. H. Bhat and B. Want, "Magnetic, dielectric and complex impedance properties of lanthanum and magnesium substituted strontium hexaferrite," *J. Mater. Sci. Mater. Electron.*, **27**, 12582–12590 (2016).

[114] Q. Fang, H. Cheng, K. Huang, J. Wang, R. Li, and Y. Jiao, "Doping effect on crystal structure and magnetic properties of chromium-substituted strontium hexaferrite nanoparticles," *J. Magn. Magn. Mater.*, **294**, 281–286 (2005).

[115] R. K. Mudsainiyan, S. K. Chawla, and S. S. Meena, "Correlation between site preference and magnetic properties of Co–Zr doped $BaCo_xZr_xFe_{(12-2x)}O_{19}$ prepared under sol – gel and citrate precursor sol – gel conditions," *J. Alloys Compd.*, **615**, 875–881 (2014).

[116] S. K. Chawla, S. S. Meena, P. Kaur, R. K. Mudsainiyan, and S. M. Yusuf, "Effect of site preferences on structural and magnetic switching prop- erties of CO–Zr doped strontium hexaferrite $SrCo_xZr_xFe_{(12-2x)}O_{19}$," *J. Magn. Magn. Mater.*, **378**, 84–91 (2015).

[117] H. Z. Wang, B. Yao, Y. Xu, Q. He, G. H. Wen, S. W. Long, J. Fan, G. D. Li, L. Shan, B. Liu, L. N. Jiang, and L. L. Gao, "Improvement of the coercivity of strontium hexaferrite induced by substitution of Al^{3+} ions for Fe^{3+} ions," *J. Alloys Compd.*, **537**,

43–49 (2012).

[118] V. N. Dhage, M. L. Mane, M. K. Babrekar, C. M. Kale, and K. M. Jadhav, "Influence of chromium substitution on structural and magnetic properties of BaFe12O19 powder prepared by sol-gel auto combustion method," *J. Alloys Compd.*, **509**, 4394–4398 (2011).

[119] H. Z. Wang, Y. N. Hai, B. Yao, Y. Xu, L. Shan, L. Xu, J. L. Tang, and Q. H. Wang, "Tailoring structure and magnetic characteristics of strontium hexaferrite via Al doping engineering," *J. Magn. Magn. Mater.*, **422**, 204–208 (2017).

[120] E. Roohani, H. Arabi, R. Sarhaddi, and A. Shabani, "Magnetic and Structural Properties of $SrFe_{12-x}Cr_xO_{19}$ (x=0, 0.25, 0.5, 0.75, 1) Hexaferrite Powders Obtained by Sol–Gel Auto-Combustion Method," *J. Supercond. Nov. Magn.*, **31**, 1607–1613 (2018).

[121] I. Ali, M. U. Islam, M. S. Awan, and M. Ahmad, "Effects of Ga-Cr substitution on structural and magnetic properties of hexaferrite ($BaFe_{12}O_{19}$) synthesized by sol-gel auto-combustion route," *J. Alloys Compd.*, **547**, 118–125 (2013).

[122] J. Mohammed, T. Tchouank Tekou Carol, H. Y. Hafeez, D. Basandrai, G. R. Bhadu, S. K. Godara, S. B. Narang, and A. K. Srivastava, "Electromagnetic interference (EMI) shielding, microwave absorption, and optical sensing properties of BaM/CCTO composites in K u -band," *Results Phys.*, **13**, 102307 (2019).

[123] J. Sharma, A. Kumar, S. Kumar, and A. K. Srivastava, "Investigation of structural and magnetic properties of Tb–Ni-doped bismuth ferrite nanoparticles by auto-combustion method," *Appl. Phys. A Mater. Sci. Process.*, **123**, 522 (2017).

[124] M. J. Iqbal and S. Farooq, "Enhancement of electrical resistivity of $Sr_{0.5}Ba_{0.5}Fe_{12}O_{19}$ nanomaterials by doping with lanthanum and nickel," *Mater. Chem. Phys.*, **118**, 308–313 (2009).

[125] J. Mohammed, Tchouank Tekou Carol T., H. Y. Hafeez, D. Basandrai, G. R. Bhadu, S. K. Godara, S. B. Narang, A. K. Srivastava, "Design of nano-sized Pr^{3+}–Co^{2+}-substituted M-type strontium hexaferrites for optical sensing and electromagnetic interference (EMI) shielding in Ku band," *Appl. Phys. A*, **125**, 251 (2019).

[126] T. Kaur, S. Kumar, B. H. Bhat, B. Want, and A. K. Srivastava, "Effect on dielectric , magnetic , optical and structural properties of Nd–Co substituted barium hexaferrite nanoparticles," *Appl. Phys. A*, **119**, 1531–1540 (2015).

[127] R. S. Alam, M. Moradi, M. Rostami, H. Nikmanesh, R. Moayedi and Y. Bai, "Structural , magnetic and microwave absorption properties of doped Ba-hexaferrite nanoparticles synthesized by co-precipitation method," *J. Magn. Magn. Mater.*, **381**, 1–9 (2015).

[128] W. Y. Zhao, P. Wei, X. Y. Wu, W. Wang, and Q. J. Zhang, "Lattice vibration characterization and magnetic properties of M -type barium hexaferrite with excessive iron," *J. Appl. Phys.*, **103**, 063902 (2008).

[129] A. Morel, J. M. Le Breton, J. Kreisel, G. Wiesinger, F. Kools, and P. Tenaud, "Sublattice occupation in $Sr_{1-x}La_xFe_{12-x}Co_xO_{19}$ hexagonal ferrite analyzed by Mössbauer spectrometry and Raman spectroscopy," *J. Magn. Magn. Mater.*, **242–245**, 1405–1407 (2002).

[130] S. Anjum, M. Shahid Rafique, M. Khaleeq-Ur-Rahman, K. Siraj, A. Usman, S. I. Hussain, and S. Naseem, "Investigation of induced parallel magnetic anisotropy at low deposition temperature in Ba-hexaferrites thin films," *J. Magn. Magn. Mater.*, **324**, 711–716 (2012).

[131] M. Karmakar, B. Mondal, M. Pal, and K. Mukherjee, "Acetone and ethanol sensing of barium hexaferrite particles: A case study considering the possibilities of non-conventional hexaferrite sensor," *Sensors Actuators, B Chem.*, **190**, 627–633 (2014).

[132] T. Tekou Carol Trudel, J. Mohammed, H. Y. Hafeez, B. H. Bhat, S. K. Godara, and A. K. Srivastava, "Structural , Dielectric , and Magneto-Optical Properties of Al-Cr Substituted M-Type Barium Hexaferrite," *Phys. Status Solidi a*, **216**, 1800928 (2019).

[133] Y. Slimani, A. Baykal, Md. Amir, N. Tashkandi, H. Güngüneş, S. Guner, H. S. El Sayed, F. Aldakheel, T. A. Saleh, and A. Manikandan, "Substitution effect of Cr^{3+} on hyperfine interactions, magnetic and optical properties of Sr-hexaferrites," *Ceram. Int.*, **44**, 15995–16004 (2018).

[134] S. Ebrahimi, B. Yarmand, and N. Naderi, "Enhanced optoelectrical properties of Mn-doped ZnS films deposited by spray pyrolysis for ultraviolet detection applications,"

Thin Solid Films, **676**, 31–41 (2019).

[135] N. Khatun, E. G. Rini, P. Shirage, P. Rajput, S. N. Jha, and S. Sen, "Effect of lattice distortion on bandgap decrement due to vanadium substitution in TiO_2 nanoparticles," *Mater. Sci. Semicond. Process.*, **50**, 7–13 (2016).

[136] B. Choudhury, M. Dey, and A. Choudhury, "Defect generation , d-d transition , and band gap reduction in Cu-doped TiO_2 nanoparticles," *Int. nano Lett.*, **3**, 25 (2013).

[137] P. C. A. Brito, R. F. Gomes, J. G. S. Duque, and M. A. Macêdo, "$SrFe_{12}O_{19}$ prepared by the proteic sol-gel process," *Phys. B Condens. Matter*, **384**, 91–93 (2006).

[138] Z. F. Zi, Y. P. Sun, X. B. Zhu, Z. R. Yang, J. M. Dai, and W. H. Song, "Structural and magnetic properties of $SrFe_{12}O_{19}$ hexaferrite synthesized by a modified chemical co-precipitation method," *J. Magn. Magn. Mater.*, **320**, 2746–2751 (2008).

[139] D. H. Chen and Y. Y. Chen, "Synthesis of strontium ferrite nanoparticles by coprecipitation in the presence of polyacrylic acid," *Mater. Res. Bull.*, **37**, 801–810 (2002).

[140] M. Jean, V. Nachbaur, J. Bran, and J. M. Le Breton, "Synthesis and characterization of $SrFe_{12}O_{19}$ powder obtained by hydrothermal process," *J. Alloys Compd.*, **496**, 306–312 (2010).

[141] I. Ali, M. U. Islam, M. N. Ashiq, M. A. Iqbal, N. Karamat, M. S. Awan, and S. Naseem, "Role of Tb–Mn substitution on the magnetic properties of Y-type hexaferrites," *J. Alloys Compd.*, **599**, 131–138 (2014).

[142] S. Jauhar, J. Singh, K. Chandra, S. Bansal, and S. Singhal, "Structural, morphological, magnetic and optical properties of chromium substituted strontium ferrites, $SrCr_xFe_{12-x}O_{19}$ (x=0.5, 1.0, 1.5, 2.0 and 2.5) annealed with potassium halides," *Powder Technol.*, **212**, 193–197 (2011).

[143] I. A. Auwal, A. Baykal, H. Güngüneş, and S. E. Shirsath, "Structural investigation and hyperfine interactions of $BaBi_xLa_xFe_{12-2x}O_{19}$ ($0.0{\leq}x{\leq}0.5$) hexaferrites," *Ceram. Int.*, **42**, 3380–3387 (2016).

[144] S. Shakoor, M. N. Ashiq, M. A. Malana, A. Mahmood, M. F. Warsi, M. Najam-Ul-Haq, and N. Karamat, "Electrical, dielectric and magnetic characterization of Bi-Cr

substituted M-type strontium hexaferrite nanomaterials," *J. Magn. Magn. Mater.*, **362**, 110–114 (2014).

[145] P. Xu, X. Han, and M. Wang, "Synthesis and magnetic properties of $BaFe_{12}O_{19}$ hexaferrite nanoparticles by a reverse microemulsion technique," *J. Phys. Chem. C*, **111**, 5866–5870 (2007).

[146] K. M. Batoo, S. Kumar, C. G. Lee, and Alimuddin, "Influence of Al doping on electrical properties of Ni-Cd nano ferrites," *Curr. Appl. Phys.*, **9**, 826–832 (2009).

[147] F. M. M. Pereira, M. R. P. Santos, R. S. T. M. Sohn, J. S. Almeida, A. M. L. Medeiros, M. M. Costa, and A. S. B. Sombra, "Magnetic and dielectric properties of the M-type barium strontium hexaferrite ($Ba_xSr_{1-x}Fe_{12}O_{19}$) in the RF and microwave (MW) frequency range," *J. Mater. Sci. Mater. Electron.*, **20**, 408–417 (2009).

[148] M. Anis-Ur-Rehman and G. Asghar, "Variation in structural and dielectric properties of co-precipitated nanoparticles strontium ferrites due to value of pH," *J. Alloys Compd.*, **509**, 435–439 (2011).

[149] K. Iwauchi, "Dielectric properties of fine particles of fe3o4and some ferrites," *Jpn. J. Appl. Phys.*, **10**, 1520 (1971).

[150] N. Rezlescu and E. Rezlescu, "Dielectric properties of copper containing ferrites," *Phys. Status Solidi (a)*, **23**, 575–582 (1974).

[151] I. Ali, M. U. Islam, M. S. Awan, and M. Ahmad, "Effects of Heat-Treatment Time on the Structural , Dielectric , Electrical , and Magnetic Properties of BaM Hexaferrite," *J. Mater. Eng. Perform.*, **22**, 2104–2114 (2013).

[152] R. Tang, C. Jiang, W. Qian, J. Jian, X. Zhang, H. Wang, and H. Yang, "Dielectric relaxation, resonance and scaling behaviors in $Sr_3Co_2Fe_{24}O_{41}$ hexaferrite," *Sci. Rep.*, **5**, 13645 (2015).

[153] M. F. Mostafa, M. M. Abdel-Kader, A. S. Atallah, and M. El-Nimer, "AC Dielectric and Conductivity Studies of a Perovskite Magnetic Insulator," *Phys. Status Solidi (a)*, **135**, 549–556 (1993).

[154] M. A. El Hiti, "Dielectric behavior and ac electrical conductivity of Zn-substituted Ni-Mg ferrites," *J. Magn. Magn. Mater.*, **164**, 187–196 (1996).

[155] A. M. A. El Ata, M. K. El Nimr, S. M. Attia, D. El Kony, and A. H. Al-Hammadi, "Studies of AC electrical conductivity and initial magnetic permeability of rare-earth-substituted Li-Co ferrites," *J. Magn. Magn. Mater.*, **297**, 33–43 (2006).

[156] R. Pattanayak, S. Panigrahi, T. Dash, R. Muduli, and D. Behera, "Electric transport properties study of bulk $BaFe_{12}O_{19}$ by complex impedance spectroscopy," *Phys. B Condens. Matter*, **474**, 57–63 (2015).

[157] E. Iguchi, N. Nakamura, and A. Aoki, "Electrical transport properties in semiconducting bapbxbi1-x03 using complex-plane impedance analyses," *J. Phys. Chem Solids*, **58**, 755–763 (1997).

[158] S. Zawar, S. Atiq, M. Tabasum, S. Riaz, and S. Naseem, "Highly stable dielectric frequency response of chemically synthesized Mn-substituted $ZnFe_2O_4$," *J. Saudi Chem. Soc.*, **23**, 417-426 (2019).

[159] Y. Song, J. Zheng, M. Sun, and S. Zhao, "The electromagnetic and microwave absorbing properties over the microwave range," *J. Mater. Sci. Mater. Electron.*, **27**, 4131–4138 (2016).

[160] R. B. Jotania and P. A. Patel, "Microstructure and Dielectric Properties of Mn Substituted $Sr_2Cu_2Fe_{12}O_{22}$ (Cu_2Y) Hexaferrite Powder," *Int. J. Eng. Res. Appl.*, **2**, 494–498 (2012).

[161] D. Basandrai, R. K. Bedi, A. Dhami, J. Sharma, S. B. Narang, K. Pubby, A. Gupta, and A. K. Srivastava, "Aluminum and chromium substituted Z-type hexaferrites for antenna and microwave absorber applications," *J. Sol-Gel Sci. Technol.*, vol. **85**, 59–65 (2018).

[162] M. Zhang, J. Dai, L. Yin, X. Kong, Q. Liu, Z. Zi, and Y. Sun, "Mg doping effect on the magnetic properties of Y-type hexaferrite $Ba_{0.5}Sr_{1.5}Zn_{2-x}Mg_xFe_{12}O_{22}$," *J. Alloys Compd.*, **689**, 75–80 (2016).

[163] S. Ounnunkad, "Improving magnetic properties of barium hexaferrites by La or Pr substitution," *Solid State Commun.*, **138**, 472–475 (2006).

[164] M. J. Iqbal and F. Liaqat, "Physical and Electrical Properties of Nanosized Mn- and Cr-Doped Strontium Y-Type Hexagonal Ferrites," *J. Am. Ceram. Soc.*, **93**, 474–480

(2010).

[165] S. C. Mazumdar and A. K. M. A. Hossain, "Synthesis and Magnetic Properties of $Ba_2Ni_{2-x}Zn_xFe_{12}O_{22}$ Hexaferrites," *World J. Condens. Matter Phys.*, **2**, 181–187 (2012).

[166] I. Ali, M. Ahmad, M. U. Islam and M. S. Awan, "Substitution effects of La^{3+} ions on the structural and magnetic properties of Co_2Y hexaferrites synthesized by sol–gel autocombustion method," *J. sol-gel Sci. Technol.*, **68**, 141–149 (2013).

[167] S. H. Mahmood, F. S. Jaradat, A.-F. Lehlooh, and A. Hammoudeh, "Structural properties and hyper fi ne interactions in Co–Zn Y-type hexaferrites prepared by sol–gel method," *Ceram. Int.*, **40**, 5231–5236 (2014).

[168] S. Bierlich and J. Töpfer, "Zn- and Cu-substituted Co_2Y hexagonal ferrites : Sintering behavior and permeability," *J. Magn. Magn. Mater.*, **324**, 1804–1808 (2012).

[169] G.F.M.PiresJúnior, H. O. Rodrigues, J. S. Almeida, E. O. Sancho, J. C. Góes, M. M. Costa, J. C. Denardin, A. S. B. Sombra, "Study of the dielectric and magnetic properties of Co_2Y, Y-type hexaferrite ($Ba_2Co_2Fe_{12}O_{22}$) added with PbO and Bi_2O_3 in the RF frequency range," **493**, 326–334 (2010).

[170] E. Wichers, "Report of the Committee on Atomic Weights of the American Chemical Society," *J. Am. Chem. Soc.*, **74**, 2447–2450 (1952).

[171] N. Adeela, U. Khan, M. Iqbal, S. Riaz, M. Irfan, H. Ali, K. Javed, I. Bukhtiar, K. Maaz, and S. Naseem, "Structural and magnetic response of Mn substituted Co_2 Y-type barium hexaferrites," *J. Alloys Compd.*, **686**, 1017–1024 (2016).

[172] I. Ali, M. U. Islam, M. S. Awan, M. Ahmad, M. N. Ashiq, and S. Naseem, "Effect of Tb^{3+} substitution on the structural and magnetic properties of M-type hexaferrites synthesized by sol–gel auto-combustion technique," *J. Alloys Compd.*, **550**, 564–572 (2013).

[173] H. Khanduri, M. C. Dimri, H. Kooskora, I. Heinmaa, G. Viola, H. Ning, M. J. Reece, J. Krustok, and R. Stern, "Structural , dielectric , magnetic , and nuclear magnetic resonance studies of multiferroic Y-type hexaferrites Structural , dielectric , magnetic , and nuclear magnetic resonance studies," *J. Appl. Phys.*, **112**, 073903 (2012).

[174] O. Mirzaee, R. Mohamady, A. Ghasemi, and Y. A. Farzin, "Study of the magnetic and structural properties of Al-Cr codoped Y-type hexaferrite prepared via sol gel auto-combustion method," *Int. J. Mod. Phys. B*, **29**, 1550090 (2015).

[175] I. A. Auwal, A. Baykal, S. Güner, and H. Sözeri, "Magneto-optical properties of $SrBi_xLa_xFe_{12-2x}O_{19}$ (0.0≤x≤0.5) hexaferrites by sol-gel auto-combustion technique," *Ceram. Int.*, **43**, 1298–1303 (2017).

[176] A. Baykal, H. Güngüneş, H. Sözeri, Md. Amir, I. Auwal, S. Asiri, S. E. Shirsath, and A. Demir Korkmaz, "Magnetic properties and Mössbauer spectroscopy of Cu-Mn substituted $BaFe_{12}O_{19}$ hexaferrites," *Ceram. Int.*, **43**, 15486–15492 (2017).

[177] T. Koutzarova, S. Kolev, I. Nedkov, K. Krezhov, D. Kovacheva, B. Blagoev, C. Ghelev, C. Henrist, R. Cloots, and A. Zaleski, "Magnetic Properties of Nanosized $Ba_2Mg_2Fe_{12}O_{22}$ Powders Obtained by Auto-combustion," *J. Supercond. Nov. Magn.*, **25**, 2631–2635 (2012).

[178] M. Ahmad, M. Ahmad, I. Ali, W. Ahmad, G. Mustafa, M. N. Akhtar, A. Ali, G. Abbas, and M. ud-Din Rana, "Temperature dependent structural and magnetic behavior of Y-type hexagonal ferrites synthesized by sol-gel autocombustion," *J. Alloys Compd.*, **651**, 749–755 (2015).

[179] G. Murtaza, R. Ahmad, T. Hussain, R. Ayub, I. Ali, M. A. Khan, and M. N. Akhtar, "Structural and magnetic properties of Nd–Mn substituted Y-type hexaferrites synthesized by microemulsion method," *J. Alloys Compd.*, **602**, 122–129 (2014).

[180] Y. Bai, J. Zhou, Z. Gui, L. Li, and L. Qiao, "The physic properties of Bi–Zn codoped Y-type hexagonal ferrite," *J. Alloys Compd.*, **450**, 412–416 (2008).

[181] J. T. Lim, M. H. Won, T. Kouh, and C. S. Kim, "Mossbauer Studies of Y-type Hexaferrite with Aluminum Doping," *J. Korean Phys. Soc.*, **62**, 1815-1818 (2013).

[182] G. Albanese, M. Carbucicchio, A. Deriu, G. Asti, and S. Rinaldi, "Influence of the Cation Distribution on the Magnetization of Y-type Hexagonal Ferrites," *Appl. Phys.*, **7**, 227–238 (1975).

[183] A. Nikzad, A. Ghasemi, M. K. Tehrani, and G. R. Gordani, "Y-Type Strontium Hexaferrite : the Role of Al Substitution , Structural , and Magnetic Consequence," *J.*

Supercond. Nov. Magn., **28**, 3579–3586 (2015).

[184] I. Ali, M. U. Islam, I. Sadiq, N. Karamat, A. Iftikhar, and M. Azhar Khan, A. shah, M. Athar, I. Shakir, and M. N. Ashiq, "Synthesis and magnetic properties of (Eu–Ni) substituted Y-type hexaferrite by surfactant assisted co-precipitation method," *J. Magn. Magn. Mater.*, **385**, 386-393 (2015).

[185] X. Liu, W. Zhong, S. Yang, Z. Yu, B. Gu, and Y. Du, "Structure and magnetic properties of La^{3+}-substituted strontium hexaferrite particles prepared by sol-gel method," *Phys. Status Solidi Appl. Res.*, **193**, 314–319 (2002).

[186] J. Xu, G. Ji, H. Zou, Y. Zhou, and S. Gan, "Structural, dielectric and magnetic properties of Nd-doped Co_2Z-type hexaferrites," *J. Alloys Compd.*, **509**, 4290–4294 (2011).

[187] M. J. Chua, Z. H. Yang, and Z. W. Li, "Structural and microwave attenuation characteristics of ZnCuY barium ferrites synthesized by a sol–gel auto combustion method," *J. Magn. Magn. Mater.*, **368**, 19-24 (2014).

[188] A. Globus and M. Guyot, "Wall Displacement and Bulging in Magnetization Mechanisms of the Hysteresis Loop," *Phys. status solidi b*, **52**, 427–431 (1972).

[189] I. Odeh, H. M. El Ghanem, S. H. Mahmood, S. Azzam, I. Bsoul, and A-F. Lehlooh, "Dielectric and magnetic properties of Zn-substituted Co_2Y barium hexaferrite prepared by sol–gel auto combustion method," *Phys. B Phys. Condens. Matter*, **494**, 33–40 (2016).

[190] D. Ravinder and P. Vijaya Bhasker Reddy, "High-frequency dielectric behaviour of Li-Mg ferrites," *Mater. Lett.*,. **57**, 4344–4350 (2003).

[191] A. Elahi, M. Ahmad, I. Ali, and M. U. Rana, "Preparation and properties of sol–gel synthesized Mg-substituted Ni_2Y hexagonal ferrites," *Ceram. Int.*, vol. **39**, 983–990 (2013).

[192] V. V Warhate and D. S. Badwaik, "The Structural , Dielectric and AC Conductivity Studies of TiCo Substituted Sr2NiZn Y-Type Hexa Nanoferrites," *Iinternational J. Sci. Res.*, 22–24 (2015).

[193] M. Wu, L. Liu, X. Gao, and Z. Liu, "Electric and magnetic properties of Y-type

Ba$_2$Mg$_2$Fe$_{12}$O$_{22}$ hexaferrites with various Co doping," *J. Mater. Sci. Mater. Electron.*, **27**, 10516-10524 (2016).

[194] J. Mohammed, I. I. Garba, K. U. Yerima, A. Muhammad, U. F. Zulfatu, M. S. Abubakar, J. Sharma, T. Tchouank Tekou Carol, S. Kumar, and A. K. Srivastava, "Structural and Dielectric Properties of Polycrystalline Calcium Copper Titanate (CCTO)," *Adv. manufacturing and Mat. Sci.*, 369-378 (2018).

[195] P. Kum-onsa, P. Thongbai, B. Putasaeng, T. Yamwong, and S. Maensiri, "Na$_{1/3}$Ca$_{1/3}$Bi$_{1/3}$Cu$_3$Ti$_4$O$_{12}$: A new giant dielectric perovskite ceramic in ACu3Ti4O12compounds," *J. Eur. Ceram. Soc.*, **35**, 1441–1447 (2015).

[196] P. Liang, X. Wang, X. Chao, and Z. Yang, "Electric response and improved dielectric properties in BiCu$_3$Ti$_3$FeO$_{12}$," *J. Alloys Compd.*, **734**, 9–15, (2018).

[197] R. Kashyap, R. K. Mishra, O. P. Thakur, and R. P. Tandon, "Structural, dielectric properties and electrical conduction behaviour of Dy substituted CaCu$_3$Ti$_4$O$_{12}$ ceramics," *Ceram. Int.*, **38**, 6807–6813 (2012).

[198] L. Singh, I. W. Kim, B. C. Sin, S. K. Woo, S. H. Hyun, K. D. Mandal, and Y. Lee, "Combustion synthesis of nano-crystalline Bi$_{2/3}$Cu$_3$Ti$_{2.90}$Fe$_{0.10}$O$_{12}$ using inexpensive TiO2 raw material and its dielectric characterization," *Powder Technol.*, **280**, 256–265 (2015).

[199] X. Huang, H. Zhang, M. Wei, Y. Lai, and J. Li, "Effect of semiconductive grain and microstructure on the dielectric properties of CaCu$_3$Ti$_4$O$_{12}$ceramics with Sr^{2+} doping," *J. Alloys Compd.*, **708**, 1026–1032 (2017).

[200] A. Thakur, R. R. Singh, and P. B. Barman, "Synthesis and characterizations of Nd^{3+} doped SrFe$_{12}$O$_{19}$ nanoparticles," *Mater. Chem. Phys.*, **141**, 562–569 (2013).

[201] M. Ahmad, F. Aen, M. U. Islam, S. B. Niazi, and M. U. Rana, "Structural, physical, magnetic and electrical properties of La-substituted W-type hexagonal ferrites," *Ceram. Int.*, **37**, 3691–3696 (2011).

[202] A. F. L. Almeida, R. S. De Oliveira, J. C. Góes, J. M. Sasaki, A. G. Souza Filho, J. Mendes Filho, and A. S. B. Sombra, "Structural properties of CaCu$_3$Ti$_4$O$_{12}$ obtained by mechanical alloying," *Mater. Sci. Eng. B*, **96**, 275–283 (2002).

[203] R. Sankar Ganesh, S. K. Sharma, N. Abinnas, E. Durgadevi, P. Raji, S. Ponnusamy, C. Muthamizhchelvan, Y. Hayakawa, and D. Y. Kim, "Fabrication of the flexible nanogenerator from BTO nanopowders on graphene coated PMMA substrates by sol-gel method," *Mater. Chem. Phys.*, **192**, 274–281 (2017).

[204] R. A. Golda, A. Marikani, and D. P. Padiyan, "Mechanical synthesis and characterization of $Bi_4Ti_3O_{12}$ nanopowders," *Ceram. Int.*, **37**, 3731–3735 (2011).

[205] L. Singh, I. W. Kim, B. C. Sin, K. D. Mandal, U. S. Rai, A. Ullah, H. Chung, and Y. Lee, "Dielectric studies of a nano-crystalline $CaCu_{2.90}Zn_{0.10}Ti_4O_{12}$ electro-ceramic by one pot glycine assisted synthesis from inexpensive TiO_2 for energy storage capacitors," *RSC Adv.*, **4**, 52770–52784 (2014).

[206] S. Jesurani, S. Kanagesan, R. Velmurugan, C. Thirupathi, M. Sivakumar, and T. Kalaivani, "Nanoparticles of the giant dielectric material, calcium copper titanate from a sol-gel technique," *Mater. Lett.*, **65**, 3305–3308 (2011).

[207] M. Feng, X. Huang, H. Tang, and X. Liu, "Effects of surface modification on interfacial and rheological properties of CCTO/PEN composite films," *Colloids Surfaces A Physicochem. Eng. Asp.*, **441**, 556–564 (2014).

[208] A. Sadeghzadeh Attar, E. Salehi Sichani, and S. Sharafi, "Structural and dielectric properties of Bi-doped barium strontium titanate nanopowders synthesized by sol-gel method," *J. Mater. Res. Technol.*, **6**, 108–115 (2017).

[209] N. Kolev, R. P. Bontchev, A. J. Jacobson, V. N. Popov, V. G. Hadjiev, A. P. Litvinchuk, and M. N. Iliev, "Raman spectroscopy of $CaCu_3Ti_4O_{12}$," *Phys. Rev. B*, **66**, 132102 (2002).

[210] R. Parra, R. Savu, L. A. Ramajo, M. A. Ponce, J. A. Varela, M. S. Castro, P. R. Bueno, and E. Joanni, "Sol-gel synthesis of mesoporous $CaCu_3Ti_4O_{12}$ thin films and their gas sensing response," *J. Solid State Chem.*, **183**, 1209–1214 (2010).

[211] C. Mu, Y. Song, H. Wang, and X. Wang, "Room temperature magnetic and dielectric properties of cobalt doped $CaCu_3Ti_4O_{12}$ ceramics," *J. Appl. Phys.*, **117**, 17B723 (2015).

[212] R. Bhargava and S. Khan, "Enhanced optical properties of Cu_2O anchored on reduced

graphene oxide (rGO) sheets," *J. Phys. Condens. Matter*, **30**, 335703 (2018).

[213] M. M. Rashad, A. O. Turky, and A. T. Kandil, "Optical and electrical properties of $Ba_{1-x}Sr_xTiO_3$ nanopowders at different Sr^{2+} ion content," *J. Mater. Sci. Mater. Electron.*, **24**, 3284–3291 (2013).

[214] R. Keshav, M. Padiyar, N. Meghana, and M. G. Mahesha, "Analysis of PV deposited ZnTe thin films through Urbach tail and photoluminescence spectroscopy," *J. Lumin.*, **194**, 257–263 (2018).

[215] A. A. Akl and S. A. Mahmoud, "Optik Effect of growth temperatures on the surface morphology , optical analysis , dielectric constants , electric susceptibility , Urbach and bandgap energy of sprayed NiO thin fi lms," *Opt. - Int. J. Light Electron Opt.*, **172**, 783–793 (2018).

[216] S. Jesurani, S. Kanagesan, R. Velmurugan, and T. Kalaivani, "Phase formation and high dielectric constant of calcium copper titanate using sol-gel route," *J. Mater. Sci. Mater. Electron.*, **23**, 668–674 (2012).

[217] M. J. Iqbal, M. N. Ashiq, and I. H. Gul, "Physical, electrical and dielectric properties of Ca-substituted strontium hexaferrite ($SrFe_{12}O_{19}$) nanoparticles synthesized by co-precipitation method," *J. Magn. Magn. Mater.*, **322,** 1720–1726 (2010).

[218] P. Liu, Y. Lai, Y. Zeng, S. Wu, Z. Huang, and J. Han, "Influence of sintering conditions on microstructure and electrical properties of $CaCu_3Ti_4O_{12}$ (CCTO) ceramics," *J. Alloys Compd.*, **650**, 59–64 (2015).

[219] Z. Liu, G. Jiao, X. Chao, and Z. Yang, "Preparation, microstructure, and improved dielectric and nonlinear electrical properties of $Na_{1/2}La_{1/2}Cu_3Ti_4O_{12}$ ceramics by sol–gel method," *Mater. Res. Bull.*, **48**, 4877–4883 (2013).

[220] L. Singh, U. S. Rai, K. D. Mandal, and N. B. Singh, "Progress in the growth of $CaCu_3Ti_4O_{12}$ and related functional dielectric perovskites," *Prog. Cryst. Growth Charact. Mater.*, **60**, 15–62 (2014).

[221] J. Liu, C. G. Duan, and W. N. Mei, "Dielectric properties and Maxwell-Wagner relaxation of compounds $ACu_3Ti_4O_{12}$ ($A=Ca,Bi_{2/3},Y_{2/3},La_{2/3}$)," *J. Appl. Phys.*, **98**, 093703 (2005).

[222] S. El Kossi, F. I. H. Rhouma, J. Dhahri, and K. Khirouni, "Structural and electric properties of $La_{0.7}Sr_{0.25}Na_{0.05}Mn_{0.9}T_{i0.1}O_3$ ceramics," *Phys. B Condens. Matter*, **440**, 118–123 (2014).

[223] T. Ben Ghzaiel, W. Dhaoui, F. Schoenstein, P. Talbot, and F. Mazaleyrat, "Substitution effect of Me = Al, Bi, Cr and Mn to the microwave properties of polyaniline/BaMeFe11O19for absorbing electromagnetic waves," *J. Alloys Compd.*, **692**, 774–786 (2017).

[224] H. M. Kuo, T. F. Hsui, Y. S. Tuo, and C. L. Yuan, "Microwave adsorption of core-shell structured $Sr(MnTi)_xFe_{12-2x}O_{19}$/PANI composites," *J. Mater. Sci.*, **47**, 2264–2270 (2012).

[225] P. Saini, V. Choudhary, B. P. Singh, R. B. Mathur, and S. K. Dhawan, "Polyaniline-MWCNT nanocomposites for microwave absorption and EMI shielding," *Mater. Chem. Phys.*, **113**, 919–926 (2009).

[226] J. Deng, C. He, Y. Peng, J. Wang, X. Long, P. Li, and A. S. C. Chan, "Magnetic and conductive Fe_3O_4–polyaniline nanoparticles with core–shell structure," *Synthetic Metals*, **139**, 295–301 (2003).

[227] A. Mostafaei and A. Zolriasatein, "Synthesis and characterization of conducting polyaniline nanocomposites containing ZnO nanorods," *Prog. Nat. Sci. Mater. Int.*, **22**, 273–280 (2012).

[228] T. H. Ting, R. P. Yu, and Y. N. Jau, "Synthesis and microwave absorption characteristics of polyaniline / NiZn ferrite composites in 2 – 40 GHz," **126**, 364–368 (2011).

[229] P. K. Khanna, N. Singh, S. Charan, and A. K. Viswanath, "Synthesis of Ag/polyaniline nanocomposite via an in situ photo-redox mechanism," *Mater. Chem. Phys.*, **92**, 214–219 (2005).

[230] P. Thomas, K. Dwarakanath, and K. B. R. Varma, "In situ synthesis and characterization of polyaniline-$CaCu_3Ti_4O_{12}$ nanocrystal composites," *Synth. Met.*, **159**, 2128–2134 (2009).

[231] P. Gautam, A. Khare, S. Sharma, N. B. Singh, and K. D. Mandal, "Characterization of

$Bi_{2/3}Cu_3Ti_4O_{12}$ ceramics synthesized by semi-wet route," *Prog. Nat. Sci. Mater. Int.*, **26**, 567–571 (2016).

[232] X. Liu, W. Zhong, S. Yang, Z. Yu, B. Gu, and Y. Du, "Influences of La^{3+} substitution on the structure and magnetic properties of M-type strontium ferrites," *J. Magn. Magn. Mater.*, **238**, 207–214 (2002).

[233] A. Thakur, R. R. Singh, and P. B. Barman, "Structural and magnetic properties of La^{3+} substituted strontium hexaferrite nanoparticles prepared by citrate precursor method," *J. Magn. Magn. Mater.*, **326**, 35–40 (2013).

[234] B. Tian and G. Zerbi, "Lattice dynamics and vibrational spectra of polypyrrole," *J. Chemical Physics*, **92**, 3886 (1990).

[235] F. Moura, A. Z. Simões, R. C. Deus, M. R. Silva, J. A. Varela, and E. Longo, "Intense photoluminescence emission at room temperature in calcium copper titanate powders," *Ceram. Int.*, **39**, 3499–3506 (2012).

[236] S. Pongpaiboonkul, D. Phokharatkul, J. H. Hodak, A. Wisitsoraat, and S. K. Hodak, "Enhancement of H_2S-sensing performances with Fe-doping in $CaCu_3Ti_4O_{12}$ thin films prepared by a sol-gel method," *Sensors Actuators, B Chem.*, **224**, 118–127 (2016).

[237] H. R. Virdee and R. E. Hester, "In situ resonance Raman spectroscopic investigation of a polypyrrole modified gold electrode," *Croat. Chem. Acta*, **61**, 357–374 (1988).

[238] H. N. T. Le, M. C. Bernard, B. Garcia-Renaud, and C. Deslouis, "Raman spectroscopy analysis of polypyrrole films as protective coatings on iron," *Synth. Met.*, **140**, 287–293 (2004).

[239] S. Biswas and L. T. Drzal, "Multilayered nanoarchitecture of graphene nanosheets and polypyrrole nanowires for high performance supercapacitor electrodes," *Chem. Mater.*, **22**, 5667–5671 (2010).

[240] S. Ghosh, G. A. Bowmaker, R. P. Cooney, and J. M. Seakins, "Infrared and Raman spectroscopic studies of the electrochemical oxidative degradation of polypyrrole," *Synth. Met.*, **95**, 63–67 (1998).

[241] C. J. Zhong, Z. Q. Tian, Z. W. Tian, "In Sltu Electron Spin Resonance and Raman Spectroscopic Studies of the Electrochemical Process of Conducting Polypyrrole

Films," *J. Phys. Chem.*, **94**, 2171–2175 (1990).

[242] Y. C. Liu, B. J. Hwang, W. J. Jian, and R. Santhanam, "In situ cyclic voltammetry-surface-enhanced Raman spectroscopy: Studies on the doping-undoping of polypyrrole film," *Thin Solid Films*, **374**, 85–91 (2000).

[243] Y. Furukawa, S. Tazawa, Y. Fujii, and I. Harada, "Raman spectra of polypyrrole and its 2,5-13C-substituted and C-deuterated analogues in doped and undoped states," *Synth. Met.*, **24**, 329–341 (1988).

[244] C. Selvaraj, S. Kumar, N. Munichandraiah, and L. G. Scanlon, "Reduced Graphene Oxide-Polypyrrole Composite as a Catalyst for Oxygen Electrode of High Rate Rechargeable Li-O$_2$ Cells," *J. Electrochem. Soc.*, **161**, 554–560 (2014).

[245] S. J. Vigmond, V. Ghaemmaghami, and M. Thompson, "Raman and resonance-Raman spectra of polypyrrole with application to sensor–gas probe interactions," *Can. J. Chem.*, **73**, 1711–1718 (2006).

[246] K. Bukowska, J.; Jackowska, "In situ raman studies of polypyrrole and polypyrrole films," *Synth. Met.*, **35**, 143–150 (1990).

[247] S. Lee, K. Y. Shin, and J. Jang, "Enhanced magnetorheological performance of highly uniform magnetic carbon nanoparticles," *Nanoscale*, **7**, 9646–9654 (2015).

[248] A. Hojjati-Najafabadi, A. Ghasemi, and R. Mozaffarinia, "Magneto-electric features of BaFe$_{9.5}$Al$_{1.5}$CrO$_{19}$-CaCu$_3$Ti$_4$O$_{12}$ nanocomposites," *Ceram. Int.*, **43**, 244–249 (2017).

[249] A. H. Najafabadi, A. Ghasemi, and R. Mozaffarinia, "Development of novel magnetic-dielectric ceramics for enhancement of reflection loss in X band," *Ceram. Int.*, **42**, 13625–13634 (2016).

[250] A. Khare, S. S. Yadava, P. Gautam, N. K. Mukhopadhyay, and K. D. Mandal "Effect of sintering on the dielectric properties of 0.5BaTiO$_3$-0.5Bi$_{2/3}$Cu$_3$Ti$_4$O$_{12}$ nanocomposite synthesized by solid state route," *J. Mat. Sci.: Mat. Electro.*, **28**, 5523-5530 (2017).

[251] K. Raghava Reddy, K. Pill Lee, and A. Iyengar Gopalan, "Self-assembly approach for the synthesis of electro-magnetic functionalized Fe3O4/polyaniline nanocomposites: Effect of dopant on the properties," *Colloids Surfaces A Physicochem. Eng. Asp.*, **320**,

49–56 (2008).

[252] N. Roosz, M. Euvrard, B. Lakard, and L. Viau, "A straightforward procedure for the synthesis of silica @ polyaniline core- shell nanoparticles," *Colloids Surfaces A Physicochem. Eng. Asp.*, **573**, 237–245 (2019).

[253] M. Jinish Antony, C. Albin Jolly, K. Rohini Das, and T. S. Swathy, "Normal and reverse AOT micelles assisted interfacial polymerization for polyaniline nanostructures," *Colloids Surfaces A Physicochem. Eng. Asp.*, **578**, 123627 (2019).

[254] V. Pratap, A. K. Soni, S. Dayal, S. M. Abbas, A. M. Siddiqui, and N. E. Prasad, "Electromagnetic and absorption properties of U-type barium hexaferrite- epoxy composites," *J. Magn. Magn. Mater.*, **465**, 540–545 (2018).

[255] J. Zhou, Z. Yao, and T. Yao, "Synthesis and electromagnetic property of $Li_{0.35}Zn_{0.3}Fe_{2.35}O_4$ grafted with polyaniline fibers," *Appl. Surf. Sci.*, **420**, 154–160 (2017).

[256] Y. Wang, Y. Huang, Q. Wang, Q. He, and L. Chen, "Preparation and electromagnetic properties of Polyaniline(polypyrrole)-$BaFe_{12}O_{19}$/$Ni_{0.8}Zn_{0.2}Fe_2O_4$ ferrite nanocomposites," *Appl. Surf. Sci.*, **259**, 486–493 (2012).

[257] X. Tang and Y. Yang, "Surface modification of M-Ba-ferrite powders by polyaniline: Towards improving microwave electromagnetic response," *Appl. Surf. Sci.*, **255**, 9381–9385 (2009).

[258] G. P. Karpacheva, "Hybrid Magnetic Nanocomposites Containing Polyconjugated Polymers," *Polym. Sci. Ser. C*, **58**, 131–146 (2016).

[259] C. Zhao, M. Shen, Z. Li, R. Sun, A. Xia, and X. Liu, "Green synthesis and enhanced microwave absorption property of reduced graphene oxide-SrFe 12 O 19 nanocomposites," *J. Alloys Compd.*, **689**, 1037–1043 (2016).

[260] H. Cheng, S. Wei, Y. Ji, J. Zhai, X. Zhang, and J. Chen, C. Shen, "Synergetic e ffect of Fe_3O_4 nanoparticles and carbon on fl exible poly (vinylidene fluoride) based fi lms with higher heat dissipation to improve electromagnetic shielding," *Compos. Part A*, **121**, 139–148 (2019).

[261] H. Feng, D. Bai, L. Tan, N. Chen, and Y. Wang, "Preparation and microwave-

absorbing property of EP/BaFe$_{12}$O$_{19}$/PANI composites," *J. Magn. Magn. Mater.*, **433**, 1–7 (2017).

[262] T. Kuang, L. Chang, F. Chen, Y. Sheng, D. Fu, and X. Peng, "Facile preparation of lightweight high-strength biodegradable polymer/multi-walled carbon nanotubes nanocomposite foams for electromagnetic interference shielding," *Carbon*, **105**, 305–313 (2016).

[263] J. Prasad, A. K. Singh, J. Shah, R. K. Kotnala, and K. Singh, "Synthesis of MoS2-reduced graphene oxide/Fe$_3$O$_4$ nanocomposite for enhanced electromagnetic interference shielding effectiveness," *Mater. Res. Express*, **5**, 055028 (2018).

[264] X. Ma, B. Shen, L. Zhang, Y. Liu, W. Zhai, W. Zheng, "Porous superhydrophobic polymer / carbon composites for lightweight and self-cleaning EMI shielding application," *Compos. Sci. Technol.*, **158**, 86–93 (2018).

[265] H. Yang, Z. Yu, P. Wu, H. Zou, and P. Liu, "Electromagnetic interference shielding effectiveness of microcellular polyimide/in situ thermally reduced graphene oxide/carbon nanotubes nanocomposites," *Appl. Surf. Sci.*, **434**, 318–325 (2018).

[266] A. Ameli, P. U. Jung, and C. B. Park, "Electrical properties and electromagnetic interference shielding effectiveness of polypropylene/carbon fiber composite foams," *Carbon*, **60**, 379–391 (2013).

List of publications

1. **<u>Tchouank Tekou Carol T.</u>**, <u>J. Mohammed</u>, Bilal Hamid Bhat, H. Y. Hafeez, Sachin Kumar Godara, **<u>A. K. Srivastava</u>**, "Structural, dielectric, and magneto-optical properties Al-Cr substituted M-type Barium Hexaferrite", *Phys. Status Solidi Appl. Mater. Sci*., **Impact Factor: 1.795**

   DOI: https://doi.org/10.1002/pssa.201800928

View online: https://onlinelibrary.wiley.com/doi/abs/10.1002/pssa.201800928

2. **<u>Tchouank Tekou Carol T.</u>**, J. Mohammed, Bilal Hamid Bhat, Sanjay Mishra, Sachin Kumar Godara, **<u>A. K. Srivastava</u>**, "Effect of Cr-Bi substitution on the structural, optical, electrical and magnetic properties of strontium hexaferrites", Physica B: Physics of condensed matter, **Impact Factor: 1.874**

   DOI: https://doi.org/10.1016/j.physb.2019.411681

View online: https://www.sciencedirect.com/science/article/abs/pii/S0921452619305745

3. **<u>Tchouank Tekou Carol T.</u>**, J. Mohammed, Richa Bhargava, Shakeel Khan, Sanjay Mishra, Sachin Kumar Godara, **<u>A. K. Srivastava</u>**, "Crystal structure refinement, optical properties, dielectric and impedance spectroscopy of Ni^{2+}-Co^{2+} substituted bismuth copper titanate (BCTO)", Materials Chemistry and Physics, **Impact Factor: 2.781**

   DOI: https://doi.org/10.1016/j.matchemphys.2020.122933

View online: https://www.sciencedirect.com/science/article/abs/pii/S0254058420303102

4. **<u>Tchouank Tekou Carol T.</u>**, J. Mohammed, D. Basandrai, Sachin Kumar Godara, Gopala R. Bhadu, Sanjay Mishra, Neha Aggarwal, S.B. Narang, **<u>A. K. Srivastava</u>**, "X-band Shielding of Electromagnetic Interference (EMI) by Co_2Y Barium Hexaferrite, Bismuth Copper Titanate (BCTO), and Polyaniline (PANI) composite", Journal of Magnetism and magnetic Materials, **Impact Factor: 2.683**

   DOI: 10.1016/j.jmmm.2020.166433

View online: https://ui.adsabs.harvard.edu/abs/2020JMMM..50166433T/abstract

Other papers

1. Effect of Cr-Ni substitution on optical, electrical and magnetic properties of Co_2Y barium hexaferrites (Under review)

2. Structural, magnetic and optical properties of combination of Hexagonal ferrite, bismuth copper titanate and polypyrrole (To be communicated)

Oral presentation (conference proceedings)

1. **Tchouank Tekou Carol T.**, Jyoti Sharma, J. Mohammed, Sachin Kumar, and **A. K. Srivastava**, "Effect of temperature on the magnetic properties of nano-sized M-type barium hexagonal ferrites" Citation: AIP Conference Proceedings 1860, 020008 (2017);
   DOI: 10.1063/1.4990307

View online: http://dx.doi.org/10.1063/1.4990307

2. **Tchouank Tekou Carol T.**, J. Mohammed, Jyoti Sharma, U. T. Isma'il, Sachin Kumar, H. Y. Hafeez and **A. K. Srivastava**, "Structural, dielectric and magnetic properties of Al-Mn substituted nano-sized M-type strontium hexagonal ferrites"
   DOI: https://doi.org/10.1016/j.matpr.2019.06.392

View online: https://www.sciencedirect.com/science/article/pii/S2214785319317626

3. **Tchouank Tekou Carol T.**, Amar Srivastava, J. Mohammed, Shaweta Sharma, G. Mukhtar, **A. K. Srivastava**, "Investigation of energy band of the composite of hexaferrites and polyaniline",
   DOI: https://doi.org/10.1007/s42452-020-2516-7

View online: https://link.springer.com/content/pdf/10.1007/s42452-020-2516-7.pdf

4. **Tchouank Tekou Carol T.**, J. Mohammed, G. Mukhtar, N. Halilu, R. S. Getso, Z. H. Abdullahi, D. Basandrai, **A. K. Srivastava**, "Structural and Optical Properties of $Ba_{0.7}Dy_{0.3}Fe_{11.4}Cr_{0.3}O_{19}$/polyaniline (PANI) nanocomposites for optoelectronics"
   DOI: 10.1088/1742-6596/1531/1/012001

International conference attended

1. International Conference on "Recent Advances in Fundamental and Applied Sciences (RAFAS 2016) held at Lovely Professional University, Punjab, India on 25th-26th December 2016.

2. International Conference on Nanotechnology: Ideas, Innovations and Initiatives (ICN:3I-2017) organised by Department of Mechanical & Industrial Engineering and Centre of Nanotechnology, Indian Institute of Technology (IIT) Roorkee, India on December 6-8, 2017

3. International Conference on Physics, Society and Technology (ICPST-2019) held at University of Delhi, New Delhi, India on January 17-19, 2019

4. International Conference on "Recent Advances in Fundamental and Applied Sciences (RAFAS 2019) held at Lovely Professional University, Punjab, India on 05th-06th November 2019.

Workshops attended

1. Workshop on Scientific Writing Using Typesetting Software LaTeX organised by Department of Mathematics, School of Physical Sciences and Chemical Engineering, Lovely Professional University, Punjab, India on 6-7 April 2019.

2. National Workshop on Advance Instrumentation, organised by Central Instrumentation Facility, Division of Research and Development, Lovely Professional University, Punjab, India on 20th April, 2019.

Curriculum vitae

Personal Data

Name: Tchouank Tekou Carol Trudel

Nationality: Cameroonian

Marital Status: Single

Date of Birth: 01/01/1992

Email address: ttctcadel@gmail.com

Career objective

To contribute to the development of science in the world and in my country in particular

Educational institutions attended

Lovely Professional University, Punjab State, India	2016-2019
University of Yaounde I, Yaounde, Cameroon	2010-2015
Classic high school of Nkolbisson, Yaounde, Cameroon	2008-2010

Academic qualifications

PhD. Physics	2016-2019
M. Sc. Physics	2013-2015
B. Sc. Physics	2010-2013

Research Topics

B. Sc. Physics (2013)
M. Sc. Physics (2015)
Topic of thesis: AB initio study of the electronic structure of nanotubes of gallium nitride.

PhD. Physics (2019)
Topic of thesis: Study of Composites Comprising of Hexaferrite, Bismuth Copper Titanate and Conducting Polymer for Electromagnetic Shielding.

Software

Origin, Inkscape, X-powder, LaTeX, Imagej, IRsolution, SPSS, Vesta and Fullproof

Data interpretation strength

XRD, FTIR, Raman spectroscopy, FESEM/EDX, TEM/HRTEM/SAED, UV-vis spectroscopy, Impedance analyser, LCR meter, VSM, and VNA

Hobby

Playing football, singing the praises of the LORD

Professional experience

Relationship Marketing Consultant

Referee

Dr. A. K. Srivastava (PhD. Thesis Advisor)

(Associate Professor)

Department of physics,

Lovely Professional University,

School of Physical Sciences and Chemical Engineering,

Phagwara-144411,

Punjab, India.